

https://dspace.org/

Boron and nitrogen doped carbons for photochemical degradation reactions.

Tetana, Zikhona Nobuntu

2014-06-19
http://hdl.handle.net10539/14811

Downloaded from a DSpace repository. https://dspace.org/

BORON AND NITROGEN DOPED CARBONS FOR PHOTOCHEMICAL DEGRADATION REACTIONS

by

Zikhona Nobuntu Tetana

Student Number: 0002145N

A thesis submitted to the Faculty of Science at The University of the Witwatersrand, Johannesburg, in fulfilment of the requirements for the degree of

Doctor of Philosophy in Chemistry

Johannesburg, 2013

DECLARATION

I declare that this thesis is my own, unaided work under the supervision of Professor Neil J. Coville and Professor Rui W.M. Krause. It is being submitted for the degree of Doctor of Philosophy in the University of the Witwatersrand, Johannesburg. It has not been submitted before for any degree or examination in any other University.

(Signed) Zikhona Nobuntu Tetana

On this ----------day of ---------- 2013

ABSTRACT

TiO_2 photocatalytic technology has a great potential for industrial use to provide solutions to the energy crisis and serious environmental challenges. Carbon nanomaterials such as nitrogen and boron doped multiwalled carbon nanotubes (MWCNTs) and carbon spheres (CSs) can be considered as good supports for TiO_2 because of their unique properties, which favour the diffusion of reacting agents. TiO_2-carbon composites are increasingly becoming important in the future of photocatalytic degradation of dye pollutants, because carbon materials can efficiently adsorb pollutants in water and also increase the photoactivity of TiO_2 by acting as electron traps, thereby stabilizing the charge carriers and slowing down the rate of electron-hole recombination. In this study we investigate N and B doped MWCNTs and CSs and compare their activities with undoped carbons as potential supports for TiO_2 catalyst.

A CVD method was used to prepare high quality nitrogen-doped multiwalled carbon nanotubes (N-MWCNTs) using acetonitrile as the nitrogen and carbon source and acetylene as a carbon source over an Fe-Co/$CaCO_3$ catalyst in the temperature range 700-850 °C. The effect of synthesis parameters (growth temperature and CH_3CN vaporization temperature) on the yield, size, quality, morphology and thermal stability of the N-MWCNTs was studied. The resulting materials were characterized by TEM, SEM, TGA, BET, XPS, CN elemental analysis and Raman spectroscopy. TEM analysis revealed that the nanotubes exhibit bamboo-like structures with rough surfaces and a relatively uniform diameter. The bamboo compartment distance decreased with increase in synthesis temperature due to the increased nitrogen content in the N-MWCNTs. The SEM examination showed that at high synthesis temperatures carbon spheres (CSs) with chain-like morphology and large sizes were also formed along with the N-MWCNTs. The XPS and CN elemental analysis data revealed that nitrogen atoms were successfully doped into the carbon walls. The amount of nitrogen incorporated in the N-MWCNTs varied with increasing growth time and CH_3CN vaporization temperature.

In another study, the synthesis of N-doped carbon spheres (N-CSs) using a vertical CVD reactor in the absence of a metal catalyst was evaluated. The effects of varying gas flow rates,

using C_2H_2 as a carbon source, CH_3CN as a nitrogen (and carbon) source and Ar as a carrier gas, for the production of nitrogen doped (and undoped) CSs using a vertical CVD reactor. The surface and structural properties of the carbon spheres were investigated TEM, XRD, Raman spectroscopy, BET surface area and pore size measurements, thermogravimetric analysis, CN elemental analysis, and XPS. The size of the carbon materials and the amount of nitrogen incorporated can be controlled by tuning the feedstock flow rates. The carbon spheres have high purity (> 99%). Both XPS and CN elemental analysis confirmed the presence of nitrogen in the N-containing materials. The maximum nitrogen concentration in these materials is ~2.9% when the total gas flow rate is 140 ml/min and ~4.4 % when the total gas flow rate is increased to 540 ml/min. CN elemental analysis indicated that the nitrogen concentration increased with increasing total gas flow rate, suggesting that both the yield and the concentration of the N-atoms in the N-containing CSs closely correlate with the total gas flow rate used. The N-doped CSs showed lower thermal stability and degree of graphitization as compared to the undoped CSs.

The synthesis of boron-containing multiwalled carbon nanotubes (B-MWCNTs) was achieved. B-MWCNTs were formed in the temperature range 700-900 °C via a CVD method using Fe-Co/$CaCO_3$ as the catalyst, acetylene as the carbon precursor and trimethyl borate as boron (and carbon) sources. The effects of boron doping and pyrolysis temperature on the formation of B-MWCNTs were studied. The resulting materials were characterized by TEM, EDX, TGA, BET, XPS, XRD, FT-IR and Raman spectroscopy. The synthesis temperature and the boron source played a key role in determining the structures of the products. A range of different structures were synthesized: rough and bamboo-like tubes in which the inside of the contained compartments, bulbous-shaped catalyst filled tubes as well as solid and core-shell CSs. The optimum temperature for the synthesis of the B-MWCNTs was found to be 800 °C (B = 1.6%, as determined by XPS analysis). The B-MWCNTs exhibited good thermal stability in air.

Large amounts of core-shell boron-doped carbon spheres (B-CSs) have been formed via a non-catalytic CVD method at 900 °C using acetylene as the carbon precursor and trimethyl borate as carbon and boron sources. The B-CSs were synthesized using either a horizontal or a vertical furnace. The properties of the produced materials were compared to undoped carbon spheres (CSs) synthesized in a vertical furnace. The morphology, size and yield of the B-CSs were tuned by varying the ratio of the Ar to H_2 gas ratios including the type of furnace

(horizontal vs. vertical furnace). TEM was used to evaluate the morphology and the diameter of the produced materials. The undoped CSs were spherical and solid, while boron-doping produced core-shell spherical CSs. The B-CSs produced from 100% Ar, both made in a horizontal furnace (average diameter 400 nm, shell thickness 25 nm) or in a vertical furnace (average diameter 350 nm, shell thickness 50 nm) were not uniform in size. The B-CSs produced from a mixture of Ar to H_2 gas with ratios varying from 95:5 to 0:100 were uniform in size and had average diameters of 250 nm with shell thickness of 50 nm. Two samples synthesized with 100% Ar and 100% H_2 were analyzed by XPS. The level of boron doping in these two samples was found to be 3.92 and 0.19 wt% of B, respectively. The thermal stability, purity and quality of the CSs were evaluated by TGA, XRD and Raman spectroscopy. BET analysis and FT-IR spectroscopy were used to evaluate the surface areas, and the chemical bonding found in the synthesized carbon spheres. A possible formation mechanism for the B-CSs is proposed.

Some of the synthesized N and B doped MWCNTs, N and B doped CSs as well as undoped MWCNTs and CSs were used as supports for TiO_2 catalyst. The TiO_2-C composites with different TiO_2:C ratios were prepared by a sol-gel method in order to investigate their photocatalytic activity under solar irradiation for the degradation of erythrosine B in aqueous solution. Data were compared with a commercial TiO_2, Degussa P25. The prepared composites were characterized by TEM, XRD, Raman spectroscopy, FT-IR, XPS techniques. The presence of doped carbon nanomaterials at lower levels enhanced photoefficiency of TiO_2 as compared to TiO_2 with higher C levels and commercial TiO_2.

DEDICATION

I would like to dedicate this thesis to the following people:

- Tetana family: Bulelwa, Lindile, Xolisa, Zibuko, Mwezi, Lunga, Liyabona and Lithalomso. I wish to thank you for all the prayers, support and motivation since the beginning of my studies.

- My best friend and fiancé John Cabunda who never stopped showing me his intense love and support throughout the years.

ACKNOWLEDGEMENTS

Foremost, I would like thank my supervisor Professor Neil J. Coville outstanding contributions to the success of this research project. His expertise and patience significantly added to my research skills. He made a difference in my life and became more of a father than a supervisor.

I would also like to offer my sincere gratitude to my co-supervisors Professor Rui W.M. Krause (Rhodes University) and Dr Sabelo D. Mhlanga (University of Johannesburg, DFC) for their kind guidance and fruitful discussions.

This thesis would not have been complete without the facilities provided by the University of the Witwatersrand and University of Johannesburg (DFC) to conduct my research. Special thanks go to Alex, Sacko and Nsika from University of Johannesburg for their assistance with the photocatalysis experiments.

I also thank Dr R.M. Erasmus of the Raman and Luminescence Laboratory, School of Physics at the University of the Witwatersrand, for the Raman spectroscopy analysis, Mr W. Jordaan of the National Metrology Institute of South Africa, Pretoria, and Ms Edith Antunes (Rhodes University), for the XPS measurements as well as Mr M.F. Philpott from the ARC - Institute for Soil, Climate and Water, for C and N elemental analysis. The invaluable technical support given by the University of the Witwatersrand Microscopy and Microanalysis Unit is also appreciated. Special thanks go to Prof. M. J. Witcomb, Prof. A. Ziegler and the late Mr. A. R. Seema.

I am also grateful to Dr Messai Mamo (University of Johannesburg), Prof. Alan Sustaita (Universidade Federal do Paraná), Prof. Ivo Hümmelgen (Universidade Federal do Paraná), Mr George Bepete (School of Chemistry, Wits University), Prof. Sekhar Ray (School of Physics, Wits University), Dr. Rudolph Erasmus (School of Physics, Wits University) and Dr. Ashish Mathur (NIBEC, University of Ulster, UK), for their fruitful collaboration.

I would also like to thank all CATOMAT group members, past and present, for providing an interesting and enjoyable working environment.

This research would not have been possible without the financial assistance of CSIR and DST/NRF Centre of Excellence in Strong Materials. I am also grateful for The Vice-Chancellor Merit scholarship award.

I thank my family for the support they provided me throughout my entire life. I owe special thanks to my fiancé John Cabunda who supported, encouraged and advised me. May the Lord God bless you for all you have done.

I finally wish to thank God Almighty for His endless love, support, strength, and courage He gave as I engaged in this research.

PUBLICATIONS AND PRESENTATIONS

Publications

1. **Z.N. Tetana**, S.D. Mhlanga, G. Bepete, R.W.M. Krause, and N.J. Coville, "The synthesis of nitrogen-doped multiwalled carbon nanotubes using an Fe-Co/$CaCO_3$ catalyst", *South African Journal of Chemistry"*, 2012, 65, 39-49.
2. G. Bepete, **Z.N. Tetana**, S. Lindner, M.H. Rümmeli, Z. Chiguvare and N.J. Coville. "The use of aliphatic alcohol chain length to control the nitrogen type and content in nitrogen doped carbon nanotubes". *Carbon*, 2013, 52, 316-325.
3. M.A. Mamo, A.O. Sustaita, **Z.N. Tetana**, N.J. Coville and I.A. Hümmelgen, "Nitrogen-doped, boron-doped and undoped multiwalled carbon nanotube/polymer composites in WORM memory devices", *Nanotechnology*, 2013, 24, 125203 /1-125203/7.
4. C. Papo, **Z. Tetana**, P. Franklyn, S. Mhlanga, Synthesis and Study of Carbon/TiO_2 and Carbon/TiO_2 Core-shell Micro-/nanospheres with Increased Density, *Journal of Materials Research.*, 2013, 28, 440-444.
5. S.C. Ray, **Z.N. Tetana**, R. Erasmus, W.-F. Pong and N.J. Coville, "Nitrogen-doped carbon spheres: an X-ray absorption near-edge structure spectroscopy study", *Applied Physics A*: *Materials Science & Processing*, 2013, DOI 10.1007/s00339-013-7853-6.
6. S.C. Ray, **Z.N. Tetana**, R. Erasmus, A. Mathur and Neil J. Coville, "Carbon spheres for energy applications: Raman and X-ray photoemission spectroscopy studies", *International Journal of Energy Research*, 2013, Special Issue on Nano Energy Technologies, DOI: 10.1002/er.3079.
7. **Z.N. Tetana**, S.D. Mhlanga, R.W.M. Krause, and N.J. Coville, "Large-scale synthesis of nitrogen-doped carbon spheres (N-CSs) using a vertical CVD reactor". **To be submitted.**
8. **Z.N. Tetana**, S.D. Mhlanga, R.W.M. Krause, and N.J. Coville, "The synthesis and characterization of boron-containing multiwalled carbon nanotubes using an Fe-Co/$CaCO_3$ catalyst". **To be submitted.**

9. **Z.N. Tetana**, S.D. Mhlanga, R.W.M. Krause, and N.J. Coville, "Novel CVD syntheses and characterization of core-shell boron-doped carbon spheres". **To be submitted.**
10. **Z.N. Tetana**, S.D. Mhlanga, R.W.M. Krause, and N.J. Coville, Photocatalytic activities of carbon nanomaterials coated with TiO_2 for the degradation of erythrosine B". **To be submitted.**

Presentations

1. The Synthesis of Nitrogen-Doped Multiwalled Carbon Nanotubes Using an Fe-Co/$CaCO_3$ Catalyst". Oral presentation, Vaal University of Technology. Obtained **1st Prize** in the PhD category at the Young Researchers Symposium (NYRS), 14th October 2011.
2. Z.N. Tetana, "Large-scale synthesis of nitrogen-doped carbon spheres (N-CSs) using a vertical CVD reactor", Oral presentation, University of the Free State, Nano Africa 2012 conference, 1st April 2012.
3. Z.N. Tetana, S.D. Mhlanga, R.W.M. Krause and N.J. Coville, "The Synthesis of Nitrogen-Doped Multiwalled Carbon Nanotubes Using an Fe-Co/$CaCO_3$ Catalyst", Student poster presentation workshop, DST/NRF CoE in strong materials, University of the Witwatersrand, 30th May 2012.
4. Z.N. Tetana, "Boron doping effects in carbon spheres". Oral presentation, DST/NRF CoE in strong materials research showcase, University of the Witwatersrand, 26th October 2012. Obtained **1st Prize.**
5. Z.N. Tetana, "Boron and nitrogen doped carbons for photochemical degradation reactions", PhD exit talk, School of Chemistry, University of the Witwatersrand, 24th July 2013.

TABLE OF CONTENTS

Title **Page Number**

DECLARATION.....I

ABSTRACT..... II

DEDICATION.....VI

ACKNOWLEDGEMENTS VII

PUBLICATIONS AND PRESENTATIONS.....IX

TABLE OF CONTENTS XI

LIST OF FIGURES XVIII

LIST OF TABLES XXVIII

ABBREVIATIONS..... XXXI

Chapter 1

Introduction……..1

1.1 Background and motivation……1

1.2 Aims and objectives of the study……..3

1.3 Organization of the thesis……...4

References.....6

Chapter 2

Literature review…….....8

2.1 Introduction.....8

2.2 Characteristics and classification of carbon nanomaterials (CNTs and CSs).....9

2.2.1 Carbon anaotubes……9

2.2.2 Carbon spheres……...10

2.3 Synthesis of carbon nanomaterials……..10

2.3.1 Synthesis of CNTs……..10

2.3.2 Synthesis of CSs……..12

2.4 Modification of carbon nanomaterials structure……...13

2.4.1 Doping and functionalization of carbon nanomaterials……13

2.4.2 Synthesis of N and B doped carbon nanomaterials……15

2.5 The use of TiO_2 photocatalyst for water purification……15

2.6 TiO_2/carbon composite materials……18

References.....19

Chapter 3

The Synthesis of NitrogeN-Doped Multiwalled Carbon Nanotubes using an Fe-Co/$CaCO_3$ catalys...……25

3.1 Introduction……...25

3.2 Experimental…….27

3.2.1 Catalyst preparation……..27

3.2.2 Fabrication and purification of N-MWCNTs……28

3.2.3 Carbon yield calculation……..28

3.2.4 Characterization of N-MWCNTs……...29

3.3 Results and Discussion……29

3.3.1 Structural analysis of N-MWCNTs……29

3.3.2 Yield of N-MWCNTs……..36

3.3.3 BET surface area and pore volume analysis of N-MWCNTs……..37

3.3.4 Thermogravimetric analysis of N-MWCNTs……37

3.3.5 Elemental (C and N) analysis of N-MWCNTs……...41

3.3.6 Raman spectroscopy analysis of N-MWCNTs……..42

3.3.7 XPS analysis of purified N-MWCNTs grown at 800 °C using CH_3CN at r.t……...42

3.4 Conclusion……46

References……47

Appendix A: Supplementary material……..52

Chapter 4

Large-scale Synthesis of Nitrogen-Doped Carbon Spheres (N-CSs) using a vertical CVD reactor……..59

4.1 Introduction……...59

4.2 Experimental.....62

4.2.1 Synthesis of CSs and N-CSs……..62

4.2.2 Characterization of CSs and N-CSs…….63

4.3 Results and Discussion…….64

4.3.1 Structural analysis of the carbon spheres……65

4.3.1.1 TEM analysis……..65

4.3.1.2 XRD and Raman analysis of the CSs and N-CSs……68

4.3.1.3 BET surface area and pore volume analysis of CSs and N-CSs……70

4.3.1.4 Thermogravimetric analysis of the CSs and N-CSs…….71

4.3.1.5 XPS and elemental analyses of the CSs and N-CSs…….73

4.4 Formation of N-CSs……..75

4.5 Conclusions……76

References……77

Appendix B: Supplementary material……..81

Chapter 5

The Synthesis and Characterization of Boron-Containing Multiwalled Carbon Nanotubes using an Fe-Co/$CaCO_3$ catalyst.....84

5.1 Introduction.....84

5.2 Experimental.....88

5.2.1 Catalyst preparation.....88

5.2.2 Synthesis and purification of B-MWCNTs.....88

5.2.3 Characterization of B-MWCNTs…….89

5.3 Results and discussion.....90

5.3.1 Structural analysis of B-MWCNTs.....90

5.3.2 BET surface areas, pore volumes and pore diameters of the purified B-MWCNTs.....101

5.3.3 Thermogravimetric analysis (TGA) of the purified B-MWCNTs.....102

5.3.4 XPS analysis of the purified B-MWCNTs.....107

5.3.5 XRD, Raman spectroscopy and FT-IR spectroscopy analysis of the purified B-MWCNTs.....108

5.4 Conclusions.....115

References.....117

Appendix C: Supplementary material……121

Chapter 6

Novel CVD Synthesis and Characterization of Core-shell Boron-Doped Carbon Spheres.....127

6.1 Introduction.....127

6.2 Experimental.....129

6.2.1 Characterization of undoped and B-doped CSs……...131

6.3 Results and discussion.....132

6.3.1 Structural analysis of undoped and B-doped CSs.....133

6.3.2 XPS analysis of the B-doped CSs (sample 2 and sample 7) and undoped CSs.....142

6.3.3 Thermogravimetric analysis of undoped and purified B-doped CSs.....145

6.3.4 XRD and Raman spectroscopy analysis of undoped and B-doped CSs.....151

6.3.5 FT-IR studies of undoped and B-doped CSs.....157

6.3.6 Mechanism of core-shell structures formation.....159

6.4 Conclusions……..160

References……..161

Appendix D: Supplementary material……165

Chapter 7

Photocatalytic Activities of Carbon Nanomaterials Coated with TiO_2 for the Degradation of Erythrosine B.....169

7.1 Introduction…….169

7.2 Experimental.....172

7.2.1 Synthesis of TiO_2-C composite materials.....173

7.2.2 Characterization of TiO_2-C composite materials.....174

7.2.3 Evaluation of photocatalytic activities of TiO_2-C composite materials.....175

7.3 Results and discussion.....176

7.3.1 Morphology and structure of the TiO_2-C composite materials.....176

7.3.2 XRD analysis of TiO2-C composite materials.....178

7.3.3 Raman spectroscopy studies of TiO_2-C composite materials.....181

7.3.4 Fourier Transform Infrared (FT-IR) spectroscopy studies of the TiO_2-C composite material.....184

7.3.5 X-ray Photoelectron Spectroscopy (XPS) analysis of the TiO_2-0.2%B-MWCNT composite materials.....186

7.3.6 Photocatalytic activity of TiO_2-C composite materials.....189

7.4 Conclusions……..196

References……..197

Appendix E: Supplementary material……201

Chapter 8

General Conclusions and Recommendations.....202

LISTS OF FIGURES

Chapter 3

Figure 3.1: TEM images of the purified N-MWCNTs grown using CH_3CN (r.t.) and reaction temperatures of (a) 700 °C, (b) 750 °C, (c) 800 °C and (d) 850 °C.....31

Figure 3.2: TEM images of the purified N-MWCNTs grown using CH_3CN (50 °C) and reaction temperatures of (a) 700 °C, (b) 750 °C, (c) 800 °C and (d) 850 °C.....32

Figure 3.3: TEM images of the purified N-MWCNTs grown using CH_3CN (80 °C) and reaction temperatures of (a) 700 °C, (b) 750 °C, (c) 800 °C and (d) 850 °C.....33

Figure 3.4: SEM images of the purified N-MWCNTs grown at 850 °C using CH_3CN at: (a) r.t., (b) 50 °C.....35

Figure 3.5: Graph showing the amounts of N-MWCNTs grown at 700-850 °C using CH_3CN at r.t., 50 °C and 80 °C.....36

Figure 3.6: TGA and corresponding derivative profiles of the as-synthesized N-MWCNTs using CH_3CN at: (a) r.t., (b) 50 °C and (c) 80 °C.....39

Figure 3.7: Types of nitrogen-based species that can be incorporated into graphitic carbon: A) oxidised pyridinic, B) pyridinic, C) pyrrolic, D) quaternary.....41

Figure 3.8: Deconvoluted N 1s XPS spectra of the purified N-MWCNTs synthesized at 800 °C using CH_3CN at r.t.....45

Figure S1a: Diameter distributions of the purified N-MWCNTs grown at 700-850 °C using CH_3CN at r.t..……...52

Figure S1b: Diameter distributions of the purified N-MWCNTs grown at 700-850 °C using CH_3CN at 50 °C……...…….53

Figure S1c: Diameter distributions of the purified N-MWCNTs grown at 700-850 °C using CH_3CN at 80 °C……...…….54

Figure S2: SEM images of the purified N-MWCNTs grown using CH_3CN at 80 °C: (a) 800 °C and (b) 850 °C…….……55

Figure S3: TGA curves of the as-synthesized and purified N-MWCNTs grown at 700-850 °C using CH_3CN at r.t…….....55

Figure S4: TGA curves of the as-synthesized and purified N-MWCNTs grown at 700-850 °C using CH_3CN at 50 °C……...56

Figure S5: TGA curves of the as-synthesized and purified N-MWCNTs grown at 700-850 °C using CH_3CN at 80 °C……...56

Figure S6: Raman spectra of the purified (700P-850P) and as-synthesized (700-850, inset) N-MWCNTs using CH_3CN at r.t...…….....57

Figure S7: Raman spectra of the purified (700P-850P) and as-synthesized (700-850, inset) N-MWCNTs using CH_3CN at 50 °C…..…….57

Figure S8: Raman spectra of the purified (700P-850P) and as-synthesized (700-850, inset) N-MWCNTs using CH_3CN at 80 °C…..…….58

Figure S9: XPS spectra of the purified N-MWCNTs synthesized at 800 °C using CH_3CN at r.t..……...58

Chapter 4

Figure 4.1: TEM images of the undoped CSs and N-doped CSs obtained at total constant gas flow rates of 140 and 540 ml/min…..……..66
Figure 4.2: Diameter distribution of N-CSs synthesized at total constant gas flow rates of 140 and 540 ml/min…..……..67

Figure 4.3: Diameter distribution of CSs synthesized at total constant gas flow rates of 140 and 540 ml/min...…….67

Figure 4.4: XRD patterns of the synthesized CSs and N-CSs.....68

Figure 4.5: Raman spectra of the CSs and N-CSs...…….....70

Figure 4.6: TGA profiles run in air of the synthesized CSs and N-CSs.……...72

Figure 4.7: The corresponding derivative profiles of synthesized the CSs and N-CSs…72

Figure 4.8: Types of nitrogen-based species that can be incorporated into graphitic carbon: A) oxidised pyridinic, B) pyridinic, C) pyrrolic, D) quaternary…….....74
Figure 4.9: Deconvolution of the XPS N 1s peaks of the N-Ss-540.…….....75

Figure S1: The deconvoluted Raman spectrum of N-CSs-540..…….....81

Figure S2: The deconvoluted Raman spectrum of CSs-540…..…….81

Figure S3: The deconvoluted Raman spectrum of CSs-140..…….82

Figure S4: The deconvoluted Raman spectrum of N-CSs-140..…….....82

Figure S5: The survey XPS of CSs-540.…….....83

Chapter 5

Figure 5.1: Typical TEM images (taken at different magnifications) of the purified undoped MWCNTs grown at 700 °C……...90

Figure 5.2: TEM images (taken at different magnifications) of the purified B-MWCNTs grown at 700 °C……...……...……92

Figure 5.3: TEM images (taken at different magnifications) of the purified B-MWCNTs grown at 750 °C…….....……92

Figure 5.4: TEM images (taken at different magnification) of the purified B-MWCNTs grown at 800 °C.....…….....93

Figure 5.5: TEM images (taken at different magnification) showing various shapes of the unpurified carbon materials grown at 850 °C: (a) straight bamboo-like tube and catalyst filled tube with a closed end; (b) very rough bamboo-like tube; (c) elbow-shaped bamboo-like tube; (d) Y-junction hollow tube; (e) core-shell CSs; (f) catalyst filled tubes with bulbous-shaped catalysts….……..95

Figure 5.6: TEM images (taken at different magnification) showing various shapes of the purified carbon materials grown at 850 °C: (a) an open-end tube and (b) closed end tubes showing no catalyst particles inside; (c) hollow tube showing the absence of the bulbous-shaped catalysts; (d) catalyst filled tube with a closed end; (e) the corresponding EDX spectrum of the catalyst particles in (d); a catalyst and a catalyst free tube with a closed end; (g) the corresponding EDX spectrum of the catalyst particles in (f). The arrows indicate points where the corresponding EDX spectrum was collected……...97

Figure 5.7: TEM images (taken at different magnification) of the unpurified carbon materials grown at 900 °C collected from the boat: (a) CNTs with thicker walls and core-shell CSs; (b) core-shell CSs; (c) catalyst filled long tube with bulbous-shaped catalysts; (d) catalyst filled short tube with bulbous-shaped catalyst; (e) EDX spectrum of the bulbous area in (d); (f) catalyst filled tube with a closed end; (g) the corresponding EDX spectrum of the catalyst particles in (f). The arrows indicate points where the corresponding EDX spectrum was collected.....…….99

Figure 5.8: TEM images (taken at different magnification) of the purified carbon materials grown at 900 °C collected from the boat: (a) closed end tubes showing no catalyst particles inside; (b) uniform core-shell CSs; (c) various sizes of core-shell CSs; (d) thicker walled tubes with catalyst particles (the darker region); the corresponding EDX spectrum of the catalyst particles in (d). The arrow indicates a point where the corresponding EDX spectrum was collected.....……...100

Figure 5.9: TEM images of the fluffy material formed at 900 °C collected from the wall of the quartz tube: (a) solid and core-shell CSs; (b) and (c) different types of core-shell CS..…….100

Figure 5.10a: TGA curves of the purified B-MWCNTs grown at 700-900 °C compared with undoped MWCNTs....……..103

Figure 5.10b: Derivative profiles of the purified B-MWCNTs grown at 700-900 °C compared with undoped MWCNTs..…….....104

Figure 5.11a: The survey XPS of the purified B-MWCNTs grown at 800 °C..……..106

Figure 5.11b: Deconvoluted B 1s XPS spectra of the purified B-MWCNTs grown at 800 °C..…….108

Figure 5.12: XRD spectra of the purified B-doped MWCNTs grown at 700-900 °C compared with undoped MWCNTs. The asterisks label the peaks associated with the metal catalyst.....…….....109

Figure 5.13: XRD spectra of the solid and core-shell carbon spheres formed at 900 °C compared with boric acid. All peaks labeled with asterisks can be indexed as B_2O_3.....111

Figure 5.14: FT-IR spectra of the undoped and B-doped MWCNTs grown at 700-900 °C compared with boric acid. (i) undoped CNTs; B-doped MWCNTs grown at (ii) 700 °C, (iii) 750 °C, (iv) 800 °C, (v) 850 °C and (vi) 900 °C; (vii) boric acid.....…….....112

Figure 5.15: Raman spectra of the purified B-doped MWCNTs grown at 700-900 °C compared with undoped MWCNTs.....…….114

Figure S1: Diameter distributions of the purified B-MWCNTs grown at 700-850 °C……...121

Figure S2: TEM images (taken at different magnifications) of the unpurified carbon materials grown at 900 °C: (a) catalyst filled tube with bulbous-shaped catalyst; (b) the corresponding EDX spectrum of the bulbous area in (a); (c) catalyst filled tube with open end showing the entire image of (a); (d) the corresponding EDX spectrum of the catalyst particles in (c). The white arrows indicate points where the corresponding EDX spectrum was collected.....…….....122

Figure S3: TGA curves of boric acid and CSs formed at 900 °C..…….....123

Figure S4: TGA derivative curves of boric acid and CSs formed at 900 °C……..123

Figure S5: Deconvoluted C 1s XPS spectrum of B-doped MWCNTs synthesized at 800 °C..……124

Figure S6: Deconvoluted O 1s XPS spectrum of B-doped MWCNTs synthesized at 800 °C.....124

Figure S7: XRD patterns of the B-CNTs grown at 850 °C: A before and B after purification.……...125

Figure S8: XRD patterns of the B-CNTs grown at 900 °C: A before and B after purification.…….....125

Figure S9: FT-IR spectra of the CSs formed at 900 °C compared with boric acid...…….....126

Figure S10: Raman spectra of boric acid and CSs formed at 900 °C.....…….....…….....126

Chapter 6

Figure 6.1: (a) TEM and (b) SEM images showing the accretion and large quantities of undoped CSs.....……...……133

Figure 6.2: (a-e) TEM images (taken at different magnifications) of sample 1. (f) is the high magnified region of the area indicated in (e)..…….....135

Figure 6.3: (a-e) TEM images (taken at different magnifications)of sample 2. (f) is the high magnification image of one of the core-shell CSs in the sample.....…….136

Figure 6.4: (a-e) TEM images (taken at different magnifications) of sample 3 (f) is the high magnification image of the region shown in (e)..…….....138

Figure 6.5: (a-c) TEM images (taken at different magnifications) of sample 4. (d) is the high magnification image of the region shown by an arrow in (c).....……..139

Figure 6.6: (a-d) TEM images (taken at different magnifications) of sample 5….....140

Figure 6.7: (a-d) TEM images (taken at different magnifications) of sample 6….....141

Figure 6.8: (a-d) TEM images (taken at different magnifications) of sample 7.....142

Figure 6.9a: B 1s XPS spectra of sample 2.....…….....143

Figure 6.9b: B 1s XPS spectra of sample 7.……144

Figure 6.10a: TGA profiles of boric acid, undoped and boron-doped CSs heated in air..…….146

Figure 6.10b: Corresponding DTA profiles for boric acid, undoped and boron-doped CSs..……...150

Figure 6.10c: TGA and corresponding DTA profiles for unwashed and washed Sample 2…….151

Figure 6.11: XRD spectra for boric acid, undoped and boron-doped CSs…...….....152

Figure 6.12: XRD spectra of unwashed and washed sample 2.....…….....153

Figure 6.13: Raman spectra for boric acid, undoped and boron-doped CSs with excitation wavelength of 514.5 nm...……...154

Figure 6.14: Raman spectra for boric acid, unwashed and washed sample 2, with excitation wavelength of 514.5 nm.....……...156

Figure 6.15: FT-IR spectra of boric acid, undoped and boron-doped CS.…….....158

Figure 6.16: FT-IR spectra of (a) boric acid, unwashed and washed sample 2; (b) magnified FT-IR spectrum of washed sample 2.....…….....159

Figure S1: XPS survey spectrum for sample 2.....…….....165

Figure S2: XPS survey spectrum for sample 7...……...166

Figure S3: C 1s XPS spectrum for sample 2…….....166

Figure S4: C 1s XPS spectrum for sample 7....……..167

Figure S5: XPS survey spectrum for undoped CSs...……167

Figure S6: C 1s XPS spectrum for undoped CSs..……168

Figure S7: XRD pattern for boric acid...…….....168

Chapter 7

Figure 7.1: Chemical structure of erythrosine B……..…….....172

Figure 7.2: TEM image of commercial TiO_2 nanoparticles..…..…….....176

Figure 7.3: TEM images of TiO_2-0.2%C composites: (a) TiO_2-CSs, (b) TiO_2-N-CSs, (c) TiO_2-B-CSs, (d) TiO_2-MWCNTs, (e) TiO_2-N-MWCNTs, and (f) TiO_2-B-MWCNTs....177

Figure 7.4: TEM images of TiO_2-10%C composites: (a) TiO_2-CSs, (b) TiO_2-N-CSs, (c) TiO_2-B-CSs, (d) TiO_2-MWCNTs, (e) TiO_2-N-MWCNTs, and (f) TiO_2-B-MWCNTs…178

Figure 7.5: XRD patterns of TiO_2-0.2%C composite materials compared with TiO_2……179

Figure 7.6: XRD patterns of TiO_2-10%C composite materials compared with TiO_2….....180

Figure 7.7a: Raman spectra of TiO_2-0.2%C composite materials showing the TiO_2 bands.....182

Figure 7.7b: Raman spectra of TiO_2-0.2%C composite materials showing the D, G and 2D-bands. Asterisks in the figure are a result of electric spikes..……182

Figure 7.8a: Raman spectra of TiO_2-10%C composite materials showing the TiO_2 bands. Asterisks in the figure are a result of electric spikes…….183

Figure 7.8b: Raman spectra of TiO_2-10%C composite materials showing the D, G and 2D-bands...…..…….....183

Figure 7.9: FT-IR spectra of TiO_2-0.2%C composite materials: (i) TiO_2, (ii) B-CSs, (iii) N-CSs, (iv) CSs, (v) B-MWCNTs, (vi) N-MWCNTs, (vii) MWCNTs.…….....185

Figure 7.10: FT-IR spectra of TiO_2-10%C composite materials: (i) TiO_2, (ii) B-CSs, (iii) N-CSs, (iv) CSs, (v) B-MWCNTs, (vi) N-MWCNTs, (vii) MWCNTs...……...185

Figure 7.11: XPS survey scan of TiO_2-0.2%B-MWCNT composite..…….187

Figure 7.12: Deconvoluted C 1s XPS spectra of the TiO_2-0.2%B-MWCNT composite……...197

Figure 7.13: Deconvoluted O 1s XPS spectra of the TiO_2-0.2%B-MWCNT composite……...188

Figure 7.14: Deconvoluted Ti 2p XPS spectra of the TiO_2-0.2%B-MWCNT composite..……..…...189

Figure 7.15: Photodegradation of EB by TiO_2-0.2%C composite materials…….....190

Figure 7.16: Photodegradation of EB by TiO_2-10%C composite materials....….....191

Figure 7.17: A mechanism demonstrating MWCNTs as electron trappers emitted from TiO_2 nanoparticles due to UV irradiation.…….....193

Figure 7.18: Kinetics of EB degradation by TiO_2-0.2%C composite materials.....194

Figure 7.19: Kinetics of EB degradation by TiO_2-10%C composite materials..……195

Figure S7.1: EDX spectrum of TiO_2-0.2%B-MWCNTs composite material.….....201

Figure S7.2: EDX spectrum of TiO_2-10%B-MWCNTs composite material.……201

LIST OF TABLES

Chapter 3

Table 3.1: The effects of temperature on the outer diameter of the purified N-MWCNTs.....34

Table 3.2: The BET surface areas and pore volume of the purified N-MWCNTs.....37

Table 3.3: Decomposition temperatures and residual masses (determined by TGA) of the as-synthesized and purified N-MWCNTs.....40

Table 3.4: CN elemental analysis of the purified N-MWCNTs.....41

Table 3.5: The D-, G-bands and I_D/I_G ratios of the as-synthesized and purified N-MWCNTs.....42

Table 3.6: XPS analysis of the purified N-MWCNTs grown at 800 °C using CH_3CN at r.t.....45

Chapter 4

Table 4.1: Carbon yields of the CSs and N-CSs...…….....64

Table 4.2: Decomposition temperatures (determined by TGA), Raman shifts, I_D/I_G ratios, BET surface areas and pore volume data of the CSs and N-doped CSs...……70

Table 4.3: CN and XPS measurements of the synthesized carbon spheres……..73

Table S1: The resolved binding energies (eV) and atomic concentrations (%) of N, C and O toms in the N-CSs-540 and CSs-540 samples……...83

Chapter 5

Table 5.4: B-containing CNTs obtained by various synthetic methods using different catalysts and reaction temperatures...…….....85

Table 5.5: The influence of reaction temperature on the formation of boron-containing carbon materials…….....91

Table 5.3: BET surface areas and pore volumes of the purified undoped and B-doped MWCNTs..……101

Table 5.4: TGA analysis of the purified undoped and B-doped MWCNTs.....……...105

Table 5.5: XPS binding energies and chemical composition of elements in B-MWCNTs grown at 800 °C.....…….....107

Table 5.6: Wavenumbers and assignment of Infrared Absorption bands for boric acid.....113

Table 5.7: The D-, G-bands and I_D/I_G ratios of the purified undoped and B-doped MWCNTs.……115

Chapter 6

Table 6.1: Boron-doped carbon microspheres obtained by various synthetic methods using different boron sources…….....…….……...129

Table 6.2: The synthesis parameters, product yield and diameters of the undoped CSs and B-doped CSs (samples 1-7).....…….130

Table 6.3: Elemental composition from XPS of boron-doped and undoped CSs synthesized with different gas ratios...……145

Table 6.4: TGA results for boric acid, undoped and boron-doped CSs……..148

Table 6.5: D-, G-band and I_D/I_G ratios of undoped and B-doped CSs……155

Table 6.6: Wavenumbers and assignment of Infrared Absorption bands for boric acid…….158

Table S1: Surface areas, pore volume and pore diameters of undoped CSs and B-CSs…….165

Chapter 7

Table 7.1: The properties of the carbon materials used in this study.....173

Table 7.2: The average particle sizes of TiO_2-C composite materials compared with TiO_2……..……..180

Table 7.3: Dye adsorption and EB photodegradation under simulated solar irradiation....…….....191

Table 7.4: EB photodegradation rate constants under simulated solar irradiation…..195

ABBREVIATIONS

a. u.	**Arbitrary units**
BET	**Brunauer-Emmett-Teller**
B-CSs	**Boron-doped carbon spheres**
B-MWCNTs	**Boron-doped multiwalled carbon nanotubes**
CNT(s)	**Carbon nanotubes(s)**
CSs	**Carbon spheres**
CVD	**Chemical vapor deposition**
EDX	**Energy dispersive X-ray spectroscopy**
FT-IR	**Fourier transform infrared**
i.d	**Internal diameter**
I_D/I_G ratio	**The intensity ratio of D to G band**
min	**minutes**
ml/min	**Millilitre per minute**
MWCNTs	**Multiwalled carbon nanotubes**
N-CSs	**Nitrogen-doped carbon spheres**
N-MWCNTs	**Nitrogen-doped multiwalled carbon nanotubes**
o.d	**Outer diameter**
SEM	**Scanning electron microscopy**
r.t	**Rom temperature**
TGA	**Thermogravimetric analysis**
TEM	**Transmission electron microscopy**
UV-VIS	**Ultra-violet visible**

CHAPTER 1

Introduction

1.1 Background and motivation

After the reports of carbon nanotubes (CNTs) by Iijima,[1] CNTs (multiwalled or singlewalled) have increasingly attracted considerable attention in a variety of fields owing to their unique properties; large specific surface area, high purity, adsorption ability, as well as their chemical, thermal, structural, mechanical, and electronic properties.[2,3] Because of these unique properties, CNTs have found potential applications in various fields such as sensors,[4] adsorbents,[5] composite materials,[6,7] catalyst supports,[2,8] etc. Other carbon-based materials of interest are carbon nanospheres (CSs). CSs have analogous properties to graphite or fullerene, which allows them to make diamond films, lubricants and rubber additives[9] and similar to CNTs in having high strength, high thermal resistance, high oxidative inertness, light weight and sp^2 hybridized carbon atoms.[10] These CSs are relatively cheaper to produce than CNTs. When prepared by non-catalytic methods, purification is not required. In addition, they are non-porous and can be expected to be good supports in catalysis.[11] CSs have also been used as support materials to deposit metal or metal oxide nanoparticles,[12] as templates to synthesize hollow metal or metal oxide nanospheres[13a-c] and as adsorbents of metal ions in water.[14] The use of carbon nanomaterials in particular multiwalled (MW) CNTs and CSs in water treatment is very attractive and the study of CNT-based metal oxide hybrids (e.g. TiO_2, SnO_2) is becoming a promising area of research in photocatalysis and Li-ion batteries,[15a,b] owing to their improved properties over the single component materials.

However, these potential applications require introduction of functional groups covalently attached the outer surface of MWCNTs and CSs so as to make them processable and to tune their properties. Thus, to fabricate C-based composites and to enhance their adsorption capacities towards metal ions, the inert surfaces of MWCNTs and CSs can be chemically treated with acids, bases, oxidants, polymers, etc.,[16a-c] under mild conditions. Alternatively, it is also possible to functionalize MWCNTs and CSs by substitution reactions such as replacement of C atoms by B and/or N atoms,[17] a term called doping. The substitution of carbon atoms by N or B atoms in the tubular lattice of MWCNTs gives nitrogen-doped MWCNTs (N-MWCNTs) and B-doped MWCNTs (B-MWCNTs), respectively. This is

possible since the atomic sizes of B and N are similar to that of C atom. Doping of MWCNTs with B or N can be used to increase the chemical reactivity of the tube surface and to tune their electrical properties. For example, boron doping of MWCNTs renders them p-type semiconductors while nitrogen doping of MWCNTs renders them n-type semiconductors.[18] Similar properties are expected when CSs are doped with N or B atoms. Boron and nitrogen doping can introduce chemically active sites into the carbon nanomaterials framework, which act as the anchoring sites to support metal or metal oxide nanoparticles. Wang and co-workers[15b] prepared SnO_2-N-MWCNT nanocomposites which presented higher photocatalytic activity than pure SnO_2 and SnO_2-MWCNT nanocomposites for degradation of Rhodamine B. In another study, B-MWCNTs supported platinum nanoparticles facilitated the removal of CO from a Pt surface, resulting in greater electrocatalytic activity for methanol oxidation.[19] Xiong *et al.*[12] prepared nitrogen-doped CSs (N-CSs) supported cobalt catalyst which showed better Fisher-Tropsch synthesis performance than the undoped Co-CSs which was attributed to the higher cobalt dispersion of the N-CSs.

Water plays very important roles in many aspects of life. However, when contaminated it can be a major threat to the environment. Wastewater containing organic pollutants such as xanthene dyes from food, cosmetics and the textile industries are of concern because some of them are toxic and exhibit poor biodegrability.[20a,b] Therefore, effective water treatment techniques are required that significantly reduce water pollution levels. Heterogeneous photocatalysis has so far been shown to be a promising technology leading to complete destruction of organic pollutants to H_2O and CO_2, sulphates, nitrates, etc.[21a-c] Among other semiconductors used for water treatment, TiO_2 is a preferred material for eliminating toxic chemicals, owing to its low cost, low toxicity, high photocatalytic activity and chemical stability.[21c,22] Despite many attractive features, TiO_2 does have some drawbacks which impede its performance. Its disadvantage is its larger energy band gap of 3.2 eV, which restricts its use only to UV radiation, thereby limiting its practical application in the visible light region that accounts for about 50% of solar energy.[21c,22,23] Therefore, in order to solve this problem and to enhance the photocatalytic activity of TiO_2, various attempts have been made to develop visible light activated photocatalysts. These include doping TiO_2 with non-metals such as B,[24] C,[25] N,[26] F,[27] S,[28] which were reported to narrow the energy band gap of TiO_2 and shift its optical response to the visible region. Composites which contain CNTs and metal oxides are believed to have many applications as they exhibit synergistic effects between the metal oxide and the carbon phase.[29,30] Literature data has shown that TiO_2-CNT

nanocomposites can effectively adsorb organic pollutants in water and also enhance the rate of photocatalytic activity of TiO_2 nanoparticles by acting as electron traps, thereby stabilizing the charge carriers and inhibiting the rate of electron-hole (e^--h^+) recombination.[30,31]

As mentioned earlier, the application of SnO_2 photocatalysts in the presence of N-MWCNTs has been reported to enhance the photocatalytic degradation of Rhodamine B under UV light irradiation. Up to now, no studies are available on the use of composites containing N and B doped carbons (MWCNTs and CSs) and TiO_2. Taking advantage of the unique properties of the N-doped and B-doped carbons (MWCNTs and CSs), we expect that the combination of doped carbons with TiO_2 may induce charge transfer and thus improve the photocatalytic activity of TiO_2. In this study, undoped, N-doped and B-doped carbon (MWCNTs and CSs) composite photocatalysts were prepared by a sol-gel method. The materials were tested for the photocatalytic degradation of a xanthene dye, erythrosine B in aqueous solution as a model organic pollutant.

1.2 Aims and Objectives of the study

1. Synthesis and characterization of nitrogen-doped multiwalled carbon nanotubes (N-MWCNTs) by a catalytic vapour deposition (CVD) method using acetylene as a carbon source, acetonitrile as carbon and nitrogen sources and Fe-Co/$CaCO_3$ as catalyst.

2. Synthesis and characterization of nitrogen-doped carbon spheres (N-CSs) by a non-catalytic CVD method using acetylene as a carbon source and acetonitrile as carbon and nitrogen sources. The effect of different acetylene and Ar flow rates on the production of N-CSs will be investigated. The properties of the resulting materials will be compared with those of undoped CSs under the same experimental conditions but without using a nitrogen source. The synthesis of the N-CSs and undoped CSs will be carried out in avertically aligned furnace.

3. Synthesis and characterization of boron-doped multiwalled carbon nanotubes (B-MWCNTs) by a catalytic CVD method using acetylene as a carbon source, trimethyl borate as carbon and boron sources and Fe-Co/$CaCO_3$ as catalyst. The properties of the resulting materials will be compared with those of undoped MWCNTs.

4. Synthesis and characterization of boron-doped carbon spheres (B-CSs) in a horizontal and a vertical furnace by a non-catalytic CVD method using acetylene as a carbon source and trimethyl borate as carbon and boron sources. The effect of the ratio of Ar to H_2 gas flow rate on the production of the B-CSs will be investigated and data will then be compared with undoped CSs.

5. Synthesis and characterization of nanocomposites containing TiO_2 supported on the acid-treated undoped, N and B doped carbons (MWCNTs and CSs) by means of a sol-gel method. The resulting TiO_2-C nanocomposites will be characterized and evaluated as photocatalysts for the photocatalytic degradation of erythrosine B (a model pollutant) and data will be compared with a commercial TiO_2.

1.3 Organization of the thesis

Chapter 1 presents an introduction which gives the background, motivation and objectives of this thesis. The introduction is followed by Chapter 2, which gives a short literature review of the carbon nanomaterials (CNTs and CSs) used, their classification, modification with functional groups and non-metals such as nitrogen and boron, and background information on composites that are used in photocatalytic reactions. Chapter 3 presents the study on "The Synthesis of Nitrogen-Doped Multiwalled Carbon Nanotubes using an Fe-Co/$CaCO_3$ Catalyst." In Chapter 4, the results and discussion on work done on the "Large-scale Synthesis of Nitrogen-Doped Carbon Spheres (N-CSs) using a vertical CVD reactor" is presented. Chapter 5 gives the results and discussion on the work done on "The Synthesis and Characterization of Boron-Containing Multiwalled Carbon Nanotubes using an Fe-Co/$CaCO_3$ catalyst." Chapter 6 gives the extensive study on the "Novel CVD Syntheses and Characterization of Core-shell Boron-Doped Carbon Spheres." Chapter 7 reports on the "Photocatalytic Activities of Carbon Nanomaterials Coated with TiO_2 in the Degradation of Erythrosine B." Chapter 8 gives the "General Conclusions" that emanate from the study and recommendations for future work.

The work reported on this thesis has been presented at numerous conferences and seminars. The study reported in Chapter 3 has been published in the South African Journal of Chemistry, 2012, 65, 39-49. Some of the N- and B-doped materials reported in Chapters 3 and 4 have been used to make polymer composites for WORM memory devices. This article

has been published in Nanotechnology. Other publications emanating from this study will follow and be published in 2013.

References

1. S. Iijima, *Nature*, 1991, **354**, 56-58.
2. P. Serp, M. Corrias and P. Kalck, *Appl. Catal. A: General*, 2003, **253**, 337-358.
3. Y. Li, K.A. Watso, M.J. Fallbach, S. Ghase, J.G. Smith, D.M. Delozier, W. Cao, R.E. Crooks and J.W. Connel, *ACS Nano*, 2009, **3**, 2081-2094.
4. Y. Wang and J.T.W. Yeow, *Sensors*, 2009, 1-24.
5. Y.H. Li, Y.M. Zhao, W.B. Hu, I. Ahmad, Y.Q. Zhu, X.J. Peng and Z.K. Luan, *J. Phys.: Conf. Ser.*, 2007, **61**, 698-702.
6. C.-Y. Yen, Y.-F. Lin, C.-H. Hung, Y.-H. Tseng, C.-C. M. Ma, M.-C. Chang and H. Shao, *Nanotechnology*, 2008, **19**, 045604/1-045604/11.
7. W.-C. Oh, F.-J. Zhang and M.-L. Chen, *J. Ind. Eng. Chem.*, 2010, **16**, 321-326.
8. H. Xiong, M.A.M. Motchelaho, M. Moyo, L.L. Jewell and N.J. Coville, *J. Catal.*, 2011, **278**, 26-40.
9. J.-Y. Miao, D.W. Hwang, K.V. Narasimhulu, P.-I. Lin, Y.-T. Chen, S.-H. Lin and L.-P. Hwang, *Carbon*, 2004, **42**, 813-822.
10. Y.Z. Jin, C. Gao, W.K. Hsu, Y. Zhu, A. Huczko, M. Bystrzejewski., M. Roe, C.Y. Lee, S. Acquah, H. Kroto and D.R.M. Walton, *Carbon*, 2005, **43**, 1944-1953.
11. H.F. Xiong, M. Moyo, M.A.M. Motchelaho, L.L. Jewell and N.J. Coville, *Appl. Catal. A: General*, 2010, **388**, 168-178.
12. H.F. Xiong, M. Moyo, M.K. Rayner, L.L. Jewell, D.G. Billing and N.J. Coville, *ChemCatChem.*, 2010, **2**, 514-518.
13. (a) X. Sun, J. Liu and Y. Li, *Chem. Eur. J.*, 2006, **12**, 2039-2047; (b) H. Qian, G. Lin, Y. Zhang, P. Gunawan and R. Xu, *Nanotechnology*, 2007, **18**, 355602/1-355602/6; (c) J. Xu, Y. Ao and M. Chen, *Mater. Lett.*, 2009, **63**, 2442-2444.
14. X. Song, P. Gunawan, R. Jiang, S.S.J. Leong, K. Wang and R. Xu, *J. Hazard. Mater.*, 2011, **194**, 162-168.
15. (a) H. Zhang, G. Cao and Y. Yang, *Energy Environ. Sci.*, 2009, **2**, 932-943; (b) L. Wang, L. Shen, L. Zhu, H. Jin, N. Bing and L. Wang, *J. Nanomater.*, 2012, 794625/1-794625/6.
16. (a) C.Y. Yin, M.K. Aroua and W. Daud, *Sep. Purif. Technol.*, 2007, **52**, 403-415; (b) A. Dermibus, *J. Hazard. Mater.*, 2009, **167**, 1-9; (c) L. Wang, R.G. Xing, S. Liu, H.H. Yu, Y.K. Qin, K.C. Li, J.H. Feng, R.F. Li and P.C. Li, *J. Hazard. Mater.*, 2010, **180**, 577-582.

17. D. Golberg, Y. Bando, W. Han, K. Kurashima and T. Sato, *Chem. Phys. Lett.*, 1999, **308**, 337-342.
18. M. Terrones, A. Jorio, M. Endo, A.M. Rao, Y.A. Kim, T. Hayashi, H. Terrones, J.-C. Charlier, G. Dresselhaus and M.S. Dresselhaus, *Mater. Today*, 2004, **7**, 30-45.
19. S. Wang, T. Cochell and A. Manthiram, *Phys. Chem. Chem. Phys.*, 2012, **14**, 13910-13913.
20. (a) A. Dadal and M.K. Poddar, *Phamarcol. Biochem. Behav.*, 2009, **92**, 574-582; (b) T. Mizutani, *J. Environ. Public Health*, 2009, **2009**, 953952/1-953952/9.
21. (a) S. Aryal, C.K. Kim, K.-W. Kim, M.S. Khil and H.Y. Kim, *Mater. Sci. Eng. C*, 2008, **28**, 75-79; (b) M. Stylidi, D.I. Kondarides and X.E. Verykios, *Appl. Catal. B: Environmental*, 2004, **47**, 189-201; (c) A.L. Linsebigler, G. Lu and T. Yates Jr., *Chem. Rev.*, 1995, **95**, 735-758.
22. A. Fujishima and K. Honda, *Nature*, 1972, **72**, 108-114.
23. M. Ni, M.K.H. Leung, D.Y.C. Leung and K. Sumathy, *Renew. Sustain. Energy Rev.*, 2009, **11**, 401-425.
24. W. Zhao, W.H. Ma, C.C. Chen, J.C. Zhao and Z.G. Shuai, *J. Am. Chem. Soc.*, 2004, **126**, 4782-4783.
25. H. Irie, Y. Watanabe and K. Hashimoto, *Chem. Lett.*, 2003, **32**, 772-773.
26. R. Asahi, T. Morikawa, T. Ohwaki, K. Aoki and Y. Taga, *Science*, 2001, **293**, 269-271.
27. D. Li, H. Haneda, N.K. Labhsetwar, S. Hishita and N. Ohashi, *Chem. Phys. Lett.*, 2005, **401**, 579-584.
28. T. Ohno, *Water Sci. Technol.*, 2004, **49**, 159-163.
29. W. Wang, P. Serp, P. Kalck, and J.L. Faria, *J. Mol. Catal. A*, 2005, **235**, 194-199.
30. G. An, W. Ma, Z. Sun, Z. Liu, B. Han, S. Miao, Z. Miao and K. Ding, *Carbon*, 2007, **45**, 1795-1801.
31. B. Gao, G.Z. Chen and G.L. Puma, *Appl. Catal. B*, 2009, **89**, 503-509.

CHAPTER 2

Literature Review

2.1 Introduction

There is a range of established water-treatment technologies that are in current practice. These include filtration, reverse osmosis, ultraviolet radiation, chemical treatment and desalination. It has however been suggested that nanotechnology-based materials could lead to inexpensive, more durable, and more efficient water treatment technologies that will meet the needs especially of developing countries.[1] In the past decade, nanotechnology routes to water treatment have become popular. Nanotechnology is generally the application of ideas from science and engineering relating to the study of materials with one dimension less than 100 nm for use in the production of new materials and devices. These products make abundant use of physical properties associated with small scales.

Nanomaterials are the materials that are employed in nanotechnology. During the past 20 years, nanomaterials have been the subject of enormous interest. Nanomaterials, noteworthy for their very small characteristic dimensions have the potential for large industrial, biomedical, and electronic applications. Nanomaterials that are known include fullerenes, carbon nanotubes, carbon nanofibers, carbon nanospheres, composite materials or nanomaterial-based heterogeneous catalysts. Their important characteristic is a very small feature dimension in the range of 1-100 nm. Distinct properties such as large surface area and quantum effects are the major reasons why nanomaterials behave significantly differently from bulk materials.[2] These factors can enhance materials' properties such as chemical reactivity, mechanical, optical, electrical and magnetic characteristics[3] when compared to what they exhibit on a macroscale, leading to unique applications for nanomaterials.

Carbon-based TiO_2 composite materials have attracted a great deal of attention in the field of research primarily due to their novel properties and promising applications in solving water pollution problems.[4-6] In this research project the focus will be on the synthesis of boron and nitrogen doped multiwalled carbon nanotubes (MWCNTs) and carbon spheres (CSs); these materials will be compared with their undoped analogues. These carbon nanomaterials will be used to support TiO_2 catalyst for application in organic dye photocatalytic degradation. Up

to now, there is no available study showing the use of these nitrogen and boron doped carbon nanomaterials coupled with TiO_2 for photocatalytic reactions.

2.2 Characteristics and classification of carbon nanomaterials (CNTs and CSs)

2.2.1 Carbon nanotubes

Carbon nanotubes are allotropes of carbon, first highlighted in studies by Iijima[7] in 1991. Since this report, CNTs have received a great deal of interest from researchers focussing on the synthesis, functionalization and applications of CNTs. CNTs consist of graphic sheets which have been rolled up into a cylindrical shape. CNTs are one of the strongest and lightest materials known,[8] both in terms of tensile strength and elastic modulus. These nanomaterials possess many unique and remarkable properties (chemical, physical, and mechanical), which make them desirable for many applications. Such applications include use in hydrogen storage,[9a,b] nanoelectronic devices,[10a,b] flat panel displays,[11a,b] chemical force sensors,[12] scanning probes and in catalysis.[13a,b] CNTs have a diameter in the nano-range and have length(s) ranging from micro- to millimetres.[14] There are two main types of CNTs: singlewalled carbon nanotubes (SWCNTs) formed from a single graphene sheet, and multiwalled carbon nanotubes (MWCNTs) formed with additional graphene sheets wrapped around the SWCNT core. When an additional graphene tube exists around a central SWCNT, a doublewalled carbon nanotube (DWCNT) is formed. Because of their outstanding properties, CNTs can be considered as attractive candidates in diverse nanotechnological applications. SWCNTs are a very important variety of carbon nanotubes because they exhibit important electric properties that are not shared by the multi-walled carbon nanotube variants.[8]

2.2.2 Carbon spheres

The discoveries of fullerenes[15] and the "elongated" fullerenes, the CNTs,[7] have resulted in further developments in nanotechnology and nanoscience of carbonaceous structures. Spherical carbon structures are also important due to their unique properties[16a,b] and potential applications in many industrial fields.[17a-d] Because of their unique properties such as high strength, high thermal resistance and light weight, spherical carbon structures have been used in high strength composites,[18] wear-resistant materials,[19] photonic crystals, as catalyst

supports,[20] anodes in secondary lithium ion batteries[21a,b] or as an adsorbent.[22a,b] These spherical materials with different structures ranging from C_{60} and carbon onions to carbon spheres (CSs) and have closed or unclosed graphene layers.[16a] CSs have two forms: solid and hollow ones. In particular, solid CSs attract an increasing attention due to their many potential applications. These include their use as catalyst supports,[23] electrodes,[24] capsules for magnetic nanoparticles,[25] templates for synthesizing other hollow materials.[26] Hollow CSs are also of great interest due to their large surface area, chemical stability, low density, thermal insulation and high compressive strength.[27]

Serp and co-workers have classified carbon structures into three categories according to size: (i) the C_n family and the well graphitized onion like structures ranging between 2 and 20 nm; (ii) the CSs with diameters between 50 nm to 1 μm; and (iii) the carbon beads with diameters of one to several microns.[17b,18,28,29] Deshmukh *et al*.[30] reported that it is possible to classify CSs in terms of strategies used in their synthesis. They stated that procedures used to make spherical carbon materials such as chemical vapour deposition (CVD), arc discharge, laser ablation, autoclave processes etc., can produce quite different materials.

2.3 Synthesis of carbon nanomaterials

2.3.1 Synthesis of CNTs

Several techniques have been developed to produce CNTs in sizeable quantities, including hydrocarbon pyrolysis using a metal catalyst[31] and carbon monoxide disproportionation on a metal catalyst.[32] The three most commonly used techniques are discussed below:

(i) Arc discharge

CNTs were observed in 1991[7] in the carbon soot of graphite electrodes during an arc discharge, by using a current of 100 A, that was intended to produce fullerenes. However, the technique produced a complex mixture of components that required further purification to separate the CNTs from the soot and the residual catalytic metals present in the crude product. CNTs synthesized by this method are formed through arc-vaporization of two carbon rods placed end to end, separated by approximately 1 mm, in an enclosure that is usually filled with inert gas (e. g. Ar) at low pressure (between 50 and 700 mbar). The high

yield production of CNTs by this method depends on the uniformity of the plasma arc and on the temperature of the deposit produced on the carbon electrode.[33a-d]

(ii) Laser ablation

The laser ablation method was developed by Smalley[34] and co-workers in 1995 at Rice University. In this method, a pulsed laser vaporizes a graphite target in a high-temperature reactor (1200 °C) while an inert gas is added into the chamber. CNTs develop on the cooler surfaces of the reactor as the vaporized carbon condenses.[33d] Laser ablation and arc discharge are currently the major methods for obtaining high quality CNTs. However, both methods have disadvantages: (i) the methods involve evaporating the carbon source at ≥ 3000 °C, so it has been unclear how to produce CNTs in large scale; (ii) CNTs are grown in highly twisted forms, mixed with unwanted forms of carbon and/or metal species. Therefore, it is not easy to purify and control the CNTs for practical applications.[35]

(iii) Chemical Vapour Deposition (CVD)

In the CVD synthesis, a carbon sourceand gas phase metal catalyst particles, most commonly Ni, Co,[36] Fe, or a binary combination,[37] are used. Alternatively, a hydrocarbon is passed over a supported metal catalyst heated to 700 °C. CNTs grow at the sites of the metal catalyst particles; the carbon-containing gas (e.g. C_2H_2) is broken apart at the surface of the catalyst particle, and the carbon is transported through the catalyst or over the catalyst to the edges of the particle, where CNTs are formed. During the growth process, the metal particles can stay at the tips of the growing CNTs (called a tip growth method) or they can remain at the CNTs base (called a base growth method), depending on the interaction between the catalyst particle and the substrate. The diameters of the produced CNTs strongly depend on the size of the metal particles. Of the different methods of CNT synthesis, CVD is the most promising for industrial large scale production in terms of its low cost. Additionally, the growth sites are controllable by careful deposition of the catalyst.

2.3.2 Synthesis of CSs

Although fullerenes are not usually classified as carbon spheres, the spherical shape of carbonaceous materials would include them in this classification. Indeed although fullerenes were made by Kroto *et al.*[38] in small quantities, they were eventually made in large quantities by Krätschmer and co-workers.[39] After the fullerenes and CNT discoveries, various shaped materials structures such as carbon spheres[40] and onion-like structures,[41] etc. were prepared. Ugarte[40] reported that CSs with diameter of a few nanometers were obtained from soots that contain tubular and polyhedral graphitic particles formed under intense high-energy electron-beam irradiation in a high-resolution transmission electron microscopy. Carbon spheres can also be produced as a by-product during the preparation of CNTs or carbon nanofibers, where metal catalysts are employed.[28,32,40,42]

As there is an emerging need for the production of high purity carbon spheres in large quantities, many kinds of preparation methods have been developed.[43,44] CSs have been produced by the methods similar to those used to produce CNTs.[17a,17c, 21a,40,42,45] Methods such as chemical vapour deposition (CVD),[17b,29] arc plasma,[17c] mixed-valence oxide-catalytic carbonization,[18] reduction of carbides with metal catalysts,[46] and pyrolysis of carbon sources and catalyst[40] have been reported for the production of carbon spheres. The CSs obtained by Aili and co-workers from CVD methods were all made with uniform dimensions and in high purity, without any other by-products being detected.[47] Solid carbon spheres (~210 nm diameter) have been prepared by Wang and Kang[17d,29,48] using the thermal decomposition of CH_4 in the presence of a metal oxide catalyst. They claim to have a selective process to produce either carbon spheres at 1100 °C or completely pure CNTs at 950 °C. Govindaraj *et al.*[49] have prepared CSs from the pyrolysis of methane in a hydrogen atmosphere at 1140 °C without a catalyst. Qian *et al.*[18] have also used toluene as a feedstock for the production of CSs without any catalysts. Serp *et al.* have also reported on the production of CSs using a chemical vapour deposition process.[17b]

Hollow CSs have been prepared by different synthesis methods. Su *et al.*[50] synthesized hollow CSs with a controllable structure using silica spheres as templates and benzene as a carbon source by means of a CVD method. Hollow CSs have also been prepared from glucose and Zn particles at 550 °C in a stainless steel autoclave of 30 litre capacity.[51] Other methods for the preparation of hollow CSs include pyrolysis,[52] a solvothermal method[25] and a medial-reduction route.[53]

Of these, the CVD method is the most popular and most cost-effective, and is hence used for the large scale synthesis of high quality carbon spheres. Generally, the preparation of CSs using a CVD method involves a carbon-containing gas such as C_2H_2 as the carbon source. Use of an energy source, such as a plasma or a resistively heated coil, provides the energy for transforming the gaseous carbon molecules into a solid carbon material. In the reaction, the molecules then converted into reactive carbon atoms which then diffuse onto the growing carbon surface, forming carbon spheres. Li *et al.*[54] reported that the growth of carbon spheres results from the thermal decomposition of a carbon precursor into carbon atoms, followed by the precipitation of the carbon deposits. It has been reported that controlled growth and continuous mass production of CSs with uniform diameters can be achieved by varying the flow-rate and composition of the carrier gas.[18]

2.4 Modification of carbon nanomaterials structure

2.4.1 Doping and functionalization of carbon nanomaterials

Despite their unique electrical, mechanical and chemical stability properties, the chemical inertness and hydrophobicity of CNTs and CSs often inhibit their commercial utilization. To overcome these problems, CNT and CS surfaces are usually modified using either covalent or non-covalent functionalization strategies. Covalent surface functionalization involves the direct incorporation of new elements such as oxygen into the CNT and CSs surfaces. The surface properties of CNTs and CSs such as dispersion can also be changed without modifying their original structure by non-covalent surface modification approaches that include the adsorption of surfactants, polymers, or biological macromolecules.[55] Functionalization of CNTs and CSs by HNO_3, $KMnO_4$, H_2SO_4 or a mixture of HNO_3 and H_2SO_4 can lead to different oxygen-containing surface groups on carbon. These functional groups include carboxyl groups, carboxylic anhydride groups, lactone groups, phenol groups, carbonyl groups, quinone groups or ether groups.[56] The nature and the amount of oxygen-containing functional groups on the carbon nanomaterial surface is of great importance, especially when the carbon nanomaterials are used as catalyst supports.[57] These functional groups can be used to strongly bind metal particles to the surface-oxygen groups of the CNTs and CSs. The nitric acid treatment of the CNTs can simultaneously oxidize and remove the remaining metal particles from the synthesis process.

Doping the CNTsand CSs with nitrogen and boron provides an alternative route to surface modification. Doping nitrogen into carbon layers affects the physical and electronic structure, catalytic activity and electrical conductivity properties of the doped materials.[58] Jiang and Gao[59] showed that basic N-containing groups (such as amines) on the CNTs can generate hydrophilic properties and this then changes the surface properties such that the CNTs are now more easily dispersed in an aqueous medium. N-doped CNTs may also lead to the formation of electron-excess *n*-type semiconducting nanotubes.[60] CNTs doped with nitrogen can be used in many application fields. N-doped CNTs have shown high electrocatalyst performance for the oxygen reduction reactions.[61] N-doped CNTs and CSs have been used as Pd catalyst supports for use in hydrogenation reaction,[62a,b] lithium storage materials,[63] etc.

Electron deficiency in graphite can also be achieved by incorporating boron, which acts as an acceptor, into the lattice.[64a,b] Other effects that may arise in boron-doped carbon materials include: (a) boron not only acts as an acceptor by increasing the number of hole-carriers in the valence band, but it also acts as a scattering centre, therefore reducing carrier mobility; (b) the diamagnetic susceptibility decreases, due to the larger effective mass of charge carriers; (c) the electronic density of states increases because the Fermi level intercepts the valence band, therefore leading to enhanced paramagnetic susceptibility.[65] B-doped CNTs may lead to electron-deficient p-type semiconducting nanotubes.[58,66,67] It has been reported that boron lowers the Fermi energy level of a carbon material, thus increasing conductivity.[68] This also decreases the optical band gap, making it of interest in photovoltaic research.[69] Boron-doped carbon nanomaterials have also been used as metal-free electrocatalysts for the oxygen reduction reaction[70] and as catalyst support materials for methanol oxidation reactions.[71,72]

2.4.2 Synthesis of N and B doped carbon nanomaterials

Nitrogen- and boron-containing CNTs and CSs can be synthesized by the same methods most widely used to produce the undoped carbon nanomaterials. Reviews and reports on the different synthesis methods of N-doped and B-doped CNTs and CSs will be given in detail in Chapters 3-6. Generally, nitrogen-doping of carbon nanostructures can be divided into two categories[73]: (i) "in situ" doping, which is doping directly during the synthesis of porous carbon nanostructure materials; (ii) post-doping, which is post-treatment of pre-synthesized carbon nanostructure materials with a nitrogen-containing precursor (such as N_2, NH_3, etc.). The "in situ" doping is often used to make N-doped CNTs and N-doped carbon nanofibers.

Post-treatment of carbon materials in a N-containing atmosphere can also form N-doped carbons. Most of the post-doping reactions are carried out in NH_3 at high temperatures (600-900 °C).[74a-d]

Processes for the synthesis of boron-doped carbons generally fall into two categories: high temperature firing or low-pressure vacuum deposition. The high temperature route usually involves precursors (such as boric oxide and coke powder) manually mixed and placed in a furnace, followed by heating to around 2900 °C.[75,76a-c] Vacuum deposition routes use reaction chambers and deposit thin films onto substrates. The main methods that have been employed are CVD,[77] pulsed laser deposition,[78] and ion beam deposition.[79]

2.5 The use of TiO_2 photocatalyst for water purification

TiO_2 occurs in nature in the well-known phases: rutile, anatase and brookite. Since the discovery of photoelectrochemical splitting of water using titanium dioxide (TiO_2) electrodes,[79] researchers have extensively studied semiconductor-based photocatalysts. Today, TiO_2 is the most studied photocatalyst because it is non-toxic, cheap, photoreactive, chemically and biologically inert, photostable and has a strong redox ability. It is used in numerous applications, such as air purification, wastewater treatment, deodorization, self-cleaning materials, and as an antibacterial coating.[79,80] Although rutile TiO_2 has been considered photocatalytically inactive, it has been found that Degussa P25, a commercial photocatalyst that has an anatase/rutile ratio of 80%:20%, has the best performance in photocatalysis.[81] Several photocatalysts such as CdS, ZnO_2, WO_3, Fe_2O_3 and ZnS have also been studied, but the best results have been achieved with TiO_2.[82] The reason for this is that metal sulphides are not stable enough for catalysis in aqueous media due to photoanodic corrosion and they are also toxic. Fe oxides undergo photocathodic corrosion. ZnO is unstable in water and forms $Zn(OH)_2$ on the particle surface.[83]

TiO_2 responds to only a small portion of the solar spectrum in the UV region (band-gap energy of 3.0-3.2 eV). Attempts to lower the band-energy have mainly focused on transition metal doped TiO_2. Metal doped materials however are thermally unstable. It has been noted that N-doping of TiO_2 enhances the photocatalytic activity of the TiO_2. Asahi *et al*.[84] reported visible light photocatalytic degradation of methylene blue and acetaldehyde by TiO_2 films doped with N by sputtering methods. They showed that the substitution of oxygen lowers the

band gap energy of TiO_2 as the p states of the dopants mix with the oxygen 2p states, contributing to a net band-gap narrowing. In another study, boron-doped TiO_2 nanotubes showed high photocatalytic activity towards the degradation of methyl orange compared with pure TiO_2 nanotubes.[85]

In a TiO_2 photocatalytic reaction, ultraviolet radiation is required to interact with TiO_2. The process is based on the excitation of a molecule caused by light absorption, e.g. UV light, that drastically alters its ability to lose or gain electrons and promote decomposition of organic pollutants to harmless by-products.[86] The steps involved in the photodegradation of dye pollutants at the TiO_2 surface can be expressed as follows:[87]

$TiO_2 + h\nu \rightarrow TiO_2 (e^-_{cb} + h^+_{vb})$, (Equation 2.1)

$(O_2)_{ads} + e^-_{cb} \rightarrow O_2^{\bullet -}$, (Equation 2.2)

$Ti(IV)\text{-}OH + h^+_{vb} \rightarrow Ti(IV)\text{-}OH^{\bullet}$, (Equation 2.3)

$Ti(IV)\text{-}H_2O + h^+_{vb} \rightarrow Ti(IV)\text{-}OH^{\bullet} + H^+$, (Equation 2.4)

$Pollutant + OH^{\bullet} \rightarrow$ degradation products. (Equation 2.5)

The hydroxyl radicals formed on the illuminated TiO_2 surface are very strong oxidants, which can attack the adsorbed pollutant, leading to their degradation.

Numerous studies on the use of TiO_2 photocatalyst for water purification have been done. For example, Mazzarinno and co-workers[88] have used TiO_2 for the degradation of organic pollutants in water using photochemical reactors. Many other examples on the use of TiO_2 as a photocatalyst on the degradation of organic pollutants will be described in Chapter 7.

The kinetics of photocatalytic degradation of many organic compounds in TiO_2 dispersions under UV irradiation has often been modeled to the simple Langmuir-Hinshelwood equation (Equation 2.6):[89]

$$r = -\frac{dC}{dt} = \frac{kKC}{1+KC} \quad \text{(Equation 2.6)}$$

where r is the rate of disappearance of the reagent, C is the reagent concentration, k is the rate constant and K is the apparent equilibrium constant. The Langmuir-Hinshelwood equation is

simplified to a pseudo first-order expression when the concentration of the reagent is very low (Equation 2.7):

$$-\frac{dC}{dt} = k'C \quad \text{(Equation 2.7)}$$

The integration of Equation 2.7 leads to Equation 2.8. The plot of $-\ln(C/C_o)$ vs t is a straight line and its slope is k':

$$-\ln\frac{C}{C_o} = k't \quad \text{(Equation 2.8)}$$

2.6 TiO_2/carbon composite materials

With an energy gap of 3.2 eV, the TiO_2 photocatalyst can be activated only by UV light. Hence, many studies have focused on the development of visible-light-responsive photocatalysts viz: CdS, $InVO_4$, N-doped, C-doped, and S-doped TiO_2.[80,90] It is known that adsorbents such as activated carbon have been used to promote the adsorption capacity and the photocatalytic activity of TiO_2.[91] Araña *et al*.[92] used powdered activated carbon mixed with TiO_2 in photocatalytic processes. They observed that (i) the combination of powdered activated carbon and TiO_2 resulted in fast decantability in comparison with that of TiO_2 alone, (ii) a TiO_2 particle distribution on the activated carbon surface yielded a homogeneous particle size distribution and (iii) the rate of organic removal by the powdered activated carbon and TiO_2 was six times higher than that with TiO_2 alone. However, CNTs have been determined to be more attractive catalyst supports than activated carbon, owing to their adsorption, electronic, mechanical and thermal properties.[93] Previous studies reported that TiO_2-based carbon nanotubes composites (TiO_2-CNTs) have been synthesized and provide a synergistic effect which can enhance photoactivities relative to pure TiO_2 under UV or visible-light illumination.[94a-e] CNTs can trap photo-induced electrons, drastically reducing the recombination rate between the hole and electron. Also, CNTs can serve as a photosensitizer for a visible-light-response. Kuo *et al*. reported the successful preparation ofa TiO_2-CNT composite and its function as a photocatalyst and an electrically conductive catalyst.[95]

Different methods have been employed to prepare TiO_2 composites. Sol-gel and hydrothermal methods are commonly used to prepare the TiO_2 and TiO_2-CNT composite

materials. However, Yen *et al.*[96] showed that the TiO_2-MWCNT prepared by a sol-gel method caused the TiO_2 to be well dispersed on the MWCNT surface, thereby improving the surface area leading to higher efficiency in NOx photodegradation when compared to the TiO_2-MWCNT prepared by the hydrothermal method.

References

1. T. Pradeep and Anshup, *Thin Solid Films*, 2009, **517**, 6441-6478.
2. C. Buzea, I.I.P. Blandino and K. Robbie, *Biointerphases*, 2007, **2**, MR17-MR172.
3. E. Roduner, *Chem. Soc. Rev.*, 2006, **35**, 583-592.
4. W.-C. Oh and M.-L. Chen, *Bull. Korean Chem. Soc.*, 2008, **29**, 159-164.
5. G. An, W. Ma, Z. Sun, Z. Liu, B. Han, S. Miao, Z. Miao and K. Ding, *Carbon*, 2007, **45**, 1795-1801.
6. B. Gao, G.Z. Chen and G.L. Puma, *Appl. Catal. B*, 2009, **89**, 503-509.
7. S. Iijima, *Nature*, 1991, **354**, 56-58.
8. C. Wang, Z. Guo, S. Fu, W. Wu and D. Zhu, *Prog. Polym. Sci.*, 2004, **29**, 1079-1141.
9. (a) C. Liu, Y.Y. Fan, M. Liu, H.T. Cong, H.M. Cheng and M.S. Dresselhaus, *Science*, 1999, **286**, 1127-1129; (b) H.-M. Cheng, Q.-H. Yang and C. Liu, *Carbon*, 2001, **39**, 1447-1454.
10. (a) E. Frackowiak, K. Metenier, V. Bertagna and F. Beguin, *Appl. Phys. Lett.*, 2000, **77**, 2421-2423; (b) R. Martel, T. Schmidt, H.R. Shea, T. Hertel and P.H. *Avouris, Appl. Phys. Lett.*, 1998, **73**, 2447-2449.
11. (a) P.G. Collins and A. Zettl, *Phys. Rev. B*, 1997, **55**, 9391-9399; (b) X.P. Xu and G.R. Brandes, *Appl. Phys. Lett.*, 1999, **74**, 2549-.2551.
12. J. Kong, N.R. Franklin, C. Zhou, M.G. Chapline, S. Peng, K. Cho and H. Dai, *Science*, 2000, **287**, 622-625;
13. (a) H. Dai, N. Franklin and J. Han, *Appl. Phys. Lett.*, 1998, **73**, 1508-1510; (b) J.H. Hafner, C.-L. Cheung, T.H. Oosterkamp and C.M. Lieber, *J. Phys. Chem. B*, 2001, **105**, 743-746.
14. D. Pradhan and M. Sharon, *Mater. Sci. Eng.B.*, 2002, **96**, 24-28.
15. H.W. Kroto, J.R. Heath, S.C. O'Brien, R.F. Curl and R.E. Smalley, *Nature*, 1985, **318**, 162-164.
16. (a) A.J. Laurence, *Carbon*, 2006, **44**, 158-160; (b) R. Alcàntara, F.J. FernàndezMadrigal, P. Lavela, J.L. Tirado, J.M. Jiménez Mateos, C. Gómez de Salazar, R. Stoyanova and E. Zhecheva, *Carbon*, 2000, **38**, 1031-1041.

17. (a) Z.C. Kang and Z.L. Wang, *J. Phys. Chem.*, 1996, **100**, 5163-5165; (b) Ph. Serp, R. Feurer, Ph. Kalck, Y. Kihn, J.L. Faria and J.L. Figueiredo, *Carbon*, 2001, **39**, 621-626; (c) J.S. Qiu, Y.F. Li, Y.P. Wang, C.H. Liang, T.H. Wang and D.B. Wang, *Carbon*, 2003, **41**, 767-772; (d) Z.L. Wang and Z.C. Kang, *J. Phys. Chem.*, 1996, **100**, 17725-17731.
18. H.-S. Qian, F.-M. Han, B. Zhang, Y.-C. Guo, J. Yue and B.-X. Peng, *Carbon*, 2004, **42**, 761-766.
19. Y.Z. Jin, C. Gao, W.K. Hsu, Y. Zhu, A. Huczko, M. Bystrzejewski, M. Roe, C.Y. Lee, S. Acquah, H. Kroto and D.R.M. Walton, *Carbon*, 2005, **43**, 1944-1953.
20. E. Auer, A. Freund, J. Pietsch and T. Tacke, *Appl. Catal. A: General*, 1998, **173**, 259-271.
21. (a) M. Sharon, K. Mukhopadhyay, K. Yase, S. Iijima, Y. Ando and X. Zhao, *Carbon*, 1998, **36**, 507-511; (b) S. Flandrois and B. Simon, *Carbon*, 1999, **37**, 165-180.
22. (a) V.Vignal, A.W. Morawski, H. Konno and M. Inagaki, *J. Mater. Res.*, 1999, **14**, 1102-1112; (b) M. Inagaki, V. Vignal, H. Konno and A.W. Morawski, *J. Mater. Res.*, 1999, **14**, 3152-3157.
23. H.F. Xiong, M. Moyo, M.A.M. Motchelaho, L.L. Jewell and N.J. Coville, *Appl. Catal. A: General*, 2010, **388**, 168-178.
24. K.T. Lee, Y.S. Jung and S.M. Oh, *J. Am. Chem. Soc.*, 2003, **125**, 5652-5653.
25. Z.F. Wang, P.F. Xiao and X.P. Dong *Carbon*, 2006, **44**, 3277-3284.
26. W.H. Shen, Y.F. Zhu, X.P. Dong, J.L. Gu and J.L. Shi, *Chem. Lett.*, 2005, **34**, 840-841.
27. B.Y. Liu, D.C. Jia, Q.C. Meng and J.C. Rao, *Carbon*, 2007, **45**, 668-689.
28. J.Y. Miao, D.W. Hwang, K.V. Narasimhulu, P.I. Lin, Y.T. Chen, S.H. Lin and L.P. Hwang, *Carbon*, 2004, **42**, 813-822.
29. Z.C. Kang and Z.L. Wang, *Philos. Mag. B*, 1996, **73**, 905-929.
30. A.A. Deshmukh, S.D. Mhlanga and N.J. Coville, *Mater. Sci. Eng. R*, 2010, **70**, 1-28,
31. V. Ivanov, J.B. Nagy, Ph. Lambin, A. Lucas, X.B. Zhang, X.F. Zhang, D. Bernaerts, G. van Tendeloo, S. Amelinckx and J. van Landuyt, *Chem. Phys. Lett.*, 1994, **223**, 329-335.
32. S. Herreyre and P. Gadelle, *Carbon*, 1995, **33**, 234-237.

33. (a) H. Zeng, L. Zhu, G. Hao and R. Sheng, *Carbon*, 1998, **36**, 259-261; (b) Y.S. Park, K.S. Kim, H.J. Jeong, W.S. Kim, J.M. Moon, K.H. An, D.J. Bae, Y.S. Lee, G.S. Park and Y.H. Lee, *Synth. Met.*, 2002, **126**, 245-251; (c) Z. Shi, Y. Lian, F.H. Liao, X. Zhou, Z. Gu, Y. Zhang, S. Iijima, H. Li, K.T. Yue and S.-L. Zhang, *J. Phys. Chem. Solids*, 2000, **61**, 1031-1036; (d) A. Huczko, *Appl. Phys. A*, 2002, **74**, 617-638.
34. T. Guo, P. Nikolaev, A. Thess, D.T. Golbert and R.E. Smalley, *Chem. Phys. Lett.*, 1995, **243**, 49-54.
35. A.M. Cassell, J.A. Raymakers, J. Kong and H. Dai, *J. Phys. Chem. B*, 1999, **103**, 6484-6492.
36. N. Inami, M.A. Mohamed, E. Shikon and A. Fujiwara, *Sci. Technol. Adv. Mater.*, 2007, **8**, 292-295.
37. N. Ishigami, H. Ago, K. Imamoto, M. Tsuji, K. Iakoubovskii and N. Minami, *J. Am. Chem. Soc.*, 2008, **130**, 9918-9924.
38. H.W. Kroto, J.R. Heath, S.C. O'Brien, R.F. Curl and R.E. Smalley, *Nature*, 1985, **318**, 162-163.
39. W. Krätschmer, L.D. Lamb, F. Fostiropoulos and D. Huffman, *Nature*, 1990, **347**, 354-358.
40. D. Ugarte, *Nature*, 1992, **359**, 707-709.
41. K.H. An, K.K. Jeon, J.M. Moon, S.J. Eum, C.W. Yang, G.S. Park, C.Y. Park and Y.H. Lee, *Synth. Met.*, 2004, **140**, 1-8.
42. Z. Zhong, H. Chen, S. Tang, J. Ding, J. Lin and K.L. Tan, *Chem. Phys. Lett.*, 2000, **330**, 41-47.
43. W.M. Qiao, Y. Song, S.Y. Lim, S.H. Hong, S.H. Yoon, I. Mochida and T. Imaoka, *Carbon*, 2006, **44**, 158-193.
44. L. Xu, W. Zhang, Q. Yang, Y. Ding, W. Yu and Y. Qian. *Carbon*, 2005, **43**, 1084-1114.
45. D. Pradhan and M. Sharon, *Mater. Sci. Eng.B*, 2002, **96**, 24-28.
46. Z.S. Lou, Q.W. Chen, J. Gao and Y.F. Zhang, *Carbon*, 2004, **42**, 229-232.
47. M. Aili, W. Xiaomin, L. Tianbao, L. Xuguang and X. Bingshe. *Mater. Sci. Eng. A*, 2007, **443**, 54-59.
48. Z.L. Wang and Z.C. Kang, *Carbon*, 1997, **35**, 419-426.
49. A. Govindaraj, R. Sen, B.V. Nagaraju and C.N.R. Rao, *Philos.Mag. Lett.*, 1997, **76**, 363-367.
50. F. Su, X.S. Zhao, Y. Wang and J.Y. Lee, *J. Mater. Chem.*, 2006, **16**, 4413-4419.

51. F.-L. Wang, L.-L. Pang, Y.-Y. Jiang, B. Chen, D. LiN, N. Lun, H.-L. Zhu, R. Liu, X.-L. Meng, Y. Wang, Y.-J. Bai and L.-W. Yin, *Mater. Lett.*, 2009, **63**, 2564-2566.
52. L.Q. Xu, W.Q. Zhang, Q. Yang, Y.W. Ding, W.H. Yu and Y.T. Qian, *Carbon*, 2005, **43**, 1090-1092.
53. J.W. Liu, M.W. Shao, Q. Tang, X.Y. Chen, Z.P. Liu and Y.T. Qian, *Carbon*, 2003, **41**, 1682-1685.
54. Q. Li, H. Yan, J. Zhang and Z. Liu, *Carbon*, 2004, **42**, 829-835.
55. J. Cheng, K.A.S. Fernando, L.M. Veca, Y.-P. Sun, A.I. Lamond, Y.W. Lam and S.H. Cheng, *ACS Nano*, 2008, **2**, 2085-2094.
56. T.G. Ros, A.J. van Dillen, J.W. Geus and D.C. Koningsberger, *Chem. Eur. J.*, 2002, **8,** 1151-1162.
57. S. Kundu, Y. Wang, W. Xia and M. Muhler, *J. Phys. Chem. C*, 2008, **112**, 16869-16878.
58. S. Saito, *Science*, 1997, **278**, 77-78.
59. L. Q. Jiang and L. Gao, *Carbon*, 2003, **41**, 2923-2929.
60. M. Terrones, A. Jorio, M. Endo, A.M. Rao, Y.A. Kim, T. Hayashi, H. Terrones, J.-C. Charlier, G. Dresselhaus and M.S. Dresselhaus, *Mater. Today*, 2004, **7**, 30-45.
61. K.P. Gong, F. Du, Z.H. Xia, M. Durstock and L.M. Dai, *Science*, 2009, **323**, 760-764.
62. (a) K.C. Mondal, L.M. Cele, M.J. Witcomb and N.J. Coville, *Catal. Commun.*, 2008, **9**, 494-498; (b) R.S. Oosthuizen and V.O. Nyamori, *Platinum Met. Rev.*, 2011, **55**, 154-169.
63. W.H. Shin, H.M. Jeong, B.G. Kim, J.K. Kang, and J.W. Choi, *Nano Lett.*, 2012, **12**, 2283-2288.
64. (a) Y. Komatsu, *Carbon*, 1969, **7**, 177-183; (b) G. Henning, *J. Chem. Phys.*, 1965, **42**, 1167-1172.
65. A. Marchand, *Chem. Phys. Carbon*, 1971, **7**, 155-191.
66. M. Terrones, N. Grobert and H. Terrones, *Carbon*, 2002, **40**, 1665-1684.
67. O. Stephen P.M. Ajayan, C. Colliex, P. Redlich, J.M. Lambert, P. Bernier and P. Lefin, *Science*, 1994, **266**, 1683-1685.
68. E.J. Mele and J.J. Ritsko, *Phys. Rev. B*, 1981, **24**, 1000-1005.
69. F.G. Della Corte, M.G. Donato, M. Gagliardi, G. Messina, M.A. Nigro and S. Santangelo, *J. Non-Cryst. Solids*, 2006, **352**, 2647-2651.
70. L. Yang, S. Jiang, Y. Zhao, L. Zhu, S. Chen, X. Wang, Q. Wu, J. Ma, Y. Ma and Z. Hu, *Angew. Chem. Int. Ed.*, 2011, **50**, 1-6.

71. S.-J. Park and J.-M. Park, *Curr. Appl. Phys.*, 2012, 1248-1251.
72. S. Wang, T. Cochell and A. Manthiran, *Phys. Chem. Chem. Phys.*, 2012, **14**, 13910-13913.
73. C.P. Ewels and M. Glerup, *J. Nanosci. Nanotechnol.*, 2005, **5**, 1345-1363.
74. (a) R.A. Sidik, A.B. Anderson, N.P. Subramanian, S.P. Kumaranguru and B.N. Popov, *J. Phys. Chem. B*, 2006, **110**, 1787-1797; (b) L.Q. Jiang and L. Gao, *Carbon*, 2003, **41**, 2923-2929; (c) S.C. Roy, A.W. Harding, A.E. Russell and K.M. Thomas, *J. Electrochem. Soc.*, 1997, **144**, 2323-2328; (d) F. Jaouen, M. Lefevre, J.P. Dodelet and M. Cai, *J. Phys. Chem. B*, 2006, **110**, 5553-5558.
75. T. Hamada, K. Suzuki, T. Kohno and T. Sugiura, *Carbon*, 2002, **40**, 1203-1210.
76. (a) M. Endo, C. Kim, T. Karaki, Y. Nishimura, M.J. Matthews, S.D.M. Brown and M.S. Dresselhaus, *Carbon*, 1999, **37**, 561-568; (b) H. Gerhart, *J. Chem. Phys.*, 1965, **42**, 1167-1172; (c) E. Morinobu, H. Takuya, H. Seong-Hwa, E. Toshiaki and S.D. Milred, *J. Appl. Phys.*, 2001, **90**, 5670-5674.
77. B.M. Way, J.R. Dahn, T. Tiedje, K. Myrtle and M. Kasrai, *Phys. Rev. B*, 1992, **46**, 1697-1702.
78. C. Ronning, D. Schwen, S. Eyhusen, U. Vetter and H. Hofsass, *Surf. Coat. Technol.*, 2002, **158**, 382-387.
79. A. Fujishima and K. Honda, *Nature*, 1972, **238**, 37-38.
80. A. Fujishima, T.N. Rao, and D.A. Tryk, *J. Photochem. Photobiol. C: Photochem. Rev. 1*, 2000, 1-21.
81. M. Heredia and J. Duffy, *Photocatalytic destruction of water pollutants using a TiO_2 film PET bottles. Energy Engineering Program*, University of Massachusetts Lowell, 2007.
82. O. Legrini, E. Oliveros and A.M. Braun, *Chem. Rev.*, 1993, **93**, 671-698.
83. M.A. Fox and M.T. Dulay, *Chem. Rev.*, 1993, **93**, 341-357.
84. R. Asahi, T. Morikawa, T. Ohwaki, K. Aoki and Y. Taga, *Science*, 2001, **293**, 269-271.
85. L. Deng, Y. Chen, M. Yao, S. Wang, B. Zhu, W. Huang and S. Zhang, *J. Sol-Gel Sci. Technol.*, 2010, **53**, 535-541.
86. R. Molinari, M. Borgese, E. Drioli, L. Palmisano and M. Schiavello, *Catal. Today*, 2002, **75**, 77-85.
87. S. Senthilkumaar and K. Porkodi, *J. Colloid Interface Sci.*, 2005, **288**, 184-189.
88. I.M Mazzarino, P. Piccinini and L. Spinelli, *Catal. Today*, 1999, **48**, 315-321.

89. A.L. Linsebigler, G. Lu and J.T. Yates Jr., *Chem. Rev.*, 1995, **95**, 735-758.
90. M.R. Hoffmann, S.T. Martin, W. Choi and D.W. Bahnemann, *Chem. Rev.*, 1995, **95**, 69-96.
91. B. Tryba, A.W. Morawske and M. Inagaki, *Appl. Catal. B*, 2003, **41**, 427-433.
92. J. Araña, J.A.H. Melián, J.M. Doña-Rodríguez, O. González-Díaz, A. Viera, J. Pérez Peña, P.M. Marrero Sosa and V. EspinoJiménez, *Catal. Today*, 2002, **76**, 279-289.
93. P. Serp, M. Corrias and P. Kalck, *Appl. Catal. A: General*, 2003, **253**, 337-358.
94. (a) W. Wang, P. Serp, Ph. Kalck and J.L. Faria, *Appl. Catal. B: Environmental.*, 2005, **56**, 305-312; (b) S.W. Lee and W.M. Sigmund, *Chem. Commun.*, 2003, 780-781; (c) Y. Yu, J.C. Yu, J.G. Yu, Y.C. Kwok, Y.K. Che, J.C. Zhao, L. Ding, W.K. Ge and P.K. Wong, *Appl. Catal. A: General*, 2005, **289**, 186-196; (d) Y. Yu, J.C. Yu, C.-Y. Chan, Y.-K. Che, J.-C. Zhao, L. Ding, W.-K. Ge and P.-K. Wong, *Appl. Catal. B: Environmental*, 2005, **61**, 1-11; (e) Y. Ou, J.D. Lin, S.M. Fang and D.W. Liao, *Chem. Phys. Lett.*, 2006, **429**, 199-203.
95. C.-S. Kuo, Y.-H. Tseng, H.-Y. Lin, C.-H. Huang, C.-Y. Shen, Y.-Y. Li, S.I. Shah and C.-P. Huang, *Nanotechnology*, 2007, **18**, 465607/1-465607/5.
96. C.-Y. Yen, Y.-F. Lin, C.-H. Hung, Y.-H. Tseng, C.-C. Ma, M.-C. Chang and H. Shao, *Nanotechnology*, 2008, **19**, 045604/1-045604/11.

CHAPTER 3

The Synthesis of Nitrogen-Doped Multiwalled Carbon Nanotubes using an Fe-Co/$CaCO_3$ Catalyst[#]

3.1 Introduction

Since the discovery of polyhedral carbon clusters (fullerenes) in 1985,[1] new graphite-like nanostructures such as carbon nanotubes (CNTs)[2] and related nanostructures (spheres,[3] onions,[4] fibers,[5] horns,[6] etc.) have been reported. CNTs have attracted the attention of scientists in recent years for their application as catalyst supports,[7,8] nanoscale semiconductor devices,[5, 9] sensors,[7,10,11] in hydrogen storage,[12,13] scanning probes,[14] etc. More importantly, while single walled carbon nanotubes (SWCNTs) can either be metallic or semiconducting, depending on their chirality and diameter,[15,16] multiwalled carbon nanotubes (MWCNTs) present anisotropic metallic behaviour.[17] Doping of CNTs with heteroatoms provides a means of modifying the conducting and other properties of the CNTs.[18,19] Novel electronic properties can be expected if N atoms directly substitute C atoms in the graphitic lattice as the doping results in a production of an n-type conductor.[20] A high nitrogen content in CNTs leads to an increase in the CNT conductivity due to the rise of the Fermi level towards the conduction band.[21,22] Low dopant concentrations have been incorporated within the CNTs,[23] and the electronic conductance was shown to be significantly enhanced without altering the mechanical properties.[24] Nitrogen-containing CNTs have recently been reported by Gong and co-workers to be an efficient metal-free catalyst for the oxygen reduction reaction (ORR).[25] It has been reported that nitrogen-doped multiwalled CNTs (N-MWCNTs) are thermally less stable[26] and possess larger surface-active group/volume ratios, better mechanical properties, and better biocompatibility, when compared to undoped CNTs.[21,25,27]

Various synthesis methods have been used to make nitrogen-doped CNTs. These include arc discharge,[28] laser ablation,[29] substitution reactions,[30] catalytic pyrolysis of organic precursors including acetonitrile,[31] pyridine,[24] triazine,[32] and various chemical vapour deposition (CVD) methods.[33] The CVD method remains the most promising method for the commercial production of highly dense and well aligned nitrogen-doped CNTs by catalytic

Z.N. Tetana, S.D. Mhlanga, G. Bepete, R.W.M. Krause, N.J. Coville, *S. Afr. J. Chem.*, 2012, 65, 39-49.

decomposition of suitable carbon and nitrogen sources. The growth process usually involves heating a catalyst (typically to 700-1000 °C) in an atmosphere of C and N containing precursors.

To date, N-doped MWCNTs have been synthesized by thermal CVD of a nitrogen-containing organic compound in the presence of supported metal nanoparticles, by the pyrolysis of acetonitrile/alcohol mixtures over an Fe-Al/MgO catalyst,[34] by using a Co-based catalyst derived from Co/Al layered double hydroxides using methane and acetonitrile as C and N sources, respectively,[35] by using a mixture of C_2H_6/Ar/NH_3 and an Fe/Al_2O_3 catalyst,[36] by using NH_3 and CH_4 over an Fe-Mo/MgO catalyst,[37] etc. Bamboo-like CNTs have recently been synthesized by thermal decomposition of pyridine and iron phthalocyanine over an iron catalyst under an ammonia atmosphere.[38] X-ray photoelectron spectroscopy (XPS) analysis of these N-CNT samples has demonstrated three types of nitrogen atoms associated with the CNT surface, namely pyridine-like, graphite-like, and molecular nitrogen; the maximum dopant concentration was found to be in the range of 1.18-3.22 at. % over the temperature range 750-875 °C.[38] Floating catalyst CVD methods have also been proven to be a popular method to make N-CNTs. For example, Nxumalo and co-workers prepared bamboo-shaped MWCNTs by the floating catalyst CVD method using ferrocene/aniline mixtures at 900 °C.[26]

In the CVD processes when transition metal particles are used as a catalyst, it is believed that the CNT forms from the metal catalyst surface that resides at either the base[39] or the tip of a growing nanotube.[40] N-CNTs are proposed to grow only via a base growth process. Nitrogen-doping significantly alters the morphology of CNTs, typically leading to bamboo-like structures that contain regularly arranged compartments with a hollow channel.[19] It was proposed that the bamboo-like structures might be due to effects related to the catalyst particle shape, the bulk diffusion of carbon and nitrogen in the catalyst, or the slow movement of the catalyst compared to the growth rate of the CNT. It has been shown that the cup separation distance in the bamboo structure correlated with the concentration of the nitrogen in the tube.[26]

The nature of the support used during CNT synthesis plays an important role in influencing the activity of the catalyst. A number of factors need to be considered when choosing a support material, including thermal stability, solubility in acids/alcohol/water, surface area, etc.[41] High surface area materials such as SiO_2 and Al_2O_3 provide excellent supports for

catalytic CNT production.[42] However, they are not easily removed and therefore purification of CNTs made from these supports remains a challenge.

Undoped MWCNTs have been produced by decomposing a hydrocarbon gas (e.g. acetylene) over a metal catalyst supported on $CaCO_3$ such as $Ni/CaCO_3$,[43] $Co/CaCO_3$,[43,44] $Fe-Co/CaCO_3$,[41,44] and $Fe/CaCO_3$.[44,45] At the end of the reaction the CaO can be easily dissolved in dilute acids such as HNO_3 and HCl. Further, studies revealed that Fe-Co catalysts are more effective than either Fe or Co catalysts when supported on $CaCO_3$.[46-49] The success in using $CaCO_3$ as a support suggested it could also be used to make N-MWCNTs.

In this study, we report on a systematic synthesis of N-MWCNTs by the thermal decomposition of acetylene (C_2H_2) and acetonitrile (CH_3CN) as the carbon and nitrogen sources over an $Fe-Co/CaCO_3$ catalyst, under an N_2 atmosphere. This study revealed the key roles played by CH_3CN concentration and reaction temperature on the structure and quality of the materials formed that permit a control of nitrogen content in the N-MWCNTs. This work represents a continuation of earlier work in which an Fe-Co on $CaCO_3$ was used to make undoped carbon nanotubes.[41]

3.2 Experimental

3.2.1 Catalyst preparation

The $Fe-Co/CaCO_3$ catalyst was prepared by an impregnation route using an aqueous mixture of $Fe(NO_3)_3{\cdot}9H_2O$ and $Co(NO_3)_2{\cdot}6H_2O$.[41] The two metal nitrates (purchased from Sigma-Aldrich) were of analytical reagent grade and were used without further treatment. Calculated amounts of the metal nitrates were mixed and dissolved in distilled water to make a 0.3 M Fe-Co (50:50 w/w) precursor solution. This precursor solution was added dropwise to the stirred $CaCO_3$ and the mixture was left to stir for 30 minutes. The resulting metal-support mixture was then filtered and dried in an oven at 120 °C for 12 hours, cooled to room temperature, ground and sieved using a 150 µm mesh sieve. The catalyst was then calcined at 400 °C for 16 hours in air to decompose the nitrates in the catalyst. The total loading of the Fe-Co catalyst on the $CaCO_3$ was 5 mass %. These catalysts were completely characterized as reported in our earlier paper.[41]

3.2.2 Fabrication and purification of N-MWCNTs

N-MWCNTs were synthesized using a procedure similar to that reported by Mhlanga *et al.* for the synthesis of undoped MWCNTs.[41] The syntheses were carried out in a tubular quartz reactor (51 cm x 1.9 cm i.d.) placed in a horizontal furnace. C_2H_2 (Afrox) and CH_3CN (Sigma-Aldrich) were used as carbon and carbon/nitrogen sources, respectively. N_2 (Afrox) was used as a carrier gas to dilute the C_2H_2 in order to decrease the contact time between C_2H_2 and the catalyst, and consequently reduce the formation of amorphous carbon.[50] For each synthesis, 0.3 g of the catalyst was uniformly spread onto a quartz boat (120 mm x 15 mm) which was then placed in the centre of the quartz tube. A series of experiments were performed, using different acetonitrile vaporization temperatures (room temperature, 50 °C and 80 °C) and different reaction temperatures (700, 750, 800, and 850 °C). The furnace was raised to a desired temperature at 10 °C/min under flowing N_2 gas (40 ml/min) in the reaction. Once the desired temperature was reached, the N_2 (240 ml/min) and C_2H_2 (100 ml/min) were simultaneously bubbled through CH_3CN for 1 hour. After this, the bubbling of the gases through CH_3CN was stopped and the system was left to cool down to room temperature under N_2 (40 ml/min). The quartz boat was then removed from the reactor and the carbon deposits that formed along with the catalyst were weighed. Other forms of carbon materials were made when the reaction and acetonitrile heating temperatures were set to 900 °C and 80 °C, respectively. The resulting nitrogen-containing materials were purified using 55% HNO_3 under reflux in an oil bath held at 110 °C for 4 hours to remove the CaO, residual Fe-Co particles and introduce oxygen surface groups. The acid-treated carbon materials were then filtered and washed several times with distilled water (to remove the residual HNO_3) until the pH of the filtrate was neutral. The nitrogen-containing materials were dried at 120 °C for 12 hours. As-synthesized N-MWCNTs grown at 700-850 °C using $CH_3CN$are denoted as 700, 750, 800, and 850, and the purified materials are denoted as 700P, 750P, 800P, and 850P.

3.2.3 Carbon yield calculation

The yield was determined by estimating the amount of carbon reactants used and the amount of carbon produced. The carbon was contained in both reactants (C_2H_2, CH_3CN). The yield was determined from the unpurified reactants produced. The yield calculated includes carbon formed as both CNTs and carbon spheres (CSs), (see Appendix A for calculations).

Z.N. Tetana, S.D. Mhlanga, G. Bepete, R.W.M. Krause, N.J. Coville, *S. Afr. J. Chem.*, 2012, 65, 39-49.

3.2.4 Characterization of N-MWCNTs

The morphology and structural features of the nitrogen-containing nanotubes were ascertained by transmission electron microscopy (TEM) using a FEI Technai G^2 Spirit electron microscope operated at 120 kV, scanning electron microscopy (SEM) using a FEI QUANTA 400 FEG ESEM at 5 kV, and Raman spectroscopy using a Jobin-Yvon T6400 micro-Raman spectrometer equipped with a liquid nitrogen cooled charge coupled device detector. The thermal stability of the N-MWCNTs was investigated by thermogravimetric analysis (TGA) using a Perkin Elmer Pyris 1 TGA. About 10 mg of each sample was heated to 900 °C at a rate of 10 °C/min under air. The mass of all samples was kept constant (ca 10 mg) in order to reduce the effects of variability in measurements. BET surface areas of the N-MWCNTs (~ 200 mg for each measurement) were obtained through N_2 adsorption using an ASAP 2000 Micrometrics TriStar Surface Area and Porosity Analyzer. The nitrogen concentration was determined by CN elemental analysis using a Carlo Erba NA 1500 Nitrogen Carbon Sulphur Analyzer at the ARC - Institute for Soil, Climate and Water in Pretoria. The X-ray photoelectron spectroscopy (XPS) measurements were performed in a Thermo Scientific K-Alpha equipped with a monochromatic Al Kα X-ray source (1486 eV photons and 200 μm spot size), at the Department of Physics and Astronomy, Rutgers University, USA.

3.3 Results and discussion

3.3.1 Structural analysis of N-MWCNTs

Figures 3.1-3.3 show TEM images of the nitrogen-containing CNTs prepared from acetonitrile at different temperatures. It was observed that the quality of the N-MWCNTs varied as the reaction temperature increased. All the N-MWCNTs synthesized at 700-750 °C were light and spongy in texture, while all the materials prepared at 800-850 °C were coarser in texture. As mentioned in the experimental section, the as-synthesized N-MWCNTs were purified with HNO_3 to remove the CaO and residual Fe-Co particles. After purification, no significant changes to the structures and the sizes of the N-MWCNTs were observed. TEM analysis revealed that at all temperatures, the CNTs were multiwalled, randomly arranged and were found to have open ends. These open-ended N-MWCNTs may be suitable for field emission studies.[51] All the unpurified nanotubes formed contained no residual catalyst

Z.N. Tetana, S.D. Mhlanga, G. Bepete, R.W.M. Krause, N.J. Coville, *S. Afr. J. Chem.*, 2012, 65, 39-49.

particles in their tips, suggesting that they were made via a base-growth mode involving a strong interaction between Co-Fe particles and the CaO.[41,52]

Nitrogen incorporation is evidenced by the presence of bamboo-like structures in which the inside of the tube is separated into a series of compartments (Figures 3.1-3.3). Doping leads to the introduction of defects and a higher degree of disorder in the graphite tubes.[26] Evaluation of the TEM image compartment size indicates that the degree of doping increased at higher reaction and CH_3CN temperatures. However, the observed increase in nitrogen incorporation with increase in growth temperatures above 750 °C contradicts other findings in the literature. The findings in the literature suggest that as the growth temperature increases, the nitrogen content decreases.[53,54] The contradiction can be related to the difference in synthesis methods, catalysts, experimental parameters, and C and N precursors used in this study. The images also reveal that with the increase of temperature from 700-750 °C (Figures 3.1a, 3.1b, 3.2a, 3.2b, 3.3a, and 3.3b) roughening of the outer N-MWCNTs surfaces is more prominent but roughening decreases as temperature increases from 800-850 °C (Figures 3.1c, 3.1d, 3.2c, 3.2d, 3.3c, and 3.3d).

Z.N. Tetana, S.D. Mhlanga, G. Bepete, R.W.M. Krause, N.J. Coville, *S. Afr. J. Chem.*, 2012, 65, 39-49.

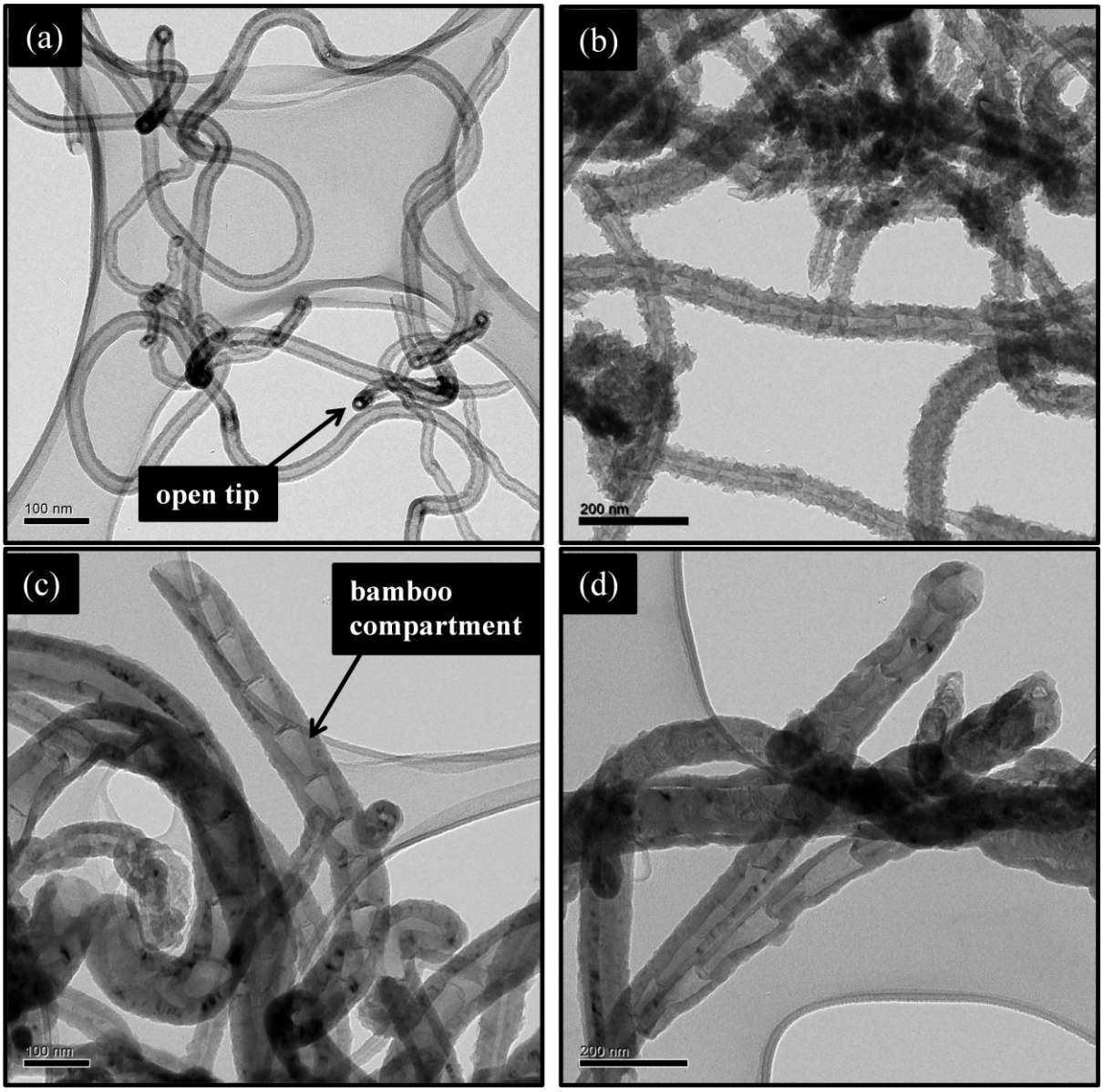


Figure 3.1: TEM images of the purified N-MWCNTs grown using CH_3CN (r.t.) and reaction temperatures of (a) 700 °C, (b) 750 °C, (c) 800 °C and (d) 850 °C.

Z.N. Tetana, S.D. Mhlanga, G. Bepete, R.W.M. Krause, N.J. Coville, *S. Afr. J. Chem.*, 2012, 65, 39-49.

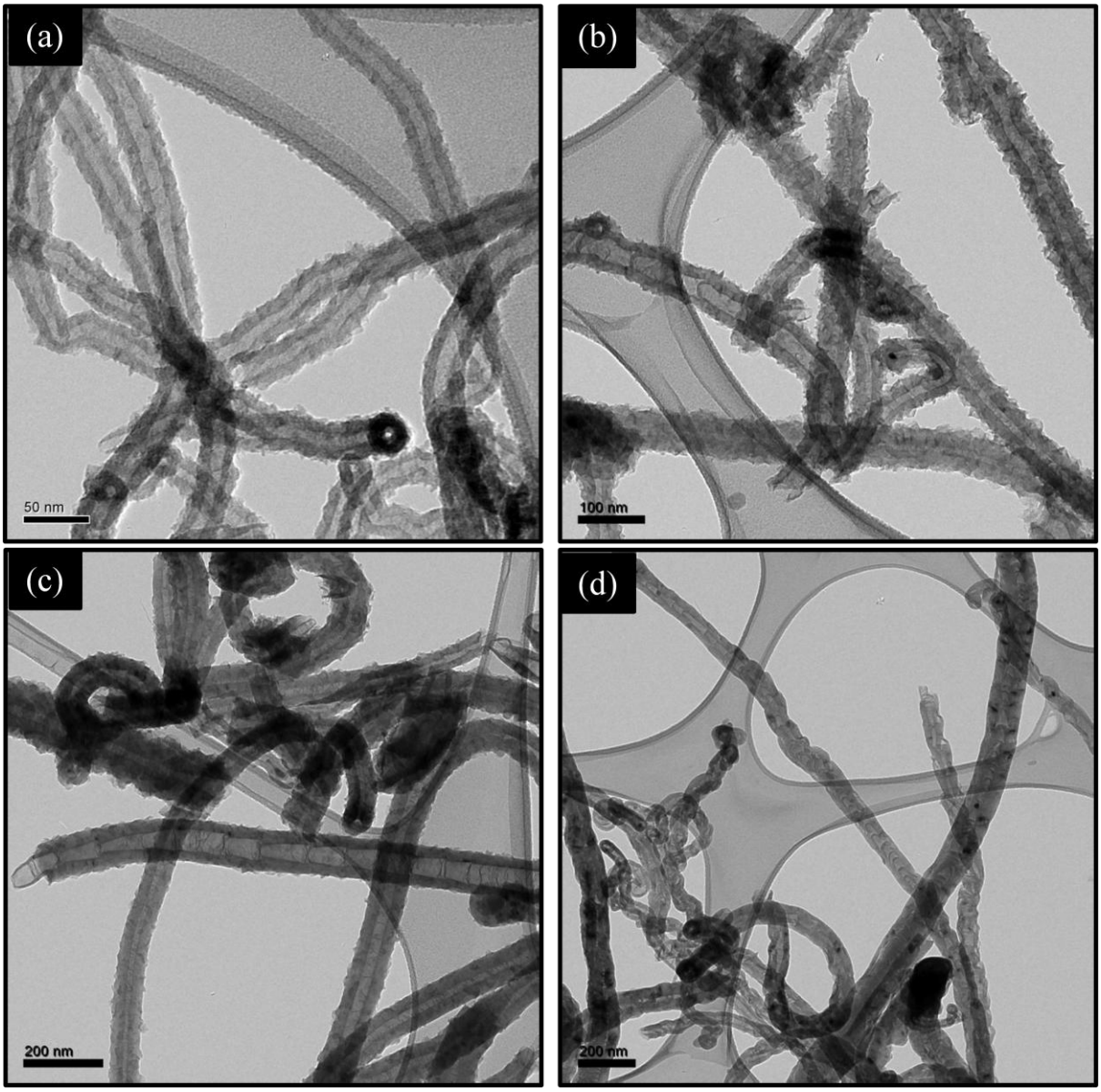


Figure 3.2: TEM images of the purified N-MWCNTs grown using CH_3CN (50 °C) and reaction temperatures of (a) 700 °C, (b) 750 °C, (c) 800 °C and (d) 850 °C.

Z.N. Tetana, S.D. Mhlanga, G. Bepete, R.W.M. Krause, N.J. Coville, *S. Afr. J. Chem.*, 2012, 65, 39-49.

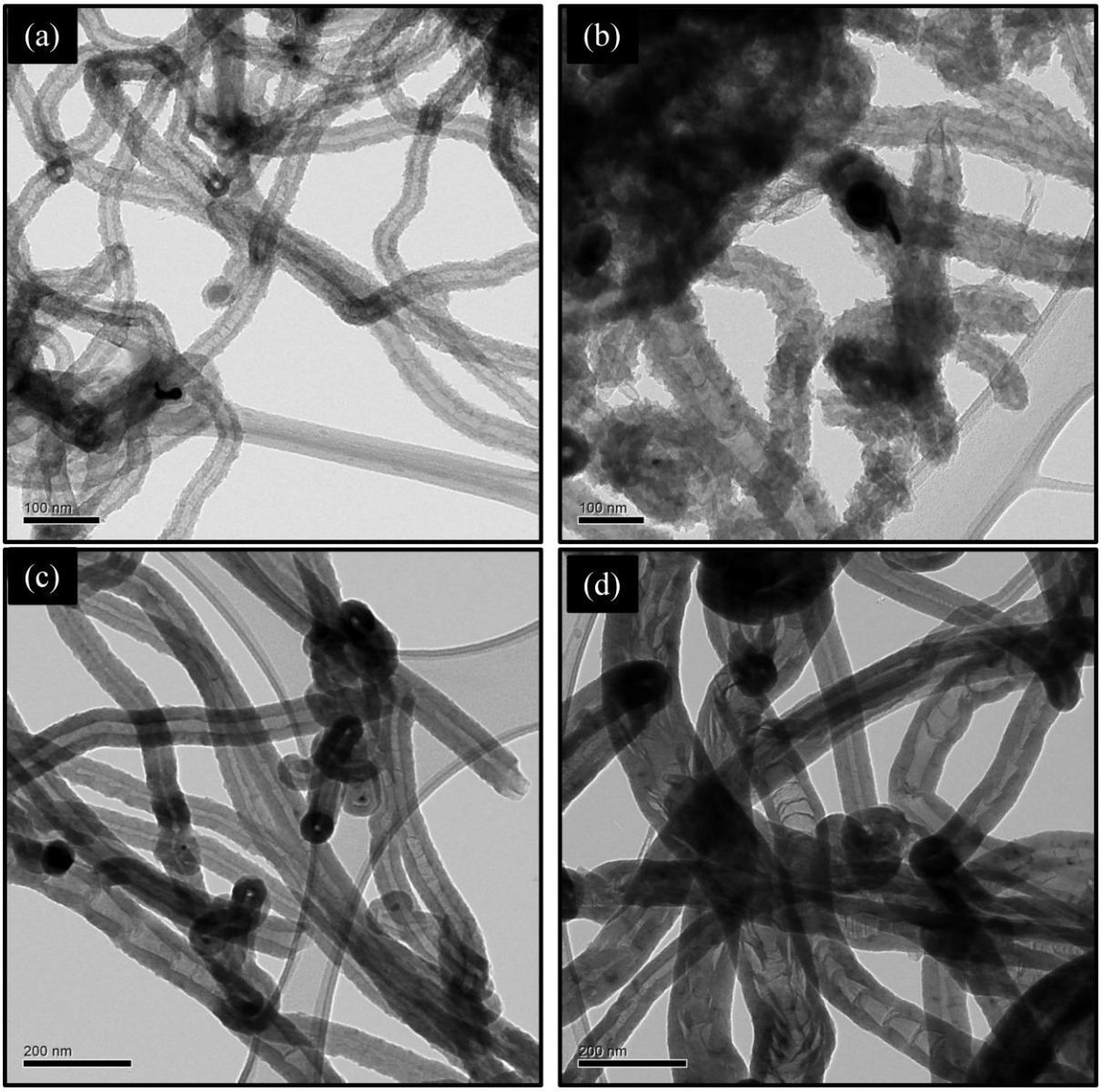


Figure 3.3: TEM images of the purified N-MWCNTs grown using CH_3CN (80 °C) and reaction temperatures of (a) 700 °C, (b) 750 °C, (c) 800 °C and (d) 850 °C.

At 700 °C the tubes appear to have rough thin walls and very few compartments. The percentage of nitrogen in these tubes is ~2.2% (see later). The N-MWCNTs grown at 750 °C at all CH_3CN heating temperatures (room temperature to 80 °C; Figures 3.1b, 3.2b and 3.3b), have very rough surfaces and gave compartments that were separated by narrow shells, formed randomly and frequently. We attribute the very rough surface texture of the N-MWCNTs at 700-750 °C to defect formation and possibly incomplete crystallization of the graphene sheets caused by lower growth temperature. TGA analysis of our N-MWCNTs grown at 700-750 °C showed no evidence of amorphous carbon (see later). At 800 °C

Z.N. Tetana, S.D. Mhlanga, G. Bepete, R.W.M. Krause, N.J. Coville, *S. Afr. J. Chem.*, 2012, 65, 39-49.

(Figures 3.1c, 3.2c, and 3.3c), as the CH_3CN vaporization temperature increased from room temperature to 80 °C, the compartment layers occurred at regular distances and became more visible and appeared to be thick and curved. At 850 °C, as the CH_3CN heating temperature increased from room temperature to 80 °C, the well curved thick compartment layers had shorter separation distances (Figures 3.1d, 3.2d, and 3.3d). The N-MWCNTs at 850 °C had a wide range of outer diameters that decreases with CH_3CN heating temperature. At 850 °C carbon spheres (CSs) were observed, also with a wide range of diameters (see Table 3.1).

Quantification of the above TEM observation was achieved by analysis of the nitrogen-containing carbon nanotubes from the TEM images (supplementary Figures S1a-c in Appendix A and Table 3.1). The data reveal that at all CH_3CN heating temperatures, as the synthesis temperature increases, the outer diameters of the N-MWCNTs also increase. As the growth temperature increased metallic catalyst particles agglomerated to form bigger particles which in turn generated larger diameters of the synthesized N-MWCNTs.[34] On the other hand, the inner diameter measurements revealed no systematic trend with respect to synthesis and CH_3CN temperatures. It is noted that at all CH_3CN temperatures, the average outer diameters of the N-MWCNTs synthesized at 700, 750, 800 and 850 °C, are relatively uniform in size (±5 nm of the average value).

Table 3.1: The effects of temperature on the outer diameter of the purified N-MWCNTs.

	CH_3CN TEMPERATURE								
	r.t.			**50 °C**			**80 °C**		
Sample	**Size distribution (nm)**	**Average diam. (nm)**	**Type of material**	**Size distribution (nm)**	**Average diam. (nm)**	**Type of material**	**Size distribution (nm)**	**Average diam. (nm)**	**Type of material**
700	22-98	30	CNTs	22-118	30	CNTs	22-158	30	CNTs
750	22-98	50	CNTs	22-138	50	CNTs	22-178	50	CNTs
800	17-143	70	CNTs	22-158	70	CNTs	40-170 75-350	70 100	CNTs CSs
850	22-220 100-450	90 150	CNTs CSs	5-195 80-450	90 130	CNTs CSs	42-220 200-450	90 250	CNTs CSs

Z.N. Tetana, S.D. Mhlanga, G. Bepete, R.W.M. Krause, N.J. Coville, *S. Afr. J. Chem.*, 2012, 65, 39-49.

Figure 3.4 and supplementary Figure S2 show representative SEM micrographs of the purified nitrogen-containing materials synthesized at 850 °C (using CH_3CN at r.t. and 50 °C) and 800-850 °C (using CH_3CN at 80 °C), respectively. The SEM images show that CSs were formed along with N-MWCNTs. The CSs were linked together in a necklace-like fashion, typical of CSs synthesized in the presence of hydrocarbons by CVD; in the absence of a catalyst.[55]

Quantitative observation of TEM and SEM images of carbon produced at 850 °C indicates that the N-MWCNT/CS ratio varied with CH_3CN heating temperature. At room temperature the N-MWCNT/CS ratio was 70/30, at 50 °C it was 65/35 and at 80 °C it was 50/50. (At a reaction temperature of 800 °C, using CH_3CN at 80 °C, the ratio was 60/40). The SEM images and Table 3.1 showed that (i) increasing CH_3CN vaporization temperature gives CSs with a larger yield and diameters, (ii) increasing growth temperature gives CSs with a larger yield and larger diameters. This is consistent with previous reports that higher temperatures favour growth of carbon spheres.[56,57] In independent studies, nitrogen-doped carbon spheres (N-CSs) have been synthesized in our laboratory using C_2H_2 and CH_3CN without the use of a catalyst. This confirms that the CSs formed here have been produced via non-catalytic synthesis procedures and contain nitrogen.

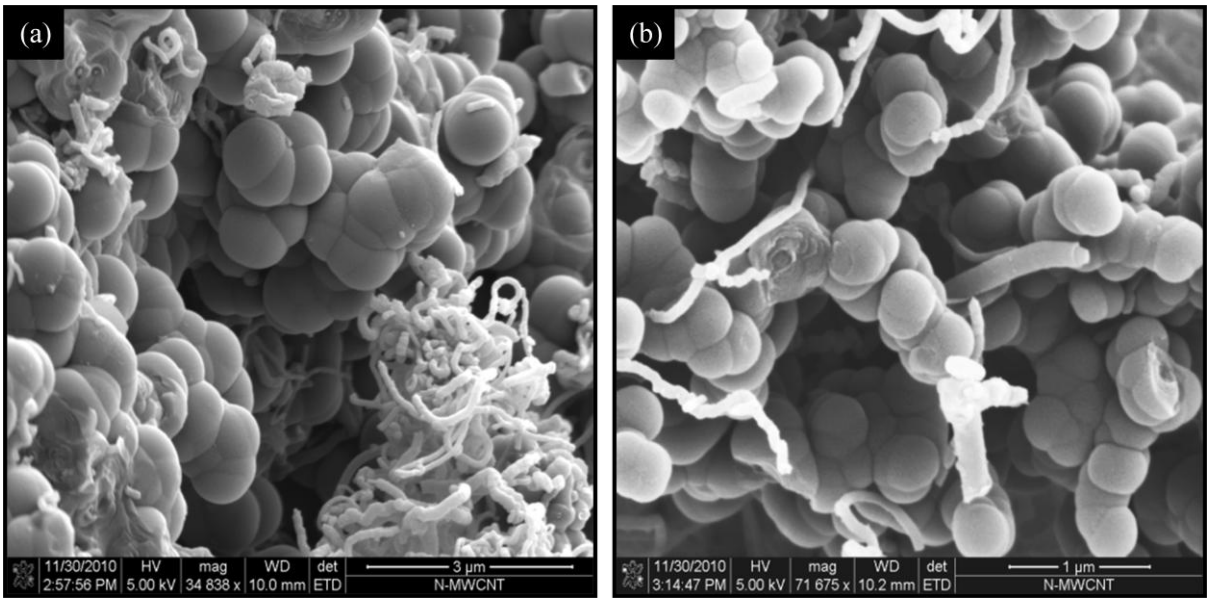


Figure 3.4: SEM images of the purified N-MWCNTs grown at 850 °C using CH_3CN at: (a) r.t., (b) 50 °C.

Z.N. Tetana, S.D. Mhlanga, G. Bepete, R.W.M. Krause, N.J. Coville, *S. Afr. J. Chem.*, 2012, 65, 39-49.

3.3.2 Yield of N-MWCNTs

In this study the yields have been determined from the amount of carbon deposited relative to the amount of carbon passed over the catalyts e.g. a yield of 16% was obtained at 800 ^{o}C. The yields are typical of N-CNT yields in these types of reactions. Yields are often quoted as the amount of product formed relative to the amount of catalyst used (a type of turn over number) and then the 'yield' can be > 1000%.[58] In catalytic CVD procedures, higher temperatures are used to produce a higher carbon yield.[55] However, at higher temperatures non-catalytic competing pathways can occur and in this study CSs formed together with the desired materials. The total yield of the as-synthesized nitrogen-containing materials increased as the synthesis temperature increased from 700-850 °C (Figure 3.5). At low reaction temperatures (700-750 °C), only small amounts of N-MWCNTs were formed. At higher temperatures (800-850 °C), the decomposition rate of C_2H_2 and CH_3CN is faster and large amounts of N-MWCNTs and N-CSs were formed. An increased CH_3CN content is seen to reduce the carbon yield (Figure 3.5).

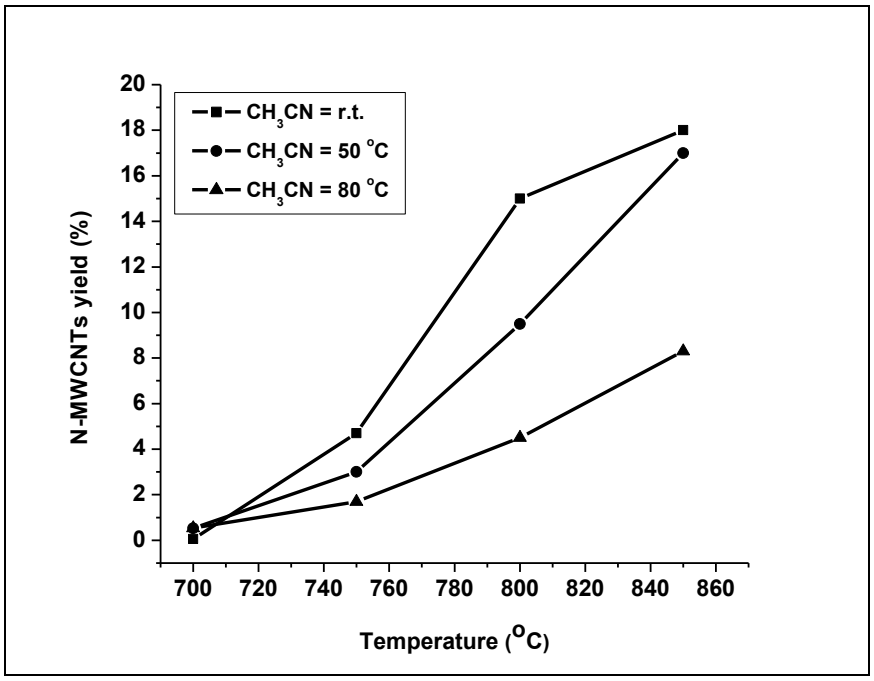


Figure 3.5: Graph showing the amounts of N-MWCNTs grown at 700-850 °C using CH_3CN at r.t., 50 °C and 80 °C.

Z.N. Tetana, S.D. Mhlanga, G. Bepete, R.W.M. Krause, N.J. Coville, *S. Afr. J. Chem.*, 2012, 65, 39-49.

3.3.3 BET surface area and pore volume analysis of N-MWCNTs

The specific surface areas and pore volume of the purified N-MWCNTs are shown in Table 3.2. The surface areas and pore volume of the purified N-MWCNTs decreased as (i) reaction temperature and (ii) CH_3CN temperature increased from 700-850 °C and r.t. to 80 °C, respectively. The observed surface areas and pore volume of the N-MWCNTs are related to (i) the formation of oxidized functional groups on the surface of N-MWCNTs,[59,60] (ii) the larger average diameters of the N-MWCNTs, which exhibit a lower external surface area at higher synthesis temperatures, (iii) the harder texture and (iv) the presence of low surface area N-CSs.

Table 3.2: The BET surface areas and pore volume of the purified N-MWCNTs.

	CH_3CN TEMPERATURE					
	r.t.		**50 °C**		**80 °C**	
Sample	**BET surface area (m^2/g)**	**Pore volume (cm^3/g)**	**BET surface area (m^2/g)**	**Pore volume (cm^3/g)**	**BET surface area (m^2/g)**	**Pore volume (cm^3/g)**
700P	138.4	0.55	142.6	0.48	97.3	0.32
750P	64.8	0.24	60.6	0.16	56.3	0.26
800P	29.6	0.076	18.1	0.060	16.5	0.056
850P	10.9	0.039	16.3	0.042	9.2	0.026

3.3.4 Thermogravimetric analysis of N-MWCNTs

The thermal stabilities of the as-synthesized and purified N-MWCNTs were evaluated using TGA under an air flow rate of 30 ml/min and a constant heating rate of 10 °C/min. TGA was also used to study the overall purity of the N-MWCNTs. Figures 3.6a-c show typical TGA profiles and the corresponding derivative curves of the as-synthesized N-MWCNTs made at 700-850 °C using CH_3CN at r.t., 50 °C and 80 °C. The TGA profiles of the purified N-MWCNTs (denoted 700P-850P) are shown in supplementary Figures S3-S5. The maxima in the first order derivative plots of the TGA curves were used to estimate decomposition temperatures of the N-MWCNTs (Table 3.3).[61]

Z.N. Tetana, S.D. Mhlanga, G. Bepete, R.W.M. Krause, N.J. Coville, *S. Afr. J. Chem.*, 2012, 65, 39-49.

According to the literature, amorphous carbon typically oxidizes in air at temperatures below 400 °C,[62,63] whereas CNTs oxidize at higher temperatures, up to 800 °C.[64] The TGA data showed that there was no mass loss below 400 °C, confirming (from TEM studies) that amorphous carbon was not observed in the as-synthesized N-MWCNTs. All N-MWCNTs synthesized at 700 °C (Figures 3.6a-c) showed weight gains at 455-553 °C due to the formation of metal oxide from incompletely oxidized catalysts.[65]

Two weight loss derivative curves occur in the high temperature region for all the as-synthesized N-MWCNTs and the peak positions vary with temperature. As seen from Table 3.3, the first peak of the derivative plot occur at 587-700 °C for all the as-synthesized N-MWCNTs and can be attributed to the degradation of N-MWCNTs while the second peak at 737-768 °C can be attributed to other carbon crystalline materials such as graphitic soot,[66] and possibly undoped MWCNTs.

For all purified N-MWCNTs synthesized using CH_3CN at r.t. and 50 °C, the carbon decomposition temperature generally increased as the reaction temperature increased from 700-800 °C and decreased at 850 °C. Moreover, when the CH_3CN heating temperature was kept at 80 °C, the decomposition temperature was more variable. Our TGA results generally agree with those reported in the literature. A number of reports suggested that an increase in nitrogen content gave rise to less thermally stable N-CNTs, due to more structural defects and disorderachieved by the introduction of reactive sites in the N-CNTs.[67,68]

Z.N. Tetana, S.D. Mhlanga, G. Bepete, R.W.M. Krause, N.J. Coville, *S. Afr. J. Chem.*, 2012, 65, 39-49.

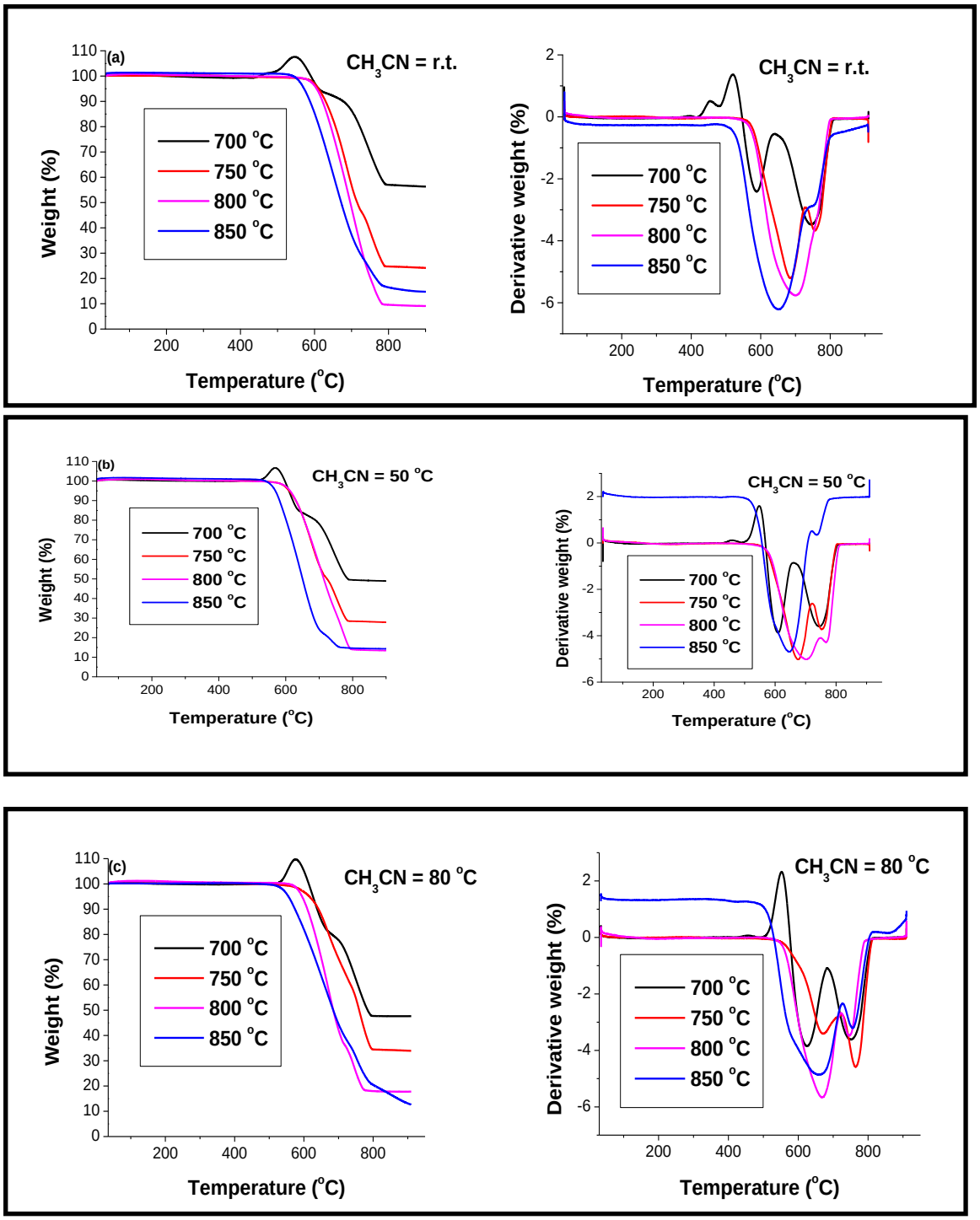


Figure 3.6: TGA and corresponding derivative profiles of the as-synthesized N-MWCNTs using CH_3CN at: (a) r.t., (b) 50 °C and (c) 80 °C.

Z.N. Tetana, S.D. Mhlanga, G. Bepete, R.W.M. Krause, N.J. Coville, *S. Afr. J. Chem.*, 2012, 65, 39-49.

Table 3.3: Decomposition temperatures and residual masses (determined by TGA) of the as-synthesized and purified N-MWCNTs.

	CH_3CN TEMPERATURE					
	r.t.		**50 °C**		**80 °C**	
Sample	**Decomposition temperature (°C)**	**Residual mass (%)**	**Decomposition temperature (°C)**	**Residual mass (%)**	**Decomposition temperature (°C)**	**Residual mass (%)**
700	587	56	611	49	623	48
700P	582	3.1	591	1.4	601	5.9
750	684	24	674	28	671	34
750P	662	0.38	626	3.4	636	2.0
800	697	8.9	703	13	668	18
800P	633	0	687	5.2	598	9.0
850	652	6.0	645	5.6	660	12
850P	626	0.38	668	2.0	658	1.5

The general drop in decomposition temperature at 850 ^oC is associated with the presence of a mixture of N-MWCNTs and CSs in the products (see Table 3.3). Usually small diameter CNTs or small bundles of the CNTs have lower combustion temperatures.[69] It is evident from our results that lower diameter N-MWCNTs, formed at a low growth temperature, decompose at a lower temperature than the large diameter N-MWCNTs prepared at a high growth temperature.[70] The results in Table 3.3 indicate a significant effect of CH_3CN vaporization temperature on the decomposition temperature of the as-synthesized N-MWCNTs. As can be seen, the as-synthesized N-MWCNTs at 700 °C show ~ 50% impurities (mainly Fe-Co/$CaCO_3$) but the yield of the impurities decreased as the synthesis temperature increased to 850 °C (~ 6% impurities). A large amount of the residual metal catalyst particles (Fe_2O_3 and Co_3O_4) was observed at lower synthesis temperatures at all CH_3CN heating temperatures.

The weight loss derivative curves of the purified N-MWCNTs (supplementary Figures S3-S5) showed noweight gains due to metal oxide formation, indicating that HNO_3 was effective in removing Co and Fe from the N-MWCNTs. It was also observed that after acid-treatment of all N-MWCNTs, the amount of residual catalyst decreased as the synthesis temperature

Z.N. Tetana, S.D. Mhlanga, G. Bepete, R.W.M. Krause, N.J. Coville, *S. Afr. J. Chem.*, 2012, 65, 39-49.

increased, suggesting that the residual Fe_2O_3 and Co_3O_4 catalyst particles were mostly removed. As shown in Table 3.3 and supplementary Figures S3-S5, the acid-treated N-MWCNTs oxidized earlier than the as-synthesized N-MWCNTs. This can be attributed to the presence of -OH and -COOH functional groups on the tubes, which assist the decomposition of the CNTs.

3.3.5 Elemental (C and N) analysis of N-MWCNTs

The purified nitrogen-containing carbon nanomaterials were also characterized by C and N elemental analysis. CN analysis confirmed the presence of nitrogen in the N-MWCNTs (Table 3.4). It is clear from the data that as the synthesis temperature increased (700 to 800 °C), the percentage of N inserted into the N-MWCNTs decreased and then increased. This arises from two effects: As the temperature increases the N doping of the CNTs decreases.[49, 53] However, at the higher temperatures, CSs form that also contain nitrogen. In independent studies,[71] it was shown that the N content of CSs increased slightly with increasing temperature. Thus, the two effects operate in opposite directions to give the results seen.

The data also showed that at 700 °C and 750 °C, as CH_3CN vaporization temperature increased (r.t. to 80 °C) the N concentration showed little variation, suggesting that the C_2H_2/CH_3CN ratio had little effect on the N-MWCNT growth.

Table 3.4: CN elemental analysis of the purified N-MWCNTs.

	CH_3CN TEMPERATURE					
	r.t. Atomic %		**50 °C Atomic %**		**80 °C Atomic %**	
Sample	**C**	**N**	**C**	**N**	**C**	**N**
700P	78.24	2.23	86.58	2.16	84.78	2.14
750P	88.89	1.44	86.91	1.76	89.82	1.68
800P	91.11	1.98	87.85	2.22	82.90	2.81
850P	88.39	3.46	94.55	3.64	87.18	4.18

Z.N. Tetana, S.D. Mhlanga, G. Bepete, R.W.M. Krause, N.J. Coville, *S. Afr. J. Chem.*, 2012, 65, 39-49.

3.3.6 Raman spectroscopy analysis of N-MWCNTs

Raman spectroscopy is an effective tool to analyze the crystallinity and the defects in carbon structures.[72] Raman spectroscopy was used to provide information on the degree of structural defects in N-MWCNTs (supplementary Figures S6-S8). The Raman spectra (also, see Table 5) show two main bands at approximately 1350-1360 cm^{-1} (D-band) and approximately 1590-1600 cm^{-1} (G-band), which are characteristic of MWCNTs. The D-band is associated with defects and impurities in the CNTs. The G-band corresponds to the stretching mode of the C-C bond in the graphite plane. The area ratio of the D- to G-bands (I_D/I_G) allows for a comparison of defects in the N-MWCNTs. A high I_D/I_G ratio indicates more defects present inside the carbon layers of CNTs. The results indicate that as the reaction temperature increases the degree of disorder increases, correlating with the higher nitrogen content (Table 3.4).

Table 3.5: The D-, G-bands and I_D/I_G ratios of the as-synthesized and purified N-MWCNTs.

	CH_3CN TEMPERATURE								
	r.t.			**50 °C**			**80 °C**		
Sample	**D-band (cm^{-1})**	**G-band (cm^{-1})**	**I_D/I_G ratio**	**D-band (cm^{-1})**	**G-band (cm^{-1})**	**I_D/I_G ratio**	**D-band (cm^{-1})**	**G-band (cm^{-1})**	**I_D/I_G ratio**
700	1352	1598	1.43	1352	1601	1.31	1354	1600	1.05
700P	1355	1595	1.44	1353	1595	1.48	1355	1597	1.52
750	1355	1600	1.41	1354	1597	1.48	1357	1601	1.47
750P	1354	1595	1.52	1352	1593	1.65	1363	1602	1.52
800	1361	1600	2.20	1360	1598	1.75	1361	1597	2.53
800P	1362	1599	1.72	1361	1594	1.87	1368	1604	1.92
850	1359	1592	2.15	1351	1614	1.68	1358	1591	1.55
850P	1359	1596	2.14	1355	1614	2.02	1360	1596	2.04

3.3.7 XPS analysis of purified N-MWCNTs grown at 800 °C using CH_3CN at r.t.

XPS was used to determine the nitrogen-doping level and the types of N-moieties in the N-MWCNTs grown at 800 °C using CH_3CN at r.t. According to van Dommele and co-workers,[73] nitrogen can be incorporated into the CNT lattice in different bonding

Z.N. Tetana, S.D. Mhlanga, G. Bepete, R.W.M. Krause, N.J. Coville, *S. Afr. J. Chem.*, 2012, 65, 39-49.

configurations (Figure 3.7); namely, (A) pyridinic oxides: which are attributed to oxidized nitrogen on the graphite layers, (B) pyridine-like N: where the N atom is sp^2 hybridized, bonding to two C atoms, (C) pyrrole-like N: where the N is sp^3 hybridized in a five-membered ring, and (D) quaternary/graphitic/substitutional N: where a graphitic carbon atom is substituted by a N atom in the graphitic sheet.

XPS spectra of the purified N-MWCNTs grown at 800 °C using CH_3CN at r.t. are displayed in supplementary Figure S9 and the results of the peak analysis are summarized in Table 3.6. Figure 3.8 shows the high-resolution N 1s XPS spectrum, which indicates the presence of nitrogen-based species on the N-MWCNTs. The N 1s peak can be deconvoluted into three peaks, representing molecular nitrogen intercalated within the walls or within the inner cavity of the CNTs (molecular N_2 at 405 eV)[74], quaternary nitrogen (N_Q at 401 eV) and pyridinic nitrogen (N_P at 398 eV).[75] The analysis of the N 1s spectra reveals that N atoms in the outer layer mainly exist as molecular N_2 (0.76%). The N 1s peak also showed quaternary N (0.35%) with a small portion of pyridinic N (0.21%). This result is in line with other observations reported in the literature.[73,74,76] For example, van Dommele and co-workers,[73] when using CH_3CN and pyridine as N sources over Fe, Co or Ni supported on Al_2O_3 or SiO_2, established that quaternary nitrogen was found when nitrogen-doped CNTs were grown at high temperatures (750 and 850 °C), while pyridinic nitrogen was predominantly present at a lower temperature (550 °C). In addition, Yadav and co-workers[53] also established the presence of quaternary N when they synthesized bamboo-shaped CNTs using spray pyrolysis of ferrocene/acetonitrile solution at 850-950 °C. The total concentration of N from XPS analysis was 1.32% (Table 3.6), consistent with the results of our CN elemental analysis (1.98%, Table 3.4). Generally, an XPS spectrum mainly reflects the information of the outer layer of the measured sample. The combination of XPS and CN analysis results here suggests that nitrogen atoms appear uniformly doped from the interior to the surface of the N-MWCNT structure.

Z.N. Tetana, S.D. Mhlanga, G. Bepete, R.W.M. Krause, N.J. Coville, *S. Afr. J. Chem.*, 2012, 65, 39-49.

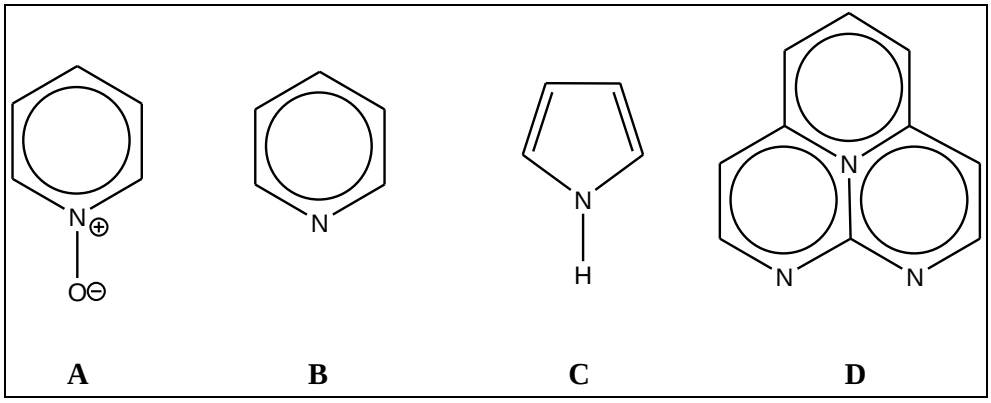


Figure 3.7: Types of nitrogen-based species that can be incorporated into graphitic carbon: A) oxidised pyridinic, B) pyridinic, C) pyrrolic, D) quaternary.[73]

Carbon and oxygen were also identified by XPS analysis (Table 3.6, peaks at about 285-289 eV and 531-533 eV, respectively). The strong C 1s peak at 284.7 eV can be assigned to sp^2 hybridized carbon (C-C bond) which is the major component in the N-MWCNTs. This value is similar to the previously reported for the N-CNTs by Ayala and co-workers.[75] The peaks at about 287 and 289 eV can be assigned to C-N bonding species[75] and O=C-O bond, respectively, due to the functionalization of N-MWCNTs by HNO_3. The O 1s peak at about 532 eV can be assigned to C-O and O-H bonds, also due to functionalization of N-MWCNTs by HNO_3. The oxygen peak is associated with C-O functionalities due to the oxygen absorbed on the surface of the CNTs,[77] the substrate on which the nanotubes were grown[78] and exposure of the sample to atmospheric air.[79]

Z.N. Tetana, S.D. Mhlanga, G. Bepete, R.W.M. Krause, N.J. Coville, *S. Afr. J. Chem.*, 2012, 65, 39-49.

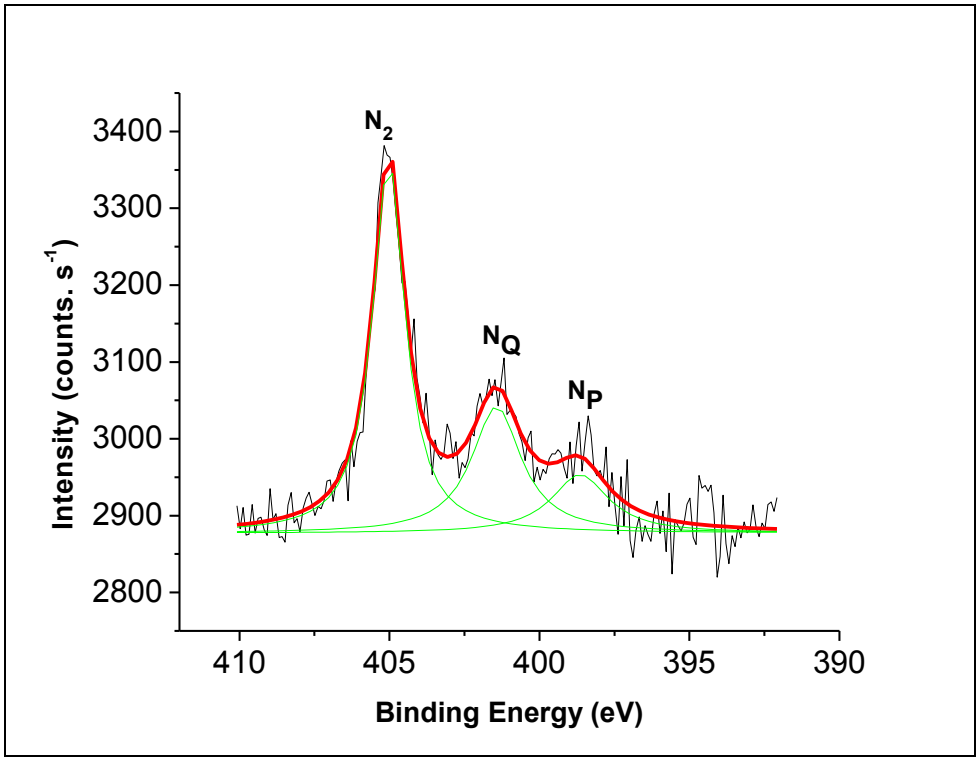


Figure 3.8: Deconvoluted N 1s XPS spectra of the purified N-MWCNTs synthesized at 800 °C using CH_3CN at r.t.

Table 3.6: XPS analysis of the purified N-MWCNTs grown at 800 °C using CH_3CN at r.t.

BINDING ENERGY (eV) (and atomic concentration (%))		
C	**N**	**O**
284.70 (71.01%)	**398.68** (0.21%)	**531.81** (5.67%)
288.56 (4.64%)	**401.45** (0.35%)	**533.61** (2.5%)
287.19 (2.26%)	**404.98** (0.76%)	**532.91** (2.76%)
286.12 (9.84%)		

Z.N. Tetana, S.D. Mhlanga, G. Bepete, R.W.M. Krause, N.J. Coville, *S. Afr. J. Chem.*, 2012, 65, 39-49.

3.4 Conclusions

Our results describe a simple method to make good yields of nitrogen-containing multiwalled carbon nanotubes with known nitrogen content. We have successfully synthesized nitrogen-doped carbon nanotubes by the catalytic pyrolysis of acetonitrile over a $CaCO_3$ supported Fe-Co catalyst. The CNTs formed were mostly multi-walled and bamboo-shaped. At higher temperatures (800-850 °C) a mixture of N-MWCNTs and CSs was observed. It is obvious that an increase in CH_3CN vaporization temperature plays a role in the formation of the nitrogen-containing materials. The study shows that the best conditions for the synthesis of high quality N-MWCNTs in good yields are 800 °C and a r.t. CH_3CN vaporization temperature, as the conditions give pure N-MWCNTs in good yield. The presence of nitrogen in all N-MWCNTs was confirmed by CN elemental analysis. The results showed that N-doping increased with an increase in CH_3CN vaporization temperature.

XPS results revealed that the nitrogen atoms were successfully doped inside the carbon walls and are trigonally bonded to graphitic carbon atoms. CN analysis and XPS data suggested that nitrogen atoms were uniformly doped throughout the N-MWCNT structure. At high synthesis temperatures, nitrogen incorporation into carbon is higher than for samples synthesized at low temperatures. This can be related to the higher number of defects in their structure, as confirmed by Raman spectroscopy. It has been shown that the properties of N-MWCNTs, i.e., the level and the type of nitrogen-doping, surface area, diameter, quality and thermal stability, can be tuned by changing the growth and CH_3CN temperatures. The high surface area and thermal stability properties of the N-MWCNTs provide advantages for the N-MWCNTs to be used in several applications in catalysis. The N-MWCNTs synthesized are suitable for use as catalyst supports for the synthesis of chemicals, in water purification, as well as in fuel cell and solar cell applications. The method used here is environmentally friendly and suitable for large scale production of N-MWCNTs.

This work has shown that N-doped MWCNTs can be synthesized over an Fe-Co/$CaCO_3$ catalyst, suggesting that this method could be used to make other doped CNTs. The study shows that operating conditions need to be clearly established. Nitrogen-doping of the CNTs are limited to ~2% using this procedure.

Z.N. Tetana, S.D. Mhlanga, G. Bepete, R.W.M. Krause, N.J. Coville, *S. Afr. J. Chem.*, 2012, 65, 39-49.

References

1. H.W. Kroto, J.R. Heath, S.C. O' Brien, R.F. Curl and R.E. Smalley, *Nature*, 1985, **318**, 162-163.
2. S. Iijima, *Nature*, 1991, **354**, 56-58.
3. (a) D. Ugarte, *Nature*, 1992, **359**, 707-709; (b) Z.C. Kang and Z.L. Wang, *Philos. Mag. B*, 1996, **73**, 905-929; (c) Z.L. Wang and Z.C. Kang, *J. Phys. Chem.*, 1996, **100**, 17725-17731.
4. (a) N. Sano, H. Wang, M. Chhowalla, I. Alexandrou and G.A.J. Amaratunga, *Nature*, 2001, **414**, 506-507; (b) X.H. Chen, F.M. Deng, J.X. Wang, H.S. Yang, G.T. Wu and X.B. Zhang, *Chem. Phys. Lett.*, 2001, **336**, 201-204; (c) X. Bing-She, *New Carbon Mater.*, 2008, **23**, 289-301.
5. (a) A. Shaikjee, P.J. Franklyn and N.J. Coville, *Carbon*, 2011, **49**, 2950-2959; (b) A. Shaikjee and N.J. Coville, *Small*, 2011, **49**, 2950-2959; (c) A. Shaikjee and N.J. Coville, *Mater. Lett.*, 2012, **68**, 273-276.
6. (a) S. Iijima, M. Yudasaka, R. Yamada, S. Bandow, K. Suenaga, F. Kokai and K. Takahashi, *Chem. Phys. Lett.*, 1999, **309**, 165-170; (b) H. Wang, M. Chhowalla, N. Sano, S. Jia and G.A.J Amaratunga, *Nanotechnology*, **15**, 2004**,** 546-550.
7. P. Serp, M. Corrias and P. Kalck, *Appl. Catal.*, 2003, **253**, 337-358.
8. M.C. Bahome, L.L. Jewel, D. Hildebrandt, D. Glasser and N.J. Coville, *Appl. Catal., A*, 2005, **287**, 60-67.
9. Y. Maeda, S. Kimura, M. Kanda, Y. Hirashima, T. Hasegawa, T. Wakahara, Y.F. Lian, T. Nakahodo, T. Tsuchiya and T. Akasaka, J. Lu, X.Zhang, Z. Gao, Y. Yu, S. Nagase, S. Kazaoui, N. Minami, T. Shimizu, H. Tokumoto, R. Saito, *J. Am. Chem. Soc.*, 2005, **127**, 10287-10290.
10. M. Terrones, A. Jorio, M. Endo, A.M. Rao, Y.A. Kim, T. Hayashi, H. Terrones, J.-C. Charlier, G. Dresselhaus and M.S. Dresselhaus, *Mater. Today Magazine*, 2004, **7**, 30-45.
11. Q. Cao and J.A. Rogers, *Adv. Mater.*, 2009, **21**, 29-53.
12. C. Liu, Y.Y. Fan, M. Liu, H.T. Cong, H.M. Cheng, and M.S. Dresselhaus, *Science*, 1999, **286**, 1127-1129.
13. H.M. Cheng, Q.H. Yong and C. Liu, *Carbon*, 2001, **39**, 1447-1454.
14. H. Dai, N. Franklin and J. Han, *Appl. Phys. Lett.*, 1998, **73**, 1508-1510.

15. N. Hamada, S. Sawada and A. Oshiyama, *Phys. Rev. Lett.*, 1992, **68**, 1579-1581.
16. R. Saito, M. Fujita, G. Dresselhaus and M.S. Dresselhaus, *Phys. Rev. B*, 1992, **46**, 1804-1811.
17. X. Wang, Y. Liu, G. Yu, C. Xu and J. Zhang, *J. Phys. Chem. B*, 2001, **105**, 9422-9425.
18. J.Y. Lao, W.Z. Li, J.G. Wen and Z.F. Ren, *Appl. Phys. Lett.*, 2002, **80**, 500-502.
19. J.W. Jang, C.E. Lee, S.C. Lyu, T.J. Lee and C.J. Lee, *Appl. Phys. Lett.*, 2004, **84**, 2877-2879.
20. O. Stephan and P. Ajayan, *Science*, 1994, **266**, 1863-1865.
21. R. Czerw, M. Terrones, J.-C. Charlier, X. Blasé, B. Foley, R. Kamalakaran, N. Grobert, H. Terrones, D. Tekleab, P.M. Ajayan, W. Blau, M. Ruhle and D.L. Carroll, *Nano Lett.*, 2001, **9**, 457-460.
22. M. Terrones, P.M. Ajayan, F. Banhart, X. Blase, D.L. Carroll, J.-C. Charlier, R. Czerw, B. Foley, N. Grobert, R. Kamalakaran, P. Kohler-Redlich, M. Ruhle, T. Seeger and H. Terrones, *Appl. Phys. A Mater.*, 2002, **74**, 355-361.
23. M. Yudasaka, R. Kikuchi, Y. Ohki and S. Yoshimura, *Carbon*, 1997, **35**, 195-201.
24. R. Sen, B.C. Satishkumar, A. Govindaraj, K.R. Harikumar, G. Raina, J.P. Zhang, A.K. Cheetham and C.N.R. Rao, *Chem. Phys. Lett.*, 1998, **287**, 671-676.
25. K. Gong, F. Du, Z. Xia, M. Durstock and L. Dai, *Science*, 2009, **323**, 760-764.
26. E.N. Nxumalo, V.O. Nyamori and N.J. Coville, *J. Organomet. Chem.*, 2008, **693**, 2942-2948.
27. A.L. Elías, J.C. Carrero-Sanchez, H. Terrones, M. Endo, J.P. Laclette and M. Terrones, *Small*, 2007, **3**, 1723-1729.
28. M. Glerup, J. Steinmetz, D. Samaile, O. Stephan, S. Enouz, A. Loiseau, S. Roth and P. Bernier, *Chem. Phys. Lett.*, 2004, **387**, 193-197.
29. Y. Zhang, H. Gu, K. Suenaga and S. Iijima, *Chem. Phys. Lett.*, **279**, 1997, 264-268.
30. D. Golberg, Y. Bando, W. Han, K. Kurashima and T. Sato, *Chem. Phys. Lett.*, 1999, **308**, 337-342.
31. S.H. Lim, H.I. Elim, X.Y. Gao, A.T.S. Wee, W. Ji, J.Y. Lee and J. Lin, *Phys. Rev. B*, 2006, **73**, 045402/1-045402/6.
32. M. Terrones, N. Grobert, J. Olivares, J.P. Zhang, H. Terrones, K. Kordatos, W.K. Hsu, J.P. Hare, P.D. Townsend, K. Prassides, A.K. Cheetham, H.W. Kroto and D.R.M. Walton, *Nature*, 1997, **388**, 52-55.

33. K. Suenaga, M. Yudasaka, C. Colliex and S. Iijima, *Chem. Phys. Lett.*, 2000, **316**, 365-372.
34. G. Bepete, Z.N. Tetana, S. Lindner, M.H. Rümmeli, Z. Chiguvare and N.J. Coville, *Carbon*, 2013, **52**, 316-325.
35. R. Xue, Z. Sun, L. Su and X. Zhang, *Catal. Lett.*, 2010, **135**, 312-320.
36. K. Chizari, I. Janowska, M. Houllé, I. Florea, O. Ersen, T. Romero, P. Bernhardt, M.J. Ledoux and C. Pham-Huu, *Appl. Catal. A: General*, 2010, **380**, 72-80.
37. K.-Y. Chun, H.S. Lee and C.J. Lee, *Carbon*, 2009, **47**, 169-177.
38. W.-X. Lv, K.-Y. Shi, L. Li and S.-Z. Shao, *Microchim. Acta*, 2010, **170**, 91-98.
39. C.J. Lee and J. Park, *Appl. Phys. Lett.*, 2000, **77**, 3397-3399.
40. M.H. Kuang, Z.L. Wang, X.D. Bai, J.D. Guo and E.G. Wang, *Appl. Phys. Lett.*, 2000, **76**, 1255-1257.
41. S.D. Mhlanga, K.C. Mondal, R. Carter, M.J. Witcomb and N.J. Coville, *S. Afr. J. Chem.*, 2009, **62**, 67-76.
42. C.J. Lee. J. Park and J.A. Yu, *Chem. Phys. Lett.*, 2002, **360**, 250-255.
43. C.-T. Hsieh, Y.-T. Lin, J.-Y. Lin and J.-L. Wei, *Mater. Chem. Phys.*, 2009, **114**, 702-708.
44. E. Couteau, K. Hernadi, J.W. Seo, L. Thiên-Nga, Cs. Mikó, R. Gaál and L. Forró, *Chem. Phys. Lett.*, 2003, **378**, 9-17.
45. C.H. See, A. Husin and A.T. Harris, *Chem. Eng. Technol.*, 2009, **32**, 1280-1284.
46. J. Cheng, X. Zhang, Z. Luo, F. Liu, Y. Ye, W. Yin, W. Liu and Y. Han, *Mater. Chem. Phys.*, 2006, **95**, 5-11.
47. H. Kathyayini, N. Nagaraju, A. Fonsec and J.B. Nagy, *J. Mol. Catal.*, 2004, **223**, 129-136.
48. E. Dervishi, Z. Li, A.R. Biris, D. Lupu, S.S. Ttrigwell and A.S. Biris, *Chem. Mater.*, 2007, **19**, 179-184.
49. T.C. Schmitt, A.S. Biris, D.W. Miller, A.R. Biris, D. Lupu, S.S. Trigwell and Z.U. Rahman, *Carbon*, 2006, **44**, 2032-2038.
50. P. Piedigrosso, Z. Konya, J.-F. Colomer, A. Fonseca, G. van Tendeloo and J.B. Nagy, *Phys. Chem. Chem. Phys.*, 2000, **2**, 163-170.
51. D. Pradhan and M. Sharon, *Mater. Sci. Eng. B.*,2002, **96**, 24-28.
52. A.-C. Dupuis, *Prog. Mater. Sci.*, 2005, **50**, 929-961.

Z.N. Tetana, S.D. Mhlanga, G. Bepete, R.W.M. Krause, N.J. Coville, *S. Afr. J. Chem.*, 2012, 65, 39-49.

53. R.M. Yadav, P.S. Dobal, T. Shripathi, R.S. Katiyar and O.N. Srivastava, *Nanoscale Res. Lett.*, 2009, **4**, 197-203.
54. P. Ghosh, M. Zamri, M. Subramanian, T. Soga, T. Jimbo, R. Katoh and M. Tanemura, *J. Phys. D: Appl. Phys.*, 2008, **41**, 155405-155412.
55. A.A. Deshmukh, S.D. Mhlanga and N.J. Coville, *Mater. Sci. Eng. R*, 2010, **70**, 1-28.
56. C.J. Lee. S.C. Lyu, H.W. Kim, J.H. Lee and K.I. Cho, *Chem. Phys. Lett.*, 2002, **359**, 115-120.
57. J.-Y. Miao, D.W. Hwang, K.V. Narasimhulu, P.-I. Lin, Y.-T. Chen, S.-H. Lin and L.-P. Hwang, *Carbon*, 2004, **42**, 813-822.
58. (a) A. Romero, A. Garrido, A. Nieto-Márquez, A. Raquel de la Osa, A. de Lucas and J.L. Valverde, *Appl. Catal. A: General*, 2007, **319**, 246-258; (b) M.M. Shaijumon and S. Ramaprabhu, *Int. J. Hydrogen Energy*, 2005, **30**, 311-317; (c) S. Lim, A. Shimizu, S.-H. Yoon, Y. Korai and I. Mochida, *Carbon*, 2004, **42**, 1279-1283.
59. M. Chen, H.-W. Yu, J.-H. Chen and H.-S Koo, *Diamond Relat. Mater.*, 2007, **16**, 1110-1115.
60. M.A.M. Motchelaho, H. Xiong, M. Moyo, L.L. Jewel and N.J. Coville, *J. Mol. Catal. A: Chem.*, 2011, **335**, 189-198.
61. J.H. Lehman, M. Terrones, E. Mansfield, K.E. Hurst and V. Meunier, *Carbon*, 2011, **49**, 2581-2602.
62. B.J. Landi, C.D. Cress, C.M. Evans and R.P. Raffaelle, *Chem. Mater.*, 2005, **17**, 6819-6834.
63. Z.J. Shi, Y.F. Lian, F.H. Liao, X.H. Zhou, Z.N. Gu, Y. Zhang, S. Iijima, H.D. Li, K.T. Yue and S.L. Zhang, *J. Phys. Chem. Solids*, 2000, **61**, 1031-1036.
64. Q. Liu, W. Ren, F. Li, H. Cong and H.-M. Cheng, *J. Phys. Chem. C*, 2007, **111**, 5006-5013.
65. I.W. Chiang, B.E. Brinson, A.Y. Huang, P.A. Willis, M.J. Bronikowski, J.L. Margrave, R.E. Smalley and R.H. Hauge, *J. Phys. Chem. B*, 2001, **105**, 8297-8301.
66. S.B. McKee and K.S. Vecchio, *J. Phys. Chem. B*, 2006, **110**, 1179-1186.
67. E.N. Nxumalo, P.J. Letsoalo, L.M. Cele and N.J. Coville, *J. Organomet. Chem.*, 2010, **695**, 2596-2602.
68. (a) X. Ma and E.G. Wang, *Appl. Phys. Lett.*, 2001, **78**, 978-980; (b) S. Maldonado, S. Morin and K.J. Stevenson, *Carbon*, 2006, **44**, 1429-1437; (c) S. Choi, K.H. Park, S. Lee and K.H. Koh, *J. Appl. Phys.*, 2002, **92**, 4007-4011.

69. Z. Li, E. Dervishi, Y. Xu, V. Saini, M. Mahmood, O.D. Oshin, A.R. Biris and A.S. Biris, *Catal. Lett.*, 2009, **131**, 356-363.
70. D.K. Singh, P.K. Iyer and P.K. Giri, *J. Appl. Phys.*, 2010, **108**, 084313/1-084313/10.
71. S. Dube and N.J. Coville, *to be published*.
72. G.F. Malgas, C.J. Arendse, N.P. Cele and F.R. Cummins, *J. Mater. Sci.*, 2008, **43**, 1020-1025.
73. S. van Dommele, A. Romero-Izquirdo, R. Brydson, K.P. de Jong and J.H. Bitter, *Carbon*, 2008, **46**, 138-148.
74. H.C. Choi, S.Y. Bae, W.S. Jang, J. Park, H.J. Song, H.-J. Shin, H. Jung and J.-P. Ahn, *J. Phys. Chem. B*, 2005, **109**, 1683-1688.
75. P. Ayala, A. Grüneis, T. Gemming, B. Büchner, M.H. Rümeli, D. Grimm, J. Schumann, R. Kaltofen, F.L. Freire Jr, H. D. Fonseca Filho and T. Pichler, *Chem. Mater.*, 2007, **19**, 6131-6137.
76. J.R. Pels, F. Kapteijn, J.A. Moulijin, Q. Zhu and K.M. Thomas, *Carbon*, 1995, **33**, 1641-1653.
77. A.E. Shalagina, Z.R. Ismagilov, O.Y. Podyacheva, R.I. Kvon and V.A. Ushakov, *Carbon*, 2007, **45**, 1808-1820.
78. M. He, S. Zhou, J. Zhang, Z. Liu and C. Robinson, *J. Phys. Chem. B*, 2005, **109**, 9275-9279.
79. C. Tang, Y. Bando, D. Golberg and F. Xu, *Carbon*, 2004, **42**, 2625-2633.

Appendix A: Supplementary material

Carbon yield calculation

$$\%\text{yield} = \frac{moles\ of\ carbon\ in\ product}{moles\ of\ carbon\ in\ C_2H_2 + \text{moles of carbon in } CH_3CN} \times 100\%$$

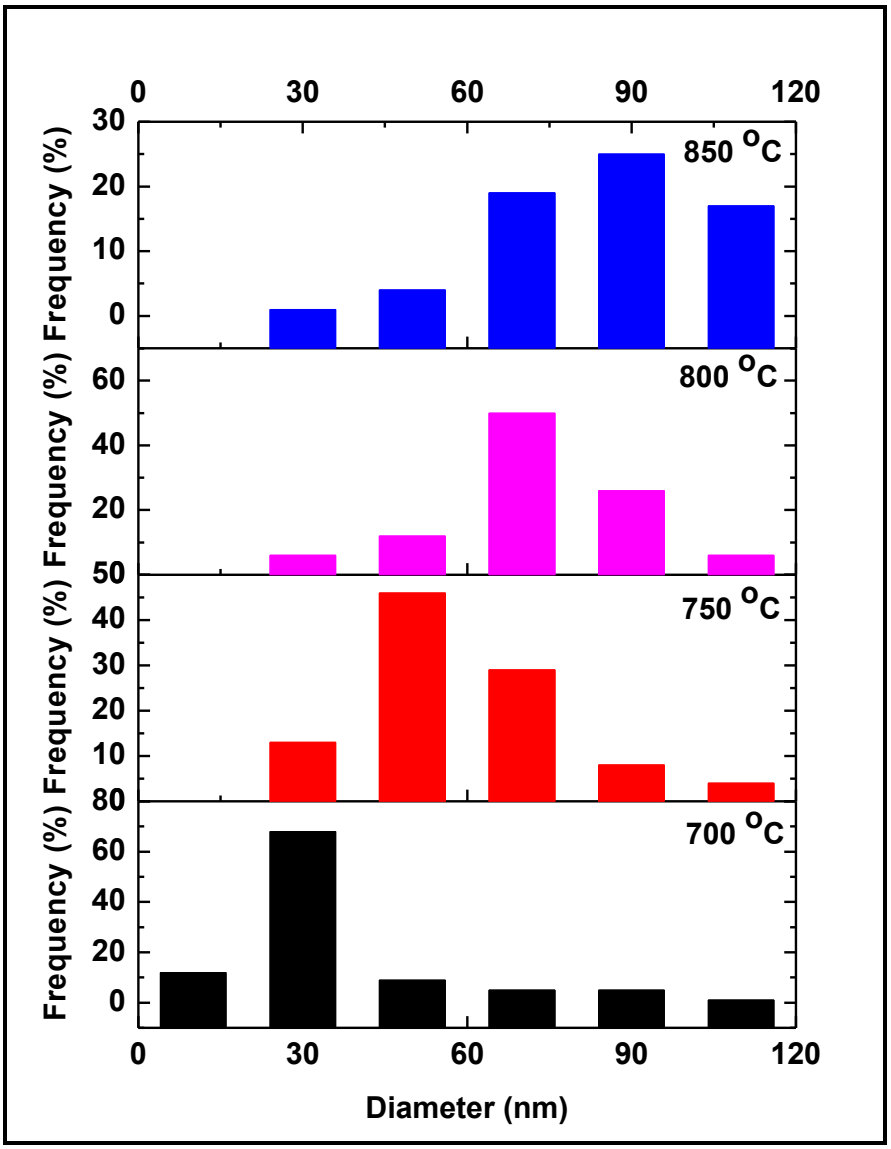


Figure S1a: Diameter distributions of the purified N-MWCNTs grown at 700-850 °C using CH_3CN at r.t.

Z.N. Tetana, S.D. Mhlanga, G. Bepete, R.W.M. Krause, N.J. Coville, *S. Afr. J. Chem.*, 2012, 65, 39-49.

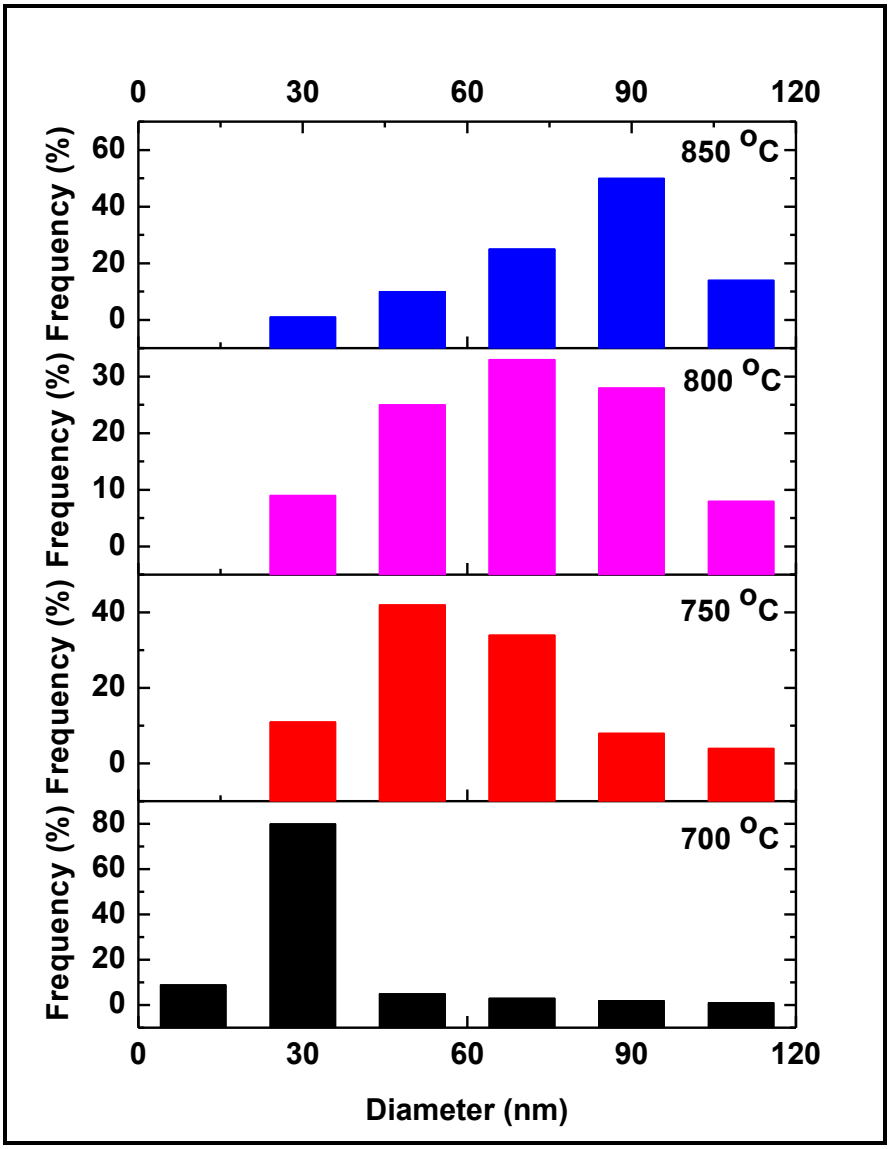


Figure S1b: Diameter distributions of the purified N-MWCNTs grown at 700-850 °C using CH_3CN at 50 °C.

Z.N. Tetana, S.D. Mhlanga, G. Bepete, R.W.M. Krause, N.J. Coville, *S. Afr. J. Chem.*, 2012, 65, 39-49.

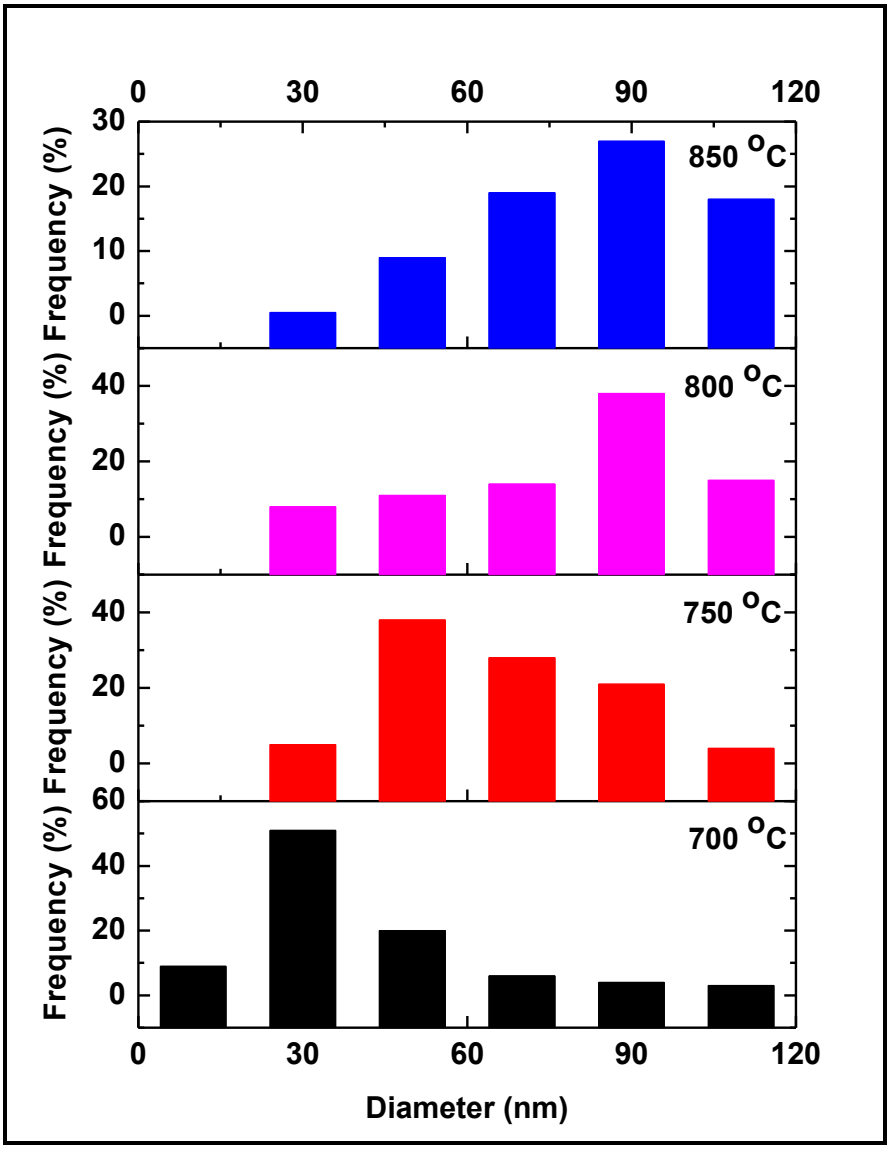


Figure S1c: Diameter distributions of the purified N-MWCNTs grown at 700-850 °C using CH_3CN at 80 °C.

Z.N. Tetana, S.D. Mhlanga, G. Bepete, R.W.M. Krause, N.J. Coville, *S. Afr. J. Chem.*, 2012, 65, 39-49.

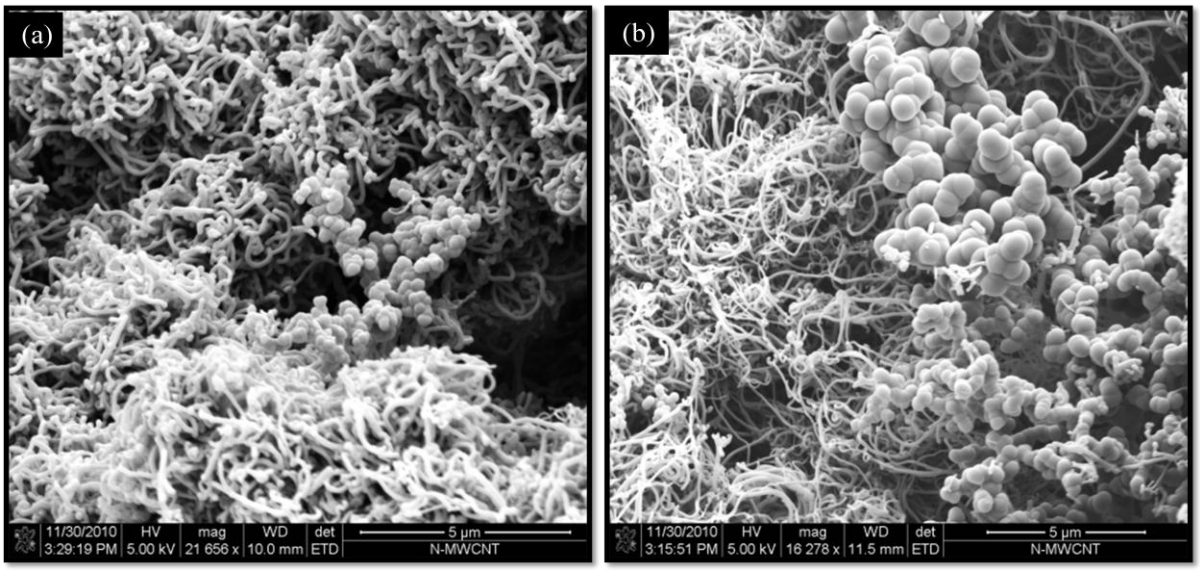


Figure S2: SEM images of the purified N-MWCNTs grown using CH_3CN at 80 °C: (a) 800 °C and (b) 850 °C.

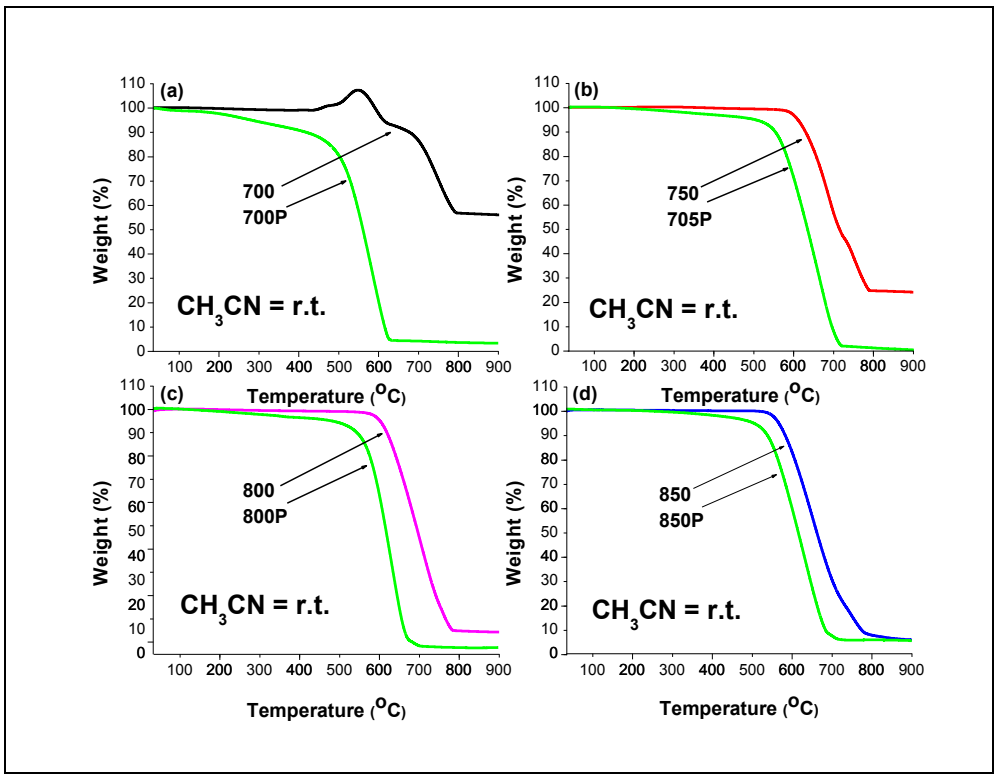


Figure S3: TGA curves of the as-synthesized and purified N-MWCNTs grown at 700-850 °C using CH_3CN at r.t.

Z.N. Tetana, S.D. Mhlanga, G. Bepete, R.W.M. Krause, N.J. Coville, *S. Afr. J. Chem.*, 2012, 65, 39-49.

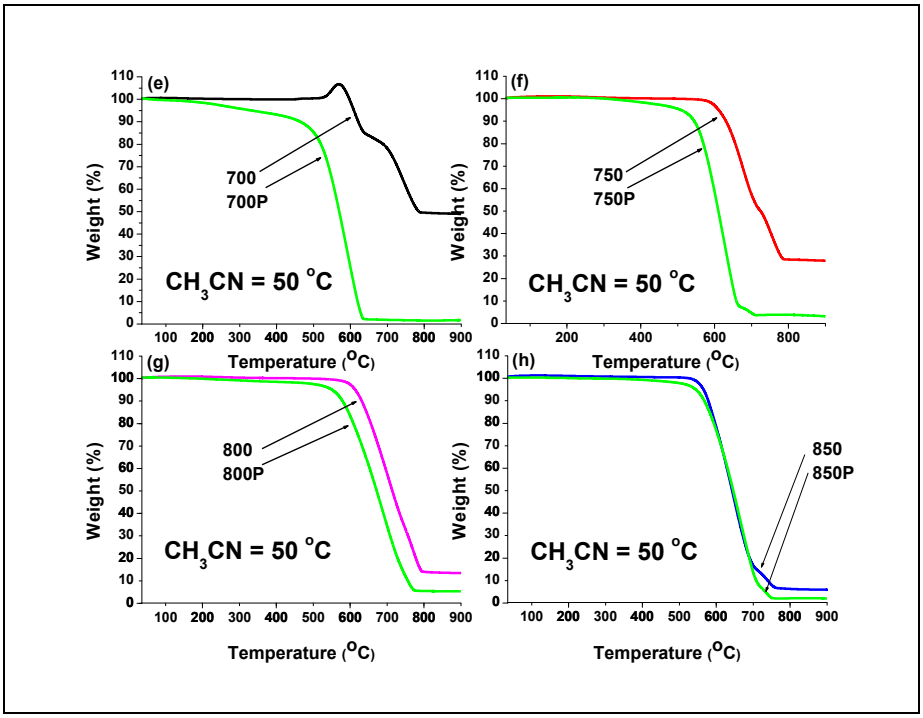


Figure S4: TGA curves of the as-synthesized and purified N-MWCNTs grown at 700-850 °C using CH_3CN at 50 °C.

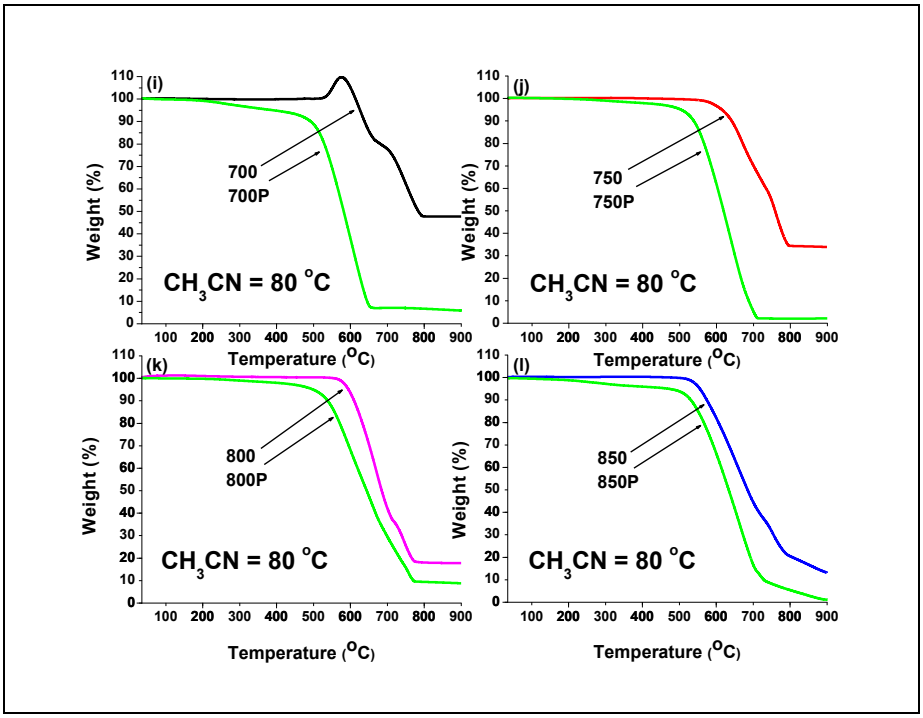


Figure S5: TGA curves of the as-synthesized and purified N-MWCNTs grown at 700-850 °C using CH_3CN at 80 °C.

Z.N. Tetana, S.D. Mhlanga, G. Bepete, R.W.M. Krause, N.J. Coville, *S. Afr. J. Chem.*, 2012, 65, 39-49.

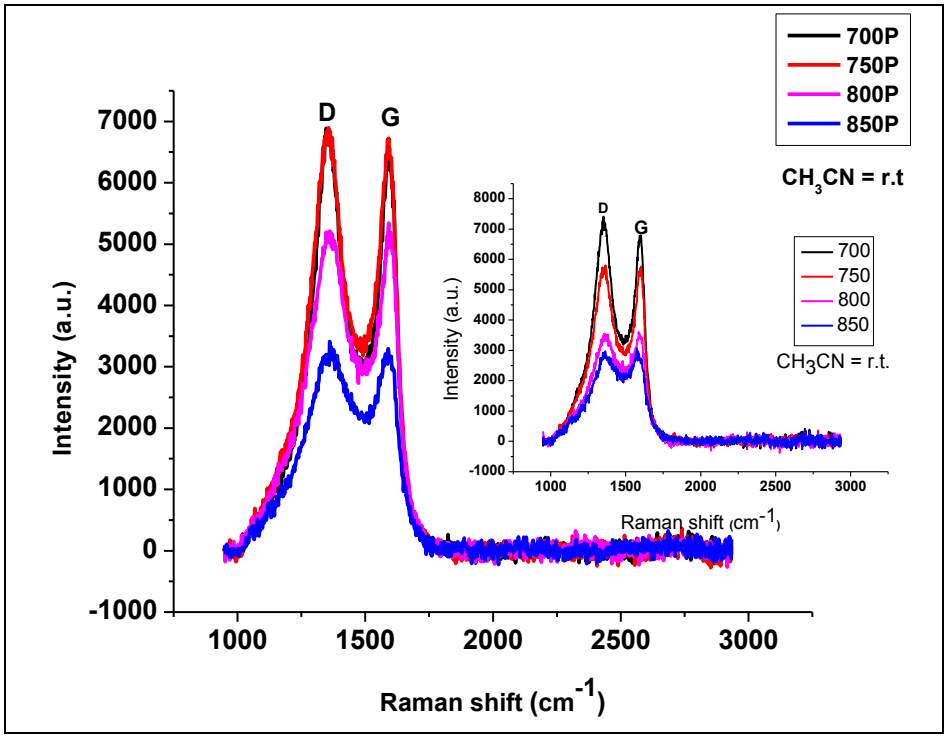


Figure S6: Raman spectra of the purified (700P-850P) and as-synthesized (700-850, inset) N-MWCNTs using CH_3CN at r.t.

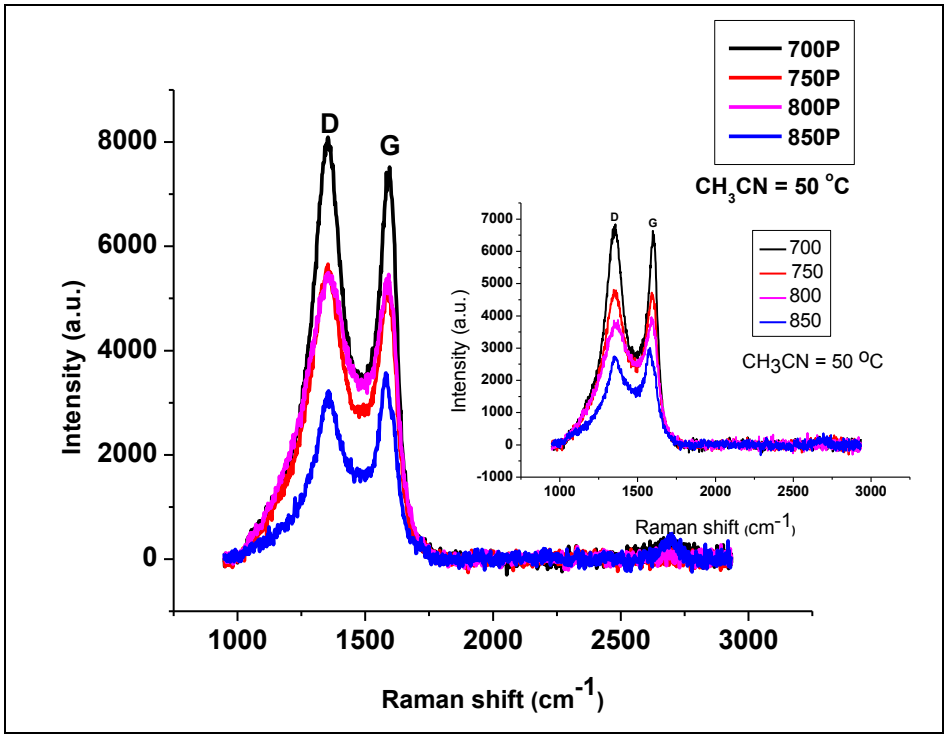


Figure S7: Raman spectra of the purified (700P-850P) and as-synthesized (700-850, inset) N-MWCNTs using CH_3CN at 50 °C.

Z.N. Tetana, S.D. Mhlanga, G. Bepete, R.W.M. Krause, N.J. Coville, *S. Afr. J. Chem.*, 2012, 65, 39-49.

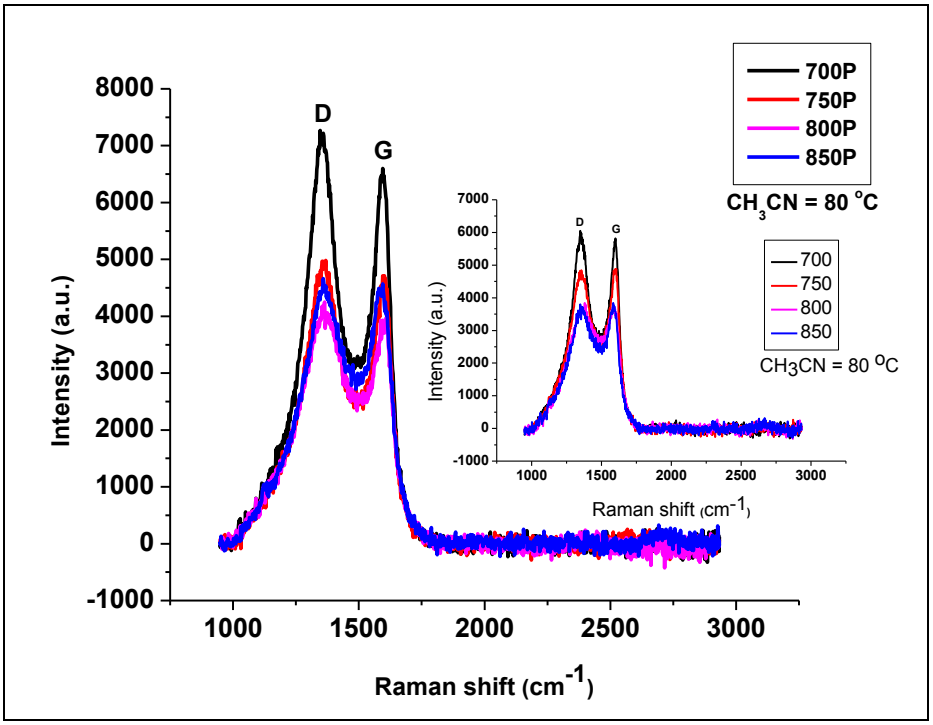


Figure S8: Raman spectra of the purified (700P-850P) and as-synthesized (700-850, inset) N-MWCNTs using CH_3CN at 80 °C.

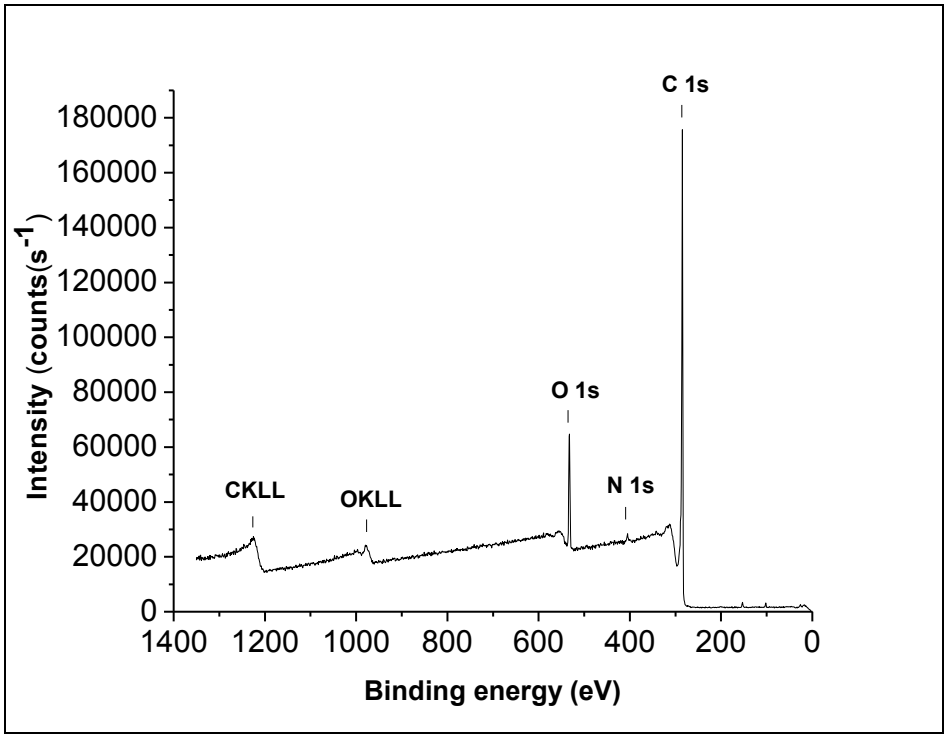


Figure S9: XPS spectra of the purified N-MWCNTs synthesized at 800 °C using CH_3CN at r.t.

Z.N. Tetana, S.D. Mhlanga, G. Bepete, R.W.M. Krause, N.J. Coville, *S. Afr. J. Chem.*, 2012, 65, 39-49.

CHAPTER 4

Large-scale Synthesis of Nitrogen-Doped Carbon Spheres (N-CSs) using a vertical CVD reactor

4.1. Introduction

In recent years, nitrogen-containing carbon materials have attracted much interest because the presence of nitrogen atoms generate materials that can be used as catalyst supports,[1-4] electrodes for lithium secondary batteries,[5,6] electrical double layer capacitors,[7-10] etc. Nitrogen is an n-type dopant. Due to its atomic size being similar to that of carbon,[11] it can readily be incorporated into carbon structures. The introduction of nitrogen into carbon materials is a useful method of altering the physical, chemical, mechanical and electronic properties of carbon materials. For example, properties such as basicity, oxidation stability[12-14] and enhanced electrocatalytic activity for fuel cells applications[15] are realized when nitrogen atoms are incorporated into carbon materials.

A number of synthetic procedures have been employed in the synthesis of nitrogen-containing carbon materials. These include in situ doping of carbon materials using nitrogen-containing precursors such as ammonia,[16,17] acetonitrile,[14,18,19] melamine,[20] pyrrole[21] or polyaniline, [22,23] as well as post-treatment of carbon materials with NH_3[24,25] or amines,[26] etc. In situ doping of carbon materials is preferred as it results in a homogeneous incorporation of nitrogen into the carbon material with a controlled chemistry. Many efforts have been made to synthesize nitrogen-doped carbon materials using this method. Nitrogen-doped carbon nanotubes (CNTs),[18,20,27] nitrogen-doped carbon nanofibers,[28,29] nitrogen-doped hollow carbon spheres[30,31,32] and nitrogen-doped solid carbon spheres,[1,33,34] have all been synthesized by methods that are similar to the synthesis of their undoped counterparts, but using nitrogen-containing precursors. Various synthesis methods have been used to make undoped and nitrogen-doped carbon materials. Among the synthesis routes used, the chemical vapour deposition (CVD) method is the most attractive because it is considered to be the best method to produce bulk amounts of carbon materials and it also offers better control over growth parameters.[35] Compared with high temperature arc-discharge and laser methods, CVD is a simple and economic technique for synthesizing carbon materials at relatively low temperature and at ambient pressure.

There are two types of CVD furnaces commonly used to make carbon materials, one has a horizontal configuration and the second has a vertical configuration. The horizontal furnaces are most popular. On the other hand, the vertical furnaces are known to have advantages over horizontal reactors because they are usually employed for the continuous mass production of carbon materials.[1b] Further, compared to the horizontal furnace, the residence time of carbon materials in a vertical furnace is relatively short.

The synthesis of solid undoped carbon spheres (CSs) and nitrogen-doped carbon spheres (N-CSs) have been reported by many researchers using the CVD method. CSs have been prepared by the pyrolysis of hydrocarbons in the presence of a catalyst. For example, Miao *et al.*[36] reported the synthesis of CSs at 650 °C using transition metal catalysts deposited on a hydrated aluminium silicate support. Lei and co-workers[37] also synthesized CSs (ranging from 600-1250 nm) by catalytic CVD using C_2H_2 as the carbon source and non-magnetic metal complexes of La, Nb, and Ti as catalyst supported by kaolin. Pyrolysis of organometallic complexes such as ferrocene (10 wt%) in pentane solution at 900-1000 °C,[38] ferrocene and anthracene mixture at 800-1000 °C,[39] as well as vanadium β-diketonenate with C_2H_2 at 700 °C,[40] have also been used as catalysts to generate CSs.

More importantly, CSs and N-CSs can be synthesized by the pyrolysis of hydrocarbons without using a catalyst. For example, Nieto-Marquez and co-workers[33] synthesized uniformly sized CSs and N-CSs (2.1-3.4 at.% N) from the direct pyrolysis of benzene, aniline or nitrobenzene at 950 °C for up to 2 hours in the absence of a catalyst. The diameter range (200-1000 nm) of their CSs did not seem to be sensitive to pyrolysis time or to the nature of the precursor.

Recently, Xiong and co-workers[34] reported the synthesis of CSs and N-CSs (ca. 700 nm, ~ 2 wt% N) by a horizontal CVD method through the pyrolysis of C_2H_2 (100 ml/min) and using 25% NH_3 solution as the nitrogen source (900 °C for 1 hour). The synthesis of N-CSs (1-1.5 wt% N, 400-750 nm diameter range) using a horizontal CVD reactor has also been demonstrated by Deshmukh *et al.*[1a] who used C_2H_2 as a carbon source and ammonium hydroxide or acetonitrile solution as a nitrogen/carbon source. In their synthesis of N-CSs, C_2H_2 was bubbled through ammonium hydroxide or acetonitrile solution at a carbonization temperature of 900 °C for 2 hours. Lazo-Cannata and co-workers[41] synthesized undoped CSs at 950 °C for 2 hours from the pyrolysis of benzene as carbon source and He (150 ml/min) as an inert gas. The produced CSs with diameters in the range 300-500 nm (average ~400 nm)

were successfully used in the absorption of phenol and nitrophenols. Qian and co-workers[42] used toluene as a precursor for the synthesis of CSs and the diameters and morphologies of the materials were linked to the carrier gas in a non-catalytic CVD approach. More recently, Mhlanga *et al.*[43] used a horizontal furnace to produce high yields of microspheres with diameters ranging from 300-1900 nm (with about 90% in the range of 800-1000 nm) through direct pyrolysis of acetylene at a flow rate of 100 ml/min over a wide temperature range (600-1000 °C) for 2 hours.

Undoped spheres can also be synthesized in a non-catalyst vertical CVD reactor. Wu and co-workers[44] used a vertical CVD reactor to prepare undoped carbon spheres using C_2H_2 (100 ml/min) as the carbon source and N_2 (1000 ml/min) as the carrier gas without any catalyst. The produced CSs were collected in a stainless steel collector mounted at the bottom of the reactor, and had diameters in the range 200-500 nm and were perfectly spherical in shape with rough surfaces. Previously, Mhlanga *et al.*[45] have also reported the controlled syntheses of CSs (50-250 nm) in a swirled floating catalytic vertical CVD reactor. Their reactor consisted of a vertical quartz tube inside a furnace. Carbon feedstock and carrier gas were uniformly mixed together with the aid of a swirled coiled mixer. The upper end of the reactor was connected to a condenser which led to two delivery cyclones where the CSs produced were collected. The CS production rate was found to increase with an increase in pyrolysis temperature (900-1000 °C) and with flow rates of the C_2H_2 (70-370 ml/min) and Ar (70-480 ml/min). Mamo *et al.*[46] also synthesized undoped CSs (124±13 nm) using a vertical CVD reactor by the pyrolysis of C_2H_2 (100 ml/min) at 900 °C. The carbon source and carrier gas (Ar, 100 ml/min) were introduced at the top of a vertically aligned tube furnace and the CSs were grown during passage through the heating zone and the material was collected in a 500 ml round bottom flask. However, to the best of our knowledge, N-doped CSs have not been synthesized using a vertical CVD reactor in the absence of a catalyst.

Herein, we report that high yields of N-CSs (and CSs) can be obtained by the pyrolysis of C_2H_2/CH_3CN (or C_2H_2), at 900 °C by means of a vertical CVD reactor. Argon was utilized as both an inert carrier gas to prevent oxidation of the carbon, and a diluent gas in order to lower the deposition rate of the C_2H_2 during the reaction. In this study we present the effects of using different gas flow rates and reactant concentrations on the large scale synthesis of N-doped CSs (and undoped CSs) with varying diameters.

It is important to mention that a blank run was performed whereby acetonitrile was used as sole C and N sources. The reaction produced no carbon. Acetonitrile as sole C and N sources is usually employed in catalytic CVD methods to make good yields of CNTs by the pyrolysis of CH_3CN over metal catalysts,[47] or in template-assisted growth of hollow N-doped CSs, in which carbon and nitrogen deposition occurs on the surface of the silica spheres.[48] It seems like the pyrolysis of sole CH_3CN is simple in the presence of a catalyst or silica spheres, in which C and N atoms diffuse into the catalyst to contribute to the growth of N-doped CNTs or hollow N-CSs. Nitrogen-doped CNTs have also been successfully prepared using CH_3CN with ferrocene [49] and CH_3CN with xylene.[50] In the case of non-catalytic CVD growth of N-CSs, CH_3CN has been used with C_2H_2 to synthesize good yields of N-CSs.[1a] However, when we used CH_3CN only, the reaction yielded no carbon product; hence we decided to use CH_3CN and C_2H_2 as an additional carbon source to enhance N-CSs growth reported here.

There are two types of furnace modality, one is a horizontal configuration and the second is a vertical configuration. The application of horizontal furnace is the most popular. Here the catalyst is placed in a ceramic or quartz boat which is put into a quartz tube. The reaction mixture containing a source of hydrocarbon and an inert gas is passed over the catalyst bed at temperatures ranging from 500 °C to 1100 °C. The system is then cooled down to room temperature. The vertical furnace configuration is usually employed for the continuous mass production of carbon fibers/nanotubes.

4.2 Experimental

4.2.1 Synthesis of CSs and N-CSs

The synthesis of the CSs and N-CSs was based on that reported by Mamo and co-workers[46] for the synthesis of undoped CSs. The synthesis of the materials was carried out in a tubular quartz reactor (having dimensions 1.5 m x 32 mm o.d) placed in a vertical CVD furnace. C_2H_2 (Afrox), Ar (Afrox) and CH_3CN (Sigma-Aldrich) were used as carbon, carrier gas and carbon/nitrogen sources, respectively. The furnace was raised to 900 °C at 10 °C/min under flowing Ar gas (40 ml/min). For the synthesis of N-CSs, the Ar (240 ml/min) and C_2H_2 (300 ml/min) were simultaneously bubbled through CH_3CN (heated to 80 °C) and were allowed to flow from top to bottom through the quartz tube for 1 hour and the carbon material was collected in a 500 ml round bottom flask. After this, the bubbling of the gases through

CH_3CN was stopped and the system was left to cool down to room temperature under an Ar atmosphere. The product (denoted here as N-CSs-540) was removed from the round bottom flask and weighed. Other nitrogen-doped CSs (denoted here as N-CSs-140) were grown by the same procedure but using different Ar (40 ml/min) and C_2H_2 (100 ml/min) flow rates.

For the synthesis of the undoped CSs, a similar procedure used for the synthesis of N-CSs was used but without the presence of CH_3CN. The materials were produced in good yields and are denoted as CSs-140 and CSs-540 for the materials grown at a total gas flow rate of 140 ml/min and 540 ml/min, respectively. The as-grown spheres were purified by Soxhlet apparatus by extraction with toluene for about 6 hours, to remove impurities such as the polycyclic aromatic hydrocarbons formed during the reaction, and then dried at 120 °C for 12 hours. The percentage yields of the synthesized undoped and N-doped CSs were calculated using the formula:

$$\%\text{yield} = \frac{moles\ of\ carbon\ in\ product}{moles\ of\ carbon\ in\ C_2H_2 + \text{moles of carbon in } CH_3CN} \times 100\%$$

4.2.2 Characterization of CSs and N-CSs

The morphology and structural features of the undoped and nitrogen-doped carbon spheres were ascertained by transmission electron microscopy (TEM) using a FEI Technai G^2 Spirit electron microscope operated at 120 kV, and Raman spectroscopy using a Jobin-Yvon T6400 micro-Raman spectrometer equipped with a liquid nitrogen cooled charge coupled device detector. The thermal stability of the produced carbon materials was investigated by thermogravimetric analysis (TGA) using a Perkin Elmer Pyris 1 TGA. About 10 mg of the samples were heated to 900 °C at a rate of 10 °C/min under air. The mass of CSs and N-CSs was kept constant (ca 10 mg) in order to reduce the effects of variability in measurements. BET surface areas of the carbon materials (~ 200 mg for each measurement) were obtained through N_2 adsorption using an ASAP 2000 Micrometrics TriStar Surface Area and Porosity Analyzer. The nitrogen concentration in the N-CSs was determined by CN elemental analysis using a Carlo Erba NA 1500 Nitrogen Carbon Sulphur Analyzer at the Agricultural Research Center, Institute for Soil, Climate and Water in Pretoria. The X-ray photoelectron spectroscopy (XPS) measurements were obtained on a Quantum 2000 Physical Electronics spectrometer (National Metrology Institute of South Africa (NMISA), Pretoria) equipped with a monochromatic Al Kα X-ray source (1486 eV) operated at 20 W. X-ray diffraction

(XRD) studies were performed on a Bruker D2 phaser equipped with Cu-Kα radiation (λ = 1.5406 Å), and the operation voltage and current were maintained at 30 kV and 10 mA, respectively. The XRD patterns were recorded in the range 10 °< 2θ <90 ° with a step size of 0.040 ° and a time of 1 s per step.

4.3 Results and discussion

The synthesis of undoped and N-doped CSs was achieved by the direct pyrolysis of C_2H_2 and C_2H_2/CH_3CN, respectively, at 900 °C for 1 hour via a vertically aligned furnace without using a catalyst. In this study, the effects of using different gas flow rates during the reactions and the properties of the resulting CSs and N-CSs are discussed. The as prepared CSs and N-Cs were all obtained in good yields (see Table 4.1). The reported yields are based on the mass of the spheres obtained after the reactions. The carbon percentage yields of the carbonaceous materials were also calculated to be in the 15-28% range (Table 4.1). It is noted that nitrogen-doped CSs gave lower percentage yield when compared to undoped CSs. The lower yield suggested that the addition of CH_3CN inhibited the nucleation of N-CSs. As compared to other results reported in the literature, the results indicate that the higher the flow rate of the carbon source and carrier gas the more spheres produced at a given time. To be specific, Deshmukh *et al.*[1a] obtained 0.5 g of N-CSs via the pyrolysis of CH_3CN and C_2H_2 (100 ml/min) at 900 °C for 2 hours in a horizontal reactor. Our reported yields here are in close agreement with the yield of CSs synthesized using a vertical furnace reported by Wu *et al.*[44] In their study, they obtained about 1.5 g/hour of CSs under the reaction conditions mentioned in the introduction, in which the yield was calculated to be 26%, using the same formula in Section 2.1.

Table 4.1: Carbon yields of the CSs and N-CSs.

Sample ID	Total weight after reaction (g) [a]	Carbon yield (%)[b]
N-CSs-540	4.05	15.4
CSs-540	3.85	19.8
N-CSs-140	2.28	18.4
CSs-140	1.81	28.0

[a] Mass of the product after the reaction (1 hour); [b]Calculated percentage carbon yield based on the starting materials

4.3.1 Structural analysis of the carbon spheres

4.3.1.1 TEM analysis

The morphology and structural features of the carbon materials (CSs and N-CSs) was examined by TEM (Figure 4.1). The TEM images reveal that the CSs were solid, spherical and have smooth surfaces. It can be observed that the CSs and N-CSs overlap each other and are linked together (accreted) to form a chain-like morphology. The diameter distribution of all the synthesized CSs and N-CSs were determined from TEM images, by measuring the diameters of about 150 carbon materials from each sample (Figures 4.2 and 4.3). The diameter histograms plotted in Figures 4.2 and 4.3 show diameters of 125 nm (55-420 nm range) for CSs-540 and also 125 nm (70-310 nm range) for N-CSs-540. On the other hand, the CSs-140 and N-CSs-140 both show larger average diameters of 450 nm with diameter distribution of 250-1050 nm. It is evident from the analysis of the diameter distribution that the method for synthesizing undoped CSs and N-doped CSs at higher gas flow rates produce smaller sized CSs and N-CSs, compared to lower gas flow rates and other carbon spheres as previously reported.[1,34,43] The CSs-140 and N-CSs-140 were found to be structurally more uniform in size that the CSs-540 and N-CSs-540. Interestingly, the addition of CH_3CN did not have a major impact on the carbon sphere diameter at the same total gas flow rate (e.g. CSs-540 vs. N-CSs-540).

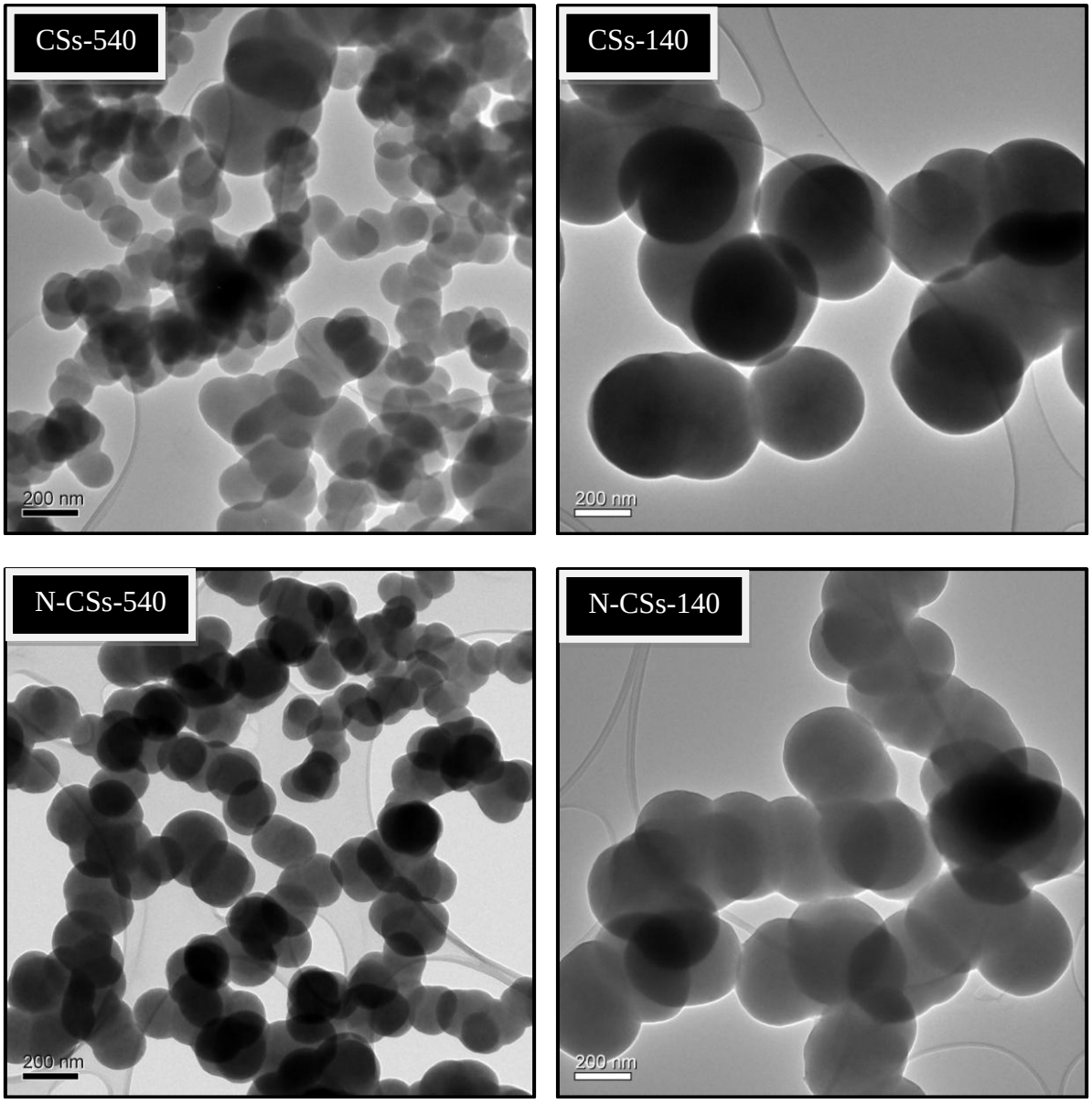


Figure 4.1: TEM images of the undoped CSs and N-doped CSs obtained at total constant gas flow rates of 140 and 540 ml/min.

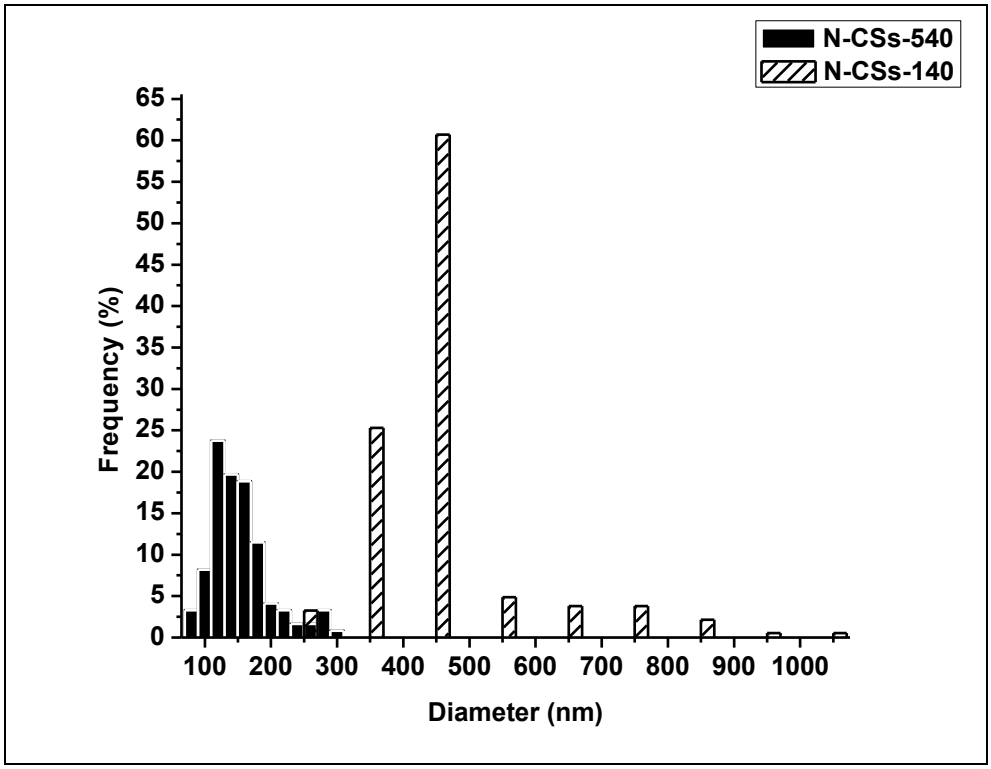


Figure 4.2: Diameter distribution of N-CSs synthesized at total constant gas flow rates of 140 and 540 ml/min.

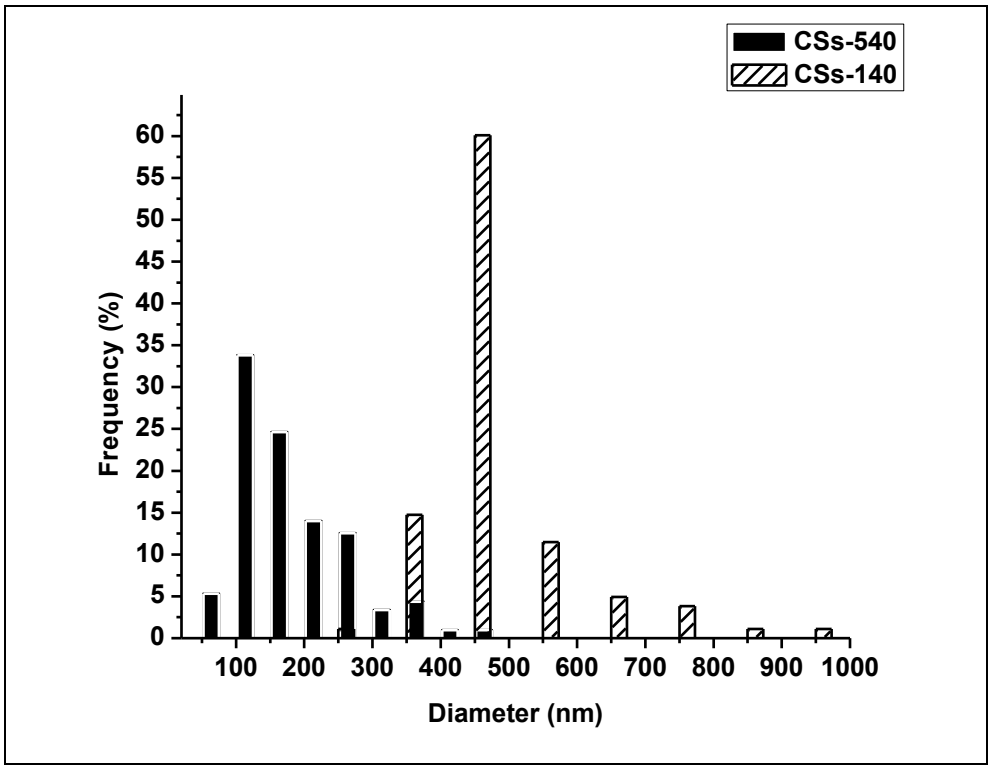


Figure 4.3: Diameter distribution of CSs synthesized at total constant gas flow rates of 140 and 540 ml/min.

4.3.1.2 XRD and Raman analysis of the CSs and N-CSs

XRD and Raman analysis were used to determine the degree of graphitization of the carbon materials. The XRD patterns of the synthesized carbon materials are shown in Figure 4.4. The diffraction peaks at around 25.2° and 43.6° in 2θ can be seen in all samples. These two broad peaks could be assigned to (002) and (100) planes of carbon materials, respectively. The broadness of both diffraction peaks and the weakness of the (100) in all samples suggest turbostratic structures of CSs with highly disordered amorphous carbon and randomly oriented graphene layers.[32] An interesting observation in the XRD patterns is that N-CSs-540 exhibits a weaker peak at 43.6° in 2θ as compared to other carbon spheres examined in this study. This is related to carbon materials containing weakly ordered graphitic structures,[32] probably due to the high nitrogen content.

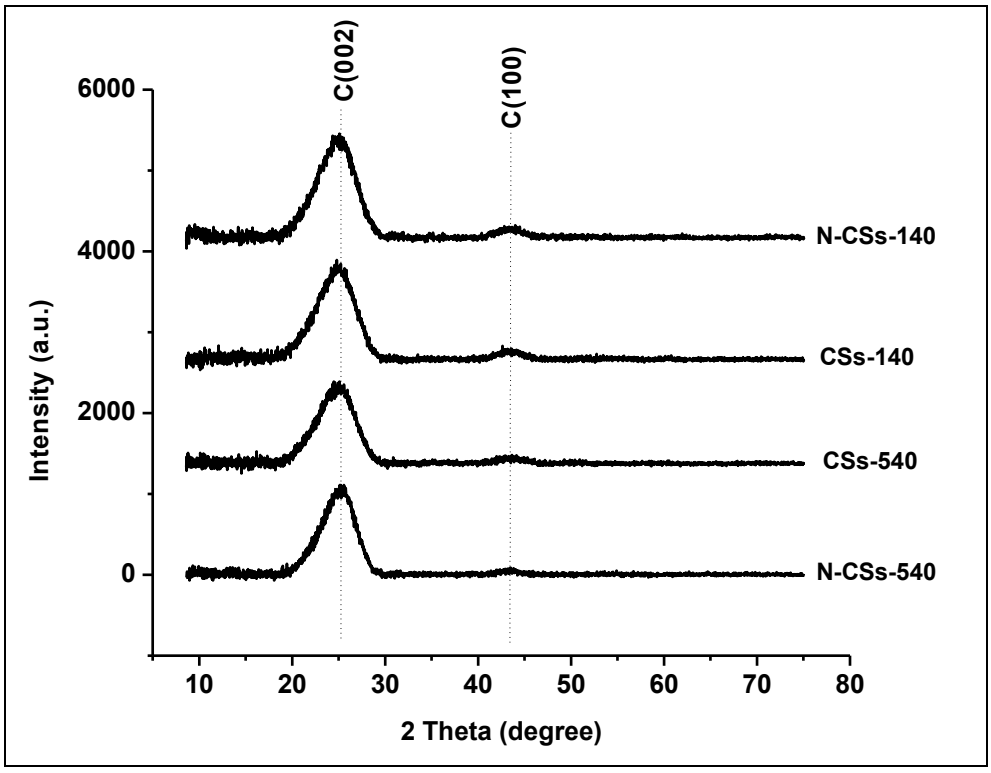


Figure 4.4: XRD patterns of the synthesized CSs and N-CSs.

Figure 4.5 shows the Raman spectra of the synthesized carbon spheres. The broader D and narrower G bands are predominant features in the spectra. The peak at around 1350 cm^{-1} (disorder-induced D band) is associated with the presence of structural defects and disorder

of carbon materials, whereas the peak at 1580-1600 cm^{-1} (G band) is related to the vibration of sp^2-bonded carbon atoms in a 2-D hexagonal lattice, resulting from the stretching modes of C=C bonds of graphite. We observed that nitrogen doping resulted in more broadening and shift of the D-band position to higher wavenumbers, as seen from Table 4.2. Figure 4.5 shows that the intensity of the G band is higher with respect to that of the D band in all the samples. This finding is unusual in nitrogen doped carbons. Some studies reported a strong and broad D band with respect to G band caused by the structural defects due to nitrogen incorporation.[27c] A more detailed evaluation was obtained after deconvolution of the bands (see Supplementary Figures S1-4). The analysis of the deconvoluted Raman spectra for all CSs and N-CSs showed a strong D band compared to a G band. Thus, Figures S1-4 confirmed the presence of defects in all the carbon structures.

The intensity of the D band divided by the intensity of the G band (I_D/I_G ratio) is usually used to evaluate the graphitic nature and quality of the carbon materials. The I_D/I_G ratios shown in Table 4.2 were calculated after the deconvolution of the Raman spectra in Supplementary Figures S1-4. The I_D/I_G ratios for the CSs-140, N-CSs-140, CSs-540, N-CSs-540 were found to be 1.05, 1.24, 1.27 and 1.29, respectively. This implies that the undoped and the nitrogen-doped CSs have many defects and low graphitized degree of order. In addition, more disorder was observed when nitrogen was added. This strongly supports the findings from the XRD analysis in Figure 4.4.

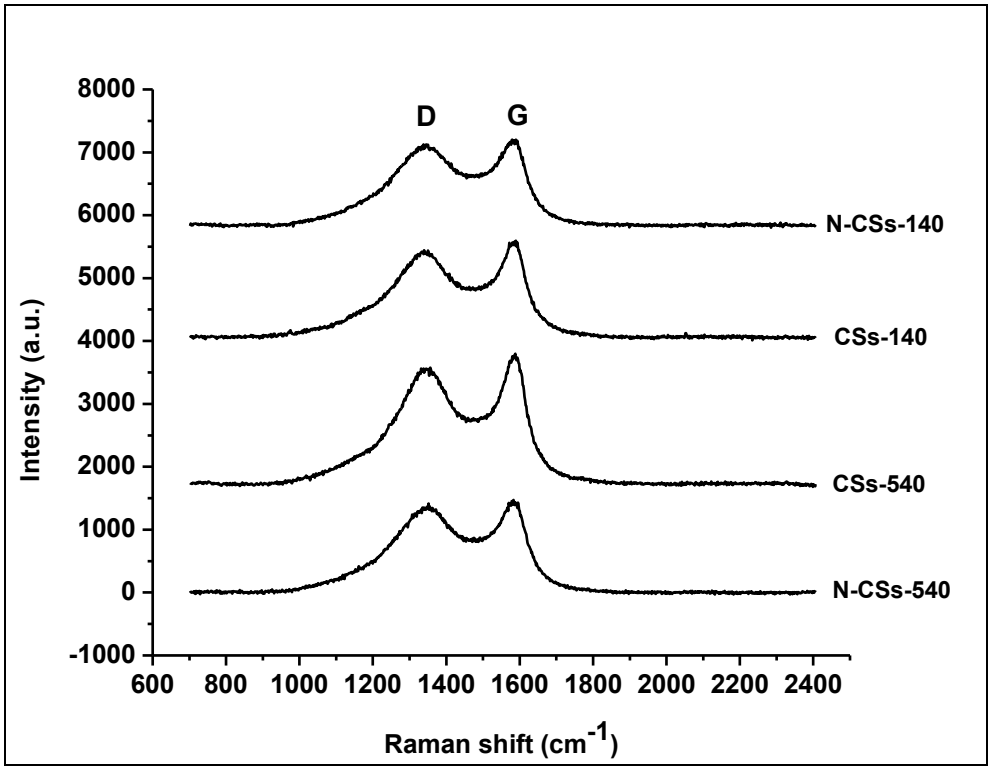


Figure 4.5: Raman spectra of the CSs and N-CSs.

Table 4.2: Decomposition temperatures (determined by TGA), Raman shifts, ID/IG ratios, BET surface areas and pore volume data of the CSs and N-doped CSs.

Sample ID	Decomposition temperature (°C)	D-band (cm^{-1})	G-band (cm^{-1})	I_D/I_G ratio	Surface area (m^2/g)	Pore volume (cm^3/g)
N-CSs-540	606, 811	1350	1587	1.29	11.8	0.026
CSs-540	597	1347	1588	1.27	11.1	0.023
N-CSs-140	612	1347	1586	1.24	7.3	0.015
CSs-140	594	1342	1586	1.05	5.9	0.013

4.3.1.3 BET surface area and pore volume analysis of CSs and N-CSs

The BET analysis was used to calculate the surface areas of the synthesized carbon materials. The CSs-140, N-CSs-140, CSs-540 and N-CSs-540 formed in this work have non-porous structures as indicated by their low BET surface areas (and pore volume) of about 6, 7, 11

and 12 m^2/g, respectively (see Table 4.2). The surface areas of the N-containing CSs were found to be slightly larger than the undoped CSs.

4.3.1.4 Thermogravimetric analysis of the synthesized CSs and N-CSs

The TGA technique was used to obtain information about the stability of the carbon materials as a function of temperature. Figures 4.6 and 4.7 demonstrate the TGA and corresponding derivative profiles of the CSs and N-CSs. Figure 4.7 and Table 4.2 indicate a weight loss due to decomposition of the carbon materials. It was established that the weight loss occurs in the 594 and 597 °C range for undoped CSs and in the 606 and 612 °C range for nitrogen-doped CSs. The decomposition temperatures determined by derivative TGA (Table 4.2) indicate the higher thermal stability of the N-CSs relative to CSs in air flow. It is also noted that N-CSs-140 (2.92 at% N) exhibited higher thermal stability than N-CSs-540 (4.41 at% N), presumably due to a decreased nitrogen content. The decrease in stability with the increased in N incorporation is attributed to the structural disorder and defects introduced by the presence of more nitrogen into the carbon lattice.[51] This phenomenon was also observed by Nxumalo and co-workers on the stability of N-doped CNTs.[27a] The appearance of another peak at 811 °C in addition to the peak at 606 °C in the N-CSs-540 correspond to the oxidation of CSs with different sizes. This suggests that the N-CSs-540 were non-uniform in size, as was evidenced by TEM studies. It is well known that smaller diameter CNTs are easily oxidized in air as compared with larger diameter CNTs.[52]

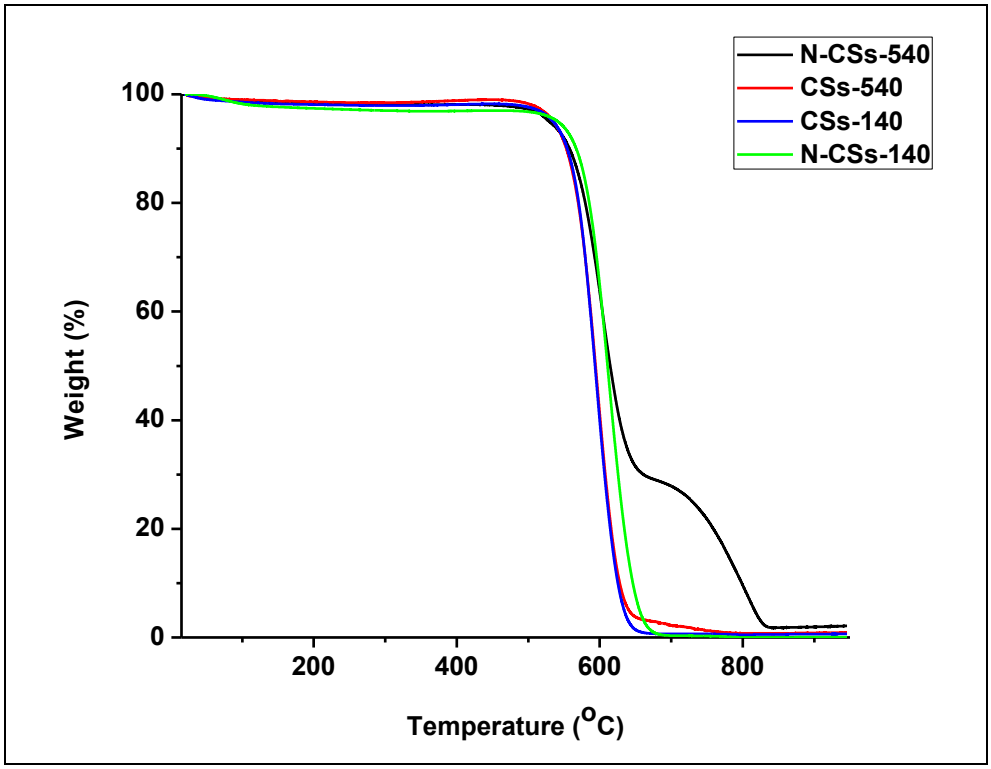


Figure 4.6: TGA profiles run in air of the synthesized CSs and N-CSs.

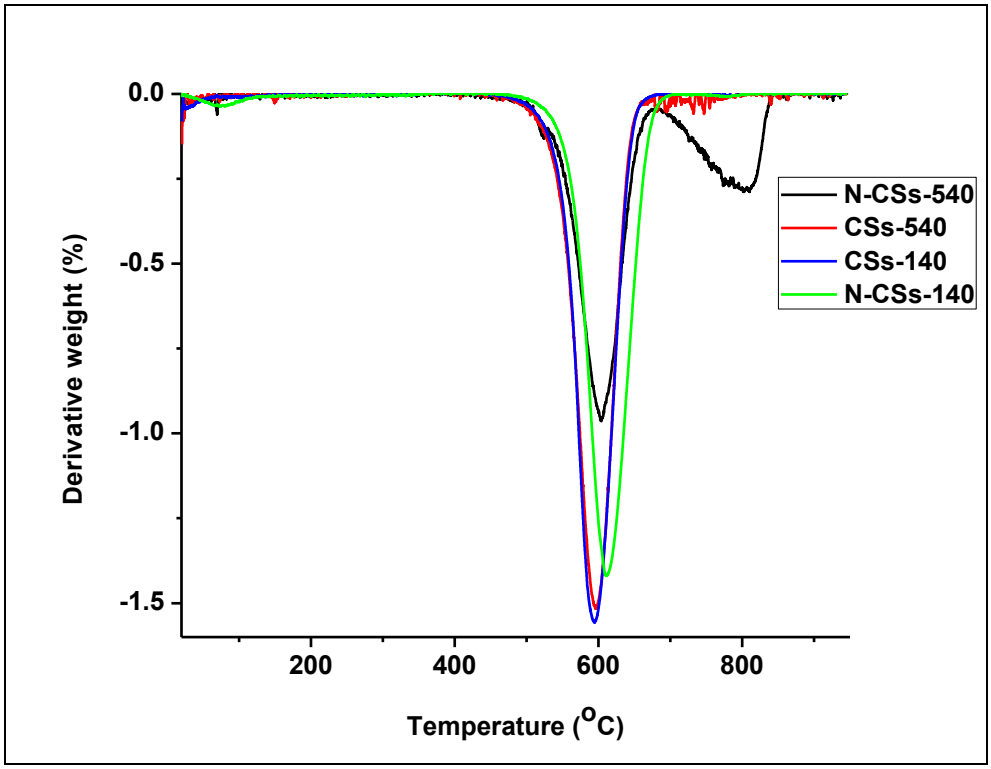


Figure 4.7: The corresponding derivative profiles of synthesized the CSs and N-CSs.

4.3.1.5 XPS and CN elemental analyses of the CSs and N-CSs

XPS and CN elemental analyses were used to quantify the concentration of C and N atoms in the synthesized CSs. Table 4.3 depicts the CN and XPS results for the synthesized materials. Carbon is the main element present, comprising more than 91 at% in all the carbon materials (Table 4.3). CN elemental analysis of the N-containing CSs demonstrates the nitrogen incorporation according to the total gas flow rate used. It has been found that the use of a total gas flow rate of 140 ml/min gives a nitrogen concentration of 2.92 at%, whereas the use of a total gas flow rate of 540 ml/min gives a nitrogen concentration of 4.41 at%. The results indicate a correlation between the total gas flow rate used and the nitrogen concentration in the formation of the N-containing CSs. With the increase of total gas flow rate, the yield/growth rate and the nitrogen concentration of the N-containing CSs increase significantly. The surface elemental composition shown in Table 4.3 shows that the nitrogen content of the N-CSs-540 to be 3.10 at%, using XPS. In contrast to the results from CN elemental analysis, the value for the nitrogen content is different for N-CS-540. Since XPS is a surface sensitive technique and elemental analysis applies to the bulk, this indicates that the nitrogen atoms are preferably bound to the outer surface in N-containing CSs. Noteworthy, the oxygen content of the N-CSs-540 is, according to CHN analysis, considerably lower (0.27%, calculated by the difference to 100%) than the oxygen content estimated by XPS analysis (3.6%). This difference still remains to be explained; the fact that elemental analysis gives bulk composition while XPS is used to measure the elemental composition of the surface cannot be excluded.

Table 4.3: CN and XPS measurements of the synthesized carbon spheres.

	CN analysis		**XPS analysis**		
Sample ID	**C (%)**	**N (%)**	**C (%)**	**N (%)**	**O (%)**
NCSs-540	95.32	4.41	93.3	3.1	3.6
NCSs-140	91.95	2.92	-	-	-
CSs-540	94.90	< 0.05	94.7	-	5.3
CSs-140	94.10	< 0.05	-	-	-

XPS has also been used to determine the binding configuration of the N-containing CSs. Table S1 in Supplementary material lists the species detected after deconvolution of the XPS peaks, i.e. the C (~285 eV), N (~400 eV), and O (~530 eV) peaks. The XPS data confirms that the N-CSs-540 consists of only carbon, nitrogen and oxygen atoms. The binding energy at 284.86 eV can be assigned to sp^2 hybridized carbon (C=C). The binding energies at 285.90, 287.90, 289.06 and 533.0 eV correspond to the bond types sp^2 C-N, sp^3 C=N,[53]-COO and O-C,[54] respectively. The traces of oxygen observed in the N-doped CSs are a result of oxygen uptake from the atmosphere when the material was exposed to the air, as suggested in the literature.[55]

Figure 4.8 shows the types of nitrogen that can be found in carbon materials. These are: (A) oxidized pyridinic-N, (B) pyridinic-N, (C) pyrrolic-N and (D) quaternary-N.[12,56] The XPS analysis shows that the N 1s core level spectra (Figure 4.9 and Table S1) for N-CSs-540 can be deconvoluted in terms of two peaks related to sp^2 (C-N=C, pyridinic-N; 398.88 eV) and sp^3 hybridization (C-N configuration, pyrrolic-N; 400.50 eV). The pyridinic nitrogen atoms have a localized electron lone pairs which are active in base catalysed reactions, and the optimisation of the amount of pyridinic-N is important for catalysis as suggested by van Dommele and co-workers.[57] Furthermore, Stoyanov and co-workers[58] have shown that nitrogen sites in N-CNTs bind strongly to metals leading to excellent metal dispersion in N-CNT/metal materials, and the CNTs doped with nitrogen can thus enhance the reactivity and the selectivity of carbon supported catalysts in many catalytic applications.[59]

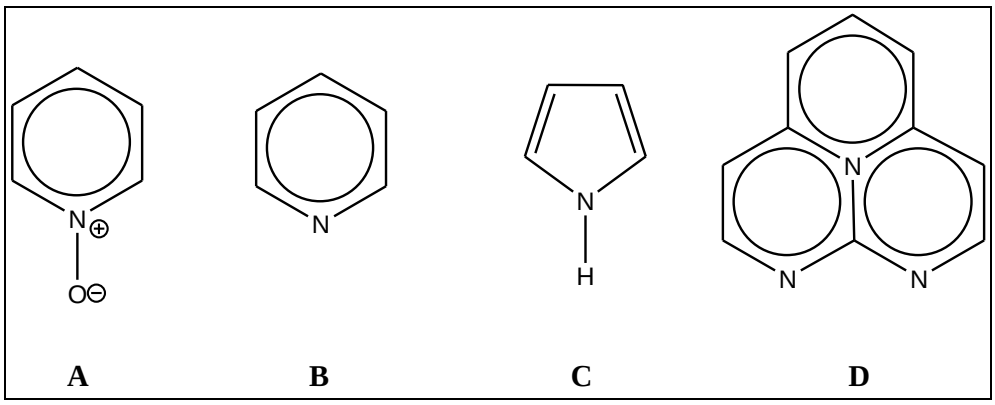


Figure 4.8: Types of nitrogen-based species that can be incorporated into graphitic carbon: A) oxidised pyridinic, B) pyridinic, C) pyrrolic, D) quaternary.[12,46]

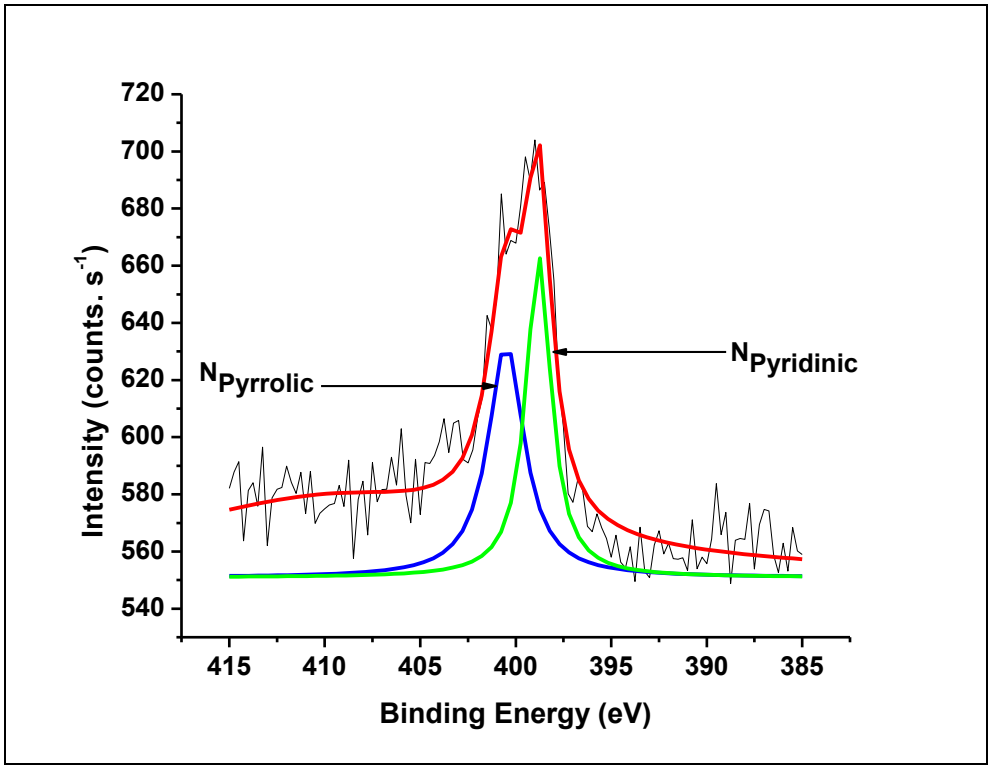


Figure 4.9: Deconvolution of the XPS N 1s peaks of the N-CSs-540.

Figure S5 presents the survey XPS of the CSs-540. As evident from the spectrum, the material consists of C and O atoms. The total amounts of C and O of the CSs-540 as detected by XPS measurements are given in Table 4.3 and supplementary material (see Figure S5). Compared with CSs-540, there is a clear decrease of C and O content on the N-CSs-540, which is induced by a nitrogen-doping effect in N-CSs-540. The CSs-540 showed a large carbon peak at 284.9 eV, attributed to the graphitic structure, similar to the N-CSs-540. The peaks at 286.6 and 288.0 eV were attributed to carbon atoms attached to different oxygen-containing groups. Moreover, the oxygen binding energy at 533.2 eV confirmed the presence of carboxylic groups on the CSs-540.

4.4 Formation mechanism of N-CSs

The mechanism of formation entails the breakdown of the carbon and nitrogen sources in the reactor. The various radicals and ions formed in the reactor nucleate to generate small carbon (and nitrogen) structures. During passage through the reactor, then continue to grow. Two important points to be noted: (1) The slower the total gas flow rate, the larger the CSs and

higher yield; (2) The CH_3CN had little effect on the size of the N-CSs (vs. CSs). Both issues can readily be understood; (3) Nitrogen incorporation retarded the nucleation of the N-CSs.

4.5 Conclusions

Nitrogen doped and undoped carbon spheres were successfully synthesized in large amounts using a vertical chemical vapour deposition technique in the absence of a catalyst. TEM images showed that the CSs synthesized at a total gas flow rate of 540 ml/min (with dimensions of 125 nm) had smaller diameters than the carbon materials synthesized at a total gas flow rate of 140 ml/min (with dimensions of 450 nm). N-CSs-540 was found to have a nitrogen content of 4.4 at% as determined by C and N elemental analysis and 3.1 at% as determined by XPS analysis, while the N-CSs-140 sample was found to have a nitrogen content of 2.92 at% as determined by C and N elemental analysis. The existence of nitrogen-atom substitution in the grapheme planes was confirmed by XPS. Two bonding configurations were obtained on doping CSs with nitrogen: pyridinic N and pyrrolic N. Analysis of Raman and XRD data revealed that the CSs synthesized here have a low degree of graphitization and the structural defects were introduced by nitrogen doping.

It is evident from the literature and our study that the vertical CVD furnace (with higher feedstock flow rates) has advantages when compared to the horizontal reactor, in terms of the continuous and large-scale production. The sizes of the CSs and N-CSs can be readily varied by varying the residence time. Thus, by controlling the gas flow rates, undoped and N-doped CSs with smaller and uniform diameters can be obtained. It was found that an increase in the total gas flow rate led to an increase in the yield and amount of nitrogen incorporated in the N-containing CSs.

The synthesized materials have low BET surface areas and, although such materials are non-porous, they can be used as catalyst supports. Furthermore, Stoyanov and co-workers[55] have shown that nitrogen sites in N-CNTs bind strongly to metals leading to excellent metal dispersion in N-CNTs/metal materials, and the CNTs doped with nitrogen can thus enhance the reactivity and the selectivity of carbon supported catalysts in many catalytic applications.[49] These supports are currently being evaluated in our group for use as catalyst supports.

References

1. (a) A.A. Deshmukh, R. Ul Islam, M.J. Witcomb, W.A.L. van Otterlo and N.J. Coville, *Chem. Cat. Chem.*, 2010, **2**, 51-54; (b) A.A. Deshmukh, S.D. Mhlanga and N.J. Coville, *Mater. Sci. Eng. R*, 2010, **70**, 1-28.
2. L.F. Mabena, S.S Ray, S.D. Mhlanga and N.J. Coville, *Appl. Nanosci.*, 2011, **1**, 67-77.
3. H. Niwa, M. Kobayashi, K. Horiba, Y. Harada, M. Oshima, K. Terakura, T. Ikeda, Y. Koshigoe, J. Ozaki, S. Miyata, S. Ueda, Y. Yamashita, H. Yoshikawa and K. Kobayashi, *J. Power Sources*, 2011, **196**, 1006-1011.
4. K. Chizari, I. Janowska, M. Houllé, I. Florea, O. Ersen, T. Romero, P. Bernhardt, M.J. Ledouxa and C. Pham-Huu, *Appl. Catal., A*, 2010, **380**, 72-80.
5. L. Li, E. Liu, Y. Yang, H. Shen, Z. Huang and X. Xiang, *Mater. Lett.*, 2010, **64**, 2115-2117.
6. Y.P. Wu, E. Rahm and R. Holze, *Electrochim. Acta.*, 2002, **47**, 3491-3507.
7. L. Zhao, L.Z. Fan, M.-Q. Zhou, H. Guan, S. Qiao, M. Antonietti and M.-M. Titirici, *Adv. Mater.*, 2010, **22**, 5202-5206.
8. L. Liao and C. Pan, *Soft Nanoscience Letters*, 2011, **1**, 16-23.
9. W. Li, D. Chen, Z. Li, Y. Shi, Y. Wan, G. Wang, Z. Jiang and D. Zhao, *Carbon*, 2007, **45**, 1757-1763.
10. W. Kim, J.B. Joo, N. Kim, S. Oh, P. Kim and J. Yi, *Carbon*, 2009, **47**, 1407-1411.
11. X.W. Liu, C.H. Lin, L.T. Chao and H.C. Shih, *Mater. Lett.*, 2000, **44**, 304-308.
12. C.P. Ewels and M. Glerup, *J. Nanosci. Nanotechnol.*, 2005, **5**, 1345-1363.
13. D.P. Kim, C.L. Lin, T. Mihalisin, P. Heiney and M.M. Labes, *Chem. Mater.*, 1991, **3**, 686-692.
14. S.H. Lim, H. I. Elim, X. Y. Gao, A. T. S. Wee, W. Ji, J. Y. Lee and J. Lin, *Phys. Rev. B*, 2006, **73**, 045402/1-045402/6.
15. K.P. Gong, F. Du, Z. Xia, M. Durstock and L. Dai, *Science*, 2009, **323**, 760-764.
16. T. Susi Z. Zhu, G. Ruiz-Soria, R. Arenal, P. Ayala, A. G. Nasibulin, H. Lin, H. Jiang, O. Stephan, T. Pichler, A. Loiseau and E.I. Kauppinen, *Phys. Status Solidi B*, 2010, **247**, 2726-2729.
17. J. Liu, S. Webster and D.L. Carroll, *J. Phys. Chem. B*, 2005, **109**, 15769-15774.
18. Z.N. Tetana, S.D. Mhlanga, G. Bepete, R.W.M. Krause and N.J. Coville, *S. Afr. J. Chem.*, 2012, **65**, 39-49.

19. Y. Hao, L. Qingwen, Z. Jin and L. Zhongfan, *Chem. Phys. Lett.*, 2003, **380**, 347-351.
20. H. Liu, Y. Zhang, R. Li, X. Sun, S. Désilets, H. Abou-Rachid, M. Jaidann and L.-S. Lussier, *Carbon*, 2010, **48**, 1498-1507.
21. S. Glenis, A.J. Nelson and M.M. Labes, *J. Appl. Phys.*, 1996, **80**, 5404-5407.
22. L. Li, E. Liu, Y. Yang, H. Shen, Z. Huang and X. Xiang, *Mater. Lett.*, 2010, **64**, 2115-2117.
23. L. Lin, H. Niu, M. Zhang, W. Song, Z. Wang and X. Bai, *Appl. Surf. Sci.*, 2008, **254**, 7250-7254.
24. R.A. Sidik, A.B. Anderson, N.P. Subramanian, S.P. Kumaraguru and B.N. Popov, *J. Phys. Chem. B*, 2006, **110**, 1787-1793.
25. F. Jaouen, M. Lefévre, J.-P. Dodelet and M. Cai, *J. Phys. Chem. B*, 2006, **110**, 5553-5558.
26. R. Pietrzak, H. Wachowska and P. Nowicki, *Energy Fuels*, 2006, **20**, 1275-1280.
27. (a) E.N. Nxumalo, V.O. Nyamori and N.J. Coville, *J. Organomet. Chem.*, 2008, **693**, 2942-2948; (b) E.N. Nxumalo, V.P. Chabalala, V.O. Nyamori, M.J. Witcomb and N.J. Coville, *J. Organomet. Chem.*, 2010, **695**, 1451-1457; (c) E.N. Nxumalo and N.J. Coville, *Materials*, 2010, **3**, 2141-2171.
28. G.N. Ilinich, B.L. Moroz, N.A. Rudina, I.P. Prosvirin and V.I. Bukhtiyarov, *Carbon*, 2012, **50**, 1186-1196.
29. J. Yuan, A.G. Márquez, J. Reinacher, C. Giordano, J. Janek and M. Antonietti, *Polym. Chem.*, 2011, **2**, 1654-1657.
30. (a) Q.-F. Lü, Z.-W. He, J.-Y. Zhang and Q. Lin, *J. Anal. Appl. Pyrol.*, 2011, **92**, 152-157; (b) Q.-F. Lü, Z.-W. He, J.-Y. Zhang and Q. Lin, *J. Anal. Appl. Pyrol.*, 2012, **93**, 147-152.
31. Y. Xia, Z.Yang, and R. Mokaya, *J. Phys. Chem. B*, 2004, **108**, 19293-19298.
32. F. Ma, H. Zhao, L. Sun, Q. Li, L. Huo, T. Xia, S. Gao, G. Pang, Z. Shib and S. Feng, *J. Mater. Chem.*, 2012, **22**, 13464-13468.
33. (a) A. Nieto-Márquez, I. Espartero, J.C. Lazo, A. Romero and J.L. Valverde, *Chem. Eng. J.*, 2009, **153**, 211-216; (b) A. Nieto-Márquez, D. Toledano, P. Sánchez, A. Romero and J.L. Valverde, *J. Catal.*, 2010, **269**, 242-251.
34. H.F. Xiong, M. Moyo, M.K. Rayner, L.L. Jewel, D.G. Billing and N. J. Coville, *Chem.Cat.Chem.*, 2010, **2**, 514-518.
35. S. Karthikeyan, P. Mahalingam and M. Karthik, *E-J. Chem.*, 2009, **6**, 1-12.

36. J.Y. Miao, D.W Hwang, K.V. Narasimhulu, P.I. Lin, Y.T. Chen, S.H. Lin and L.P. Hwang, *Carbon*, 2004, **42**, 813-822.
37. C.-M. Lei, W.-L. Yuan, H.-C. Huang, S.-W. Ho and C.-J. Su, *Synth. Met.*, 2011, **161**, 1590-1595.
38. X.-Y. Liu, B.-C. Huang and N.J. Coville, *Carbon*, 2002, **40**, 2791-2799.
39. V.O. Nyamori, N.J. Coville, *Organometallics*, 2007, **26**, 4083-4085.
40. S. Ndwandwe, P. Tshibangu and E.D. Dikio, *Int. J. Electrochem. Sci.*, 2011, 6, 749-760.
41. J.C. Lazo-Cannata, A. Nieto-Márquez, A. Jacoby, A.L. Paredes-Doig, A. Romero, M.R. Sun-Kou and J.L. Valverde, *Sep. Purif. Technol.*, 2011, **80**, 217-224.
42. H.S. Qian, F.M. Han, B. Zhang, Y.C, Guo, J. Yue and B.X. Peng, *Carbon*, 2004, **42**, 761-766.
43. S.D. Mhlanga, K.C. Mondal, N. Naidoo, N. Kunjuzwa, M.J. Witcomb and N.J. Coville, *S. Afr. J. Sci.*, 2009, **105**, 304-308.
44. H.-C. Wu, C.-T. Hong, H.-T. Chiu and Y.-Y. Li, *Diamond Relat. Mater.*, 2009, **18**, 601-605.
45. S.D. Mhlanga, N.J. Coville, S.E. Iyuke, A.S. Afolabi, A.S. Abdulkareen and N. Kunjuzwa, *J. Exp. Nanosci.*, 2010, **5**, 40-51.
46. M.A. Mamo, W.S. Machado, W.A.L. van Otterlo, N.J. Coville and I.A. Hümmelgen, *Org. Electron.*, 2010, **11**, 1858-1863.
47. Y. Hao, L. Qingwen, Z. Jin and L. Zhongfan, *Chem. Phys. Lett.*, 2003, **380**, 347-351.
48. F. Su, X. S. Zhao, Y. Wang, L. Wanga and J.Y. Lee, *J. Mater. Chem.*, 2006, **16**, 4413-4419.
49. R.M. Yadav, T. Shrippathi, A. Srivastava and O.N. Srivastava, J. *Nanosci. Nanotechnol.*, 2005, **5**, 829-824.
50. M.I. Ionescu, Y. Zhang, R. Li, H. Abou-Rachid and X. Sun, *Appl. Surf. Sci.*, 2012, **258**, 4563-4568.
51. X. Ma and E.G. Wang, *Appl. Phys. Lett.*, 2001, **78**, 978-980.
52. D.P. Singh, P.K. Iyer and P.K. Giri, *J. Appl. Phys.*, 2010, **108**, 084313-0843110.
53. J. Li, W. Zheng, C. Gu, Z. Jin, Y. Zhao, X. Mei, Z. Mu, C. Dong and C. Sun, *Carbon*, 2004, **42**, 2309-2314.
54. T.I.T. Okpalugo, P. Papakonstantinou, H. Murphy, J. McLaughlin and N.M.D. Brown, *Carbon*, 2005, **43**, 153-161.

55. C. Prado-Burguete, A. Linares-Solano, F. Rodríguez-Reinoso and C. Salinas-Martínez de Lecea, *J. Catal.*, 1991, **128**, 397-404.
56. S. van Dommele, A. Romero-Izquirdo, R. Brydson, K.P. de Jong and J.H. Bitter, *Carbon*, 2008, **46**, 138-148.
57. S. van Dommele, K.P. de Jong and J.H. Bitter, *Chem. Comm.*, 2006, 4859-4861.
58. S.R. Stoyanov, A.V. Titov and P. Král, *Chem. Rev.*, 2009, **253**, 2852-2871.
59. Y. Shao, J. Sui, G. Yin and Y. Gao, *Appl. Catal. B: Environ.*, 2008, **79**, 89-99.

Appendix B: Supplementary material

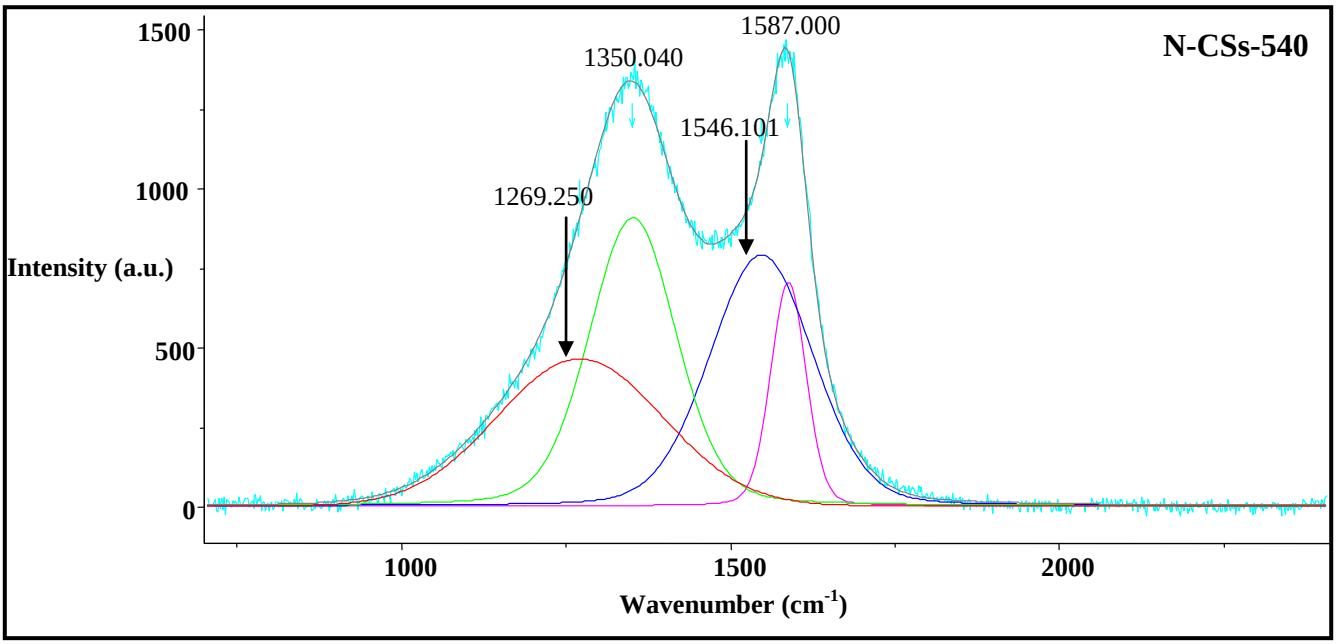


Figure S1: The deconvoluted Raman spectrum of N-CSs-540.

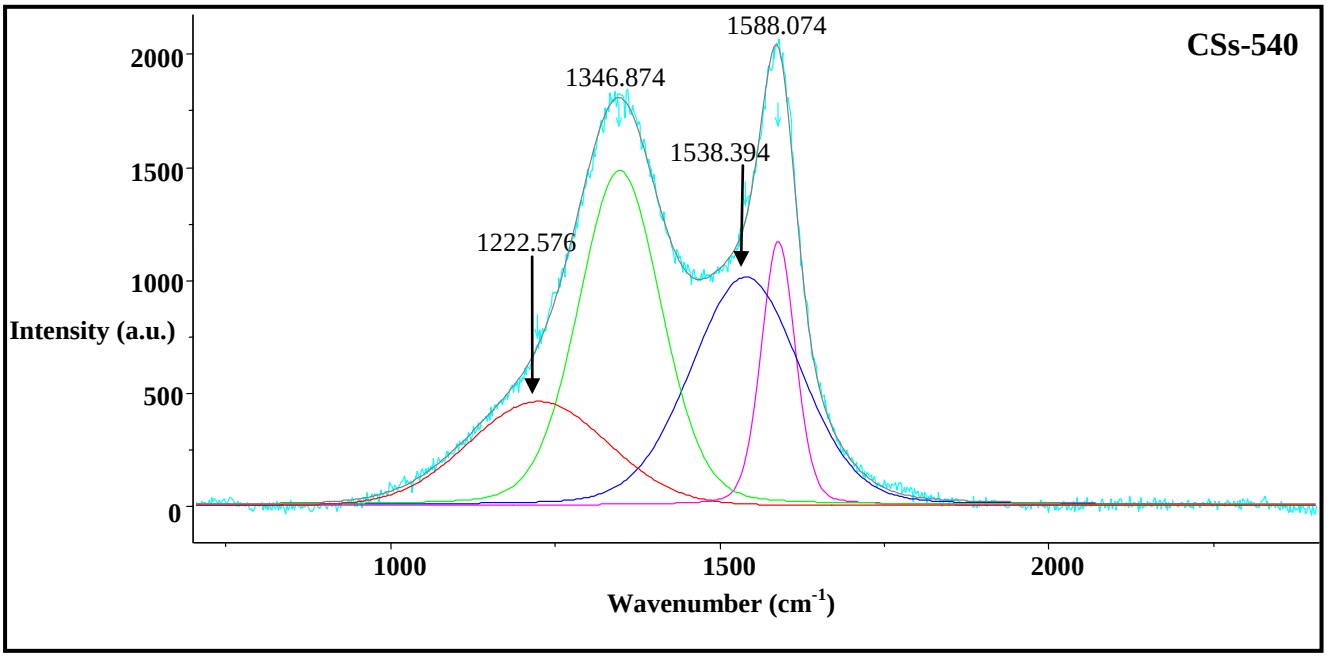


Figure S2: The deconvoluted Raman spectrum of CSs-540.

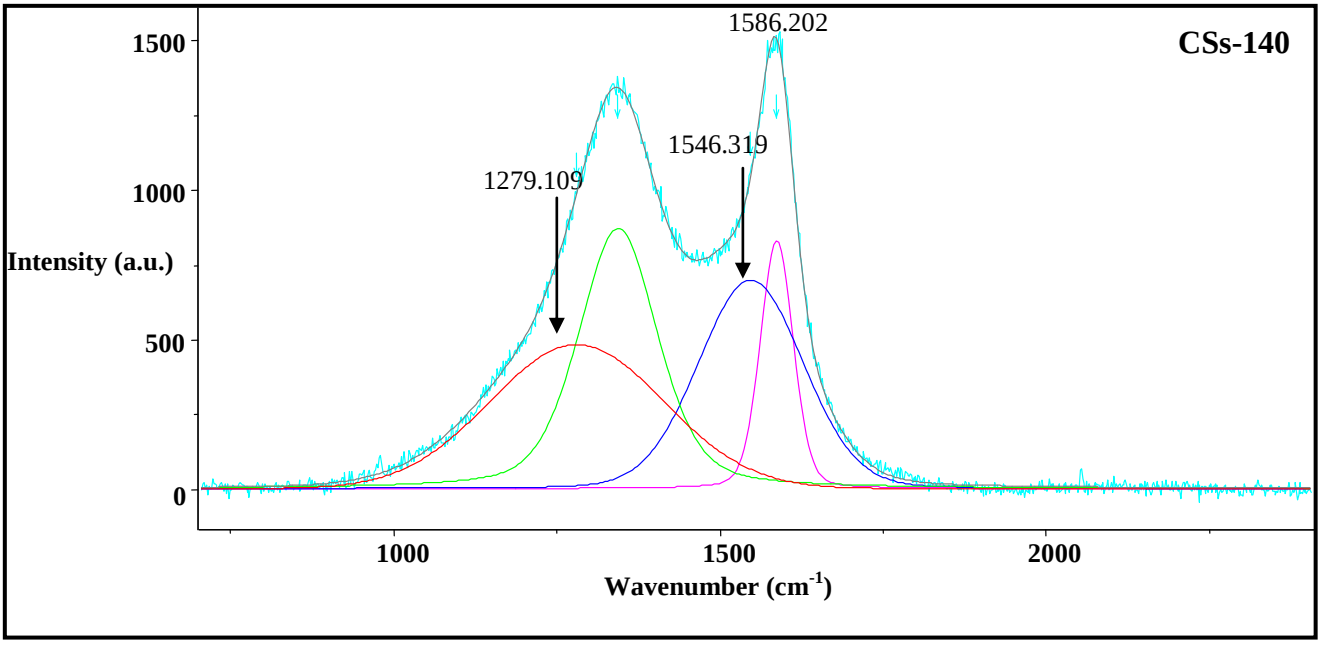


Figure S3: The deconvoluted Raman spectrum of CSs-140.

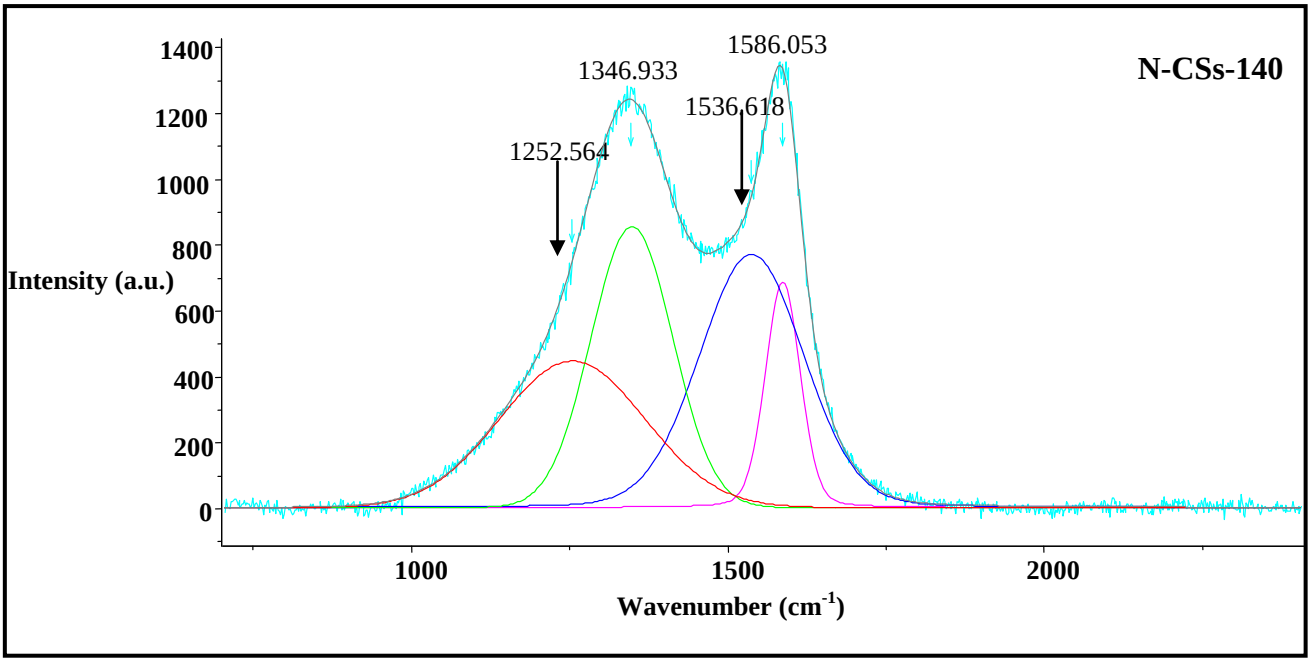


Figure S4: The deconvoluted Raman spectrum of N-CSs-140.

Table S1. The resolved binding energies (eV) and atomic concentrations (%) of N, C and O atoms in the N-CSs-540 and CSs-540 samples.

N-CSs-540 Binding energy (eV) (and atomic concentration (%))			**CSs-540** Binding energy (eV) (and atomic concentration (%))	
C	**N**	**O**	**C**	**O**
284.9 (90%)	**398.88** (62%)	**533.0**	**284.9** (93%)	**533.2**
285.90 (9%)	**400.72** (38 %)		**286.6** (6%)	
287.90 (0.6%)			**288.0** (0.6%)	
289.06 (0.3%)				

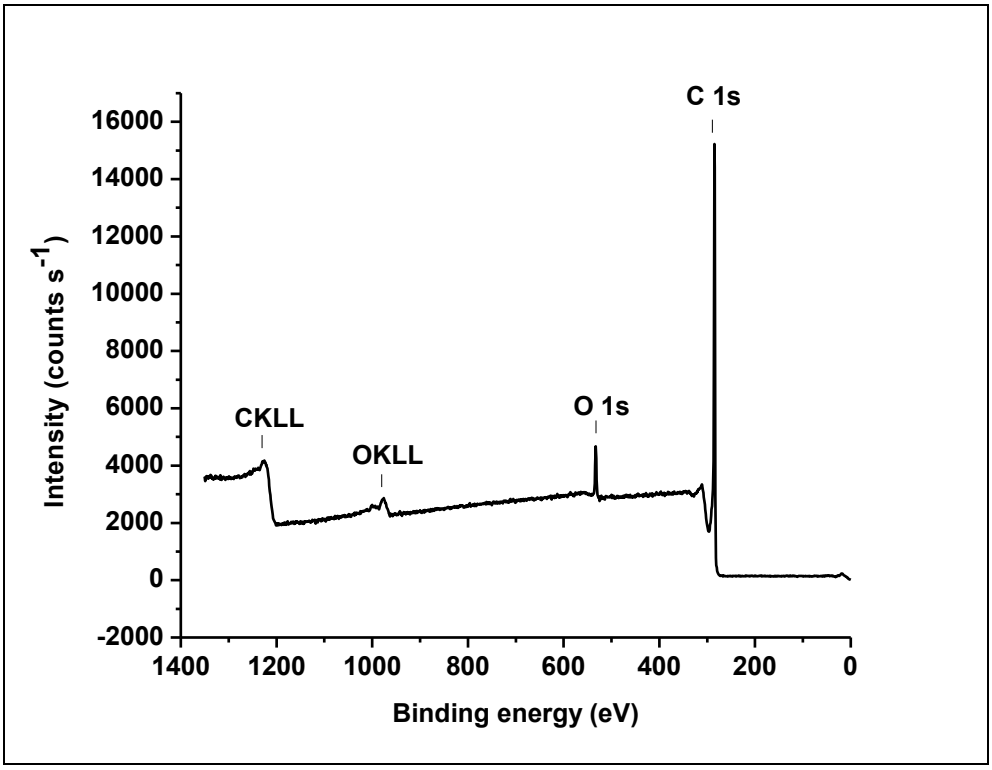


Figure S5: The survey XPS of CSs-540.

CHAPTER 5

The Synthesis and Characterization of Boron-Containing Multiwalled Carbon Nanotubes using an Fe-Co/$CaCO_3$ catalyst

---

5.1 Introduction

Since the investigation of carbon nanotubes (CNTs) by Iijima,[1] much effort has been put into the synthesis of single walled CNTs (SWCNTs) and multiwalled CNTs (MWCNTs) containing other elements such as nitrogen and boron. Substitutional atom doping of carbon nanotubes was first attempted by Stephan and co-workers[2] in 1994. They synthesized boron-nitrogen doped multiwalled carbon nanotubes using the arc-discharge method. Soon after their report, many researchers prepared B-C-N-containing nanotubes by an arc discharge method,[3] laser ablation,[4] and catalytic vapour deposition (CVD) methods,[5] using carbon-, boron- and nitrogen-containing precursors.

Chemical substitution brings about significant changes in carbon nanomaterials, in particular, substitution of boron or nitrogen in carbon nanostructures makes them p-type or n-type semi-conductors, respectively, as well as providing a means of modifying other properties of the CNTs.[6a-b] In addition, boron-doped CNTs have shown remarkable zigzag tube chirality[7] and stiffness.[8] Thus, considerable effort has been made to study both experimentally and theoretically the substitutional doping of CNTs with boron.[9-12] Carroll and co-workers[13] proposed that B substitution of CNTs leads to the formation of BC_3 nanodomains inserted in the 1D nanotube structure, giving rise to an acceptor state 0.4 eV below the Fermi level due to the realignment of this superstructure with the graphitic one.

Boron-containing CNTs can be synthesized by the same methods most widely used to produce undoped CNTs. These include high temperature arc-discharge[14] and laser ablation methods[15,16] as well as low temperature catalytic chemical vapour deposition (CCVD) methods.[17-19] Various methods have successfully been employed for making boron-containing carbon nanotubes. Table 5.1 presents some of the results on boron-containing carbon structures reported recently using different synthetic methods with different catalyst precursors and carbon/boron sources. From Table 5.1, it can be seen that the incorporation of boron in a carbon framework and the type of carbon material produced strongly depend on

the synthetic method, carbon/boron precursors, catalyst, reaction temperature and time as well as gas flow rate and pressure.

Table 5.1: B-containing CNTs obtained by various synthetic methods using different catalysts and reaction temperatures

Method	Boron-containing Precursor	Catalyst	Material produced	Boron concentration (at.% B)	Reference
Thermal CVD, 785-850 °C, Ar/H_2	$C_9H_{21}BO_3$ $C_9H_{21}BO_3/C_6H_5CH_2NH_2$	CoO thin film deposited on a SiO_2/Si substrate	B-SWCNTs B-N-SWCNTs	~ 1 ~ 1	[20]
High vacuum CVD, 800-900 °C, H_2	$C_9H_{21}BO_3$	Fe/MgO	B-SWCNTs	~ 0.6	[21(a-b)]
Laser ablation, 1100 °C, Ar	Mixture of carbon paste, elemental boron and catalyst: 0.5-3 at.% B > 3-10 at.% B	Co/Ni/B-doped graphite targets	B-SWCNTs graphite encapsulated boron carbide particles and very small number of SWCNTs + DWCNTs	< 0.05-0.1 -	[15], [16]
Arc discharge	C_2H_2 and anode rod doped with varying weight concentrations of B	-	B-MWCNTs	-	[14]
Arc discharge, He	BC_4N anode prepared by thermal decomposition of C_5H_5N-BH_3 and cathode made of graphite	-	B-C-N MWCNTs and B-MWCNTs	1-5	[22], [2], [6b]
Arc discharge, He	Hollow graphite anode filled with BN powder + pure graphite cathode	-	B-MWCNTs	-	[23], [24]
Fixed-bed flow CVD, 800 °C, 5% H_2/Ar	C_2H_2 and 1.3 M BF_3 in MeOH	Fe/$Ca(BO_3)_2$/$CaCO_3$	B-MWCNTs and carbon spheres (CSs)	< 0.5	[25]
Microwave plasma CVD, 700 °C	CH_4/H_2 and $(CH_3O)_3B$	Fe/SiO_2	B-MWCNTs	-	[26]
CVD, 950 °C, Ar, CH_4,	B_2H_6	Fe-Mo/MgO	B-DWCNTs	1	[27]
Hot filament CVD, Ar/H_2, 527 °C	C_2H_5OH/ B_2O_3 (5000 ppm) (bubbling hydrogen gas through B_2O_3 diluted in water/ethyl alcohol)	Cu substrates	B-MWCNTs	-	[18]
Laser Ablation, 500-1200 °C, Ar	Pellet made from a mixture of carbon powder with either B (rare-metallic), BN or B_4C	B-catalysed graphite	B-MWCNTs	B_4C	[28]
Arc discharge	Graphite and BN powder	Graphite and Ni/Y mixed with BN powder	C-B-N-SWCNTs	< 0.1	[29]
Arc discharge	BN and graphite soot (0-50 wt.% BN)	C:BN:Ni:Y_2O_3	B-N-SWCNTs and nano flakes	-	[30]
CVD, 1000 °C, He, H_2	C_2H_2-B_2H_6 mixture	Co nanoparticles	B-MWCNTs (bamboo-shaped)	$C_{35}B$	[17]
Induction-heating system, 1100 °C, Ar	B_2O_3 + CNTs	-	B-MWCNTs and nanorods	B_4C and $B_{13}C_2$	[31]

CVD, 1150 °C, NH_3	B_2O_3:SWCNTs 5:1	-	B-SWCNTs	15-20	[32]
CVD, 1050 °C,	B powder (99.99%):CNTs 4:1 mass ratio	-	B-MWCNTs	B_4C	[33]
CVD, 900 °C, Ar	Organoboron polymer/alumina composite membrane	-	B-MWCNTs	BC_4 and BC_3	[34]
Laser vaporization, N_2	Graphite targets containing NiB	-	B-SWCNTs	~ 1.8	[11]
CVD, 900 °C, Ar (H_2 to reduce catalyst)	THF (C_4H_8O), $C_9H_{21}BO_3$/MeOH (boron molar conc. At 0.85, 1.7 and 2.5 M)	Fe-Mo/MgO	B-DWCNTs	0.8-3.1	[35], [19]
CVD	Benzene, triphenylborane (different B content 0-2.24%)	Ferrocene	B-MWCNTs	0.86-2.24	[36]
Substitution reaction, Ar bubbled through NH_4OH, 1000 °C	Thermal annealing of SWCNTs with B_2O_3	-	B-SWCNTs	7.83	[37]
CO_2 laser pyrolysis, N_2	MgO+ $C_6H_7BO_2$ MgO+ $C_8H_{11}BO_4$ MgO+$C_{14}H_{10}$+B_2O_3 Graphite+ $C_8H_{11}BO_4$	Ceramic nanowires	B-MWCNTs	0.6-1	[38]
Substitution reaction. 1250-1350 °C, N_2	Thermal treatment of a mixture of B_2O_3 and SWCNTs	-	B-SWCNTs B-N-SWCNTs	B/C ratio ~0.1 B/N ratio ~1	[6a]
Aerosol-assisted CVD, 860 °C, Ar	Triethylborane $(C_2H_5)_3B$	25 mg/ml mixture of toluene and ferrocene (Fe:B ratio 5:1)	CB_xMWCNTs	0.7	[39]
Aerosol-based CVD 900-1100 °C	10Triethylborane:90 Toluene 10Triethylborane:2 benzyl amine: 88 Toluene	5wt% ferrocene in toluene	CB_x-MWCNTs CN_xB_y-MWCNTs	0.25 0.1	[40]
CVD, 1260 °C, NH_3	N-CNTs + B_2O_3 (held in Pt crucible)	-	$B_xC_yN_z$-MWCNTs	B/N ratio 0.92 B/C ratio 1.5	[41]
CVD, 730 °C,	H_3BO_3/MeOH solution (2 atm% B)	Fe/Si substrate	B-MWCNTs	-	[42]
CVD, 1000 °C, Ar/H_2	Melamine diborate (from melamine + H_3BO_3)	Ni-Fe coated SiO_2/Si substrate	B-C-N-MWCNTs	B = 27 C = 25 N = 31	[43]
CVD, 1700 °C N_2/H_2O (25 °C), carbon black (1500 °C)	$B_4N_3O_2H$ powder (prepared from melamine diborate) charged into a graphite crucible placed in a crucible susceptor,	-	B-N multi-walled nanotube	B/N ratio from 0.8 to 1.15	[44]

The CVD method gives higher yields of CNTs and remains the most attractive method for the production of boron-doped CNTs by catalytic decomposition of suitable carbon and boron sources. Catalytic transition metals such as Fe, Co and Ni and their alloys are often used in the production of the boron-containing CNTs. In the CVD method, the type, quality and quantity of the products produced strongly depends on the size of the catalyst particles,

reaction temperature and carbon feedstock. The growth process usually involves heating a catalyst (typically to 700-1000 °C) in an atmosphere of carbon- and boron-containing precursors. Low boron doping (< 1 at.%) of SWCNTs is achieved by the CVD method using triisopropyl borate vapour as the carbon and boron sources.[21a] Golberg and co-workers prepared boron-doped SWNTs (B/C ratio up to 0.1) by thermal treatment of B_2O_3 and SWCNTs at 1600 K in a nitrogen flow.[6a] Pyrolysis of C_2H_2-B_2H_6 mixtures over Co nanoparticles at 1000 °C in the presence of He and H_2 gases produces B-MWCNTs.[17] The nanotubes obtained by this procedure are multiwalled, have an average composition around $C_{35}B$ and contain nested cone-shaped graphene sheets in the tubular region with the metal particles from which they grow and are found at one end of the tube.

A variety of boron sources such as B_2H_6, elemental boron, B_2O_3, etc., have been successfully used to prepare boron doped CNTs as indicated in Table 5.1. However, their use as dopants faces challenges. For example, diborane (B_2H_6) is toxic, highly flammable in air and requires special handling care. In addition, it is instantly hydrolysed by water and the oxidation of B_2H_6 is extremely exothermic. Elemental boron is expensive to manufacture. The preparation methods used involve reduction of B_2O_3 with metals such as Mg or Al. However, the product is impure and contaminated with metal borides. Highly pure elemental B is also produced by decomposition of B_2H_6 at high temperatures. The use of B_2O_3 often requires high growth temperatures (1000-1350 °C),[6a,31,32,37,41] which creates structural defects inside the CNTs. Considering the above literature data, there is therefore a need for developing a technique to produce inexpensive B-doped CNTs. The present research addresses this need.

Our goal has been to synthesize multiwalled carbon nanotubes (and carbon spheres (CSs)) containing substitutional elements such as boron or nitrogen, using simple and reproducible CVD methods to give high yields of clean doped CNTs (and CSs). Potentially these fabricated materials will have tailored electrical and mechanical properties. For example we have achieved a simple route to nitrogen doped multiwalled carbon nanotubes using an Fe-Co/$CaCO_3$ catalyst.[45] The present study reports the synthesis of boron-containing CNTs obtained by the pyrolysis of C_2H_2 and $(CH_3O)_3B$ over an Fe-Co/$CaCO_3$ catalyst using a CVD method at 700-900 °C. The B-MWCNTs synthesized here can be used as supports in heterogeneous catalysis because of their desirable properties. As far as we are aware, there have been very few reports on the synthesis of boron-doped multiwalled CNTs from readily available and easy to use boron sources using an easy to prepare catalyst.[18,25,26,36] Because the

CVD method and the use of Fe-Co metals supported on $CaCO_3$ are generally recognised for producing very high purity MWCNTs.[46,47] and N-MWCNTs,[45] as well as the easy removal of $CaCO_3$ during the purification process, it is suggested to us that B-containing MWCNTs could be prepared using this method.

5.2 Experimental

5.2.1 Catalyst preparation

The Fe-Co/$CaCO_3$ catalyst was prepared by an impregnation route using an aqueous mixture of $Fe(NO_3)_3{\cdot}9H_2O$ and $Co(NO_3)_2{\cdot}6H_2O$.[46] The two metal nitrates (purchased from Sigma-Aldrich) were of analytical reagent grade and were used without further treatment. Calculated amounts of the metal nitrates were mixed and dissolved in distilled water to make a 0.3 M Fe-Co (50:50 w/w) precursor solution. This precursor solution was added dropwise to the stirred $CaCO_3$ and the mixture was left to stir for 30 minutes. The resulting metal-support mixture was then filtered and dried in an oven at 120 °C for 12 hours, cooled to room temperature, ground and sieved using a 150 µm mesh sieve. The catalyst was then calcined at 400 °C for 16 hours in air to decompose the nitrates. The total loading of the Fe-Co catalyst on the $CaCO_3$ was 5 mass %. These catalysts were completely characterized as reported earlier.[46]

5.2.2 Synthesis and purification of B-MWCNTs

B-MWCNTs were synthesized using a procedure similar to that reported by Tetana *et al.* for the synthesis of nitrogen-doped multiwalled carbon nanotubes.[45] The syntheses were carried out in a tubular quartz reactor (51 cm x 1.9 cm i.d.) placed in a horizontal furnace. C_2H_2 (Afrox) and trimethyl borate ($(CH_3O)_3B$ ≥ 99.0% (GC), purchased from Fluka Analytical), were used as carbon and carbon/boron precursors, respectively. N_2 (Afrox) was used as a carrier gas to dilute the C_2H_2 in order to decrease the contact time between C_2H_2 and the Fe-Co/$CaCO_3$ catalyst, and consequently reduce the formation of amorphous carbon.[48] For each synthesis, 0.3 g of the catalyst was uniformly spread onto a quartz boat (120 mm x 15 mm) which was then placed in the centre of a quartz tube. The furnace was raised to a desired temperature (700-900 °C) at 10 °C/min under flowing N_2 gas (40 ml/min) in the reaction.

Once the desired temperature was reached, the N_2 (240 ml/min) and C_2H_2 (100 ml/min) were simultaneously bubbled through $(CH_3O)_3B$ (at room temperature) for 1 hour. After this, the bubbling of the gases through $(CH_3O)_3B$ was stopped and the system was left to cool down to room temperature under N_2 (40 ml/min). The quartz boat was then removed from the reactor. At 900 °C, two sets of products were collected, one from the quartz boat and the second, a fluffy material, from the wall of the quartz tube close to the end of the tube. The as-produced boron-containing materials were purified using 55% HNO_3 under reflux in an oil bath held at 110 °C for 4 hours to remove the CaO, residual Fe-Co particles and introduce oxygen surface groups. The acid-treated B-CNTs were then filtered and washed several times with distilled water (to remove the residual HNO_3) until the pH of the filtrate was neutral. The boron-containing materials were dried at 120 °C for 12 hours prior to further characterization. No structural alteration as determined by TEM studies was observed after acid-treatment of the B-MWCNTs.

5.2.3 Characterization of B-CNTs

The morphology and structural features of the boron-containing carbon nanotubes were studied by transmission electron microscopy (TEM) using a FEI Technai G^2 Spirit electron microscope operated at 120 kV, equipped with an energy dispersive X-ray spectrometer (EDX), X-ray diffraction (XRD) using a Bruker D2 phaser equipped with Cu-Kα radiation (λ = 1.5406 Å), and the operation voltage of 30 kV and current of 10 mA, as well as Raman spectroscopy using a Jobin-Yvon T6400 micro-Raman spectrometer equipped with a liquid nitrogen cooled charge coupled device detector. The thermal stability and purity of the B-MWCNTs were investigated by thermogravimetric analysis (TGA) using a Perkin Elmer Pyris 1 TGA. About 10 mg of each sample was heated to 900 °C at a rate of 10 °C/min under air. The mass of the samples was kept constant (ca 10 mg) in order to reduce the effects of variability in measurements. BET surface areas of the B-CNTs (~200 mg for each measurement) were obtained through N_2 adsorption using an ASAP 2000 Micrometrics TriStar Surface Area and Porosity Analyzer. The boron concentration was determined by X-ray photoelectron spectroscopy (XPS) with data obtained on a Quantum 2000 Physical Electronics spectrometer (National Metrology Institute of South Africa (NMISA), Pretoria) equipped with a monochromatic Al Kα X-ray source (1486 eV) operated at 20 W. Fourier Transform Infrared (FT-IR) spectroscopy was used to record absorption spectra of the carbon

materials using a Brüker FT-IR spectrometer (BRUKER TENSOR 27) in the range 4000-500 cm^{-1}.

5.3 Results and discussion

5.3.1 Structural analysis of B-MWCNTs

Boron-containing MWCNTs were synthesized in the temperature range 700-900 °C and purified using nitric acid. Boron-doping effects in MWCNTs were studied by comparing the B-MWCNTs with undoped MWCNTs. TEM images of the purified undoped MWCNTs synthesized at 700 °C by the same method, using the same catalyst, but without using $(CH_3O)_3B$, were recorded (Figure 1). As seen in the figure, the undoped MWCNTs possess clean, hollow, open ends and straight unbuckled CNT walls with diameters of about 20-30 nm and an average diameter of ca. 25 nm.

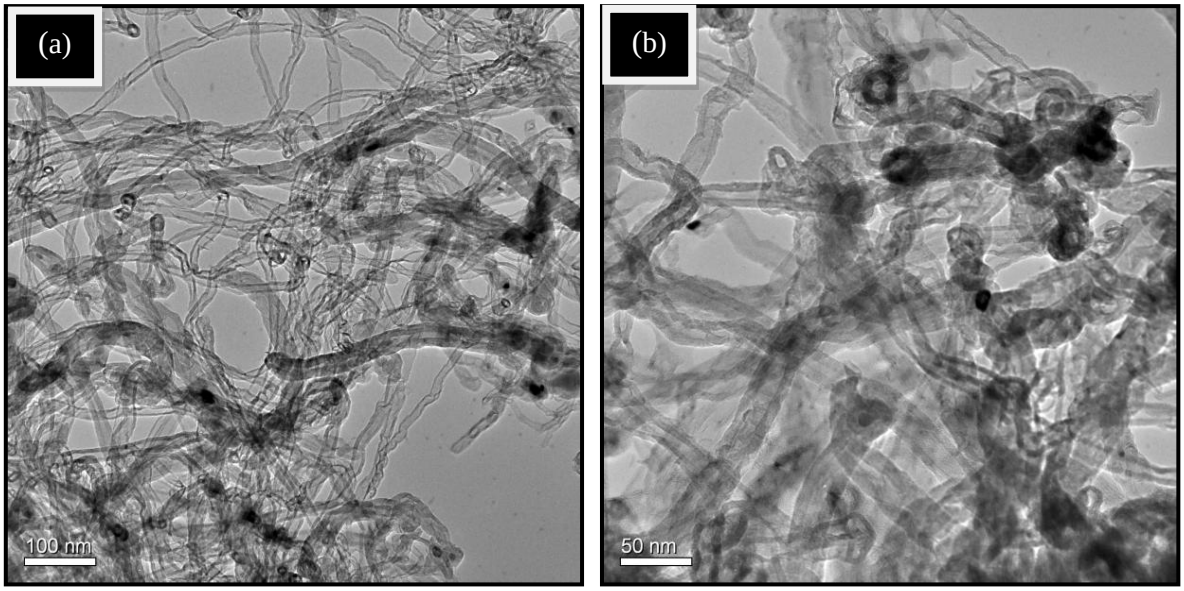


Figure 5.1: Typical TEM images (taken at different magnifications) of the purified undoped MWCNTs grown at 700 °C.

TEM images of the B-containing carbon materials made at 700-900 °C are shown in Figures 5.2 to 5.9. The results of each CVD synthesis temperature will be described and discussed in detail below. It was found that these carbon materials had defective tubular and spherical

structures, depending on the synthesis temperature used. The diameter distributions, average diameters and the type of each material produced, determined from the TEM data, are summarized in Table 5.2. Supplementary Figure S1 in Appendix C also presents the diameter distributions of the purified B-MWCNTs grown at 700-850 °C.

Generally, the B-containing MWCNTs synthesized by this method showed very different morphologies and outer diameters from the undoped MWCNTs. The B-MWCNTs were mostly curved, distorted, long, bamboo-like, had open ends and intertwined with each other. A base growth mechanism is suggested for the synthesized materials, based on TEM evidence which showed that the B-doped MWCNTs tip ends were particle free. Because of the intertwined effect, it was difficult to measure the length of most B-containing MWCNTs. The length of fairly straight B-MWCNTs was found to range from 5 to 10 micrometers.

Table 5.2: The influence of reaction temperature on the formation of boron-containing carbon materials.

Temperature (°C)	Diameter distribution (nm)	Average diameter (nm)	Type of material
700	20-30	25	undoped MWCNTs
700	12.5-62.5	43	rough B-MWCNTs
750	30-170	50	rough B-MWCNTs
800	30-210	70	bamboo-like B-MWCNTs
850	75-425 50-450 30-170 105-385 650-1150 175-375	125 150 70 175 800 225	bamboo-like B-MWCNTs, catalyst filled CNTs, catalyst inside the CNTs, bulbous-shaped catalyst, core-shell CSs and CSs shell thickness
900	50-550 75-275 30-130 100-220 300-1500 25-425	350 125 30 160 700 175	thicker walled B-MWCNTs, catalyst filled CNTs, catalyst inside the CNTs, bulbous-shaped catalyst core-shell CSs[a] and CS shell thickness
	250-1550 50-650	450 350	core-shell CSs[b] and CS shell thickness

[a] CSs collected from the quartz boat, [b] CSs collected from the wall of the quartz tube.

Figure 5.2 shows the TEM images of the B-MWCNTs made at 700 °C. The figure shows that the carbon materials exhibit very rough surfaces with average diameter of about 43 nm (see Table 5.2 and Figure S1). Thus, the addition of the boron source generates tubes that have larger diameters and a different morphology than produced without a boron source (Figure

5.1). The tubes synthesized at 750 °C (Figure 5.3) show a similar structural morphology to those made at 700 °C, and have an average diameter of 50 nm (Table 5.2 and Figure S1).

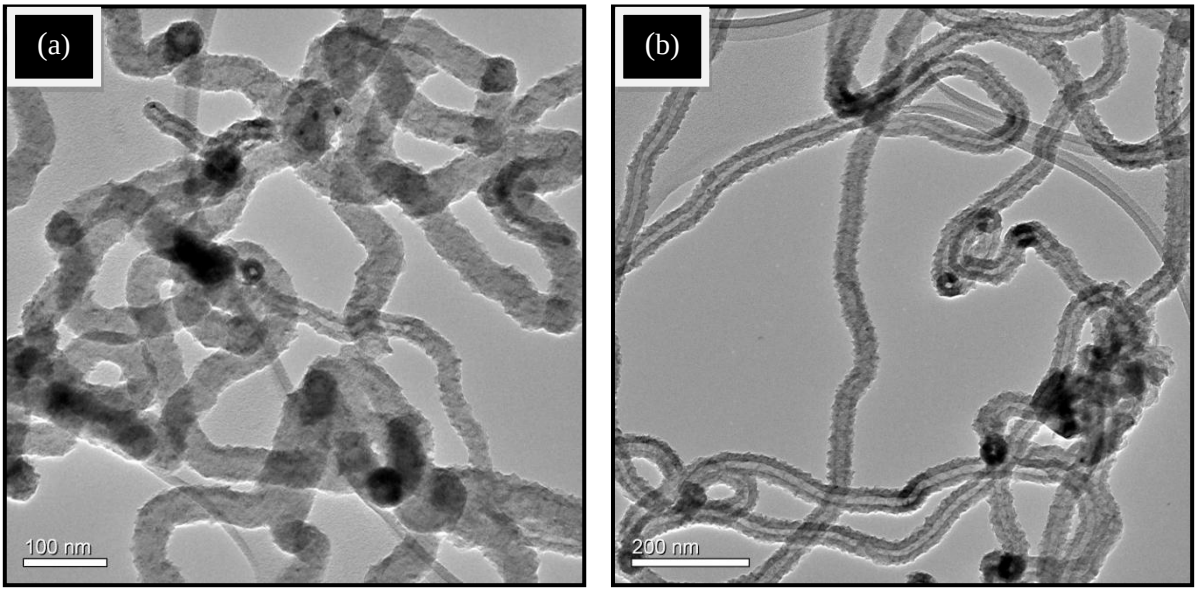


Figure 5.2: TEM images (taken at different magnifications) of the purified B-MWCNTs grown at 700 °C.

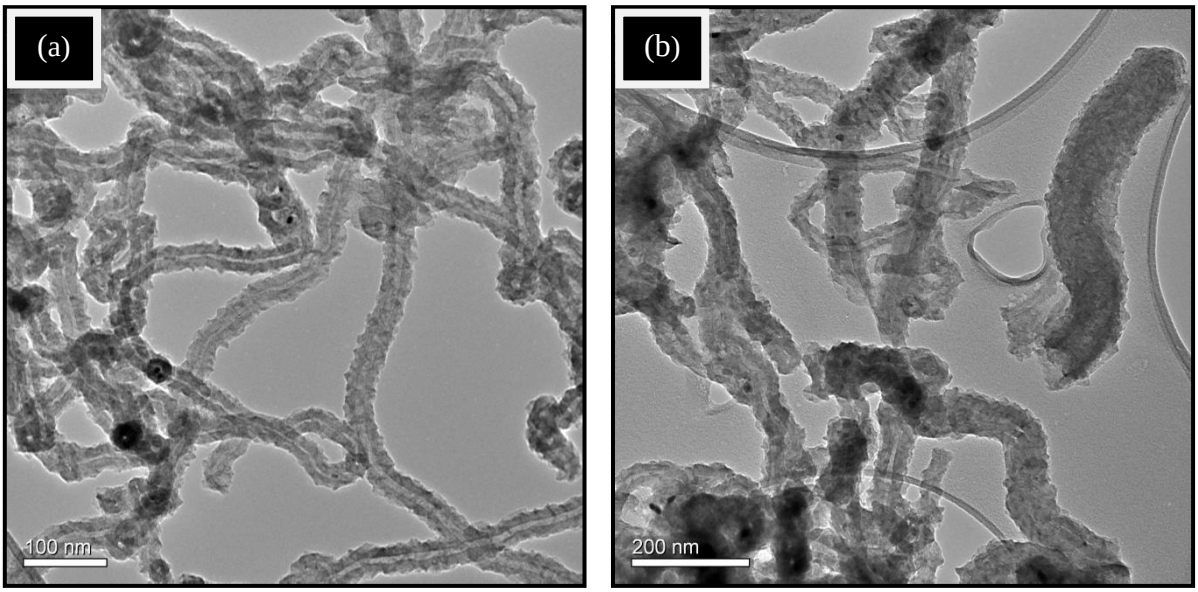


Figure 5.3: TEM images (taken at different magnifications) of the purified B-MWCNTs grown at 750 °C.

When the growth temperature was further increased to 800 °C (Figure 5.4), the average diameter of the B-MWCNTs increased to 70 nm. An increase in diameter distribution of the B-MWCNTs is conveyed by an increase in diameter of the catalyst as the reaction

temperature increases. At 800 °C, the CNT surface roughness decreased and the bamboo-like structures became more prominent.

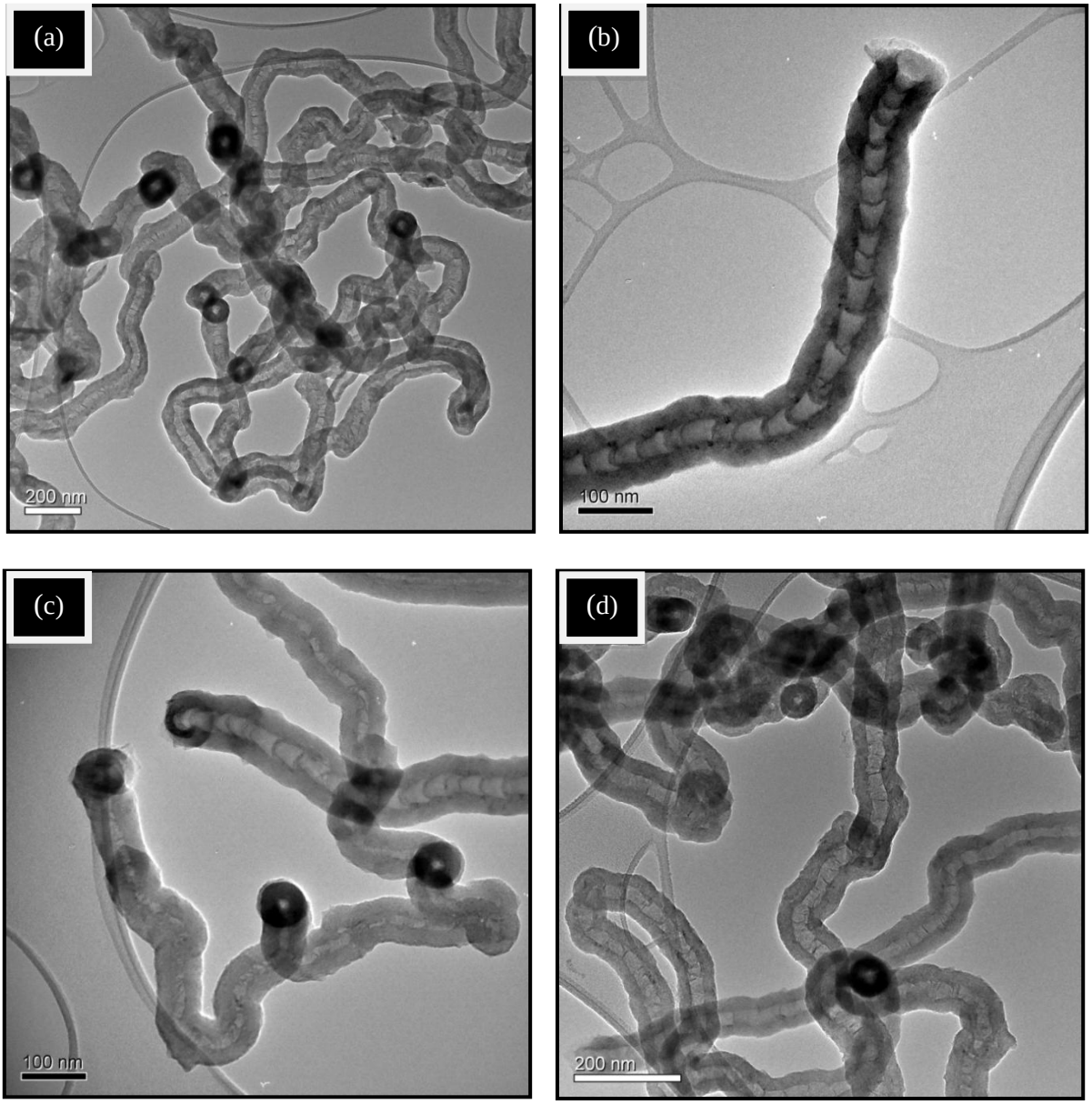


Figure 5.4: TEM images (taken at different magnification) of the purified B-MWCNTs grown at 800 °C.

Bamboo-like structures (though in their case the tubes had metal particles at the tips) have been observed in boron-containing CNTs prepared from the pyrolysis of C_2H_2-B_2H_6 mixtures over Co nanoparticles at 1000 °C.[17] Carbon nanotubes containing bamboo compartments are commonly observed in N-doped CNTs.[45,49] The bamboo-like structures seen in our B-MWCNTs are not due to the N_2 gas used during the synthesis, as confirmed by the absence of

peak at around 400 eV in XPS studies (see **Section 5.3.5**). The bamboo-like structures observed in our B-MWCNTs are due to effects related to the catalyst particle shape, the bulk diffusion of carbon and the boron source.

After purification of the B-MWCNTs synthesized at 700-800 °C there were no catalyst particles detected and the structures of the B-MWCNTs remained unchanged. However, at growth temperatures of 850 and 900 °C, changes in the products were detected after purification. Therefore we discuss in detail the carbon products of both raw and the purified samples grown at 850 and 900 °C.

TEM images of the unpurified sample synthesized at 850 °C (Figure 5.5) showed that the carbons produced were quite varied. A wide range of shapes were observed: (a) straight bamboo-like (indicated by red arrows) tubes and catalyst filled tubes (indicated by white arrows) with a closed end, (b) very rough bamboo-like tubes, (c) elbow-shaped bamboo-like tubes, (d) Y-junction tubes, (e) core-shell carbon spheres and (f) catalyst filled tubes with bulbous-shaped catalysts.

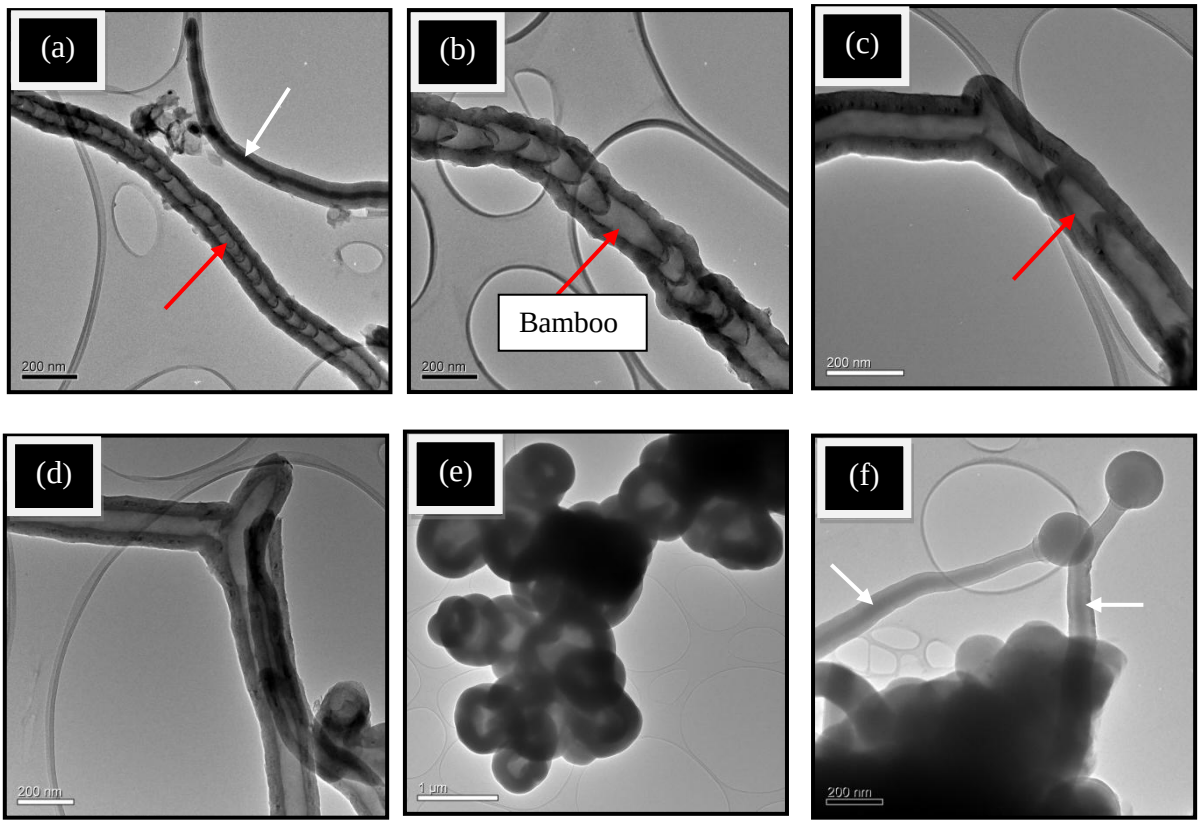


Figure 5.5: TEM images (taken at different magnification) showing various shapes of the unpurified carbon materials grown at 850 °C: (a) straight bamboo-like tube and catalyst filled tube with a closed end; (b) very rough bamboo-like tube; (c) elbow-shaped bamboo-like tube; (d) Y-junction hollow tube; (e) core-shell CSs; (f) catalyst filled tubes with bulbous-shaped catalysts.

Quantitative analysis of TEM data showed that the majority of the product was made up of CNTs (~85%), catalyst filled tubes with bulbous-shaped catalysts (~10%) and core-shell CSs (~5%). The finding of a wide range of structures obtained by using a boron source is not unique. Hashim and co-workers[39] synthesized CB_x-MWCNT 3D solid structures via an aerosol-assisted CVD using ferrocene as a catalyst and triethylborane as the boron source at 860 °C for 30 minutes. In their synthesis, they obtained a range of tube morphologies: elbow junctions, Y-junctions, four-way covalent nanojunctions in series and two overlapping CBx-MWNTs welded together assisted by boron doping. In our study, we also found elbow-shaped bamboo-like tube and Y-shaped tubes (Figures 5.5c and 5.5d). Other shaped carbon materials found in our materials synthesized at 850 °C were core-shell carbon spheres (Figure 5.5e). In a recent study we have successfully grown B-doped core-shell carbon spheres from

C_2H_2 and trimethyl borate at 900 °C without using a catalyst.[50] Thus the spherical structures formed in this study most likely did not require a catalyst.

The diameters of all these structures are presented in Table 5.2. The CNTs had an average outer diameter of about 125 nm. The bulbous structures shown in Figure 5.5f and supplementary Figure S2 are unusual. EDX was performed to determine the chemical composition of the filled CNTs and the bulbous regions. The EDX spectrum (Figure S2b) of the bulbous structure in Figure S2a showed that the bulbous region was composed of C, Fe and Ca and O, with dimensions that varied from 105-385 nm. It was found that the bulbous-shaped metal particles were significantly larger (~175 nm in average) than the diameters of the CNTs. The TEM image reported in Figure S2c and EDX analysis (Figure S2d) indicated that the inside of the CNTs was filled with Fe, Ca and O. The metal particles inside the CNTs had diameters ranging from 30-170 nm. The metal particles in the bulbous structure and the metal nanoparticles encapsulated inside the CNTs obviously came from the Fe-Co/$CaCO_3$ catalyst. Ma and co-workers[44] reported similar structures resembling bulbous-shaped structures formed in their study. These materials were made from the CVD pyrolysis of $B_4N_3O_2H$ precursor (prepared from melamine diborate) at high temperature (1700 °C) in an N_2/H_2O gas environment in the absence of a catalyst. The obtained nanotubes exhibited bulbous tips filled with amorphous B-N-O materials. It was suggested that the B-N-O-based bulbous tips might play a catalytic role in the BN nanotube tip-growth process. Clearly, in this study the metal filled CNT were formed during the growth process (i.e. *in situ*). Recently, Koós *et al.*[40] also found Fe particles encapsulated inside the CNTs in their study of B-doped and N/B-doped carbon nanotubes.

Figure 5.6 presents some of the TEM images of the purified carbon materials synthesized at 850 °C. In addition to the bamboo-like and hollow tubes present in the purified sample (not shown), the TEM images showed unfilled open and closed end tubes (Figures 5.6a and 5.6b) as well as clean tubes with no bulbous materials (Figure 5.6c).

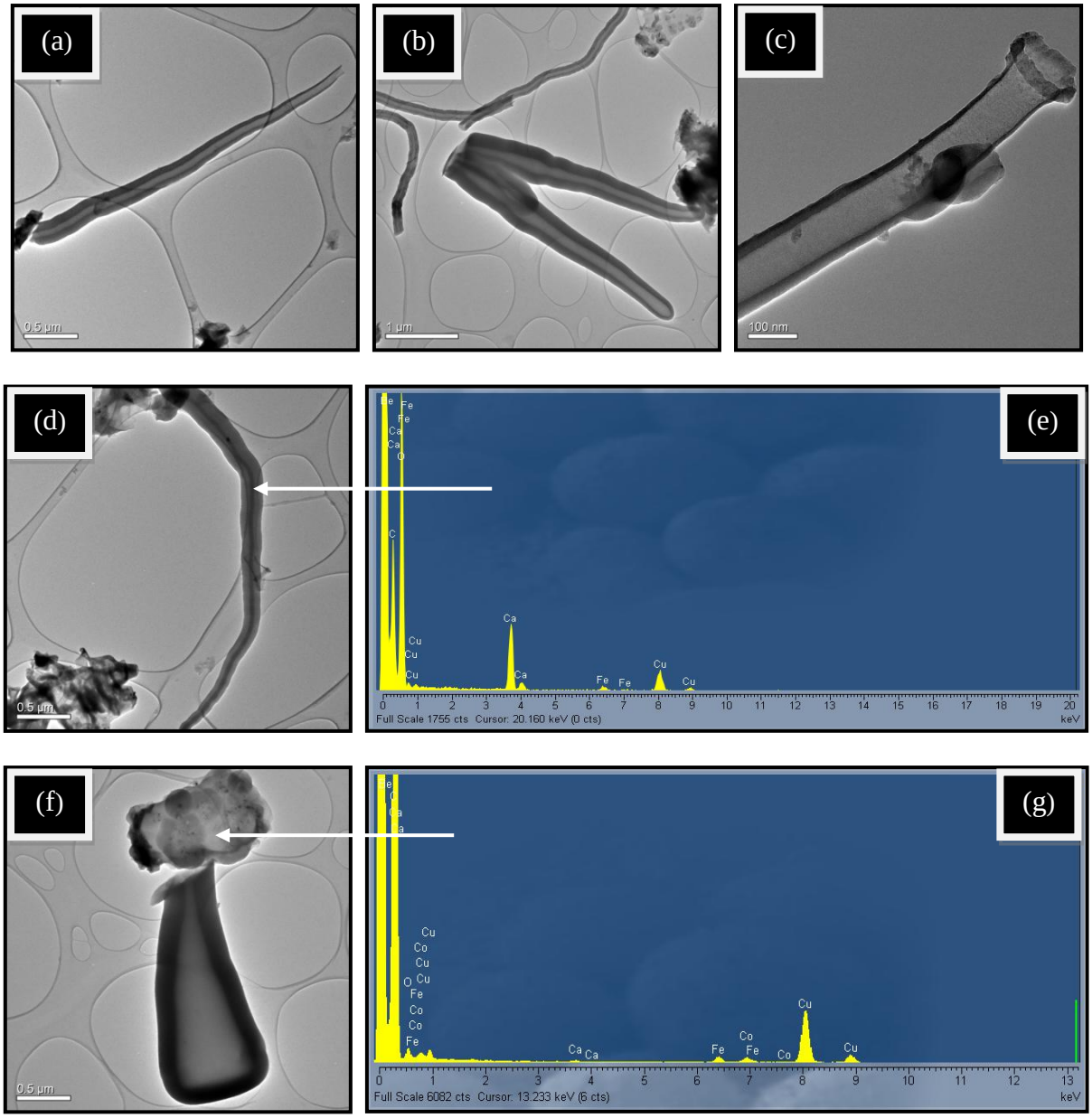


Figure 5.6: TEM images (taken at different magnification) showing various shapes of the purified carbon materials grown at 850 °C: (a) an open-end tube and (b) closed end tubes showing no catalyst particles inside; (c) hollow tube showing the absence of the bulbous-shaped catalysts; (d) catalyst filled tube with a closed end; (e) the corresponding EDX spectrum of the catalyst particles in (d); a catalyst and a catalyst free tube with a closed end; (g) the corresponding EDX spectrum of the catalyst particles in (f). The arrows indicate points where the corresponding EDX spectrum was collected.

The catalyst filled CNT (Figure 5.6d) and its corresponding EDX spectrum (Figure 5.6e) showed that the catalyst particles were still observed after nitric acid treatment. The EDX spectrum (Figure 5.6g) of the catalyst particles in Figure 5.6f showed the presence of the Fe, Co and Ca metal particles. The bulbous shaped catalysts were not seen after purification. These results show that the purification step did not remove the entire catalyst particles in the sample.

As mentioned earlier, the reaction temperature of 900 °C produced two sets of products, one found in the boat and the other on the walls of the tube. Similar structures described at a reaction temperature of 850 °C were also found at 900 °C. TEM examination (Figure 5.7) of the unpurified sample product from the boat showed that the sample exhibited a mixture of (a) CNTs and core-shell carbon spheres, (b) core-shell carbon spheres, (c) long catalyst filled tubes with bulbous-shaped catalyst, (d) short catalyst filled tube with bulbous-shaped catalyst and (f) catalyst filled tube. About 1% of the product was CNTs with thicker walls of about 350 nm, ~4% was catalyst filled CNTs and ~95% was core-shell CSs with average diameters of 700 nm and shell thickness of 175 nm. EDX analysis shown in Figure 5.7e and Figure 5.7g confirmed the presence of Fe and Ca particles inside the CNTs.

Figure 5.8 shows the TEM images of the sample from the boat after acid treatment. The figure shows the existence of (a) closed end tubes showing no catalyst particles inside, (b) uniform core-shell carbon spheres, (c) various sizes of core-shell carbon spheres, (d) thicker walled tubes with catalyst particles (the darker region). The corresponding EDX spectrum of the catalyst particles in (d) confirmed the presence of Fe, Co and Ca particles, indicating that some catalyst particles were not completely removed by purification.

The TEM images of the sample from the wall of the quartz tube are shown in Figure 5.9. The sample consisted of a fluffy carbon material consisting of only carbon spheres (which contained about 95% core-shell CSs and 5% solid CSs): (a) a mixture of core-shell and solid carbon spheres as well as (b) and (c) core-shell carbon spheres with different sized-shell thickness. Solid carbon spheres have been reported to form at high temperatures.[45]

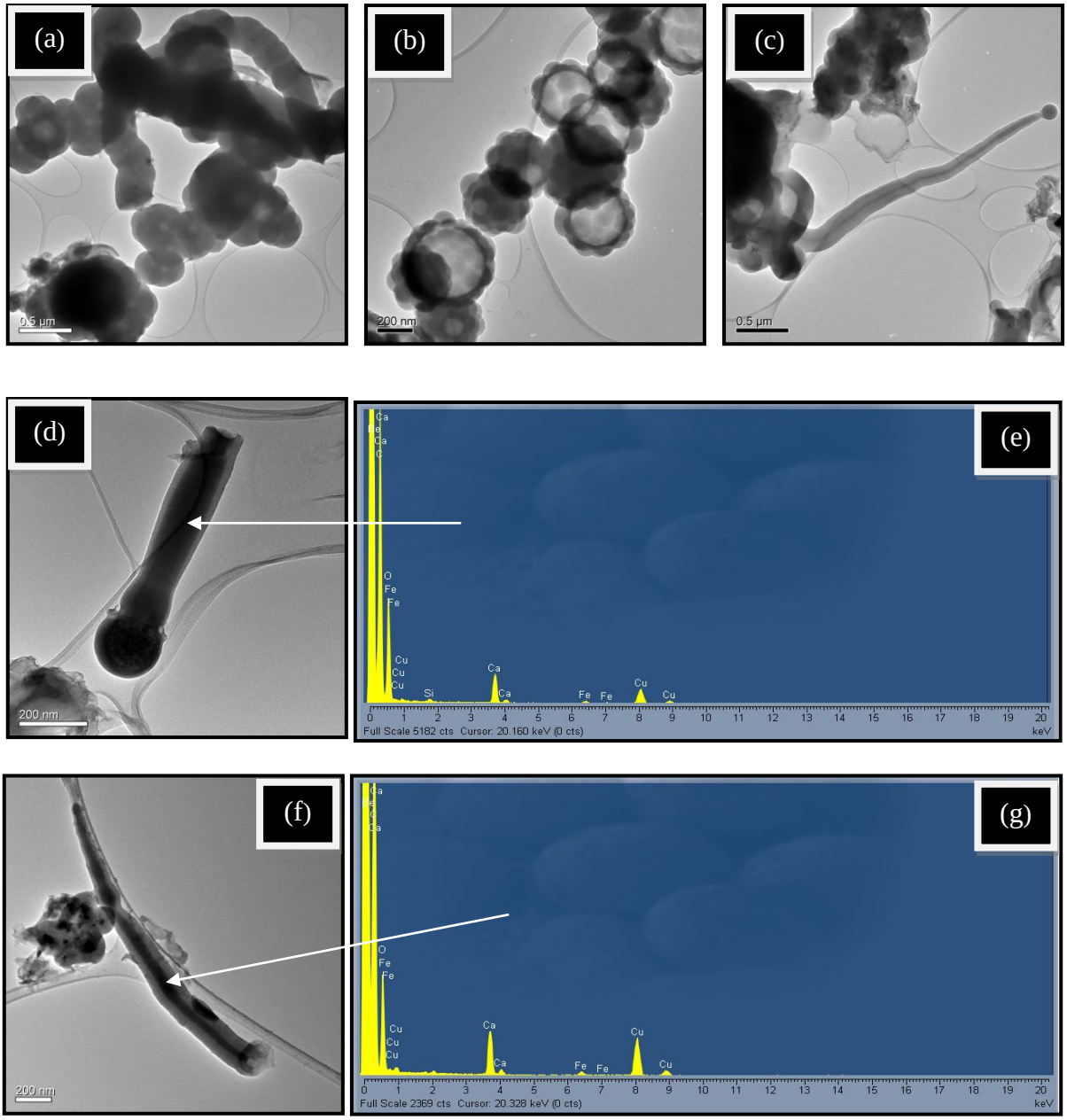


Figure 5.7: TEM images (taken at different magnification) of the unpurified carbon materials grown at 900 °C collected from the boat: (a) CNTs with thicker walls and core-shell CSs; (b) core-shell CSs; (c) catalyst filled long tube with bulbous-shaped catalysts; (d) catalyst filled short tube with bulbous-shaped catalyst; (e) EDX spectrum of the bulbous area in (d); (f) catalyst filled tube with a closed end; (g) the corresponding EDX spectrum of the catalyst particles in (f). The arrows indicate points where the corresponding EDX spectrum was collected.

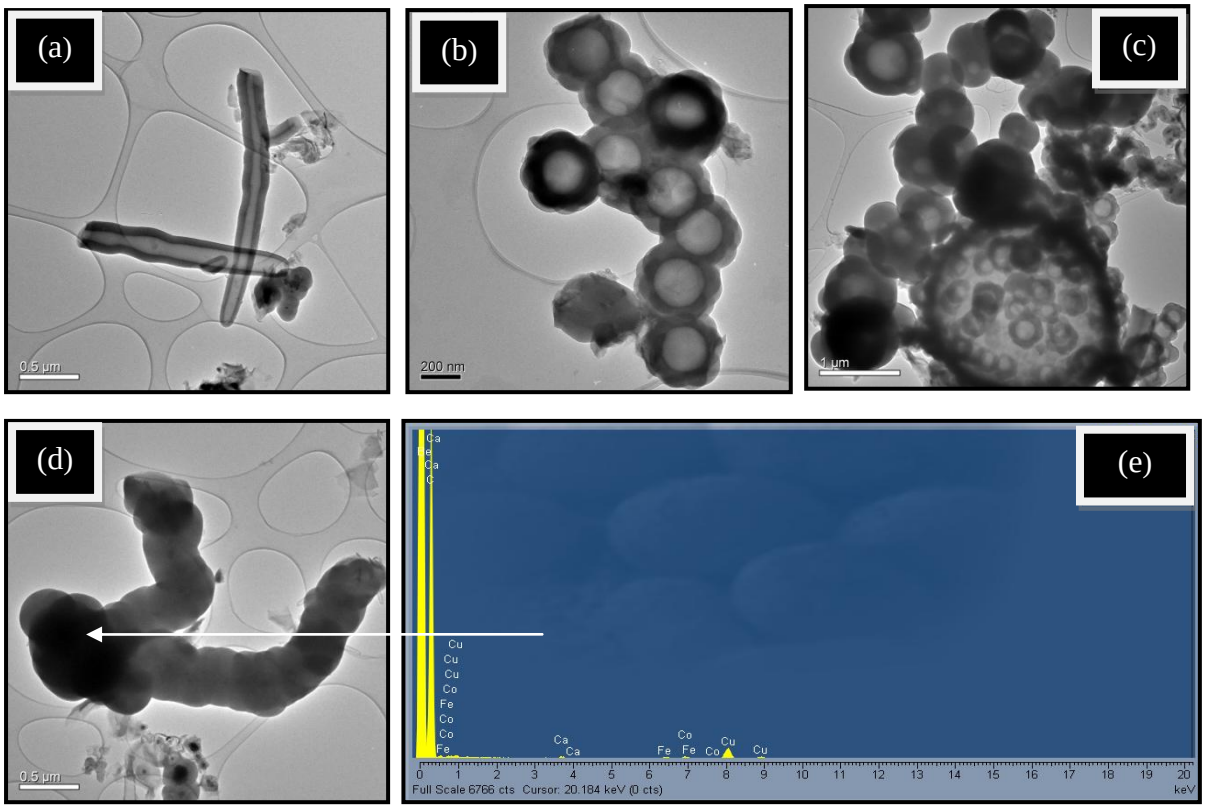


Figure 5.8: TEM images (taken at different magnification) of the purified carbon materials grown at 900 °C collected from the boat: (a) closed end tubes showing no catalyst particles inside; (b) uniform core-shell CSs; (c) various sizes of core-shell CSs; (d) thicker walled tubes with catalyst particles (the darker region); the corresponding EDX spectrum of the catalyst particles in (d). The arrow indicates a point where the corresponding EDX spectrum was collected.

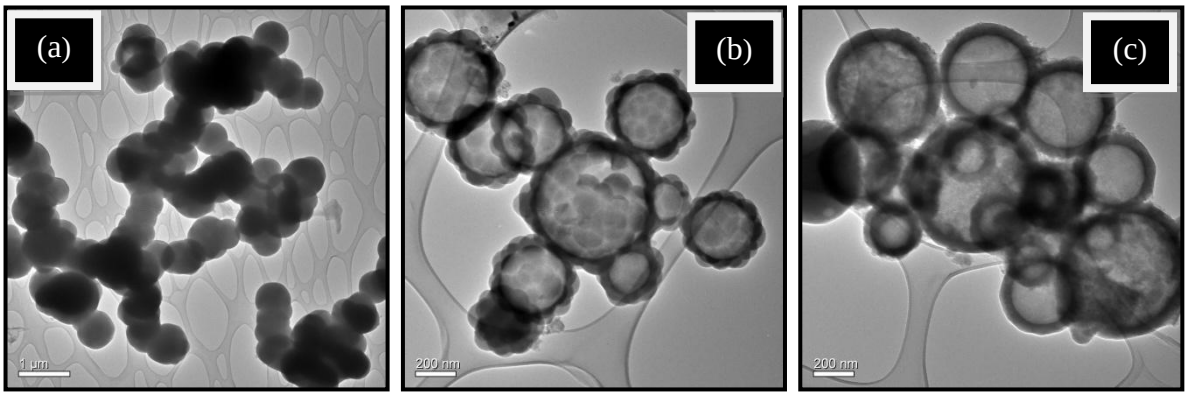


Figure 5.9: TEM images of the fluffy material formed at 900 °C collected from the wall of the quartz tube: (a) solid and core-shell CSs; (b) and (c) different types of core-shell CSs.

It is well known that different types of catalysts are active at different reaction temperatures. Thus, at 850-900 °C, non-catalytic competing pathways are occurring and thus other nanostructured materials formed together with the desired materials. The formation of spherical materials suggest that boron-doped CSs with core-shell structures could be synthesized at 850-900 °C by the same method but without using any catalyst. These results indicate that control of the synthesis temperature is crucial for the synthesis of B-MWCNTs with specific morphologies. Thus, the generation of clean B-MWCNTs using an Fe-Co/$CaCO_3$ catalyst requires growth temperatures of not greater than 800 °C. These results show that 700-850 °C growth temperatures presented CNTs with many structural defects leading to rough bamboo-like and elbow-like tubes.

5.3.2 BET surface areas, pore volumes and pore diameters of the purified B-MWCNTs

Table 3 lists the specific surface areas, pore volume and pore diameters of the purified undoped and B-doped MWCNTs synthesized at different growth temperatures. The undoped CNTs showed higher surface area when compared to the B-containing carbon materials. It can be observed that the specific surface areas of the B-MWCNTs decreased sharply with synthesis temperature. The surface area of the CNTs is directly related to the average diameter of the CNTs.[51]

Table 5.3: BET surface areas and pore volumes of the purified undoped and B-doped MWCNTs.

Temperature (°C)	Surface area (m^2/g)	Pore volume (cm^3/g)	Pore diameter (nm)
Undoped CNTs	144	0.54	14.5
700	95.1	0.50	21.4
750	76.7	0.42	22.1
800	41.9	0.13	13.1
850	13.2	0.03	8.8
900[a]	35.0	0.16	17.5
900[b]	0.48	0.02	128.9

[a] Carbon material collected from the quartz boat, [b] CSs collected from the wall of the quartz tube.

The B-MWCNTs synthesized at 700-750 °C gave higher surface areas when compared to B-MWCNTs at 800-900 °C, possibly due to the smaller catalyst particle size yielding smaller diameter tubes at the lower reaction temperature. The lower surface area observed at higher synthesis temperatures is related to the lower surface area carbon spheres and catalyst particles present in the samples. The relatively higher surface areas observed at 700-800 °C suggest possibilities for the use of B-doped MWCNTs for applications as new catalyst supports, in materials science and in other various areas where high surface area CNTs are required.

5.3.3 Thermogravimetric analysis (TGA) of the purified B-MWCNTs

To investigate the purity and thermal stability of the purified B-MWCNT samples, thermogravimetric analysis was carried out. Figures 5.10a and 5.10b show the TGA and derivative weight curves of the purified B-MWCNTs (collected from the quartz boat) compared with undoped CNTs. The B-MWCNTs showed complete decomposition between 601-679 °C under air (see Figure 5.10b and Table 5.4). The decomposition temperatures of the B-MWCNTs made at 750-900 °C were higher than that of undoped CNTs, but interestingly, the B-MWCNTs made at 700 °C were thermally less stable than undoped CNTs.

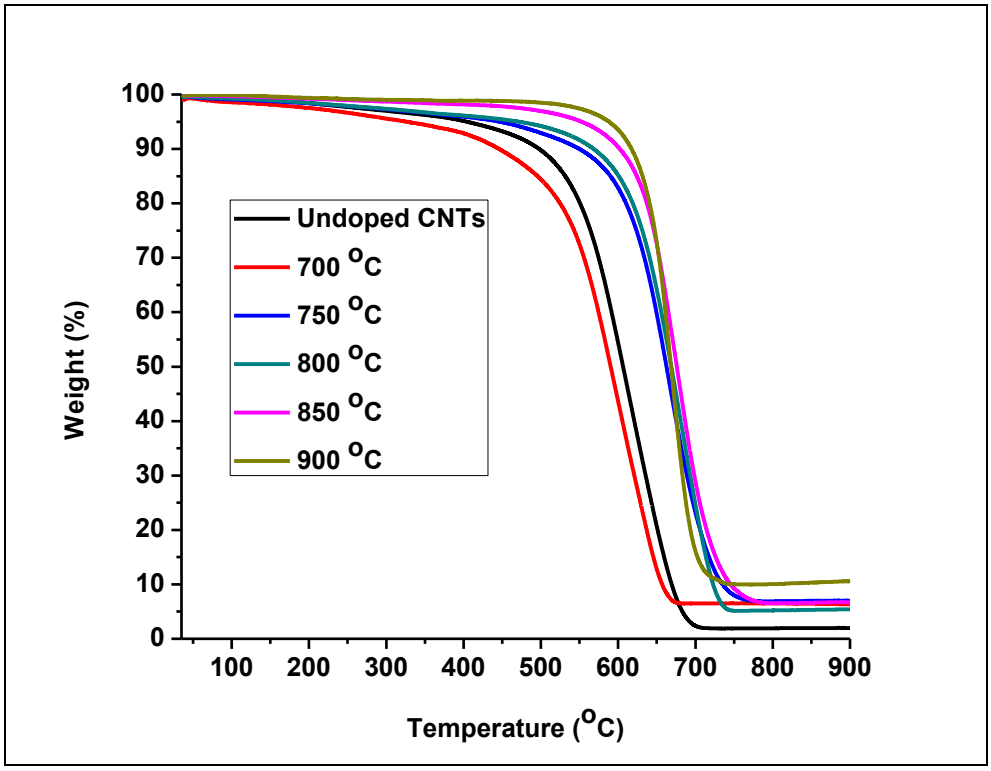


Figure 5.10a: TGA curves of the purified B-MWCNTs grown at 700-900 °C compared with undoped MWCNTs.

The catalyst content in the materials can be determined from the residual mass %, as seen in Table 5.4. Figure 5.10a reveals that the B-MWCNTs purity is greater than 90%, while > 98% for undoped CNTs. The residual mass slightly increased with reaction temperature. In a previous study done by Mhlanga and Coville[52] on the TGA of undoped CNTs (made by the same method but without using $(CH_3O)_3B$), the catalyst impurities (~4-6%) could not be removed even after long acid treatment using a wide range of acid treatments. It was mentioned that the impurities could be either embedded within the graphite walls of the CNTs or were to be found in the inner hollow central tube, indicating that the metal would have little influence on the thermal behaviour of the CNTs in air. In this study, the bulk residual mass also arose from the catalyst particles found in the filled tubes as confirmed by TEM and EDX studies.

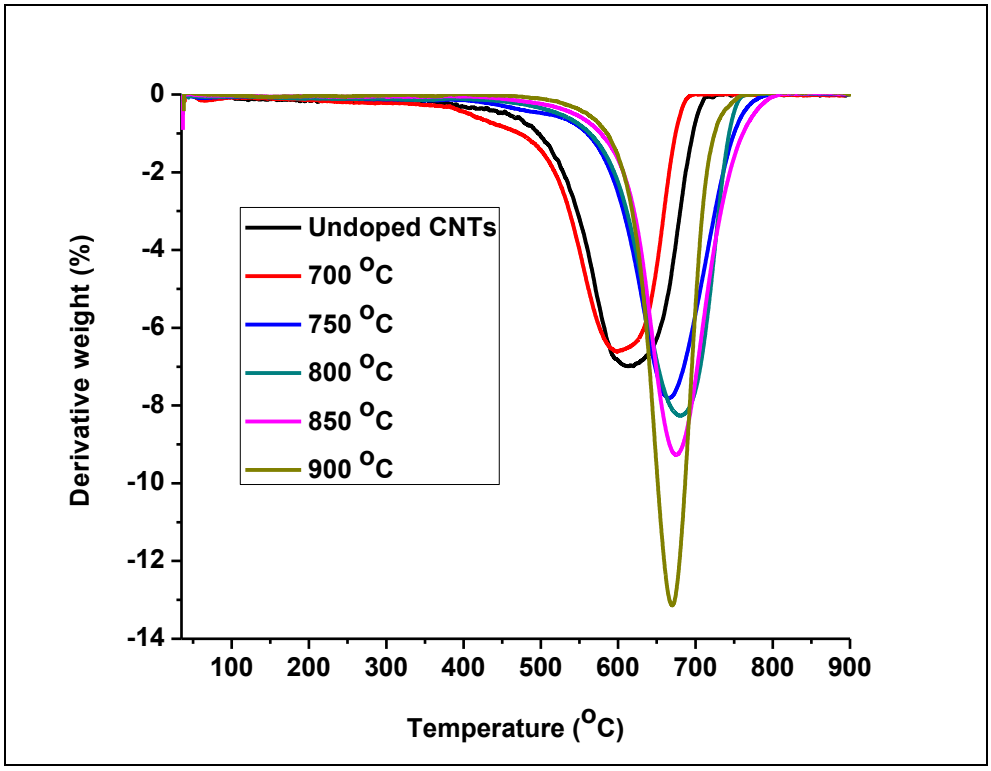


Figure 5.10b: Derivative profiles of the purified B-MWCNTs grown at 700-900 °C compared with undoped MWCNTs.

The TGA data of the sample synthesized at 900 °C and collected from the wall of the quartz tube is presented in Figures S3 and S4 and compared with boric acid. TGA of boric acid was performed to get a better understanding of the temperatures where thermal events occur in the boron-containing CSs. Boric acid (H_3BO_3) theoretically contains 56.30% boron oxide (B_2O_3) and 43.70% water (H_2O), with a melting point of 171 °C. Thermal decomposition of boric acid depicted in Figures S3 and S4 show two mass loss steps. The first decomposition which started at 141 °C corresponding to a weight loss of 34.80%, was due to the dehydration of H_3BO_3 forming HBO_2. The second stage showed a weight loss of 8.20% at 256 °C which was due to the dehydration of HBO_2 producing a white hard B_2O_3 material, leaving a residual mass of 56.40% (see Table 5.4). Our results agree with theoretical percentages and those reported by Nyambo *et al.*[53] on their TGA analysis of boric acid. They reported that the first stage which occurred between 100 and 180 °C with a weight loss of 34%, was due to the dehydration of H_3BO_3 into HBO_2, while the second one between 180 and 400 °C, with a weight loss of 10% attributed to dehydration of HBO_2 into B_2O_3, leaving 56% residual mass.

Table 5.4: TGA analysis of the purified undoped and B-doped MWCNTs.

Growth Temperature (°C)	Decomposition Temperature (°C)	Residual mass (%)
Undoped CNTs	616	1.8
700	601	6.5
750	666	6.9
800	679	5.4
850	676	6.4
900[a]	671	10.1
900[b]	108, 160, 730	20.9
Boric acid	141, 256	56.4

[a] Carbon material collected from the quartz boat, [b] CSs collected from the wall of the quartz tube.

As shown in Figures S4, for the sample synthesized at 900 °C and collected from the wall of the quartz tube, the three peaks located at 108, 160 and 730 °C in the derivative curve correspond to the maximum release of moisture, dehydration of HBO_2 in the B-CSs and decomposition of carbon spheres, respectively. From Figure S3, the residual mass (about 21%) was assigned to B_2O_3, implying that the core-shell carbon spheres contain B_2O_3 or B-C that is oxidized at high temperature.

5.3.4 XPS analysis of the purified B-MWCNTs

X-ray photoelectron spectroscopy (XPS) was employed to determine the boron content in the purified B-MWCNTs. The chemical composition of the B-MWCNTs synthesized at 800 °C and determined by XPS is shown in Figure 5.11a. The figure shows that the sample mainly contained carbon, oxygen and boron atoms. No nitrogen species were detected in the XPS spectrum. Table 5.5 lists the XPS binding energies, atomic concentrations and the possible chemical bonds of the species found in the B-MWCNTs grown at 800 °C. The relative atomic concentrations of C, B and O estimated from XPS were 83.8%, 1.6% and 14.6%, respectively.

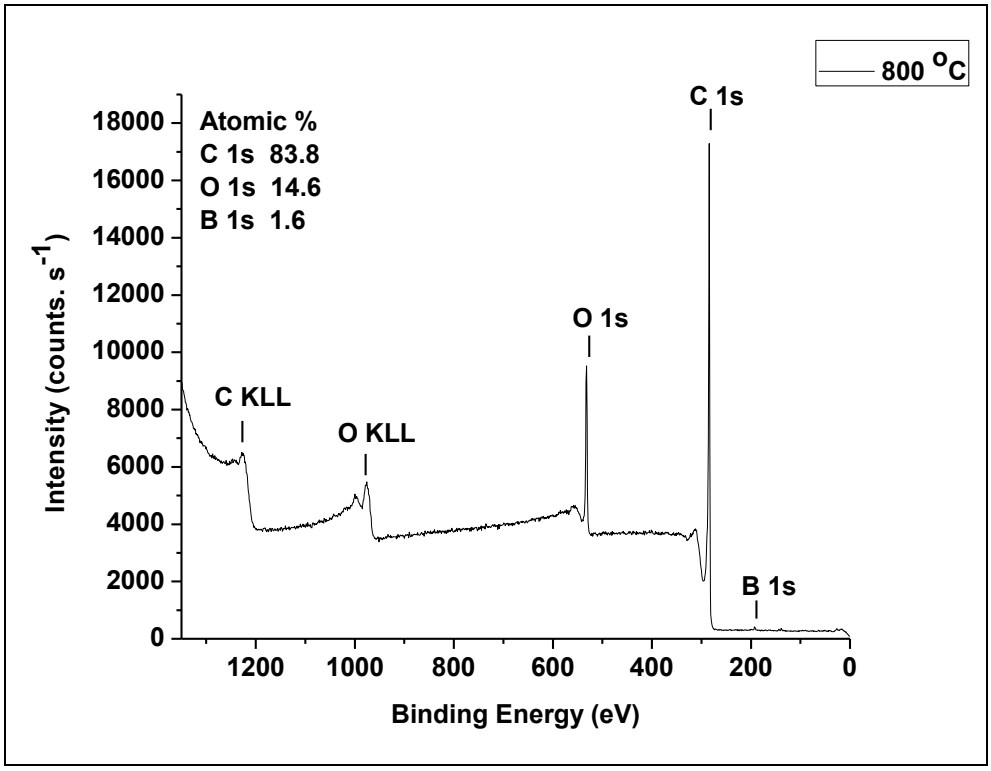


Figure 5.11a: The survey XPS of the purified B-MWCNTs grown at 800 °C.

The deconvolution of B1s spectrum can be achieved by fitting with only one peak at 192.2 eV (Figure 5.11b). On the basis of the literature binding energies reported for B attached to C atoms in a graphitic state (188.5 eV),[54] B-C in B_4C bonding environment (187.9 eV), as well as oxide-related species in BC_2O (190 ± 0.1 eV), BCO_2 (192 ± 0.1 eV) and B_2O_3 (193.2 ± 0.1 eV),[35,54-57] the peak at ~192 eV found in our B-MWCNTs synthesized at 800 °C can be assigned. The B in our B-MWCNTs appears to have B with mixed B-C and B-O bonding as found in BCO_2 nanodomains, as well as B_2O_3. Ayala *et al.*[21a] observed the presence of a defined peak between 191.5 and 192.1 eV using XPS analysis in their B-doped SWCNTs. They suggested that the peak should be attributed to the substitutional configuration of B within the carbon nanotubes. The binding energy peak at 199 eV can be assigned to a 1s σ* resonance. The binding energy peak at 199 eV in boron-doped SWCNTs has been attributed to other crystalline phases containing boron as characterized by electron energy loss spectroscopy (EELS).[11] Similar binding energies in boron-doped tubes have been observed by Hashim *et al.*[39] at 202 eV by EELS analysis, at 197 eV,[38] 198 and 199.5 eV,[21a] by XPS analysis. They suggested that other boron-containing compounds were present in their boron-doped carbons.

Table 5.5: XPS binding energies and chemical composition of elements in B-MWCNTs grown at 800 °C.

Element	Atomic concentration (%)	Binding energy (eV)	Probable bonds
C	83.8	284.9 (85.8%) 286.4 (9.3%) 287.6 (1.4) 289.1 (3.5%)	C-C C-O C=O O-C=O
O	14.6	531.7 (5.5%) 532.5 (52.0%) 533.8 (42.5%)	C=O C-OH C-OH
B	1.6	192.2 199.0	Mixed B-C and B-O bonds in BCO_2; B_2O_3 1s σ* resonance

The C 1s spectrum (Figure S5) could be deconvoluted and gave 4 peaks corresponding to sp^2 C-C bonding (284.9 eV), and C-O and C=O bonding (286.4 to 289.1 eV).[35] No peak was observed at ~281 eV corresponding to a B-C bond,[21a] presumably due to the low boron concentration in our sample.[35] The O 1s spectrum (Figure S6) exhibited three peaks at ~531, 532 and 533 eV (see Table 5.5), that can be assigned to carbonyl oxygen atoms in esters and hydroxyls. The composition of oxygen from Table 5.5 is 14.6%. Usually, the elemental analysis and XPS data of undoped CNTs yield oxygen contents of 1-5%. Compared to the expected oxygen content in undoped CNTs, the amount of 14.6% can be accounted by the presence of boron oxides, which was also suggested by the B 1s spectrum.

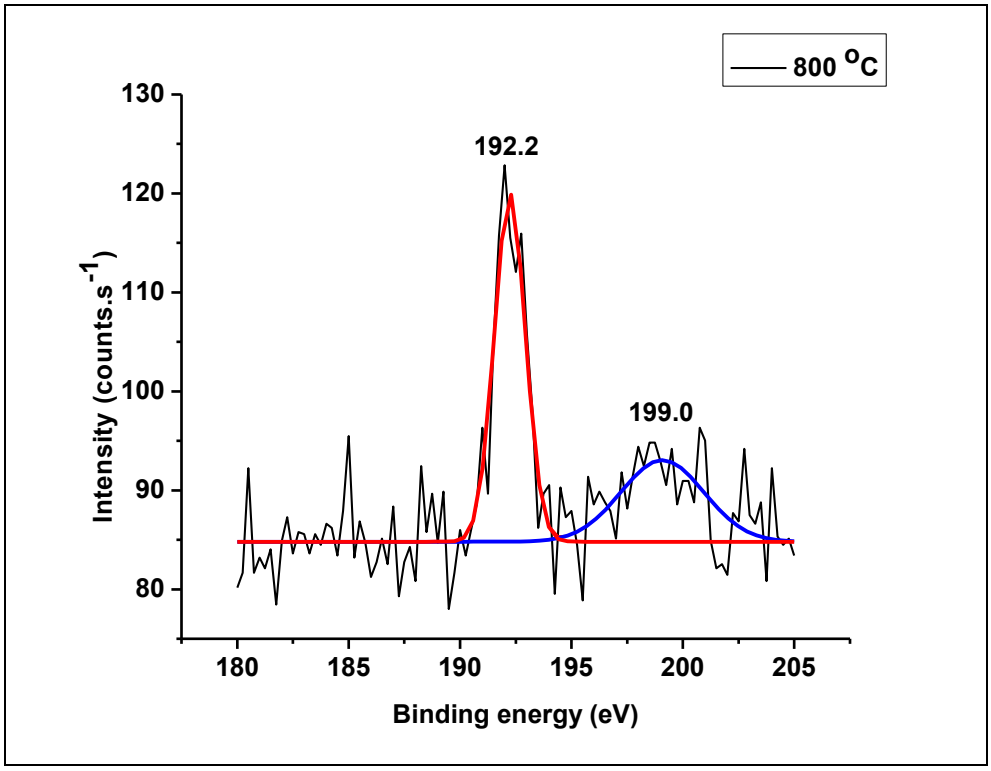


Figure 5.11b: Deconvoluted B 1s XPS spectra of the purified B-MWCNTs grown at 800 °C.

5.3.5 XRD, Raman spectroscopy and FT-IR spectroscopy analysis of the purified B-MWCNTs

In addition to chemical analysis, the phase content and the crystal structure of the B-doped MWCNTs were studied using XRD (Figures 5.12) as well by the Raman (Figure 5.14) and FT-IR spectroscopy (Figure 5.15). The XRD pattern (Figure 5.12) of the undoped CNTs revealed the presence of three peaks at 2θ values of 26.7, 43.3, 45.3° corresponding to (002), (100) and (101) planes of graphitic carbon. The diffraction patterns (Figure 5.12) of all B-doped MWCNTs exhibited more peaks in comparison to that of the undoped CNTs. The peaks at 25.8, 42.8 and 44.8° can be indexed as typical (002), (100) and (101) diffraction planes of hexagonal graphitic carbon, respectively. For the B-MWCNTs, the (002) peak downshifted to a lower 2θ angle of 25.8° compared to the undoped CNTs. In addition, the (002) peak corresponding to a interlayer spacing 0.34 nm of the nanotubes, is in good agreement with the literature on B-doped CNTs.[39] The downshifting of the (002) diffraction peak in B-doped MWCNTs is associated with the presence of boron within the lattice which is known to enhance crystallinity, as suggested by Hashim *et al.*[39] and others.[58]

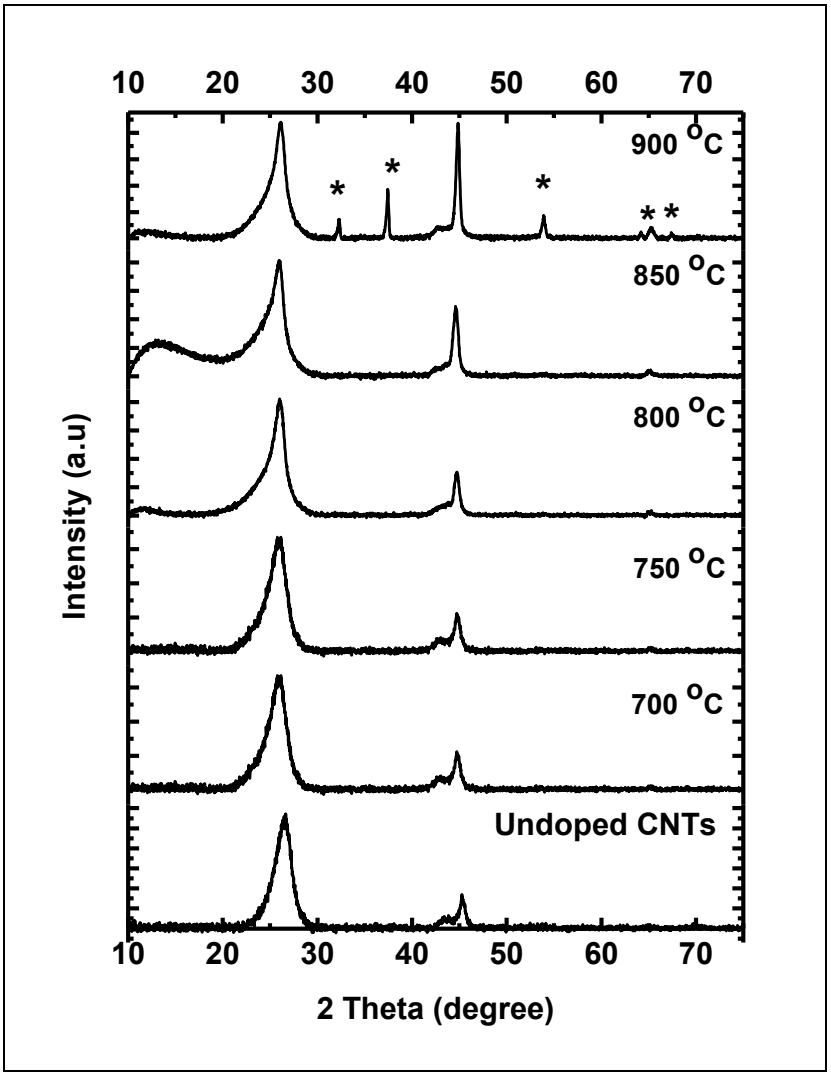


Figure 5.12: XRD spectra of the purified B-doped MWCNTs grown at 700-900 °C compared with undoped MWCNTs. The asterisks label the peaks associated with the metal catalyst.

The sharp graphitic peaks of the B-MWCNTs became more intense and broader from 700 to 900 °C, while the (100) peak became shallow with increasing growth temperature. The XRD patterns of the B-MWCNTs showed no evidence of the B_4C phases. Although no incorporation of boron was evidence (XRD patterns) in B-MWCNTs, the amount of boron present in the precursor ($(CH_3O)_3B$) clearly had an appreciable effect on the morphology of the MWCNTs, which was different from the undoped ones. In addition, the acid treated B-MWCNTs grown at 900 °C showed peaks (labelled with asterisks) which can be attributed to the residual metal catalyst (see below for further discussion). This observation is in good agreement with the TGA, TEM and EDX data reported earlier.

Figure S7 and S8 give the XRD spectra of the B-MWCNTs synthesized at 850 °C and 900 °C, respectively, before and after purification. The XRD patterns of the unpurified B-MWCNTs (Figure S7A) synthesized at 850 °C showed the presence of the metal particles originating from the Fe-Co/$CaCO_3$ catalyst, while the purified sample (Figure S7B) showed the presence of few peaks corresponding to metal particles, implying that most of the catalyst was removed after purification. The unpurified B-MWCNTs made at 900 °C revealed the XRD peaks (Figure S8A) related to Fe-Co/$CaCO_3$ catalyst. There was evidence from the XRD patterns (Figure S8B) of the B-MWCNTs produced at 900 °C that acid treatment was unable to remove all the catalyst particles, as also evidenced by TEM and EDX studies. At both 850 and 900 °C, the XRD data also revealed that the graphitic peaks in the unpurified samples were very weak but were greatly enhanced after purification, while the peak intensities corresponding to the catalyst particles decreased after purification (e.g. Figure S8B).

Figure 5.13 compares the XRD patterns of the boric acid and CSs formed at 900 °C. The sharp diffraction peaks indicated by the asterisks can be attributed to the crystalline phase of B_2O_3 in the CSs. XRD data suggest that B_2O_3 was incorporated into the CSs, which is consistent with the TGA results. No diffraction peaks due to boron carbides (B_4C) were observed. The broad peak at ~25.4° in the CSs can be indexed to a (002) reflection similar to the graphite characteristic peak (26.5°), while the low intensity peak at 44.6° can be ascribed to the (100) reflection. The broader (002) peak indicated a low degree of graphitization and that the structure of the CSs is amorphous. It can be observed that the (002) peak shifted to a lower angle (25.4°) for the CSs than for the graphite characteristic peak (26.5°). This result may be due to the effect of B_2O_3 incorporation into the CSs.

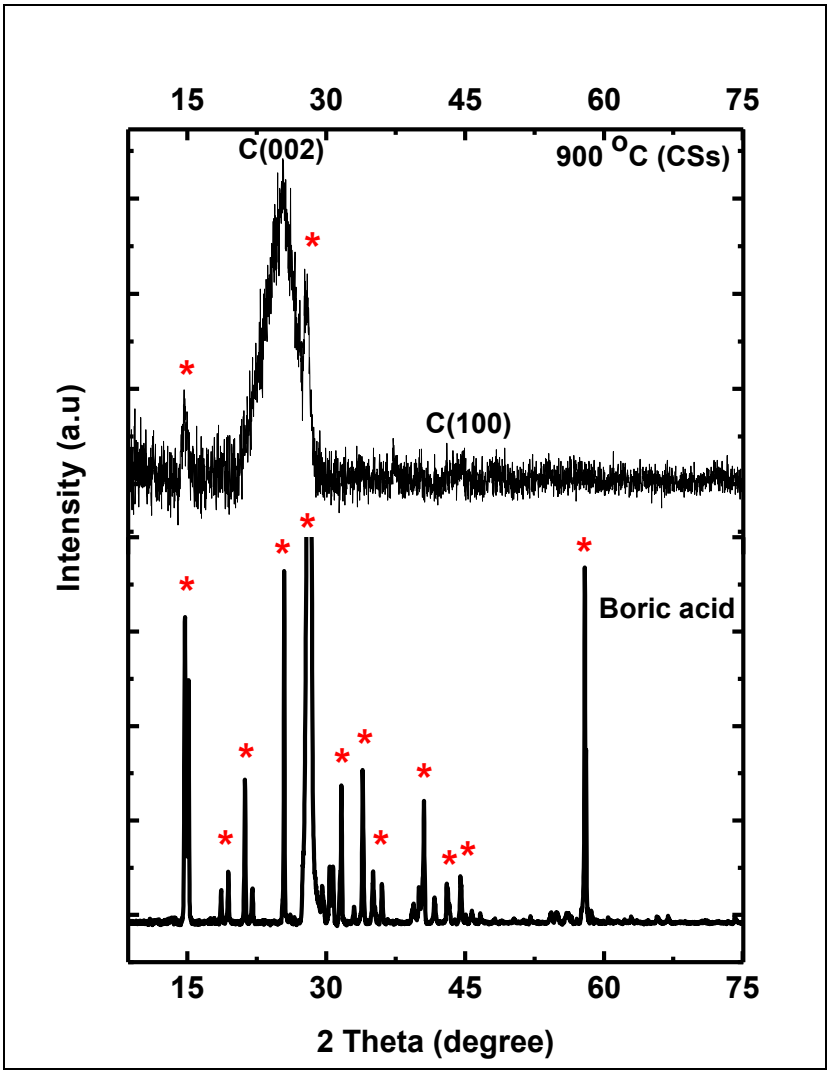


Figure 5.13: XRD spectra of the solid and core-shell carbon spheres formed at 900 °C compared with boric acid. All peaks labelled with asterisks can be indexed as B_2O_3.

FT-IR spectra of the undoped and purified B-doped MWCNTs are shown in Figure 5.14 and are compared with boric acid. The FT-IR bands labelled in the spectrum of the boric acid were assigned as shown in Table 5.6. These positions correspond with the FT-IR bands of boric acid reported by Andrews *et al.*[59] and others.[60] Figure 5.14 reveals two bands at 1020 and 1055 cm^{-1} (the highlighted region) in the boric acid and the B-doped MWCNTs synthesized at 800, 850 and 900 °C, which are not observed in the undoped MWCNTs and B-doped MWCNTs synthesized at 700 and 750 °C. The FT-IR results further confirmed B-O incorporation into the CNTs at 800-900 °C. The presence of these bands can also be associated with doping of CNTs with boron substitution in the carbon network. It has been reported that the C-B band usually occurs at 1050-1200 cm^{-1}.[34] In their B-substituted

SWCNTs, Borowiak-Palen *et al.*[32] observed peaks at 807, 1050 and 1385 cm^{-1}. They assigned the peak at 1050 cm^{-1} to typical boron carbide related phonons. On the other hand, Oki *et al.*[61] reported on the FT-IR spectrum of a CNT-B_2O_3 nanocomposite material, which showed B_2O_3 characteristic peaks at 1458, 1195 and 798 cm^{-1}. Côté *et al.*[62] also reported the FT-IR spectrum of B-C bonds at 1026 cm^{-1}. Following the literature data, we assign the peaks at 1020 and 1055 cm^{-1} of the B-MWCNTs synthesized at 800-850 °C to a mixture of B-O and B-C bands. The weakness of these peaks in the samples synthesized at 700 and 750 °C is a sign of very little boron incorporation in the CNTs at these growth temperatures. The IR bands at ~2330-1995 cm^{-1} found in all B-CNTs but absent in the boric acid spectrum, can be attributed to CO_2.

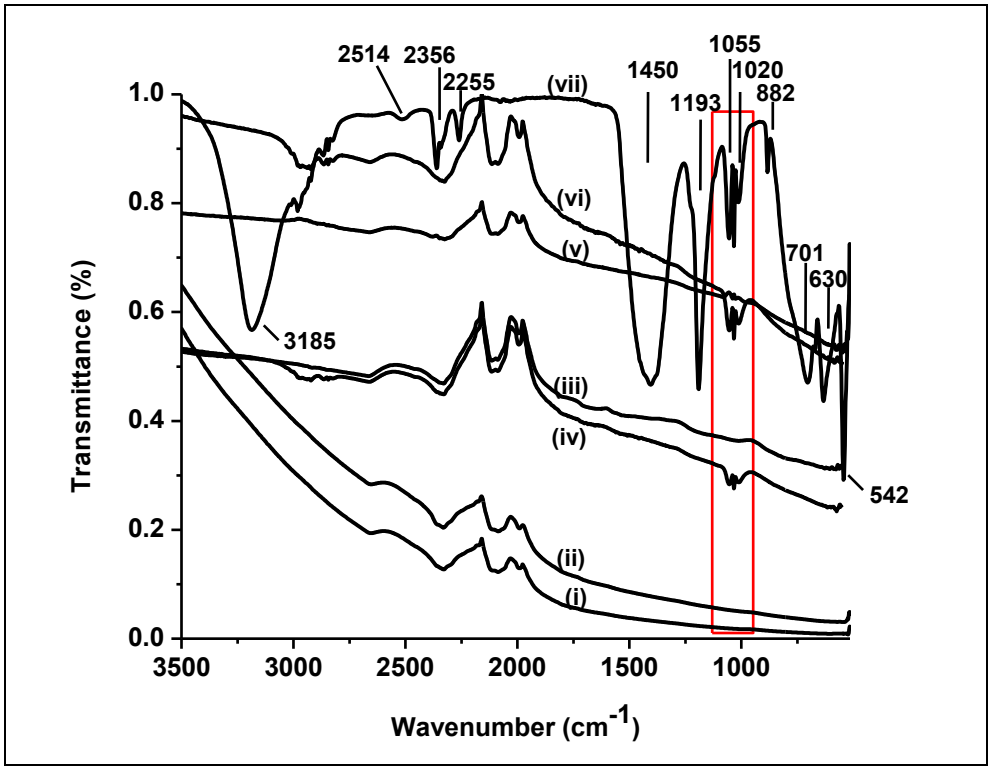


Figure 5.14: FT-IR spectra of the undoped and B-doped MWCNTs grown at 700-900 °C compared with boric acid. (i) undoped CNTs; B-doped MWCNTs grown at (ii) 700 °C, (iii) 750 °C, (iv) 800 °C, (v) 850 °C and (vi) 900 °C; (vii) boric acid.

Figure S9 compares the FT-IR spectra of the boron-containing CSs formed at 900 °C and boric acid. As can be seen, the FT-IR spectrum of the CSs demonstrates the presence of most IR bands found in boric acid, which imply B_2O_3 incorporation into the CSs. These results are consistent with TGA and XRD results of the B-containing CSs.

Table 5.6: Wavenumbers and assignment of Infrared Absorption bands for boric acid.

Position (cm^{-1})	**Assignment**	**Reference**
549	O-B-O bending	[60c]
630	Symmetric BO_3 deformation	[60(a-d)]
701	Symmetric BO_3 deformation	[60c]
882	Symmetric B-O stretching vibrations	[60(a-d)]
1055 and 1020	B-O-H bending	[59]
1193	Asymmetric B-O-H bending	[60(a-d)]
1450	Asymmetric B-O stretching vibration	[60(a-d)]
2255, 2356, 2514	Overtone bands involving B-O bending and stretching vibrations	[60c]
3270 s	Symmetric O-H stretching vibration	[60(a-d)]

Raman spectra of the purified undoped and boron-doped MWCNTs are given in Figure 5.15. Three peaks were clearly identified at ~1350 cm^{-1} (D-band), ~1592 cm^{-1} (G-band) and ~2695 cm^{-1} (2D-band) in all CNT samples that were analysed. The D-band is a typical sign of impurities and defective graphitic structures. The G-band is a characteristic feature of the graphitic layers and is derived from the carbon-carbon stretching mode due to the tangential vibration of carbon. The peak at ~2695 cm^{-1} is called the 2D peak (also called G´), and is an overtone (second-order) D peak.[63] The D to G peak intensity ratio (I_D/I_G) is often used as the measure of the amount of defects and disorder in carbon nanomaterials. Table 5.7 lists the D-, G-, 2D-band values and I_D/I_G ratios of the purified undoped and B-doped MWCNTs. Compared to the undoped MWCNTs, the D and the G band of the B-MWCNTs down shifted. The Raman spectra indicated that the B-doped MWCNTs showed higher D-band intensities than G-band intensities and the D-band intensities became wider and decreased with increasing growth temperature due to structural defects formed by the presence of boron in the hexagonal carbon network.[39] The I_D/I_G ratio decreased with increasing growth

temperature from 700-800 °C but increased at 850-900 °C. Interestingly, the sample prepared at 800 °C had the lowest I_D/I_G ratio, indicating low defects and improved crystallinity. The high I_D/I_G ratios in the B-MWCNTs were associated with defects caused by the very rough surface CNTs at 700-750 °C and a variety of disordered shaped carbon nanostructures and catalyst impurities at 850-900 °C. These results indicate that the B-MWCNTs were abundant with disordered structures caused by boron-doping, and it shows that the graphitic degree of these carbon materials decreases with increase in reaction temperature.

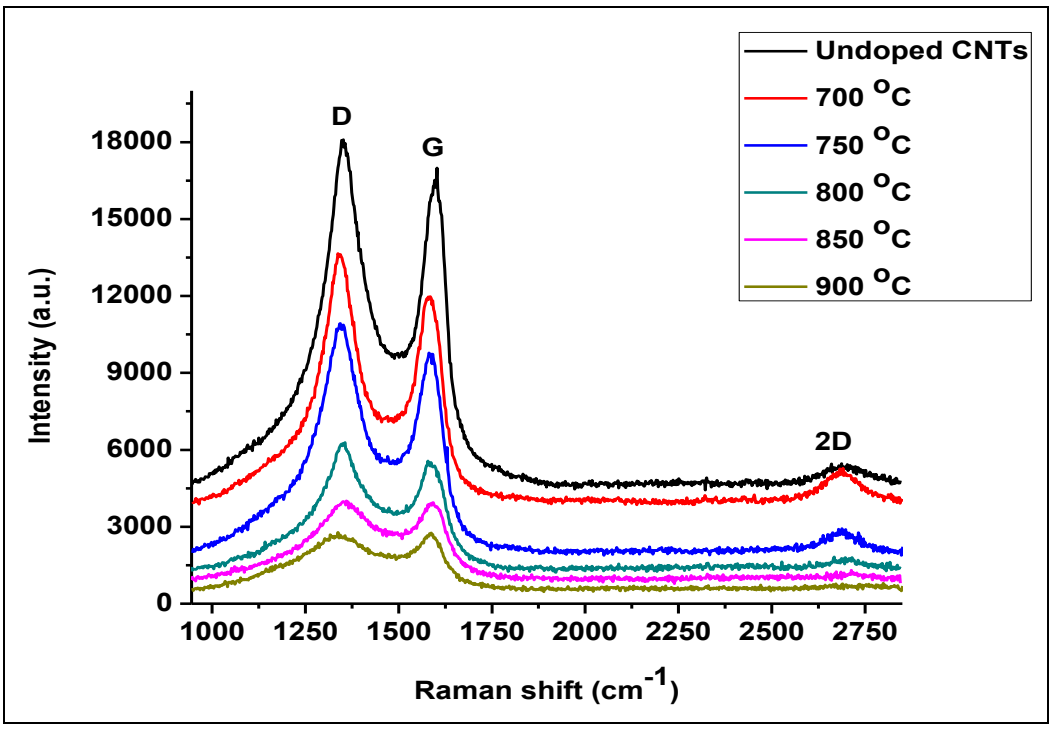


Figure 5.15: Raman spectra of the purified B-doped MWCNTs grown at 700-900°C compared with undoped MWCNTs.

The intensity of the 2D-band decreased as the reaction temperature increased from 700-900 °C. In their study of boron-doped double walled CNTs, Lyu *et al.*[35] established that the intensity of the 2D-band (or G´-band) decreased as the triisopropyl borate concentration increased from 0 to 2.5 M, respectively. They suggested that their results may be due to the combination of the weaker B-C bonding compared to the C-C bonding energies. The Raman spectroscopy data suggest that boron incorporation in our B-doped MWCNTs increased as the reaction temperature increased. Figure S10 depicts the Raman spectra of the CSs formed at 900 °C compared with boric acid. The CSs have two characteristic Raman bands at 1347 and 1591 cm^{-1}, corresponding to D- and G- modes of graphite carbon. The I_D/I_G value of 1.58

for the CSs (Table 5.7) suggests structural defects and disordered graphitic layers in the sample. As can be seen, there is a shoulder in the spectra of the CSs which coincides with the presence of boric acid at 1166 cm^{-1}. This result further confirmed the presence of B_2O_3 in the CSs. This conclusion is supported by the TGA, XRD and FT-IR spectroscopy studies which are reported earlier.

Table 5.7: The D-, G-bands and I_D/I_G ratios of the purified undoped and B-doped MWCNTs.

Temperature (°C)	D-band (cm^{-1})	G-band (cm^{-1})	I_D/I_G ratio	2D-band (cm^{-1})
Undoped CNTs	1353	1598	1.22	2695
700	1343	1578	1.49	2686
750	1346	1588	1.33	2685
800	1350	1592	1.08	2695
850	1356	1596	1.37	2697
900[a]	1339	1590	1.64	2689
900[b]	1347	1591	1.58	2699

[a] Carbon material collected from the quartz boat, [b] CSs collected from the wall of the quartz tube after the end of the high temperature region.

5.4 Conclusions

In summary, boron-doped multiwalled carbon nanotubes have been successfully synthesized from C_2H_2 (carbon source), $(CH_3O)_3B$ (carbon and boron source), and Fe-Co/$CaCO_3$ catalyst by a CVD method at 700-900 °C. In this study, various multiwalled carbon nanotubes synthesized included distorted and bamboo-shaped nanotubes, catalyst filled tubes with bulbous-shaped catalysts as well as solid and core-shell carbon spheres. The addition of the boron source generates tubes that have larger diameters and a different morphology than produced without a boron source. It was found that the growth temperature played an important role in determining the morphology of the carbon structures and $T \leq 800$ °C was optimal for the synthesis of only MWCNTs. Based on the TEM images (which showed only CNTs), XRD, XPS and FT-IR data which evidenced boron doping; the best synthesis temperature to produce clean B-MWCNTs is 800 °C. The MWCNTs at 800 °C growth temperature were doped with boron up to 1.6 at.%, as confirmed by XPS analysis. TEM data and Raman spectroscopy confirmed that the B-doped MWCNTs contain a large number of

defects. Our study has shown that boron-doping and growth temperature significantly alters the morphology of CNTs, typically leading to rough surfaces and bamboo-like structures that contain regularly arranged compartments with a hollow channel. This approach is expected to provide a new route for the synthesis of boron-doped MWCNTs and boron-doped CSs, the physical properties which are of great interest. These materials can be suitable as supports for metals in catalysis.

References

1. S. Iijima, *Nature*, 1991, **354**, 56-58.
2. O. Stephan, P.M. Ajayan, C. Colliex, P. Redlich, J.M. Lambert, P. Bernier and P. Lefin, *Science*, 1994, **266**, 1683-1685.
3. Z. Wengsieh, K. Cherrey, N.G. Chopra, X. Blasé, Y. Miyamoto, A. Rubio, M.L. Cohen, S.G. Louie, A. Zettl and, A.R. Gronsky, *Phys. Rev. B*, 1995, **51**, 11229-11232.
4. Y. Zhang, H. Gu, K. Suenaga and S. Iijima, *Chem. Phys. Lett.*, 1997, **279**, 264-269.
5. M. Terrones, *Chem. Phys. Lett.*, 1996, **257**, 576-582.
6. (a) D. Golberg, Y. Bando, W. Han, K. Kurashima and T. Sato, *Chem. Phys. Lett.*, 1999, **308**, 337-342; (b) W.K. Hsu, S.Y. Chu, E. Munoz-Picone, J.L. Boldu, S. Firth, P. Franchi, B. Roberts, A. Schilder, H. Terrones, N. Grobert, Y.Q. Zhu, M. Terrones, M.E. McHenry, H.W. Kroto and D.R.M. Walton, *Chem. Phys. Lett.*, 2000, **323**, 572-579.
7. X. Blasé, J.C. Charlier, A.D. Vita and R. Car, *Phys. Rev. Lett.*, 1999, **83**, 5078-5081.
8. A. Agarwal, H. Yinnon, D.R. Uhlmann, R.T. Pepper and C.R. Desper, J. *Mater. Sci.*, 1986, **21**, 3455-3466.
9. M. Endo, H. Muramatsu, T. Hayashi, Y. A. Kim, G. Van Lier, J.C. Charlier, H. Terrones, M. Terrones and M.S. Dresselhaus, *Nano Lett.*, 2005, **5**, 1099-1105.
10. W.H. Moon and H.J. Hwang, *Physica E*, 2005, **28**, 419-422.
11. J.L. Blackburn, Y. Yan, C. Engtrakul, P.A. Parilla, K. Jones, T. Gennett, A.C. Dillon and M.J. Heben, *Chem. Mater.*, 2006, **18**, 2558-2566.
12. D. Golberg, Y. Bando, K. Kurashima and T. Sato, *Diam. Relat. Struct.*, 2001, **10**, 63-67.
13. D.L. Carroll, Ph. Redlich, X. Blase, J.-C. Charlier, S. Curran, P.M. Ajayan, S. Roth, and M. Ruhle, *Phys. Rev. Lett.*, 1998, **81**, 2332-2335.
14. J. Maultzsch, S. Reich, C. Thomsen, S. Webster, R. Czerw, D.L. Carroll, S.M.C. Vieira, P.R. Birkett and C.A. Rego, *Appl. Phys. Lett*., 2002, **81**, 2647-2649.
15. K. McGuire, N. Gothard, P.L. Gai, M. S Dresselhaus, G. Sumanasekera and A.M. Rao, *Carbon*, 2005, **43**, 219-227.
16. P.L. Gai, O. Stephan, K. McGuire, A.M. Rao, M.S. Dresselhaus, G. Dresselhaus and C. Colliex, *J. Mater. Chem.*, 2004, **14**, 669-675.
17. B.C. Satishkumar, A. Govindaraj, K.R. Harikumar, J.-P. Zhang, A.K. Cheetham and C.N.R. Rao, *Chem. Phys. Lett.*, 1999, **300**, 473-477.

18. H.J. Ceragioli, A.C. Peterlevits, J.C.R. Quispe, A. Larena, M.P. Pasquetto, M.A. Sampaio and V. Baranauskas, *J. Phys.: Conf. Ser.*, 2008, **100**, 052029/1-052029/4.
19. J.-H. Kang, H.C. Jang, J.M. Choi, S.C. Lyu and J.H. Sok, *Journal of Magnetics*, 2012, **17**, 9-12.
20. S. Suzuki and H. Hibino, *Carbon*, 2011, **49**, 2264-2272.
21. (a) P. Ayala, W. Plank, A. Grüneis, E. I. Kauppinen, M.H. Rümmeli, H. Kuzmany and T. Pichler, *J. Mater. Chem.*, 2008, **18**, 5676-5681; (b) S. Daothong, J. Parjanne, E.I. Kauppinen, M. Valkeapää, T. Pichler, P. Singjai and P. Ayala, *Phys. Status Solidi B*, 2009, **246**, 2518-2522.
22. Ph. Redlich, M.J. Loeffler, P.M. Ajayan, J. Bill, F. Aldinger and M. Rühle, *Chem. Phys. Lett.*, 1996, **260**, 465-470.
23. M. Terrones, W.K. Hsu, S. Ramos, R. Castillo and H. Terrones, *Fullerene Sci. Technol.*, 1998, **6**, 787-800.
24. W.K. Hsu, S. Firth, P. Redlich, M. Terrones, H. Terrones, Y.Q. Zhu, N. Grobert, A. Schilder, R.J.H. Clark, H.W. Kroto and D.R.M. Walton, *J. Mater. Chem.*, 2000, **10**, 1425-1429.
25. K.C. Mondal, N.J. Coville, M.J. Witcomb, G. Tejral and J. Havel, *Chem. Phys. Lett.*, 2007, **437**, 87-91.
26. C.F. Chen, C.L. Tsai and C.L. Lin, *Diam. Rel. Mater.*, 2003, **12**, 1500-1504.
27. L.S. Panchakarla, A. Govindaraj, and C.N.R. Rao, *ACS Nano*, 2007, **1**, 494-500.
28. K. Hirahara, K. Suenaga, S. Bandow and S. Iijima, *Chem. Phys. Lett.*, 2000, **324,** 224-230.
29. L.-J. Li, M. Glerup, A.N. Khlobystov, J.G. Wiltshire, J.-L. Sauvajo, R.A. Taylor and R.J. Nicholas, *Carbon*, 2006, **44**, 2752-2757.
30. N.R. Arutyunyan, R. Arenal, E.D. Obraztsova, O. Stephan, A. Loiseau, A.S. Pozharov and V.V. Grebenyukov, *Carbon*, 2012, **50**, 791-799.
31. W. Han, Y. Bando, K. Kurashima and T. Sato, *Chem. Phys. Lett.*, 1999, **299**, 368-373.
32. E. Borowiak-Palen, T. Pichler, G.G. Fuentes, A. Graff, R.J. Kalenczuk, M. Knupfer and J. Fink, *Chem. Phys. Lett.*, 2003, **378,** 516-520.
33. Q. Jiang, L. Qian, J. Yi, X. Zhu and Y. Zhao, *Front. Mater. Sci. China*, 2007, **1**, 379-382.
34. M. Sankaran and B. Viswanathan, *Carbon*, 2007, **45**, 1628-1635.
35. S.C. Lyu, J.H. Han, K.W. Shin and J.H. Sok, *Carbon*, **49**, 2011, 1532-1541.

36. L. Yang, S. Jiang, Y. Zhao, L. Zhu, S. Chen, X. Wang, Q. Wu, J. Ma, Y. Ma and Z. Hu, *Angew. Chem. Int. Ed.*, 2011, **50**, 7132-7135.
37. V. Saini. Z. Li, S. Bourdo, V.P. Kunets, S. Trgwell, A. Couraud, J. Rioux, C. Boyer, V. Nteziyaremye, E. Dervishi, A.R. Biris, G.J. Salamo, T. Viswanathan and A.S. Biris, *J. Appl. Phys.*, 2011, **109**, 014321/1-014321/6.
38. M. Bystrzejewski, A. Bachmatiuk, J. Thomas, P. Ayala, J. Serwatowski, H.-W. Hübers, T. Gemming, E. Borowiak-Palen, T. Pichler, R.J. Kaleńczuk, B. Büchner and M.H. Rümmeli, *Phys. Status Solidi RRL*, 2009, **3**, 193-195.
39. D.P. Hashim, N.T. Narayanan, J.M. Romo-Herrera, D.A. Cullen, M.G. Hahm, Peter Lezzi, J.R. Suttle, D. Kelkhoff, E. Muñoz-Sandoval, S. Ganguli, A.K. Roy, D.J. Smith, R. Vajtai, B.G. Sumpter, V. Meunier, H. Terrones, M. Mauricio, Terrones and P.M. Ajayan, *Sci. Rep.*, 2012, **2**, 363/1-363/8.
40. A.A. Koós, F. Dillon, E.A. Obraztsova, A. Crossley, N. Grobert, *Carbon*, 2010, **48**, 3033-3041.
41. W.-Q. Han, J. Cumings, X. Huang, K. Bradley, A. Zettl, Chem. Phys. Lett., 2001, **346**, 368-372.
42. S. Ishii, T. Watanabe, S. Ueda, S. Tsuda, T. Yamaguchi and Y. Takano, *Physica C*, 2008, **468**, 1210-1213.
43. E. Iyyamperumal, S. Wang and L. Dai, *ACS Nano*, 2012, **6**, 5259-5265.
44. R.Z. Ma, Y. Bando and T. Sato, *Chem. Phys. Lett.*, 2001, **337**, 61-64.
45. Z.N. Tetana, S.D. Mhlanga, G. Bepete, R.W.M. Krause and N.J. Coville, *S. Afr. J. Chem.*, 2012, **65**, 39-49.
46. S.D. Mhlanga, K.C. Mondal, R. Carter, M.J. Witcomb and N.J. Coville, *S. Afr. J. Chem.*, 2009, **62**, 67-76.
47. L.F. Giraldo, B. L. López and W. Brostow, *Polym. Eng. Sci.*, 2009, **49**, 896-902.
48. P. Piedigrosso, Z. Konya, J.-F. Colomer, A. Fonseca, G. van Tendeloo and J.B. Nagy, *Phys. Chem. Chem. Phys.*, 2000, **2**, 163-170.
49. E.N. Nxumalo, P.J. Letsoalo, L.M. Cele and N.J. Coville, *J. Organomet. Chem.*, 2010, **695**, 2596-2602.
50. Z.N. Tetana, S.D. Mhlanga, R.W.M. Krause and N.J. Coville, Synthesis of B-doped core-shell carbon spheres, *to be published*
51. D. Sebastian, I. Suelves, M.J. Lazaro and R. Moliner, *J. Power Sources*, 2009, **192**, 51-56.
52. S.D. Mhlanga and N.J. Coville, *J. Nanosci. Nanotechnol.*, 2010, **10**, 5027-5035.

53. C. Nyambo, E. Kandare and C.A. Wilkie, *Polym. Degrad. Stab.*, 2009, **94**, 513-520.
54. W. Cermignani, T.E. Paulson, C. Onneby and C.G. Pantano, *Carbon*, 1995, **33**, 367-374.
55. Y. Liu, L. Zhang, L. Cheng, W. Yang and Y. Xu, *J. Ceram. Process. Res.*, 2009, **10**, 257-262.
56. S. Jacques, A. Guette, X. Bourrat, F. Langlais, C. Guimon and C. Labrugere, *Carbon*, 1996, **34**, 1135-1143.
57. P. Ayala, J. Reppert, M. Grobosch, M. Knupfer, T. Pichler, and A.M. Rao, *Appl. Phys. Lett.*, 2010, **96**, 183110-183113.
58. M. Terrones, N. Grobert and H. Terrones, *Carbon*, 2002, **40**, 1665-1684.
59. L. Andrews and T.R. Burkholder, *J. Phys. Chem.*, 1992, **97**, 7203-7210.
60. (a) E. F. Medvedev and A. Sh. Komarevskaya, *Glass Ceram.*, 2007, **64**, 42-46; (b) R.E. Zeebe, *Geochim. Cosmochim. Acta*, 2005, **69**, 2753-2766; (c) J.P. Parsons and M.E. Milberg, *J. Am. Ceram. Soc.*, 1960, **43**, 326-330; (d) S. Mondal and A.K. Banthia, *J. Eur. Ceram. Soc.*, 2005, **25**, 287-29.
61. A. Oki, L. Adams and Z. Luo, *Inorg. Chem. Commun.*, 2008, **11**, 275-278.
62. A.P. Côté, A.I. Benin, N.W. Ockwig, M. O'Keeffe, A.J. Matzger and O.M. Yaghi, *Science*, **310**, 1166-1170.
63. A.C. Ferrrari, J.C. Meyer, V. Scardaci, C. Casiraghi, M. Lazzeri, F. Mauri, S. Piscanec, D. Jiang, K.S. Novoselov, S. Roth and A.K. Geim, *Phys. Rev. Lett.*, 2006, **97**, 187401-187403.

Appendix C: Supplementary material

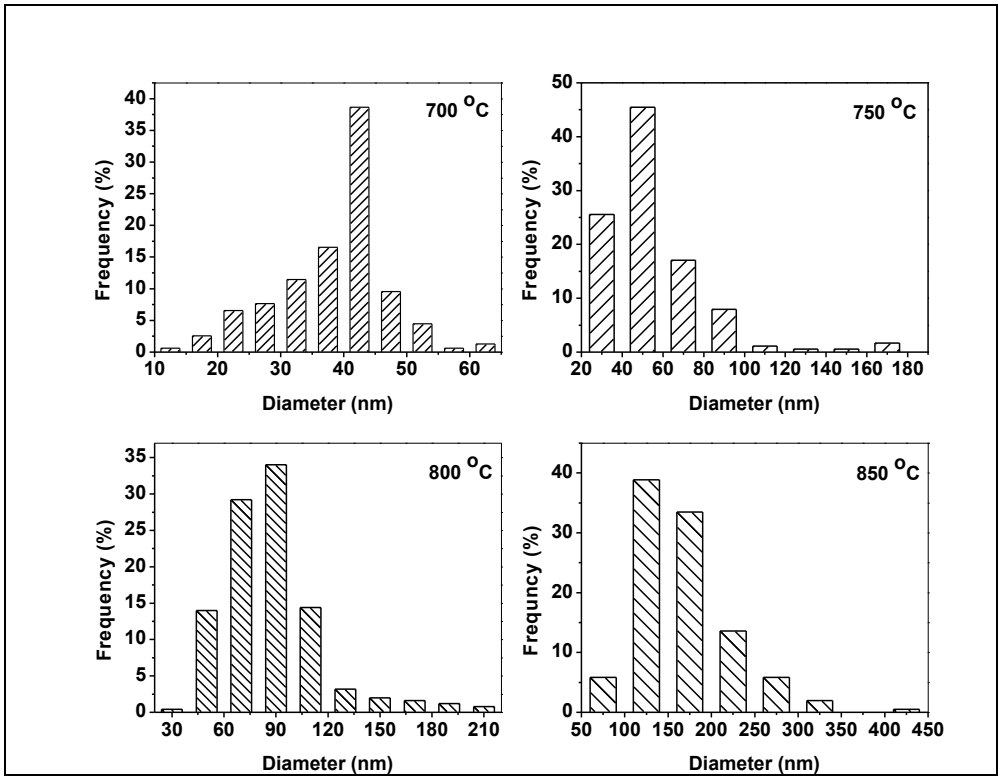


Figure S1: Diameter distributions of the purified B-MWCNTs grown at 700-850 °C.

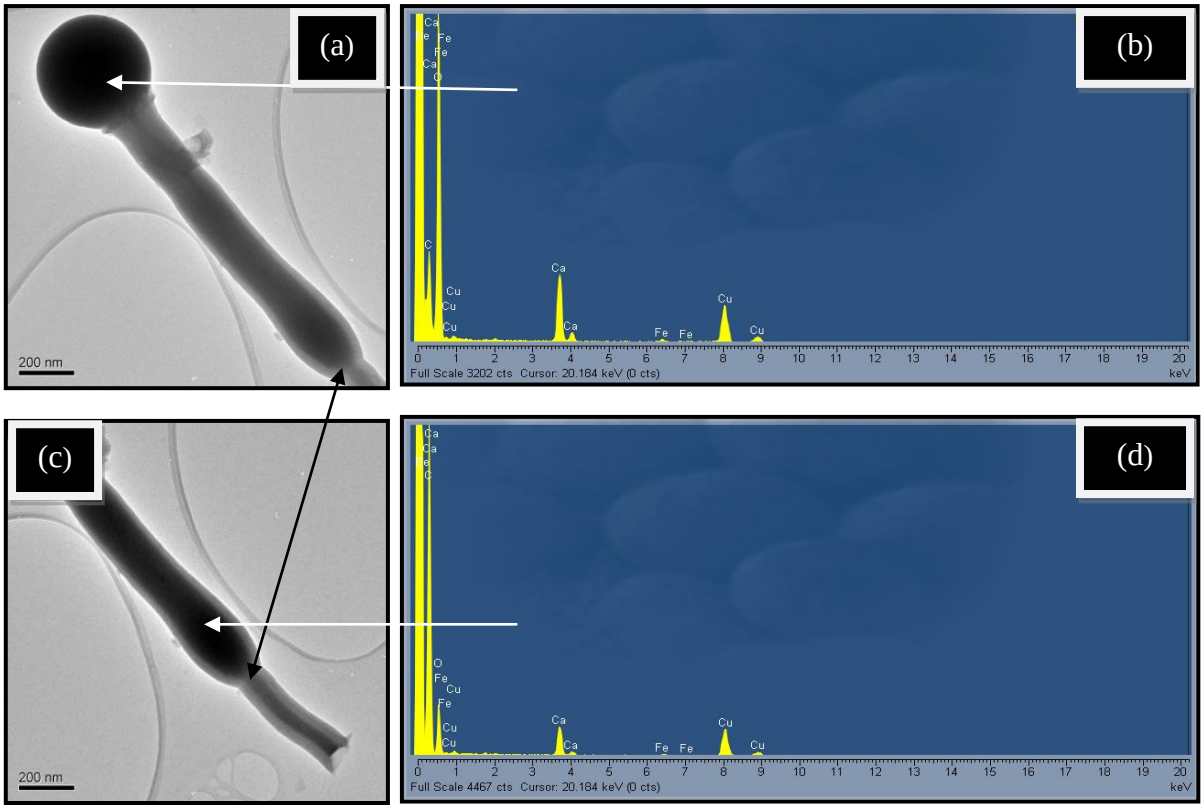


Figure S2: TEM images (taken at different magnifications) of the unpurified carbon materials grown at 900 °C: (a) catalyst filled tube with bulbous-shaped catalyst; (b) the corresponding EDX spectrum of the bulbous area in (a); (c) catalyst filled tube with open end showing the entire image of (a); (d) the corresponding EDX spectrum of the catalyst particles in (c). The white arrows indicate points where the corresponding EDX spectrum was collected.

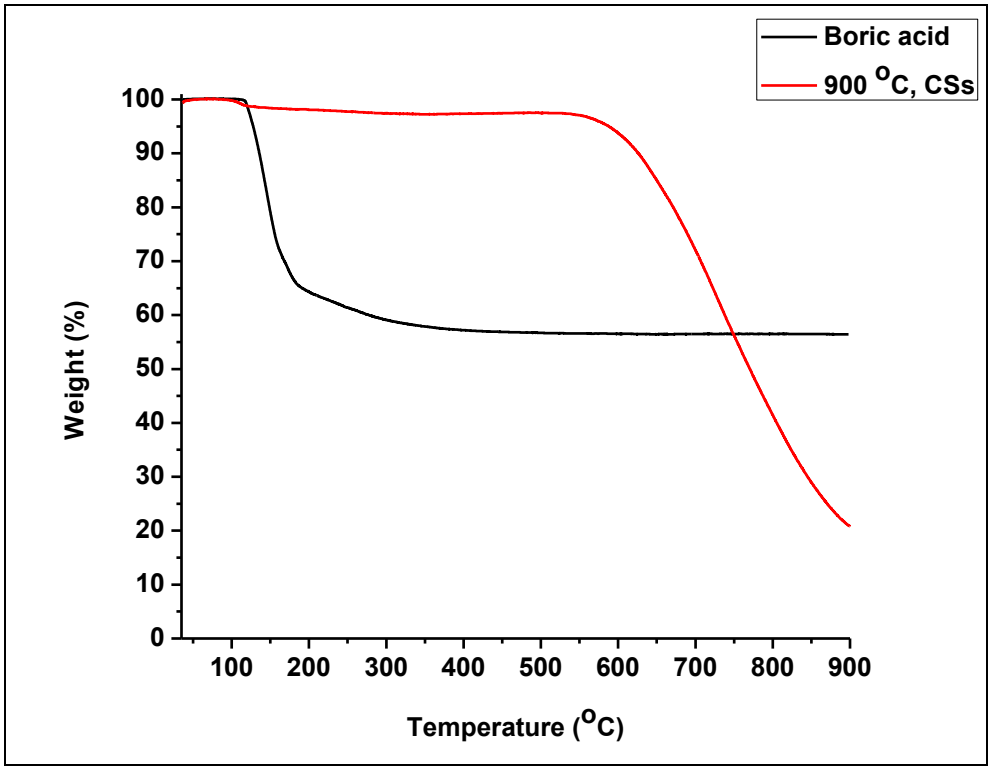


Figure S3: TGA curves of boric acid and CSs formed at 900 °C.

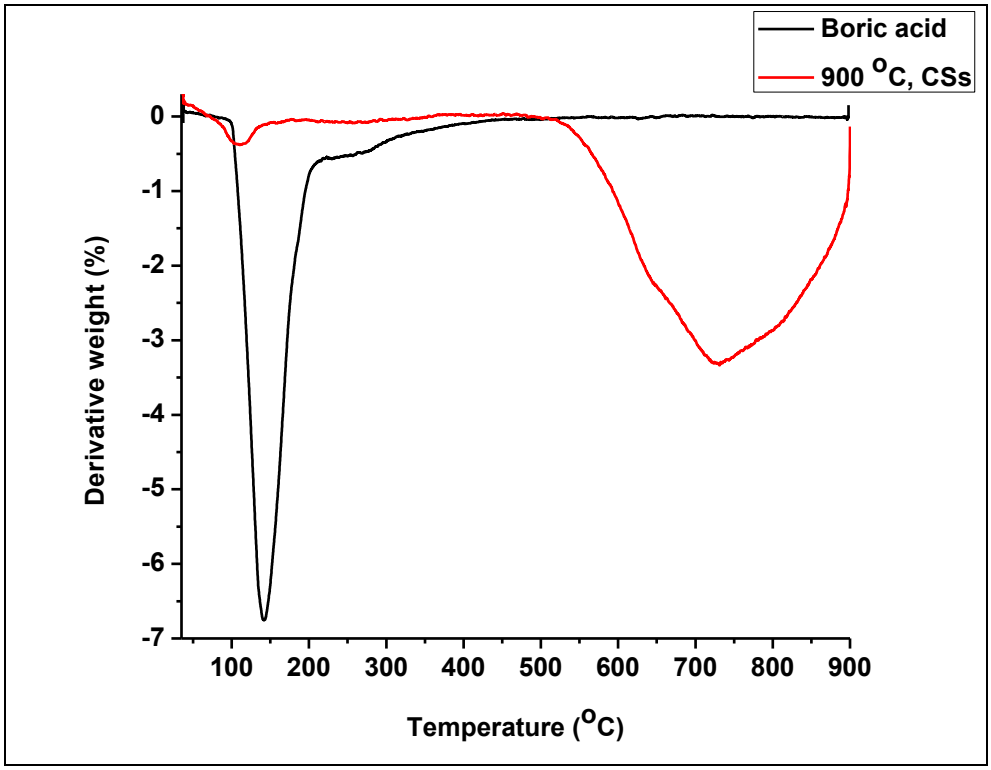


Figure S4: TGA derivative curves of boric acid and CSs formed at 900 °C.

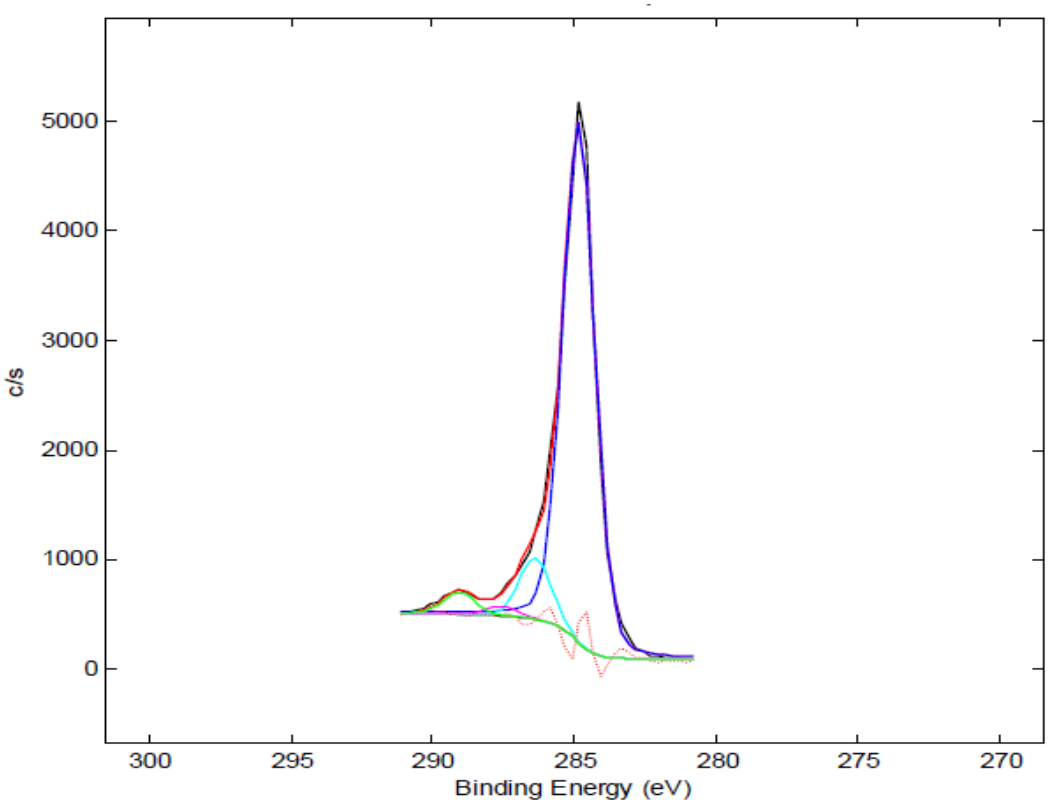


Figure S5: Deconvoluted C 1s XPS spectrum of B-doped MWCNTs synthesized at 800 °C

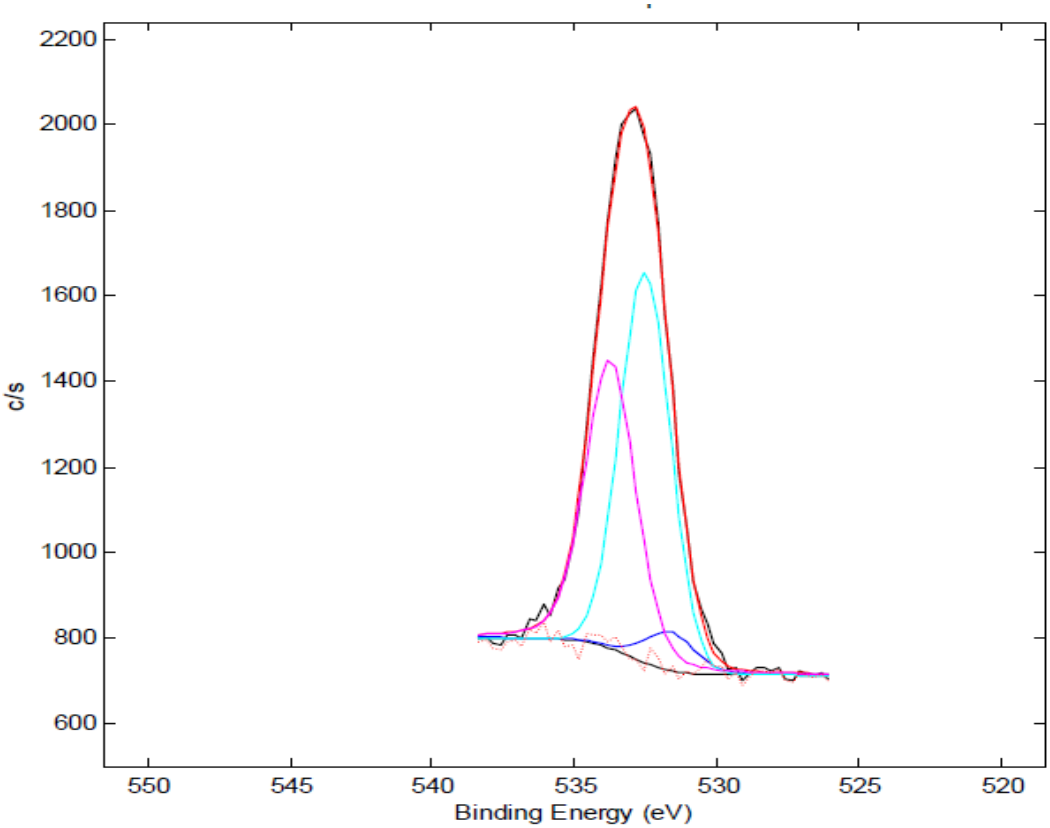


Figure S6: Deconvoluted O 1s XPS spectrum of B-doped MWCNTs synthesized at 800 °C.

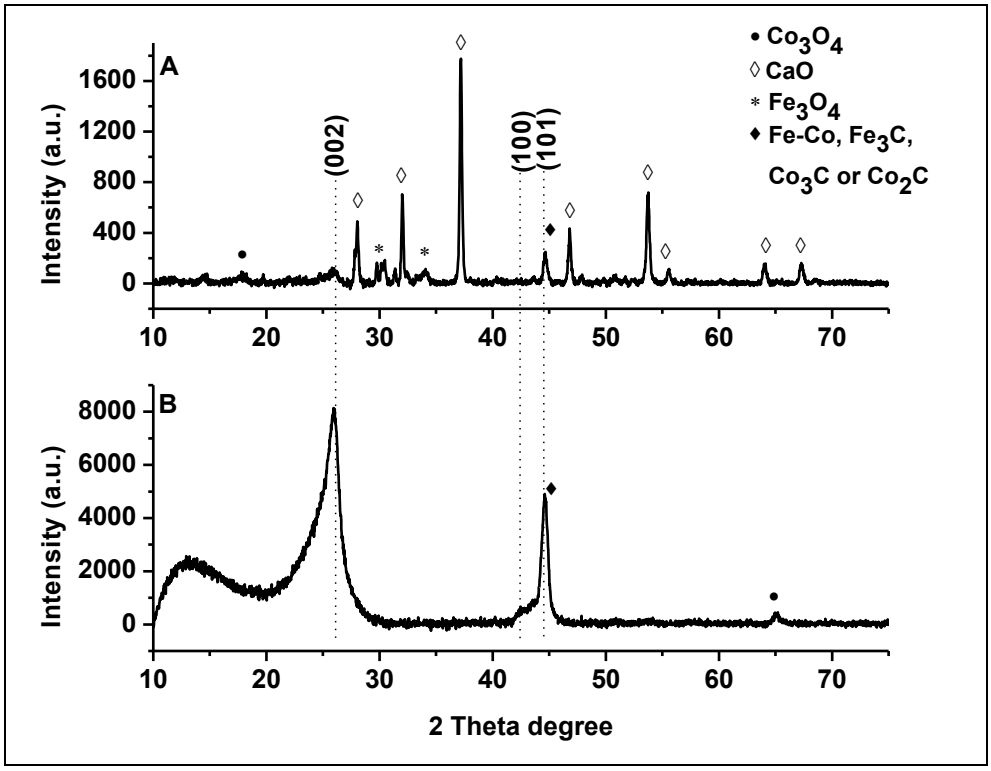


Figure S7: XRD patterns of the B-CNTs grown at 850 °C: A before and B after purification.

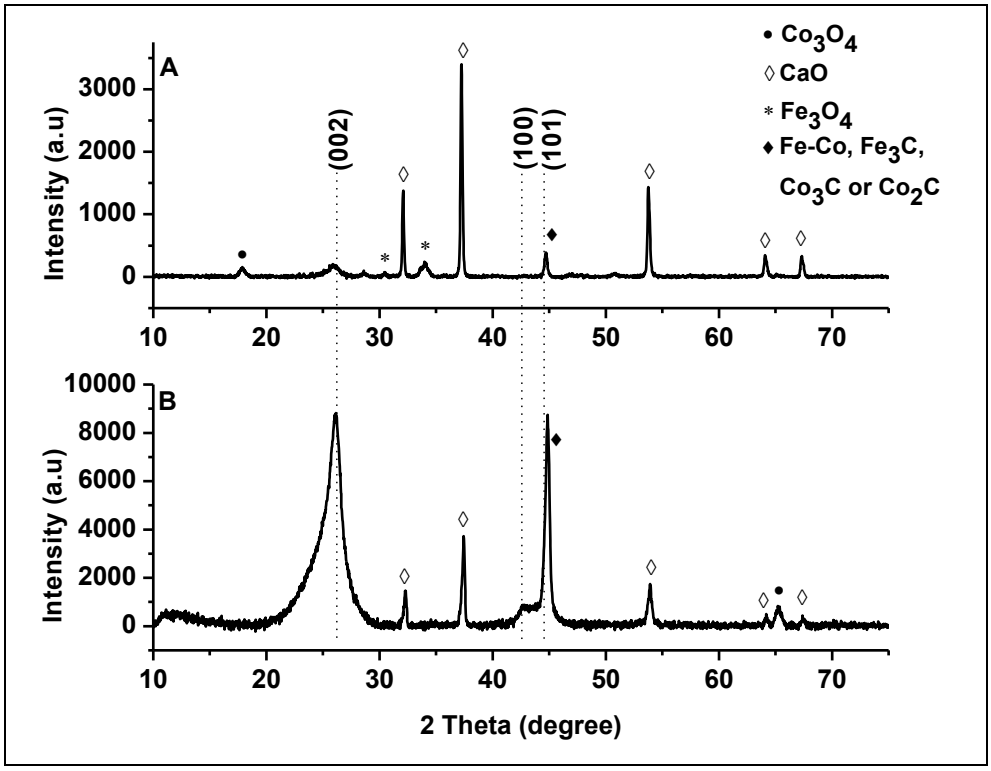


Figure S8: XRD patterns of the B-CNTs grown at 900 °C: A before and B after purification.

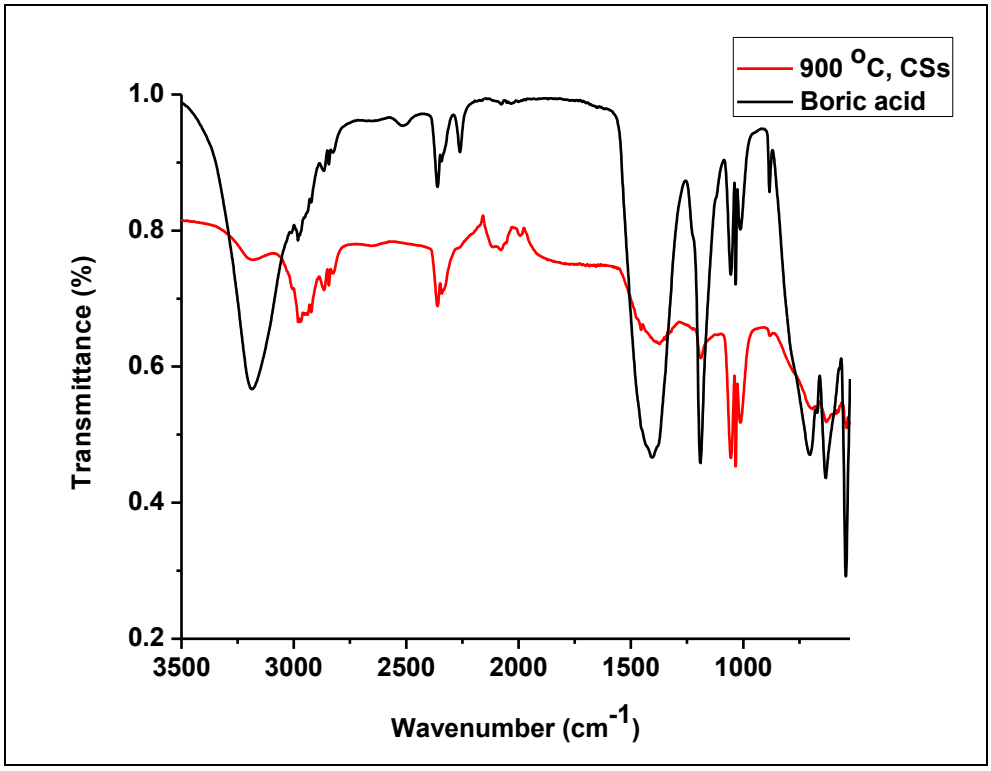


Figure S9: FT-IR spectra of the CSs formed at 900 °C compared with boric acid.

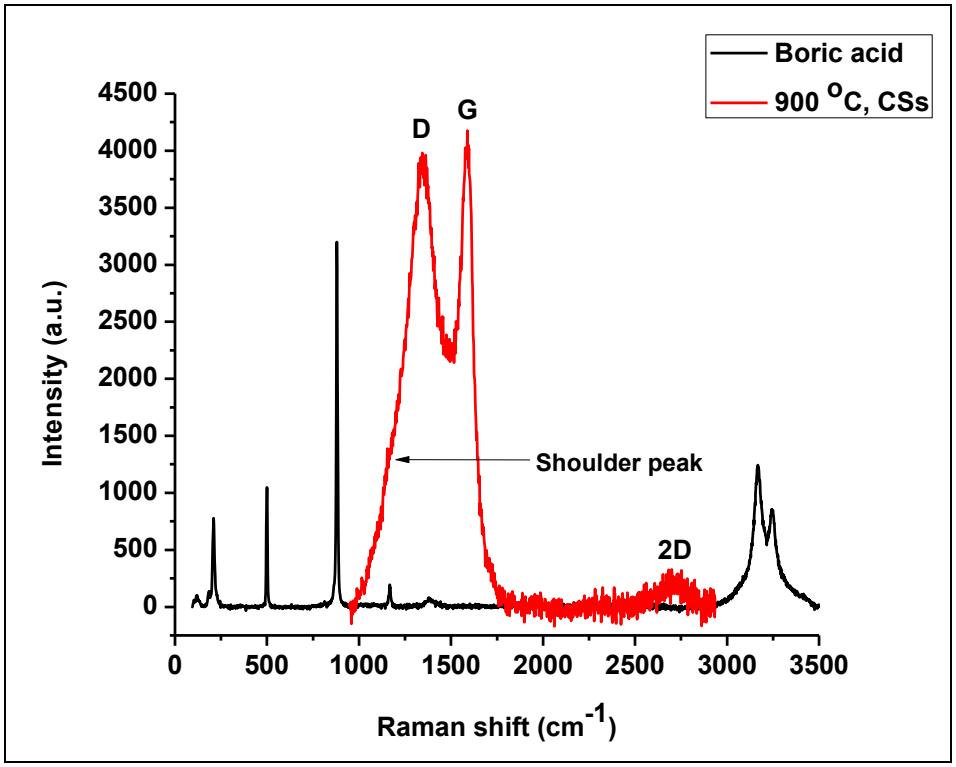


Figure S10: Raman spectra of boric acid and CSs formed at 900 °C.

CHAPTER 6

Novel CVD Syntheses and Characterization of Core-shell Boron-Doped Carbon spheres

---

6.1 Introduction

Carbon nanomaterials such as carbon nanotubes (CNTs), carbon spheres (CSs), carbon fibers, etc, have been studied because of their novel electronic and chemical properties.[1a] The diverse range of structures and morphologies produced by carbon are determined by its unique ability to form sp, sp^2 and sp^3 bonds. Spheres made of carbon can have different morphologies; they can be solid, hollow or core-shell.[1] Solid carbon nanospheres have been studied extensively for decades and have attracted an increasing attention because of their excellent properties (high specific surface area, high chemical inertness, thermal insulation, low effective density, high comprehensive strength)[2] and extensive applications. Such applications include their use as supports for catalysts,[3-6] in lithium-ion batteries,[7] hydrogen storage media,[7,8] drug delivery,[9] templates for synthesis of other hollow materials,[10] fuel cells[11] etc. In more recent years, hollow carbon spheres have attracted much attention and several ways of preparing hollow CSs such as template assisted,[8,12] pyrolysis,[13,14] medial-reduction,[15] hydrothermal,[16] solvothermal[17,18] and CVD[19,20] methods have been developed.

Doping of carbon with heteroatoms such as nitrogen and boron has a significant effect on the structure of a carbon material. For example, multiwalled CNTs doped with nitrogen and boron were found to typically have bamboo-like structures and contained structural defects in their carbon layers.[21-24] It is further known that boron doping improves the electronic properties[25-27] and the crystallinity of CNTs.[26] Doping of solid CSs,[28,29] hollow CSs,[30-32] multiwalled CNTs,[22,25] singlewalled CNTs[33-35] and carbon nanofibers[36-38] with nitrogen (and boron) has been used for altering the electronic properties of the carbons for specific applications.

There is a paucity of information available on boron-doped carbon spheres[39-42] (see summary in Table 6.1). Mondal *et al.*[39] synthesized boron-doped carbon microspheres by a non-catalytic chemical vapour deposition (CVD) method using 1.3 M BF_3/MeOH as the boron source and acetylene as the carbon source. During the synthesis, the furnace was heated to 800 °C and C_2H_2 (100 ml/min) was allowed to bubble through a 1.3 M BF_3 in methanol

solution for 2 hours. The synthesized boron-doped CSs (boron content of 0.13±0.03 at.%) were found to be uniform in size (650-800 nm) and had core-shell structures with a shell thickness of about 11 nm. Hidetaka and co-workers[40] synthesized boron- and nitrogen-containing carbon microspheres at 1000-1600 °C from a chelate resin, in which N-methyl glucamate functional groups formed an ester with borate ions. Hollow B-doped CSs were achieved by removing the silica spheres with 20 wt% HF solution. BCN hollow spheres were also prepared by pyrolyzing a polymeric precursor made from $B_3N_3Cl_3$ and aniline at 1000 °C for 1 hour in an N_2 atmosphere.[41] More recently, Ravat *et al.* used monodisperse silica spheres as template to synthesize hollow B-doped microspheres with a diameter of 1200 nm.[42] Bose and Yang[43] prepared boron-doped microspheres by a CVD method inside a quartz tube inserted in a 2-stage furnace. In the synthesis, 0.34 g of ferrocene was dissolved in 23.6 g of 1.0 M BCl_3 solution in p-xylene. The solution was injected and vaporized in the first furnace (kept at 200 °C). A H_2 (60 ml/min) and Ar (90 ml/min) mixture was used to transport the vapour from the first furnace to the second furnace (950 °C) for 30 minutes. The authors obtained B-doped microspheres of onion-like structure with diameters of less than 700 nm, a surface area of 220 m^2/g, boron to carbon ratio from 1:4 to 1:12 and a material that exhibited a much higher electrical conductivity than CNTs. From the above it is clear that no simple procedure exists to make B-doped hollow CSs.

We report here the novel direct synthesis of boron-doped core-shell CSs (B-CSs) by means of horizontal and vertical CVD furnaces at 900 °C without using a catalyst or a template. This work follows our previous studies on boron-doped multiwalled CNTs,[23] which revealed that core-shell CSs could be synthesized at 850-900 °C along with B-doped CNTs using a horizontal furnace. In this study, $(CH_3O)_3B$ was used as the boron (and carbon) source and C_2H_2 as the carbon source. Different ratios of the carrier gases (Ar, H_2) were used to vary the morphology and size of the B-CSs. For comparison, the synthesis of undoped carbon spheres using a vertical reactor and their structural characteristics were also synthesized and studied.

It has been shown that CVD is a viable technique to prepare carbons with a high boron content (up to 15 at.% B) of homogeneously distributed boron.[44] Furthermore the vertical CVD furnace is usually the tool of choice for the cost-effective and continuous mass production of carbon product when compared to a horizontal furnace. In the CVD synthesis of carbon nanomaterials, a gaseous or liquid hydrocarbon (e.g. C_2H_2, C_2H_4, toluene, etc) source is used to produce CSs (or CNTs). To avoid oxidation of the carbon, the furnace is purged continuously with inert gas during the reaction. N_2, Ar, H_2 or He gases are usually

employed for this purpose. In addition, it has been reported that H_2 promotes the growth of CNTs while preventing the formation of amorphous carbon particles.[45]

Table 6.1: Boron-doped carbon microspheres obtained by various synthetic methods using different boron sources.

Method	Experimental conditions	B and C sources	Morphology	Diameter	B content	Reference
Non-catalytic CVD	800 °C 2 hours	1.3 M BF_3/MeOH C_2H_2	Core-shell	650-800 nm	0.13 ± 0.03%	[39]
Non-catalytic CVD	1000-1600 °C 1 hour Ar	B/N-containing chelate resin	Hollow	140-340 μm	4.4-4.8%	[40]
Non-catalytic CVD	1000 °C, 1 hour, N2	$1B_3N_3H_3Cl_3$:0.6 aniline	Hollow	1-2 μm	B:C:N 1:1.08:0.94	[41]
Template (silica spheres) CVD	900 °C 4 hours Ar/N_2	1.0 M BCl_3 in heptane	Hollow	1200 nm	1%	[42]
Catalytic CVD (2 stage furnace)	Stage 1 (200 °C) Stage 2 (950 °C) 30 min, $Ar:H_2$ 60:90	Ferrocene and BCl_3 solution in 1.0 M p-xylene	Solid	< 700 nm	B:C 1:4 to 1:12	[43]

6.2 Experimental

The B-CSs were synthesized using either horizontal or vertical CVD furnaces. Acetylene (C_2H_2, Afrox) was chosen as carbon source and trimethyl borate ($(CH_3O)_3B$ ≥ 99.0% (GC), Fluka Analytical) was used as both carbon/boron sources for the growth of B-CSs. Ar and H_2 (both purchased from Afrox)were used as carrier gases. In a previous study, undoped and N-doped CSs were synthesized at 900 °C using a vertical furnace, and it was observed that the use of higher gas flow rates (C_2H_2, 300 ml/min and Ar, 240 ml/min) compared to lower gas flow rates (C_2H_2, 100 ml/min and Ar, 40 ml/min) gave higher yields and smaller diameters of carbon spheres.[46] In addition, Miao and co-workers reported that yields of CSs increased with increasing flow rates of C_2H_2.[47] Our choice of gas flow rates used in this study was based on the undoped and N-doped CS studies. The B-CSs synthesized using horizontal and vertical furnaces were named as shown in Table 6.2. All the synthesized materials in this study were purified by Soxhlet extraction in toluene for about 6 hours to remove polycyclic aromatic hydrocarbons, dried at 120 °C for 12 hours and then analysed.

Table 6.2: The synthesis parameters, product yield and diameters of the undoped CSs and B-doped CSs (samples 1-7).

Sample ID	Type of furnace	Ar (%)	H_2 (%)	Reaction time (min)	Product yield (g)	Outer diameter distribution (nm)	Average diameter (nm)	Average shell thickness (nm)
Undoped CSs	Vertical	100	0	60	3.85	55-420	125	none
Sample 1	Horizontal	100	0	60	0.15	225-725	400	25
Sample 2	Vertical	100	0	30	1.26	150-650	350	50
Sample 3	Vertical	95	5	30	1.37	150-775	250	50
Sample 4	Vertical	90	10	30	2.46	150-750	250	50
Sample 5	Vertical	80	20	30	2.51	150-750	250	50
Sample 6	Vertical	50	50	30	2.66	150-750	250	50
Sample 7	Vertical	0	100	30	2.88	150-850	250	50

Undoped CSs: The synthesis of the materials was carried out in a tubular quartz reactor (having dimensions 1.5 m x 32 mm o.d) placed in a vertical CVD furnace. C_2H_2 (Afrox) and Ar (Afrox) were used as carbon and carrier gas sources, respectively. The furnace temperature was raised to 900 °C at 10 °C/min under flowing Ar gas (40 ml/min). Once the desired temperature was reached, Ar (240 ml/min) and C_2H_2 (300 ml/min) were allowed to flow from top to bottom through the quartz tube for 1 hour and the carbon material was collected in a 500 ml round bottom flask. The system was then left to cool down to room temperature under an Ar atmosphere. The product was removed from the round bottom flask and weighed (3.85 g, Table 6.2).

Sample 1: The synthesis of B-CSs was carried out in a tubular quartz reactor (51 cm x 1.9 cm i.d.) placed in a horizontal furnace. The furnace temperature was raised to 900 °C at 10 °C/min under flowing Ar gas (40 ml/min) in the reaction. Once the desired temperature was reached, the Ar (240 ml/min) and C_2H_2 (300 ml/min) were simultaneously bubbled through $(CH_3O)_3B$ (room temperature) for 1 hour. After this, the bubbling of the gases through $(CH_3O)_3B$ was stopped and the system was left to cool down to room temperature under an Ar atmosphere (Table 6.2).

Sample 2: The synthesis of B-CSs was carried out in a tubular quartz reactor (1.5 m x 32 mm o.d) placed in a vertical furnace. The furnace temperature was raised to 900 °C at 10 °C/min under flowing Ar gas (40 ml/min). The Ar (240 ml/min) and C_2H_2 (300 ml/min) were simultaneously bubbled through $(CH_3O)_3B$ (room temperature) and were allowed to flow

from top to bottom through the quartz tube for 30 min. The carbon material was collected in a 500 ml round bottom flask (Table 6.2). A fraction of **Sample 2** was refluxed in distilled water at 110 °C for 3 hours, filtered and dried overnight at 120 °C.

Samples 3-7: Another series of experiments similar to those used to make **Sample 2** were conducted by varying the H_2 and Ar ratios of the carrier gases with a total gas flow rate of 240 ml/min, while keeping the C_2H_2 flow rate constant at 300 ml/min. During the syntheses, the furnace was ramped to 900 °C in flowing Ar/H_2. The *in situ* doping of CSs was achieved by bubbling Ar/H_2 and C_2H_2 through the liquid $(CH_3O)_3B$ (room temperature) for 30 min (Table 6.2).

6.2.1 Characterization of undoped and B-doped CSs

The morphology, structural features and sizes of the undoped and boron-containing carbon spheres were studied by transmission electron microscopy (TEM) using a FEI Technai G^2 Spirit electron microscope operated at 120 kV, X-ray diffraction (XRD) using a Bruker D2 phaser equipped with Cu-Kα radiation (λ = 1.5405 Å), and an operation voltage of 30 kV and current of 10 mA, and Raman spectroscopy using a Jobin-Yvon T6400 micro-Raman spectrometer equipped with a liquid nitrogen cooled charge coupled device detector. Scanning electron microscopy (SEM) images of the undoped CSs were obtained on a FEI QUANTA 400 FEG ESEM operated at 5 kV. The thermal stability of the synthesized materials was investigated by thermogravimetric analysis (TGA) using a TA TGA Q500. About 10 mg of each sample was heated to 900 °C at a rate of 10 °C/min under air. The mass of the samples was kept constant (ca 10 mg) in order to reduce the effects of variability in measurements. BET surface areas of the materials (~200 mg for each measurement) were obtained through N_2 adsorption using an ASAP 2000 Micrometrics TriStar Surface Area and Porosity Analyzer. The boron concentration in samples 2 and 7 was determined by X-ray photoelectron spectroscopy (XPS) obtained on a Kratos Axis Ultra DLD XPS spectrometer equipped with both an Al (monochromatic) and dual Al/Mg anode and a charge neutralizer (Rhodes University, Grahamstown). The operating pressure was kept below $5x10^{-9}$ Torr. Each sample was etched with an Ar ion gun (at 4kV) for 5s to remove residual/adsorbed oxygen molecules on the surface of the sample. Survey XPS scans were performed with an emission current of 10 mA and the anode (HT) at 15kV. A hybrid lens in slot mode was used to acquire the survey and high resolution scans. Survey scans were collected from 1200 to 5

eV at 160 eV pass energy, with 1 eV steps and dwell times of 500 ms. High resolution scans were acquired at 40 eV pass energy, also in hybrid lens and slot mode, with steps at 0.1 eV and dwell times at 500 ms for each element at their relevant regions. The atomic percentage of carbon and oxygen in the undoped CSs was obtained from a Quantum 2000 Physical Electronics spectrometer (National Metrology Institute of South Africa (NMISA), Pretoria) equipped with a monochromatic Al Kα X-ray source (1486 eV) operated at 20 W. Fourier Transform Infrared (FT-IR) spectra were recorded in the range 4000-500 cm^{-1} on a Bruker Tensor 27 FT-IR spectrometer.

6.3 Results and discussion

As mentioned earlier, previous reports from our laboratory demonstrated the ability to obtain core-shell carbon spheres at 850-900 °C when attempts were being made to synthesize B-doped MWCNTs using a Fe-Co/$CaCO_3$ catalyst by means of a horizontal furnace.[23] In this study, the effects of using horizontal and vertical furnaces on the synthesis of boron-doped carbon spheres at 900 °C without using any catalyst were investigated. The effects of carrier gas ratios (Ar:H_2 ratio) on the B-CS formation were also investigated using the vertical furnace. The effects of boron doping in CSs using a vertical furnace with and without the boron source using similar experimental parameters were also studied.

The yields recorded in Table 2 are based on the mass of the products obtained after the reactions. It is noticed that the product yield for sample 1 was very small when compared to sample 2 and the rest of the samples (see Table 6.2). After each reaction, a white film was found on the quartz tube walls and at the entrance of the furnace. After a few reactions, the quartz tube cracked in the middle, a position where the reactions took place. This white film is attributed to the formation of boric acid or boron oxides, which reacted with the silica tube, leading to tube breakage. Thus, in a horizontal furnace, $(CH_3O)_3B$ preferentially reacted with the quartz tube rather than C_2H_2, resulting in the low yield of CSs. In a vertical furnace, although a white film was also observed on the quartz tube, the reactants and products easily fell under the influence of gravity to produce a larger amount of carbon spheres than obtained in a horizontal furnace.

The surface areas, pore volume and pore diameters of the undoped and boron-doped CSs are low as shown in supplementary Table S1 (Appendix D). The results show that sample 2 synthesized without H_2 had a lower surface area, as compared to the undoped CSs and rest of

the boron-doped CSs, with surface areas ranging from 10-15 m^2/g. The very low surface area observed for sample 1 was related to the presence of amorphous carbon (see derivative weight curve in Figure 6.10c), large diameter and possibly more disordered carbon structure. The washed sample 2 gave a surface area of 7.1 m^2/g, a pore volume of 0.032 cm^3/g and a pore diameter of 19.3 nm. The decrease in surface area was presumably due to removal of some B_2O_3 on the surface of sample 2 (see **Section 6.3.3 and 6.3.4**).

6.3.1 Structural analysis of undoped and B-doped CSs

TEM and SEM were used to study the structure and diameter distribution of the synthesized undoped and boron-doped carbon spheres. Figure 6.1 shows TEM and SEM images of the undoped CSs, which were synthesized using a $Ar:H_2$ ratio of 100:0 in a vertical reactor. The images clearly show large quantities of CSs with spherical shape, solid and smooth surfaces, as well as chain-like structures. The images also show that some spheres accrete and some overlap with each other. The undoped CSs had an outer diameter distribution in the range of 55-420 nm and an average diameter of 125 nm (see Table 6.2).

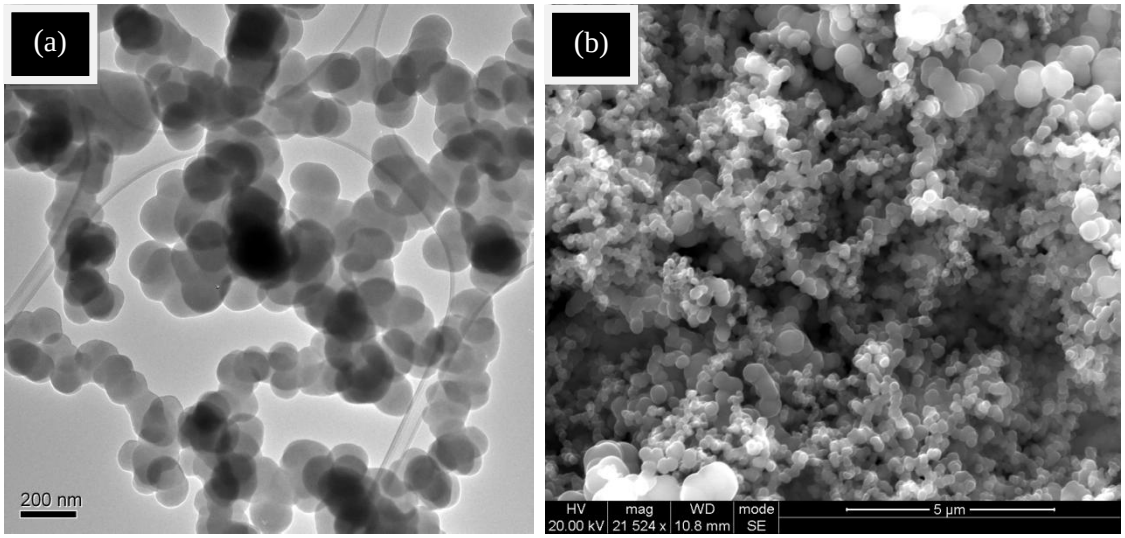


Figure 6.1: (a) TEM and (b) SEM images showing the accretion and large quantities of undoped CSs.

Figure 6.2 corresponds to a set of selected TEM micrographs (taken at different magnifications) of the B-CSs showing a range of different kinds of core-shell structures synthesized. When the reaction was performed using $(CH_3O)_3B$ and Ar:H_2 ratio of 100:0 in a horizontal reactor (sample 1), a black carbonaceous material was formed. The TEM images of the B-CSs synthesized under the same conditions but using a vertical furnace are shown in Figure 6.3 (sample 2). TEM images were recorded at different magnifications in order to compare the sample morphology. TEM analysis of samples 1 and 2 both showed chain-like core-shell structures with varying diameter distributions (225-725 nm) for the B-CSs made in the horizontal furnace and diameter distributions from 150-650 nm for the B-CSs made in the vertical furnace (Table 6.2). TEM images in Figures 6.2(c) and 6.3(c) also show that both samples 1 and 2 contain some (< 5%) spherical and accreted solid CSs. It was noticed that in samples 1 and 2 some hollow spheres accreted (Figures 6.2(b) and 6.3(b)), others overlapped with each other (Figures 6.2(d) and 6.3(b)) and some contained bubbles (Figures 6.2(b) and 6.3(c)). Sample 2 also exhibited filled core-shell CSs (see Figure 6.3(d)). From the TEM images of Sample 2, the filled core-shell CSs appear to be darker on the inside (core) as shown in Figure 6.3(d). However, a detailed study of this image by high resolution TEM (HRTEM) is required to ascertain if the filled core-shell CSs do exist or that they are solid CSs formed from C_2H_2 with or without boron.

The TEM images showed that the average outer diameter of sample 1 was ~400 nm with a carbon shell thickness of 25 nm, while the average outer diameter of sample 2 was ~350 nm with a carbon shell thickness of 50 nm. The results show that the outer diameter of sample 1 is larger than the outer diameter of sample 2, due to the short residence time in the vertical furnace. It is evident from the TEM images that the B-CSs formed in a horizontal furnace have thicker carbon shells than the B-CSs formed in a vertical reactor. Figures 6.2(f) and 6.3(f) show the high magnification TEM images of the B-CSs shells from sample 1 and 2, respectively. As can be seen, the carbon shells are composed of disordered graphitic layers and bubbles, signifying defective surfaces.

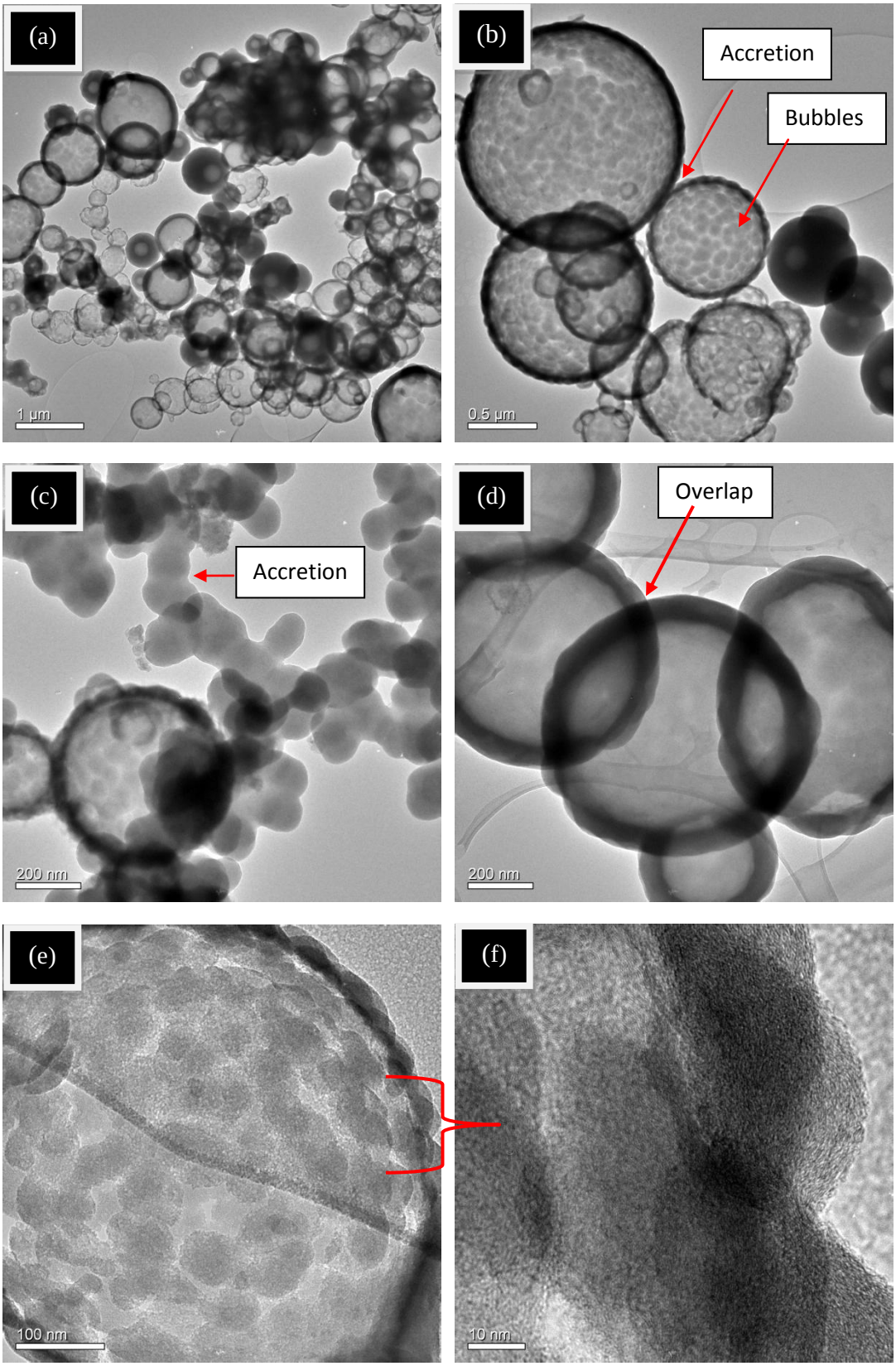


Figure 6.2:(a-e) TEM images (taken at different magnifications) of sample 1. (f) is the high magnified region of the area indicated in (e).

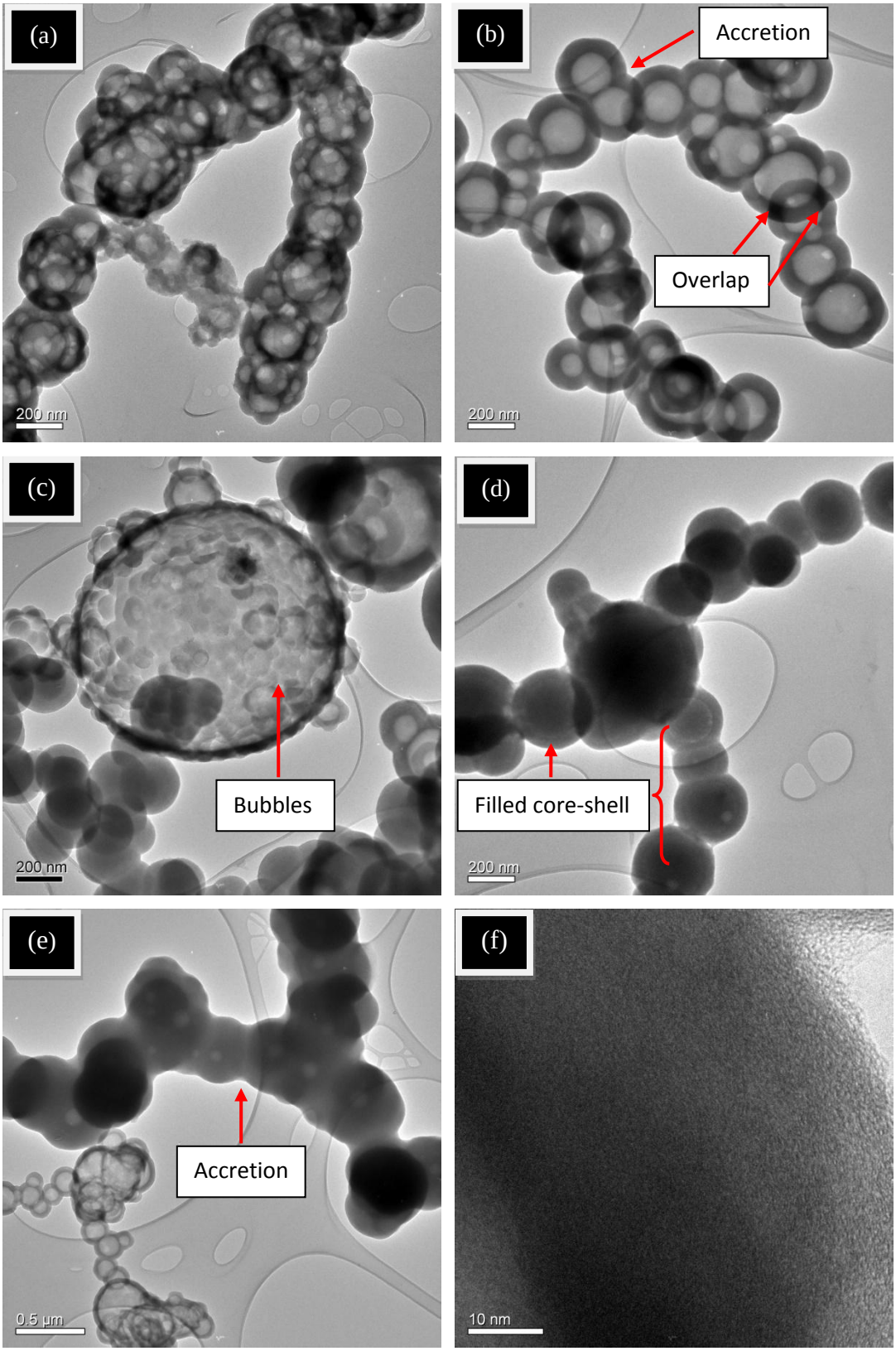


Figure 6.3: (a-e) TEM images (taken at different magnifications) of sample 2. (f) is the high magnification image of one of the core-shell CSs in the sample.

It is obvious from TEM studies that doping CSs with boron resulted in the formation of mostly core-shell structures, whereas solid undoped CSs were formed in the absence of the boron source. By comparing undoped CSs with sample 2, it was found that boron doping increased the diameter of the B-CSs compared to pristine CSs. Moreover, the product yield decreased with boron doping. These results indicate that boron doping influences the morphology, size, and the yield of the products.

The morphology of the B-CSs could also be tuned by varying the ratio of the Ar to H_2 in a vertical furnace during the synthesis. TEM was used to investigate the structure of the synthesized B-CSs in greater detail. Figures 6.4 to 6.8 shows the TEM images of samples 3-7 taken at different magnifications, showing the general morphological characteristics, from which a large quantity of core-shell carbon structures can be clearly observed. Samples 3-7 show similar characteristics to sample 2, such as accretion and overlapping of CSs, and the presence of filled and empty core-shell structures. It can be clearly seen that a difference exists between sample 2 (synthesized without using H_2) and the B-CSs synthesized in the presence of H_2 gas (samples 3-7). Compared to sample 2, which showed core-single-shell structures, samples 3-7 showed both core-single-shell and core-double-shell structures (Figures 6.3-6.7).

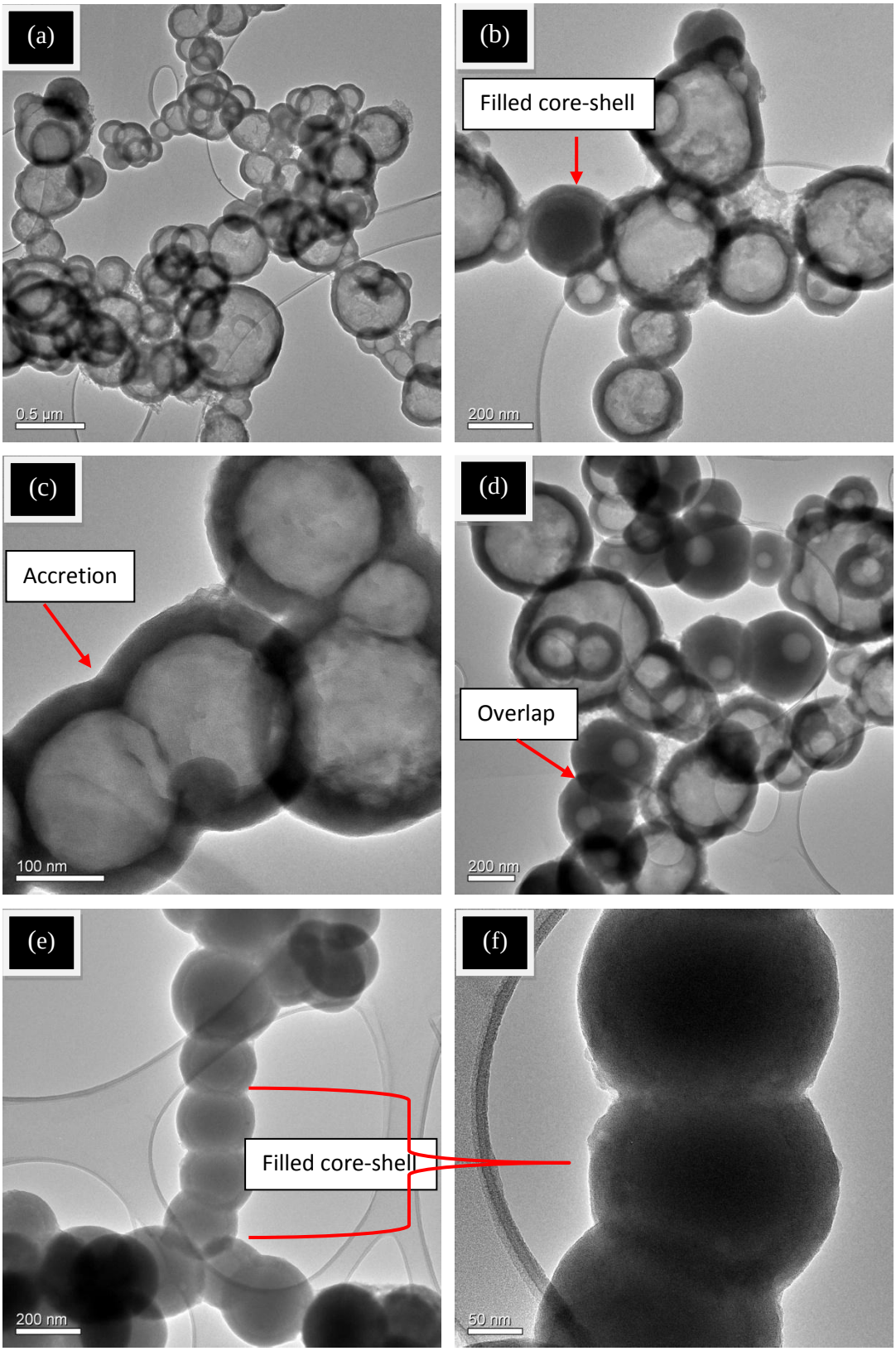


Figure 6.4: (a-e) TEM images (taken at different magnifications) of sample 3. (f) is the high magnification image of the region shown in (e).

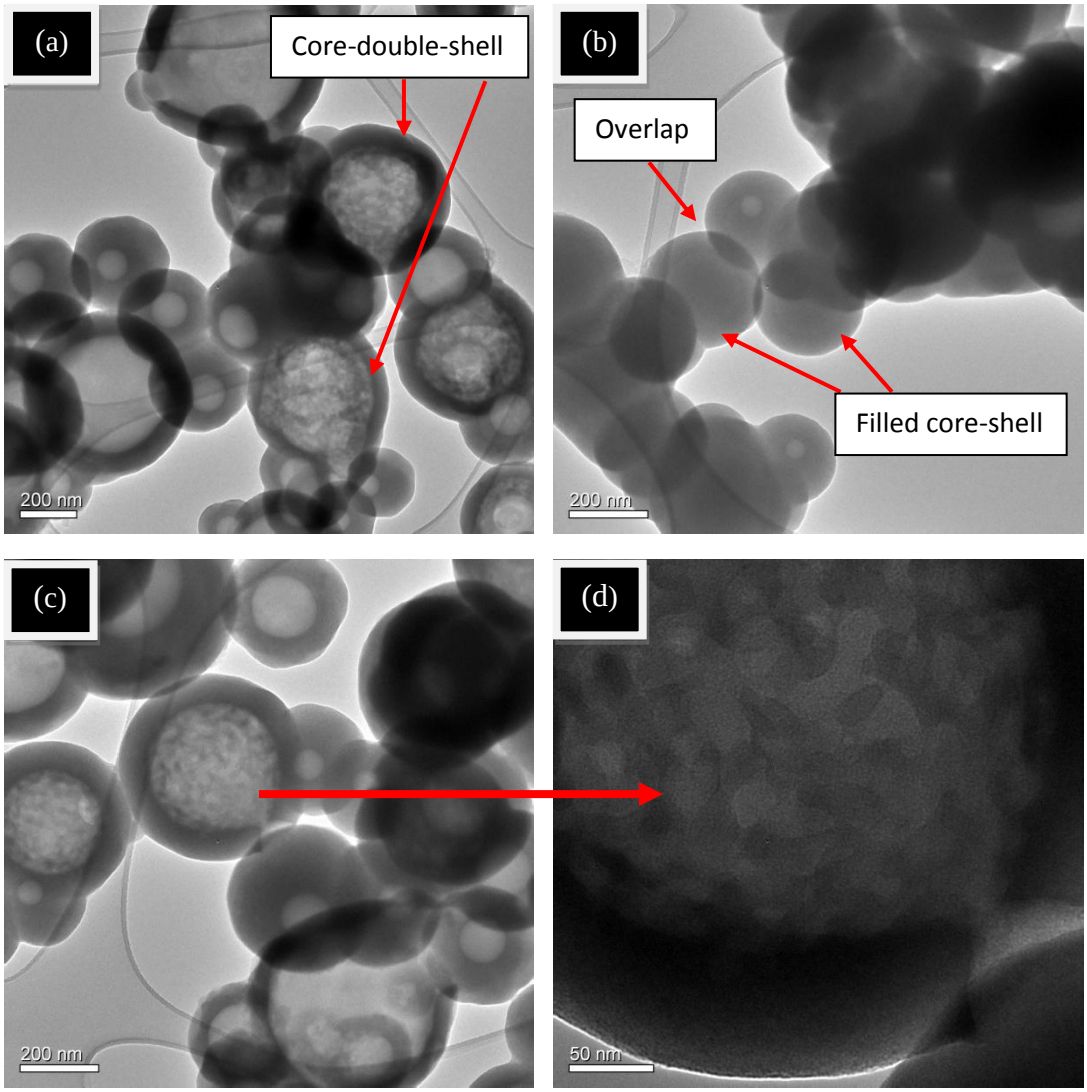


Figure 6.5: (a-c) TEM images (taken at different magnifications) of sample 4. (d) is the high magnification image of the region shown by an arrow in (c).

TEM images (Figures 6.4-6.8) also revealed that as the amount of H_2 increased, the quantity of core-double-shell structures increased. The images revealed that the B-CSs formed in the presence of H_2 gas had uniform outer diameters with average diameters of 250 nm (Table 6.2). It was also observed that the nature of a carrier gas used had an impact on the B-CS yield. A substantial increase in yield was observed as the amount of $H_2$was increased (see Table 6.2). Thus, it can be concluded that the amount of H_2 gas played an important role in the B-CS growth process. No matter what carrier gas ratio was used in a vertical furnace system, the B-CS shell thickness (around 50 nm) was uniform.

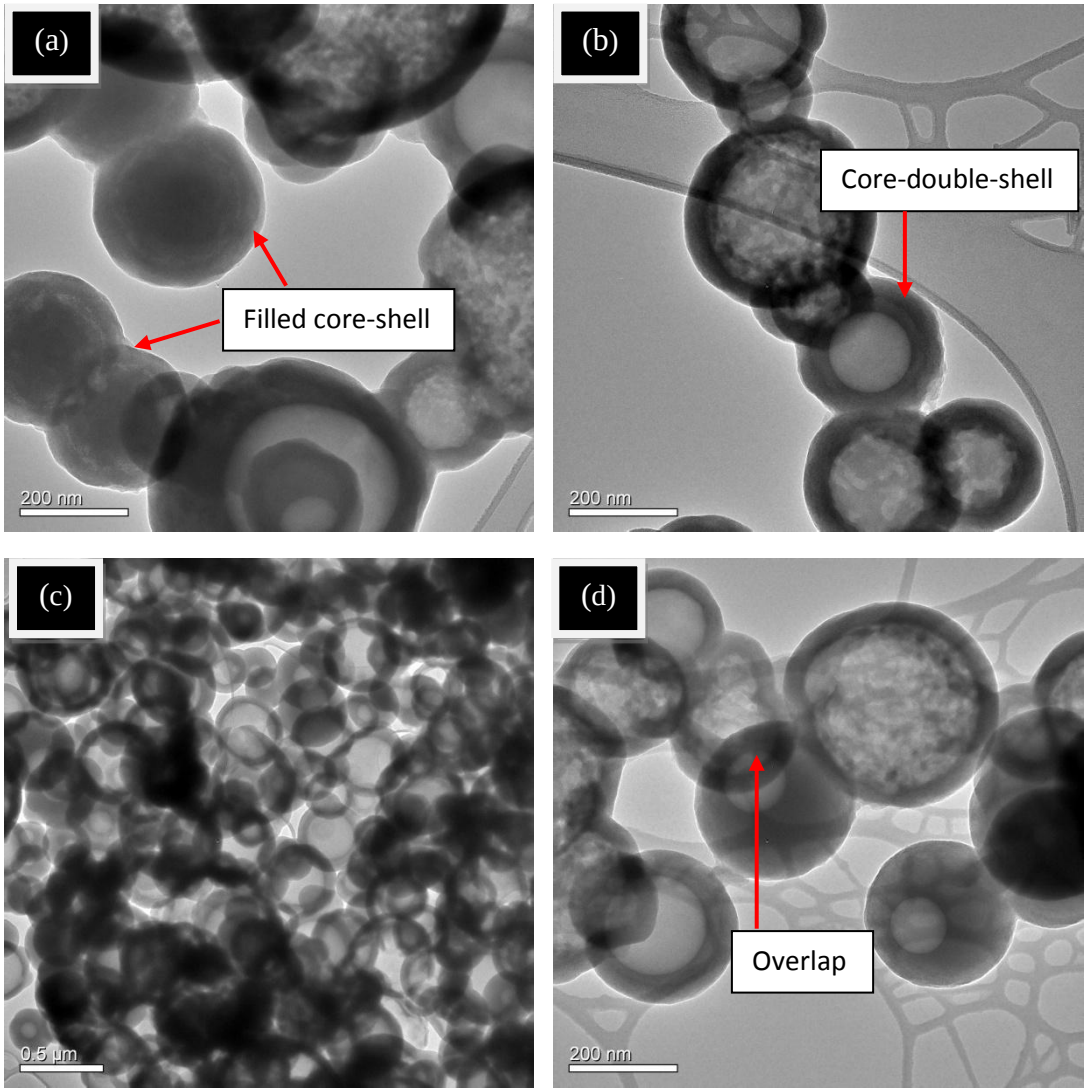


Figure 6.6: (a-d) TEM images (taken at different magnifications) of sample 5.

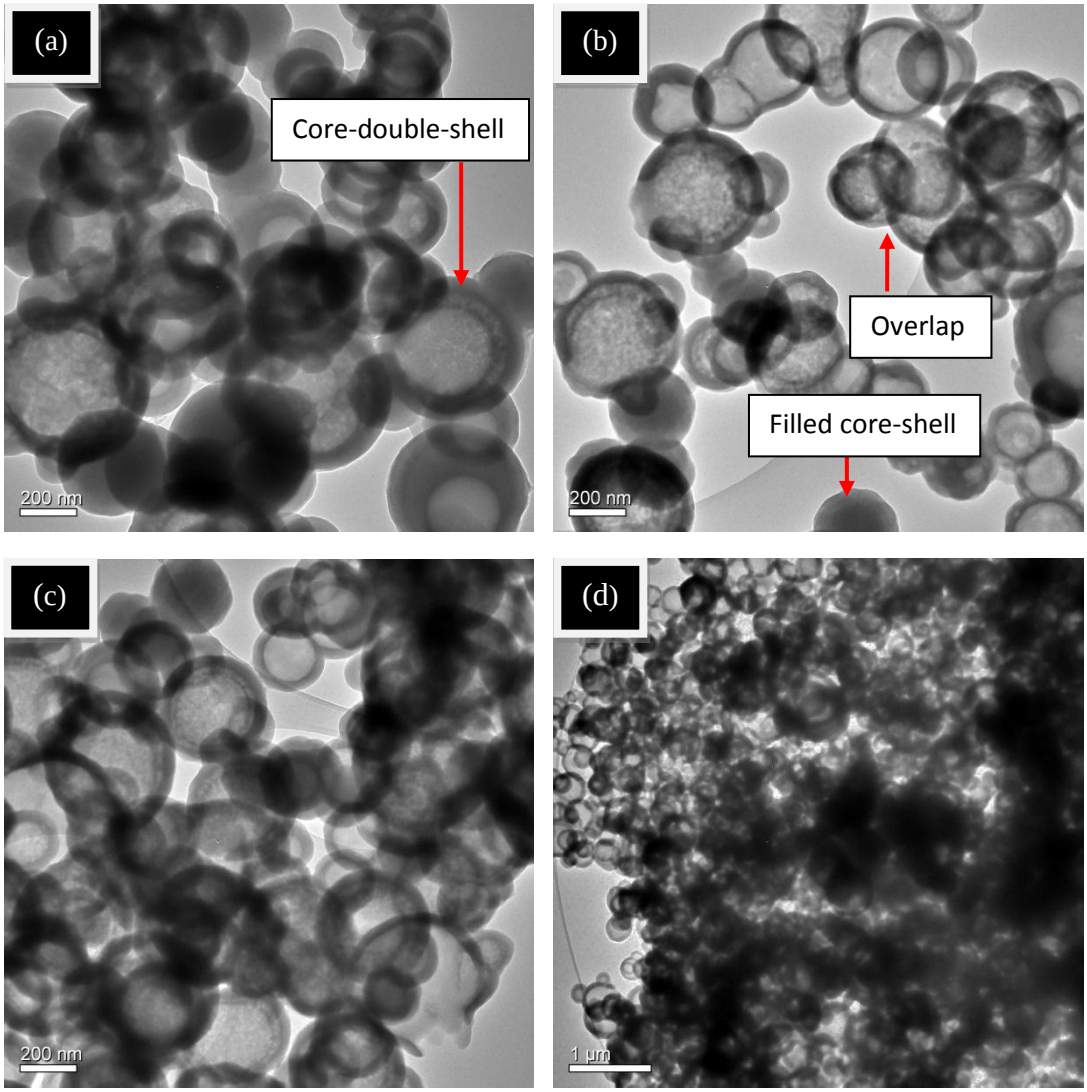


Figure 6.7: (a-d) TEM images (taken at different magnifications) of sample 6.

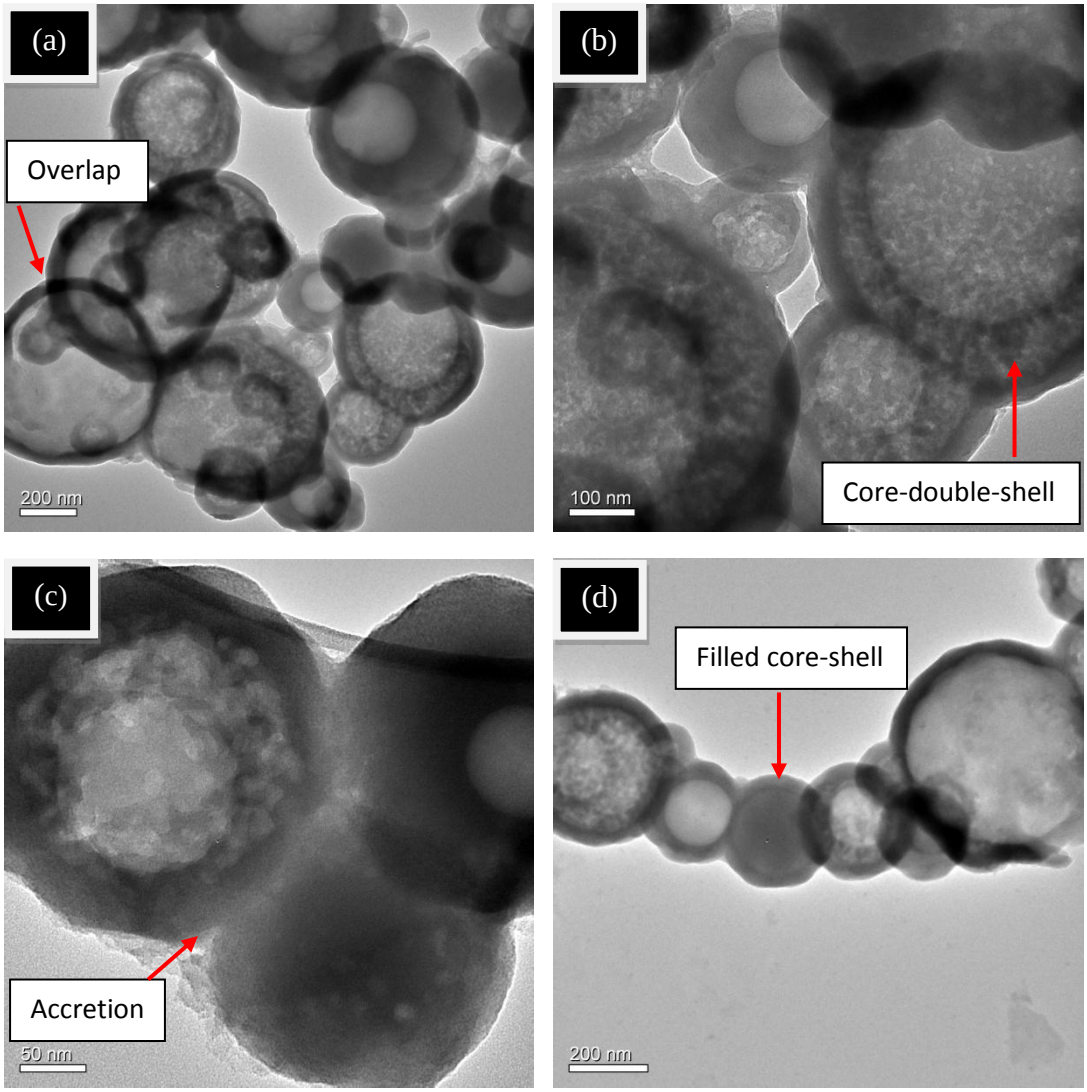


Figure 6.8: (a-d) TEM images (taken at different magnifications) of sample 7.

6.3.2 XPS analysis of the B-doped CSs (sample 2 and sample 7) and undoped CSs

To verify boron doping in the CSs, X-ray photoelectron spectroscopy (XPS) analysis of samples grown under 100% Ar (sample 2) and 100% H_2 (sample 7) were performed. Data are shown in Figures 6.9(a) and 6.9(b), respectively. The survey spectra for both samples are given in Supplementary Figures S1 and S2, clearly showing C, B and O atoms in both samples. The B 1s spectrum of sample 2 shown in Figure 6.9(a) has a major broad peak located at ~193 eV. This peak can be deconvoluted into three peaks at 191.6, 193.3 and 193.4 eV. These binding energies are significantly higher than those reported for elemental boron (187.1 eV), B_4C (187.8 eV) and BC_3 (188.8 eV).[44] Thus the 191.6 eV peak can be attributed to BCO_2 species and the 193.3-193.4 eV can be attributed to a B_2O_3 type chemical

environment of boron present in sample 2. These oxide-related species have been previously observed in the XPS of other boron-doped carbons,[48] MWCNTs,[49] SWCNTs,[50-53] and DWCNTs.[54] In Figure 6.9(b), the boron peak at 191.8 eV is attributed to BCO_2.

Peaks near 191.5 to 192.1 eV have been previously associated with substitutionally incorporated boron atoms into other carbon shaped materials, viz boron-doped SWCNTs [50-53] and boron-doped DWCNTs at 191.4 eV.[55] Furthermore, Liu and co-workers[48] reported the existence of some mixed B-C and B-O bonding states of boron in their boron-doped carbons, namely, BC_2O (190.0 eV) and BCO_2 (192.0 eV). They stated that in all these bonding states the binding energy of the B-C bonding is the same as the standard binding energy of B-C in B_4C, and the binding energy of the B-O bonding state is the same as the standard binding energy of B-O bond in B_2O_3.

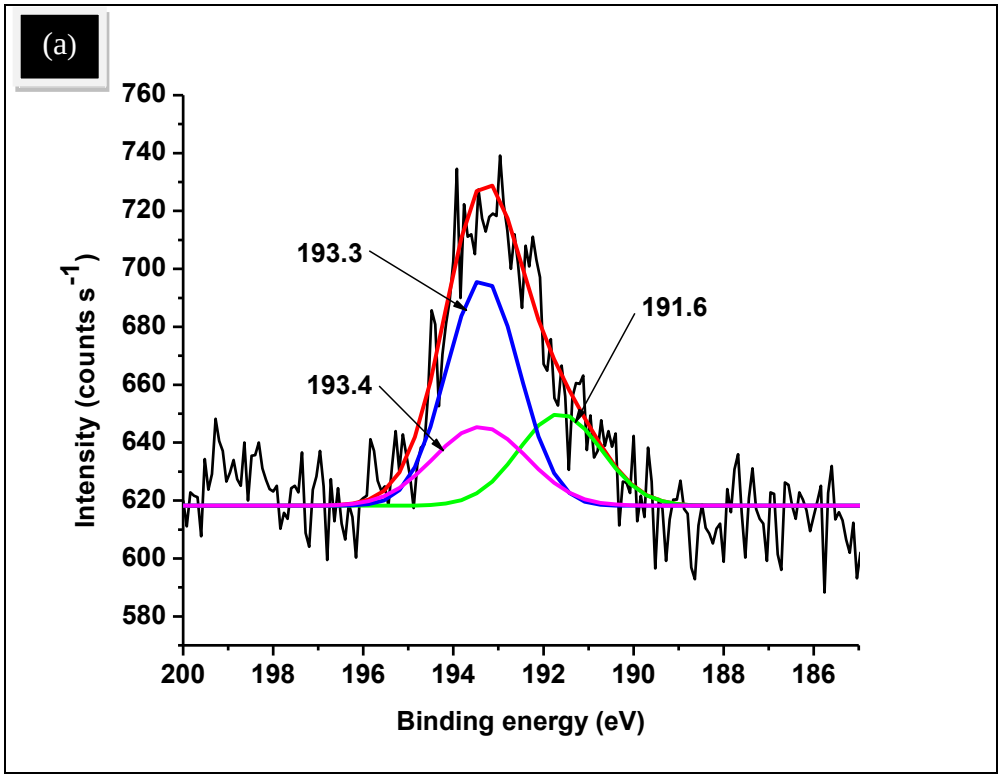


Figure 6.9a: B 1s XPS spectra of sample 2.

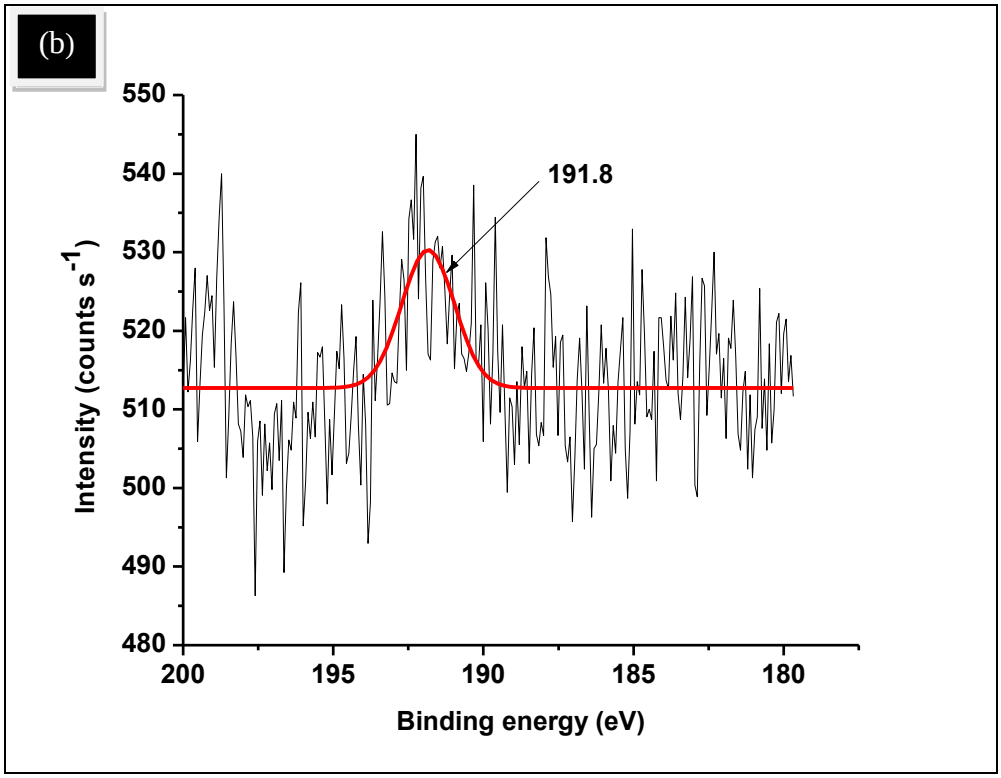


Figure 6.9b: B 1sXPS spectra of sample 7.

The corresponding carbon 1s spectra for samples 2 and 7 can be found in supplementary Figures S3 and S4, respectively. For sample 2, the main C 1s peak is positioned at 284.8 eV, which could be deconvoluted into four peaks located at 284.3, 284.9, 286.1 and 289.6 eV. These are attributed to the presence of sp^2 C-C, sp^3 C-C, C-O, and C=O bonding states, respectively.[54] The deconvoluted C 1s spectrum of sample 7 shows the four similar carbon bonding states of carbon, located at 284.7, 285.2, 286.8 and 289.4 eV. For both samples 2 and 7, there exists a fair amount of oxygen with the binding energy at 533.1eV, which is due to the presence of O-C group.[56]

Figures S5 and S6 present the survey and C 1s XPS spectra of the undoped CSs, respectively. As can be seen in the figures, the undoped CSs contain only carbon (284.9, 286.6 and 288.0 eV) and oxygen (532.7 eV) atoms and clearly indicate no sign of any boron species (~187-194 eV). Table 6.4 shows the elemental compositions of C, B and O for sample 2, sample 7 and the undoped CSs. The elemental contents of C, B and O for sample 2 were 77.10%, 3.92% and 18.98%, respectively, for sample 7 they were 84.46%, 0.19%, 15.35%, while for undoped CSs they were 94.70%, 0% and 5.30%, respectively as shown in Table 6.3. One interesting point to note is that the total boron concentration in sample 2 is much higher when compared with the boron content in sample 7. This implies that the presence of hydrogen gas

reduced the boron content in the formation of the boron-doped CSs. In addition, the boron amount in sample 7 estimated by XPS analysis was substantially lower than that found in the TGA (**Section 6.3.3**), XRD (**Section 6.3.4**) and FT-IR (**Section 6.3.5**) studies (see later). The B amount found in XPS is different from that determined by TGA and XRD studies. This is because XPS is a surface sensitive technique as compared to that of the bulk analysis techniques of TGA, XRD and Raman spectroscopy. This indicates that trace amounts of boron are on the surface of the CSs in sample 7.

Compared to B-doped CSs (samples 2 and 7), the XPS results of the undoped CSs showed very low amounts of oxygen atoms. The large amounts of oxygen atoms present in B-doped samples arose from the detection of boron oxides ($(CH_3O)_3B$). These results indicate that the boron content and the type of bonding states in the B-CSs can be tuned by varying the ratio of the Ar to H_2 in a vertical furnace.

Table 6.3: Elemental composition from XPS of boron-doped and undoped CSs synthesized with different gas ratios.

Sample ID	Ar (%)	H_2 (%)	C (%)	B (%)	O (%)
Undoped CSs	100	0	94.70	0.00	5.30
Sample 2	100	0	77.10	3.92	18.98
Sample 7	0	100	84.46	0.19	15.35

6.3.3 Thermogravimetric analysis of undoped and B-doped CSs

Thermogravimetric analysis (TGA) was conducted under an air atmosphere to investigate the thermal stability, the bulk decomposition properties and the purity of the undoped and boron-doped CSs. The TGA was also used as a detection system to confirm some components of the carbon spheres, such as C, B_2O_3 and H_2O. Figure 6.10(a) shows the plots of weight loss versus temperature for boric acid as well as undoped and B-doped CSs. The corresponding derivative profiles for these samples are shown in Figure 6.10(b). The decomposition temperatures (i.e. oxidation) and residual masses for these samples are recorded in Table 6.4. Figure 6.10(a) demonstrates that the boron-doped samples formed exhibited different oxidation behaviours from each other. The TGA curves for all of the samples doped with

boron showed a slow oxidation reaction, while that for the undoped sample had a relatively rapid reaction. The derivative weight loss curves (Figure 6.10(b)) for carbon in undoped CSs and samples 3-7 showed sharp peaks in narrow temperature ranges, while sample 1 and 2 showed broad peaks in wide temperature ranges. This suggests that the undoped CSs and samples 3-7 are uniform in size while samples 1 and 2 have varying sizes, a feature which was as also evidenced from TEM studies.

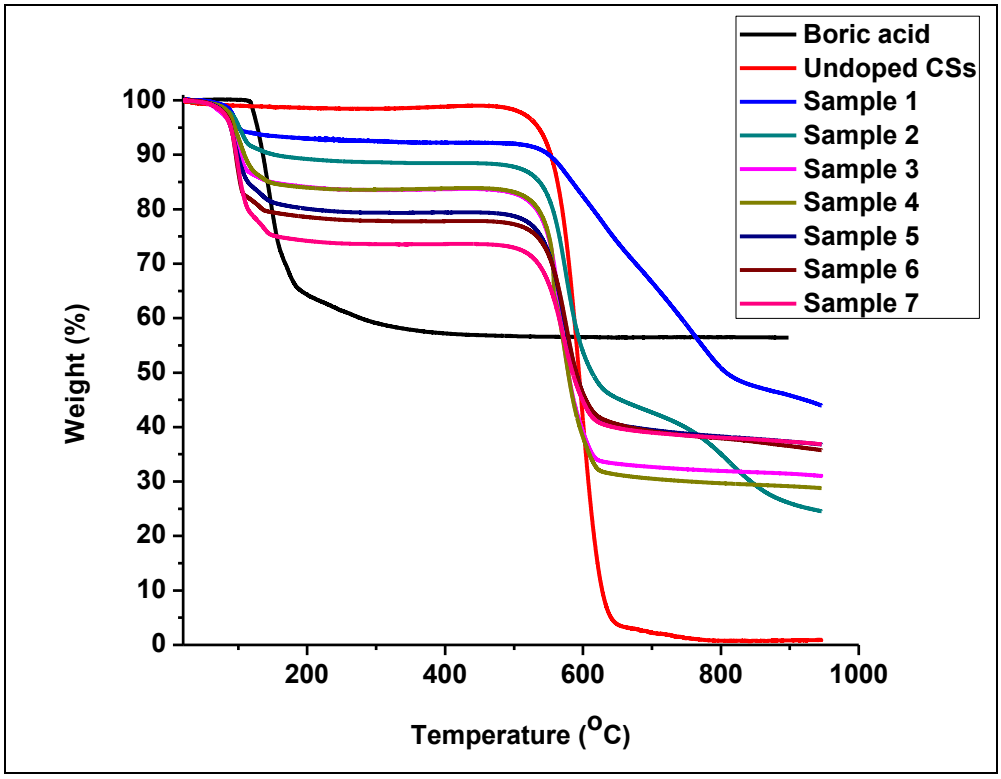


Figure 6.10a: TGA profiles of boric acid, undoped and boron-doped CSs heated in air.

Thermal analysis of boric acid was performed to get a better understanding of the temperatures where thermal events occur in the boron-containing CSs. Boric acid (H_3BO_3) itself theoretically contains 56.30% boron oxide (B_2O_3) and 43.70% water (H_2O), with a melting point of 171 °C. The resulting thermal decomposition of boric acid is shown in Figures 6.10a and 6.10b follows a two-step mechanism. The first decomposition which started at 141 °C corresponding to a weight loss of 34.80%, was due to the dehydration of H_3BO_3 forming HBO_2 (called metaboric acid). The second stage showed a weight loss of

8.20% at 256 °C which is due to the dehydration of HBO_2 producing a white hard B_2O_3 material, leaving residual mass of 56.40% (see Table 6.5). Our results agree with theoretical percentages and those reported by Nyambo *et al.*[57] on their TGA analysis of boric acid. They reported that the first stage occurred between 100 and 180 °C with a weight loss of 34% (due to the dehydration of H_3BO_3 into HBO_2) while the second one occurred between 180 and 400 °C, with a weight loss of 10% attributed to dehydration of HBO_2 into B_2O_3, leaving 56% residual mass. Therefore, the thermal decomposition of H_3BO_3 proceeds according to the following reactions:

$$H_3BO_3(s) \longrightarrow HBO_2(s) + H_2O(g)\ (\sim 100\text{-}180\ ^\circ C)$$

$$2HBO_2(s) \longrightarrow B_2O_3(s) + H_2O(g)\ \ (\sim 180\text{-}400\ ^\circ C)$$

Boron oxide reacts with water or moisture at room temperature to form boric acid, and the reaction is reversible: $B_2O_3(s) + 3H_2O(g) \rightleftharpoons 2H_3BO_3(s)$

The TGA (Figure 6.10(a)) and derivative curves (Figure 6.10(b)) for the undoped CSs showed one decomposition temperature at 597 °C due to oxidation of carbon, with a residual mass very close to zero. On the other hand, the boron-doped CSs showed thermal decomposition over the temperature range of 565-809°C and noticeable residual masses (see Table 6.4). In fact, after each TGA run, a black hard material remained in the TGA pan and this was attributed to (impure) B_2O_3. The majority of the carbon in all B-CSs decomposed at ~570 °C, a temperature lower than the oxidation temperature of the undoped CSs. The results indicate the lowered thermal stability of B-CSs due to the presence of boron. This further confirms boron incorporation into the CSs, as was demonstrated by the XPS analysis.

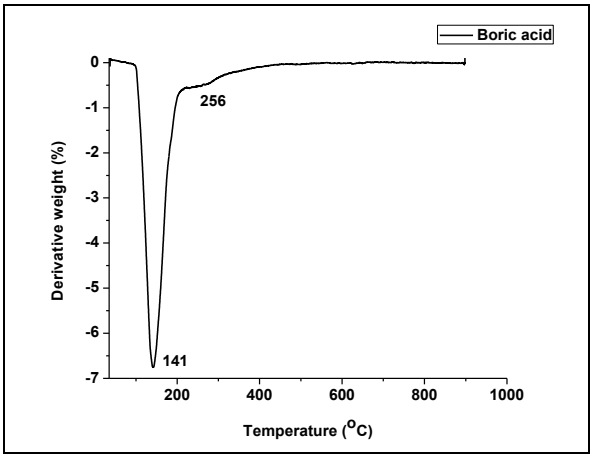
The derivative curves of the TGA for sample 1 showed additional peaks at 237, 320, 627 and 762 °C while sample 2 showed additional peaks at 320 and 809 °C. The observed peak at 237 °C for sample 1 is similar to the one found in boric acid, while the peaks at 318 °C for sample 1 and 320 °C for sample 2 correspond to amorphous-like material present in the sample. The peaks at 627 and 762 °C for sample 1 and 809 °C for sample 2 are indicative of the oxidation of CSs with different sizes. This indicates that the CSs in samples 1 and 2 are non-uniform. It is well known that smaller diameter CNTs are easily oxidized in air as compared with larger diameter CNTs.[58]

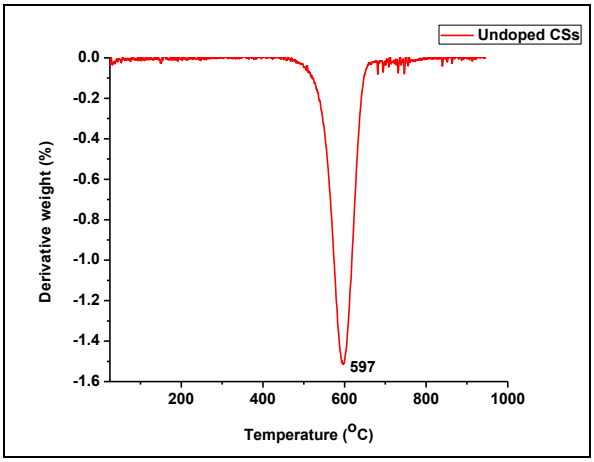
Table 6.4: TGA results for boric acid, undoped and boron-doped CSs.

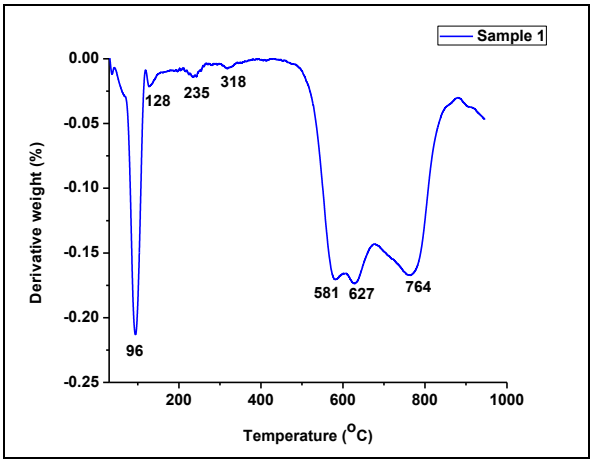
Sample ID	Type of furnace	Ar (%)	H_2 (%)	Decomposition temperature (°C)			Residual mass (%)
				H_2O[a]	H_2O[b]	C	B_2O_3
Boric acid	-	-	-		141, 256	-	56.4
Undoped CSs	Vertical	100	0	-	-	597	-
Sample 1	Horizontal	100	0	96	128, 235	318, 581, 627, 764	44.1
Sample 2	Vertical	100	0	103	134	320, 576, 809	24.5
Sample 3	Vertical	95	5	101	134	565	31.2
Sample 4	Vertical	90	10	93	134	577	29.1
Sample 5	Vertical	80	20	93	134	572	36.9
Sample 6	Vertical	50	50	96	132	577	36.0
Sample 7	Vertical	0	100	98	136	571	36.9

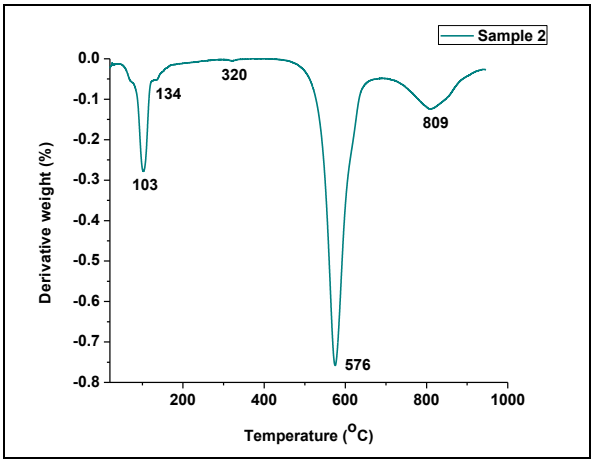
[a] = moisture from the atmosphere, [b] = dehydration of HBO_2

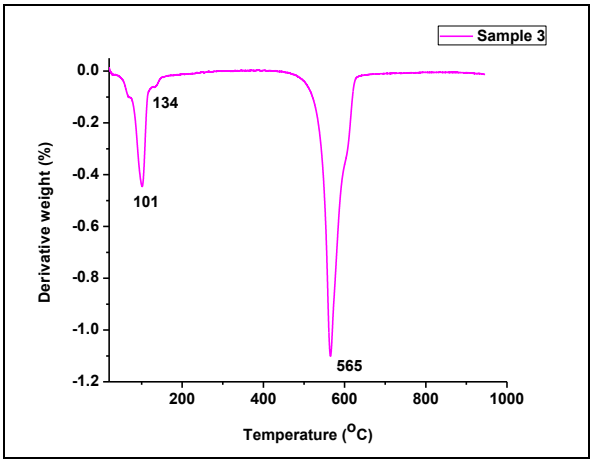
It may be noted that all B-CSs (samples 1-7) showed similar decomposition behaviour. The decomposition curves of these samples (Figure 6.10(b)) exhibited three similar peaks, one with a maximum ~100 °C, the other ~140 °C and another one ~570 °C, attributed to the elimination of moisture which was absorbed by the B-CSs from the atmosphere, dehydration of metaboric acid (HBO_2) in the B-CSs and decomposition of carbon spheres, respectively. The residual masses between 29 and 44% were associated with the presence of B_2O_3 (see Table 6.5). Residual mass for the B-CSs was higher for sample 1 and lower for sample 2 as compared to residual masses for samples 3-7. The TGA curves demonstrated that an increase in H_2 content enhanced the residual weights and purity of the B-CSs. Interestingly, the amounts of B in samples 2 and 7 were estimated to be ~4.2 and 6.4%, respectively by TGA, different from the B content determined by XPS analysis.

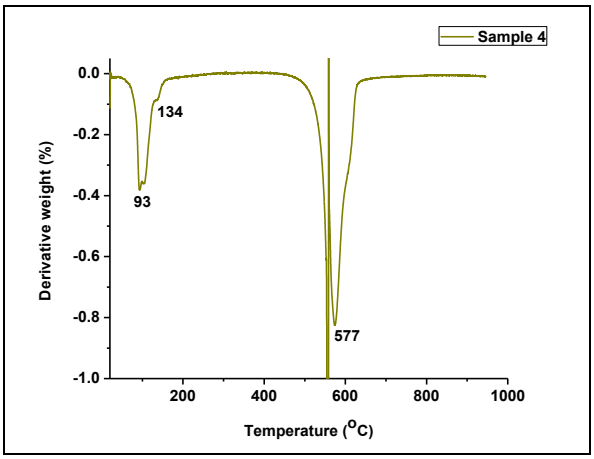

Boric acid
Derivative weight (%)
Temperature (°C)
256
141


Undoped CSs
Derivative weight (%)
Temperature (°C)
597


Sample 1
Derivative weight (%)
Temperature (°C)
128
235
318
96
581
627
764


Sample 2
Derivative weight (%)
Temperature (°C)
134
320
809
103
576


Sample 3
Derivative weight (%)
Temperature (°C)
134
101
565


Sample 4
Derivative weight (%)
Temperature (°C)
134
93
577

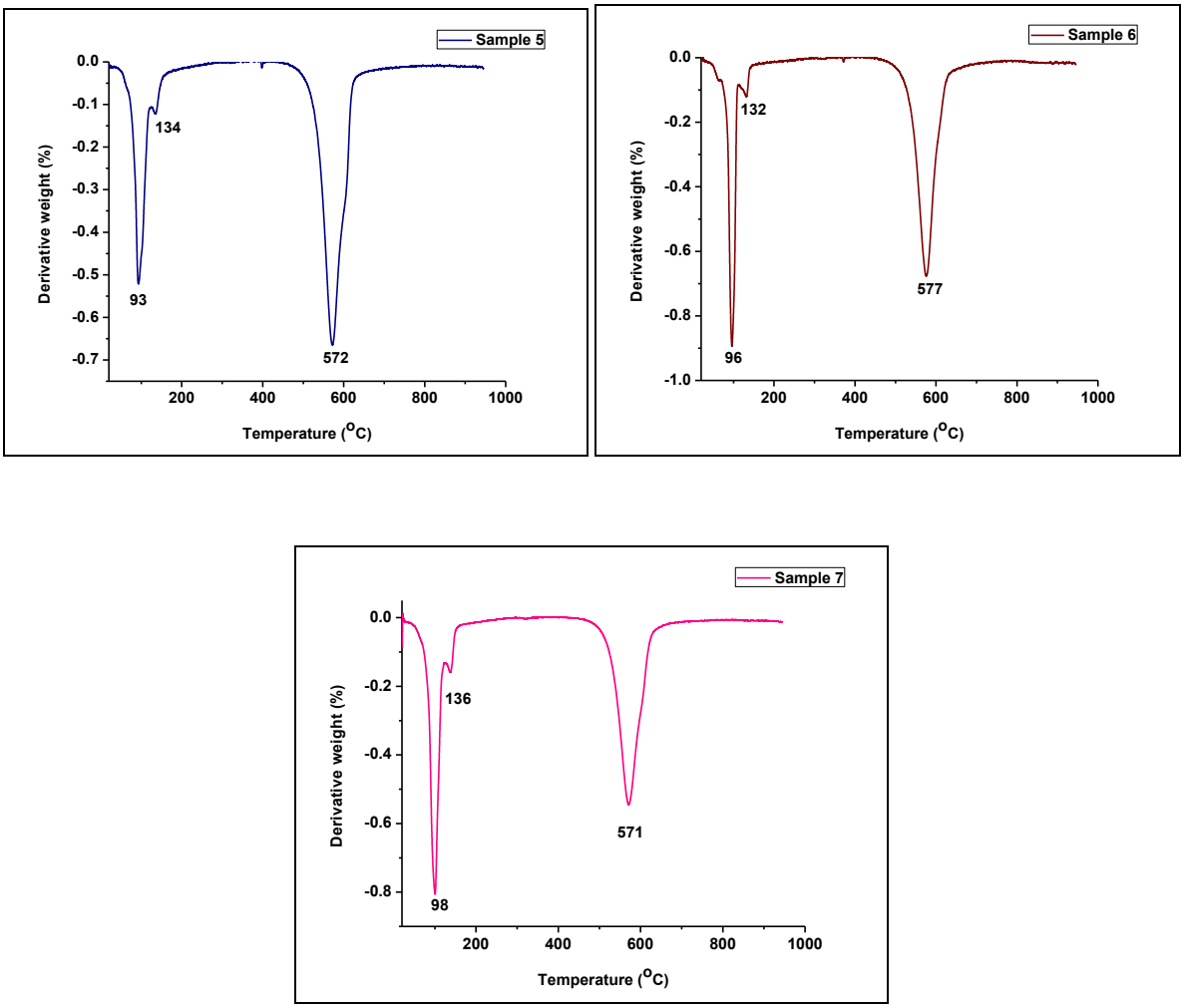


Figure 6.10b: Corresponding DTA profiles for boric acid, undoped and boron-doped CSs.

The intensities of the peaks due to dehydration of H_3BO_3 (~140 °C) to HBO_2 increased as the percentage of hydrogen gas increased during the reactions, which supports the suggested formation of high B_2O_3 content in B-CSs with increased H_2 percentage (i.e. from sample 2 to sample 7). It was also found that the B-CSs were moisture sensitive. The intensities of the peaks due to removal of moisture (~100 °C) also increased with H_2 percentage. Compared to sample 2, sample 1 showed higher peak intensities due to absorbed water and dehydration of H_3BO_3, and a higher amount of residual B_2O_3. This suggested a higher boron content in sample 1 than in sample 2. In addition to structural defects and boron incorporation, the moisture-uptake also caused a decrease in thermal stability of the B-CSs as compared to undoped CSs, which did not reveal absorption of moisture. Accordingly, the increases in residual weights of boron-containing CSs can be attributed mainly to the incorporation of

boron as B_2O_3 on the surface of the CSs, which when exposed to air absorbed moisture to form boric acid. In open air, the reverse reaction took place, where the B_2O_3 deposition the CSs, reacted with moisture and formed H_3BO_3.

B_2O_3 is known to dissolve in hot water. Thus, to assess the amount of boron doping, sample 2 with high boron content was refluxed in distilled water at 110 °C for 3 hours, filtered and dried overnight at 120 °C. Figure 6.10(c) compares the TGA profiles and their corresponding derivative curves for sample 2 and washed sample 2 in boiling water. As can be seen from the figures, the results indicate that the treatment of sample 2 with boiling water decreased the intensities of water due to moisture (~100 °C) and dehydration into H_2BO_2 (~134 °C) as well as B_2O_3 (10.8%) in the sample. The results confirmed that boiling water removed excess B_2O_3 (~14%) on the surface of the washed sample 2. It is to be noted that the carbon decomposition at ~809 °C shifted to a lower temperature for the washed sample 2.

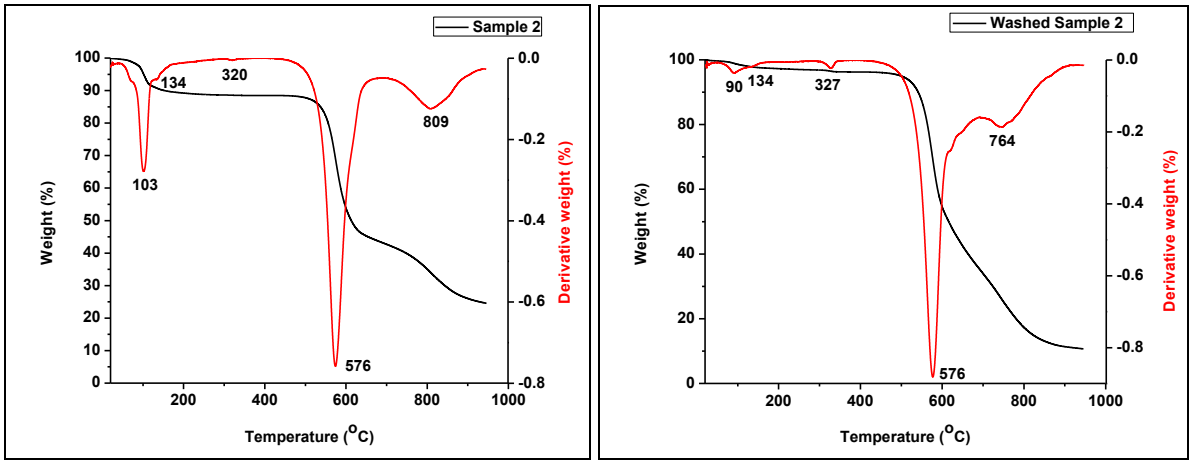


Figure 6.10c: TGA and corresponding DTA profiles for unwashed and washed Sample 2.

6.3.4 XRD and Raman spectroscopy analysis of undoped and B-doped CSs

Figure 6.11 compares the XRD patterns of the boric acid, undoped CSs and boron-doped CSs synthesized in different carrier gases. The full XRD spectrum for boric acid is shown in Supplementary Figure S7. Figure 6.11 exhibits the presence of several peaks (from 14.7° to 60°) in the materials. The sharp diffraction peaks with high intensities indicated by the asterisks originate from chemical bonds between boron and oxygen, in which the peaks can

be attributed to B_2O_3 in the B-CSs. The general trend observed here is that the B_2O_3 peak intensities substantially increased with increased H_2 amount during the reaction in a vertical furnace, but sample 1 synthesized in a horizontal furnace had the lowest B_2O_3 peak intensity overall, suggesting low B_2O_3 content in the sample. No diffraction peaks due to boron carbides (B_4C) were observed.

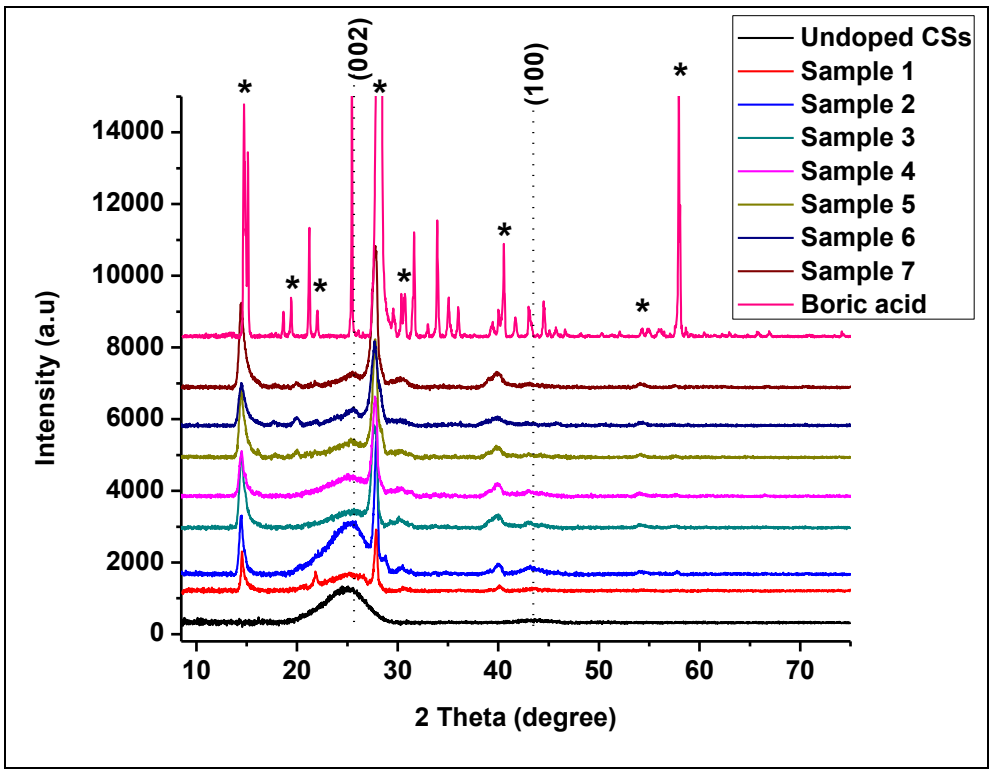


Figure 6.11: XRD spectra for boric acid, undoped and boron-doped CSs.

The broad peak at ~25.4° in all B-CSs can be indexed to a (002) reflection similar to the graphite characteristic peak (26.5°), while the peak at ~43.1° is less intense and is ascribed to the (100) reflection. On the other hand, the broad (002) peak shifted to a lower angle at 25.1° for the undoped CSs. The broader (002) peak indicated a low degree of graphitization and that the structure of the undoped CSs is amorphous.

The XRD data also revealed that the (002) and (100) peaks broadened and became weak as the H_2 content increased during the B-CS synthesis. The broader carbon peaks for samples 3-7 suggest a low degree of graphitization and the possibility of disordered carbon structure or amorphous feature, compared to sample 2. In addition, the (002) peaks of the carbon phase

for samples 3-7 are not pronounced as observed for undoped CSs and samples 1 and 2, although the carbon content in sample 7 estimated from the XPS (**Section 6.3.2**) was high enough.

Figure 6.12 shows the XRD pattern of the washed sample 2 compared with that of the original sample. After washing with boiling water, it was observed that the peaks due to B_2O_3 decreased due to removal of B_2O_3 on the surface of B-CSs and the carbon peaks were relatively broad, indicating less crystallinity as compared to the original sample. This result demonstrated the graphitization degree of sample 2 was largely enhanced, due to more boron doping.

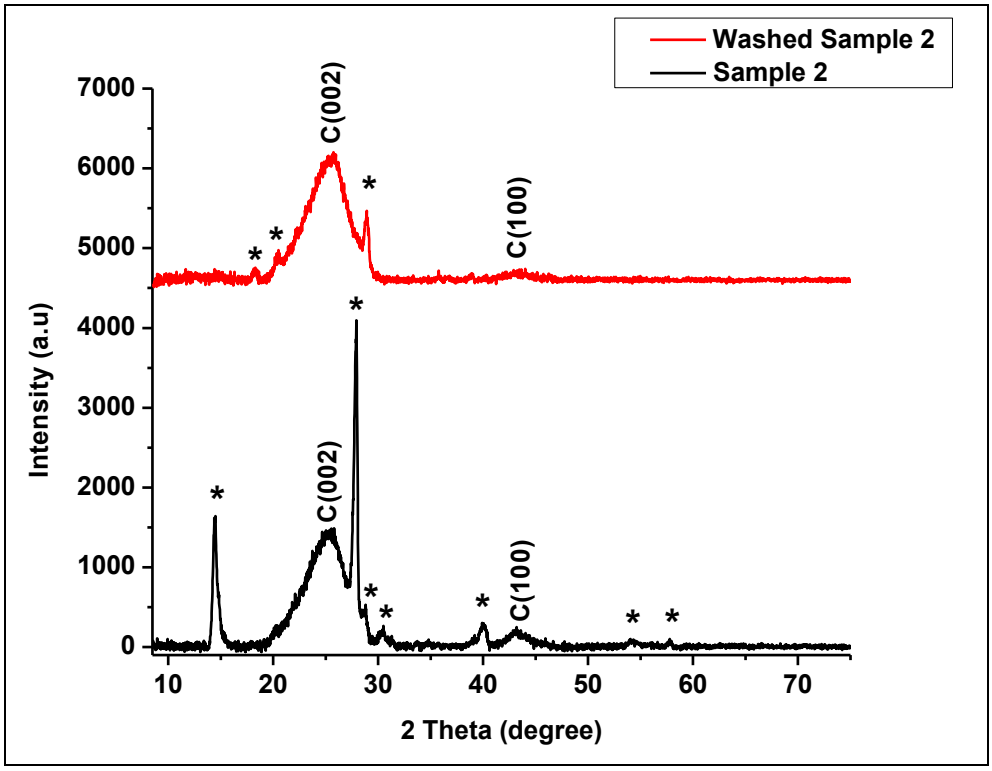


Figure 6.12: XRD spectra of unwashed and washed sample 2.

Raman spectroscopy was also used to estimate the crystalline quality of the CSs. Figure 6.13 compares the Raman spectra of the undoped CSs, B-CSs and boric acid measured at 514.5 nm excitation wavelength. A combined Gaussian-Lorentzian function (pseudo-Voigt function) was fitted to the data which gave the best fit. Two bands around 1350 and 1590 cm^{-}

[1] can be observed (see Figure 6.13 and Table 6.5) in all carbon-containing samples. The bands around 1350 cm^{-1} and 1590 cm^{-1} correspond to the disorder-induced sp^2 band (D-band) related disorder and carbon impurities (boron atoms) and the graphite highly oriented E_{2g} mode sp^2 band (G-band), respectively. The D-band intensity broadened and decreased with an increase in H_2 content during B-CS synthesis (i.e. from sample 1-7). The intensity changes result from the changes in B-CS quality induced by the presence of boron in the CSs. The B-CS Raman spectra showed a very similar behaviour, with the D-band broader and G-band narrower than in the undoped CSs. The broadness of the D-band could be a sign of the impurities (boron atoms) present in the synthesized carbon spheres.

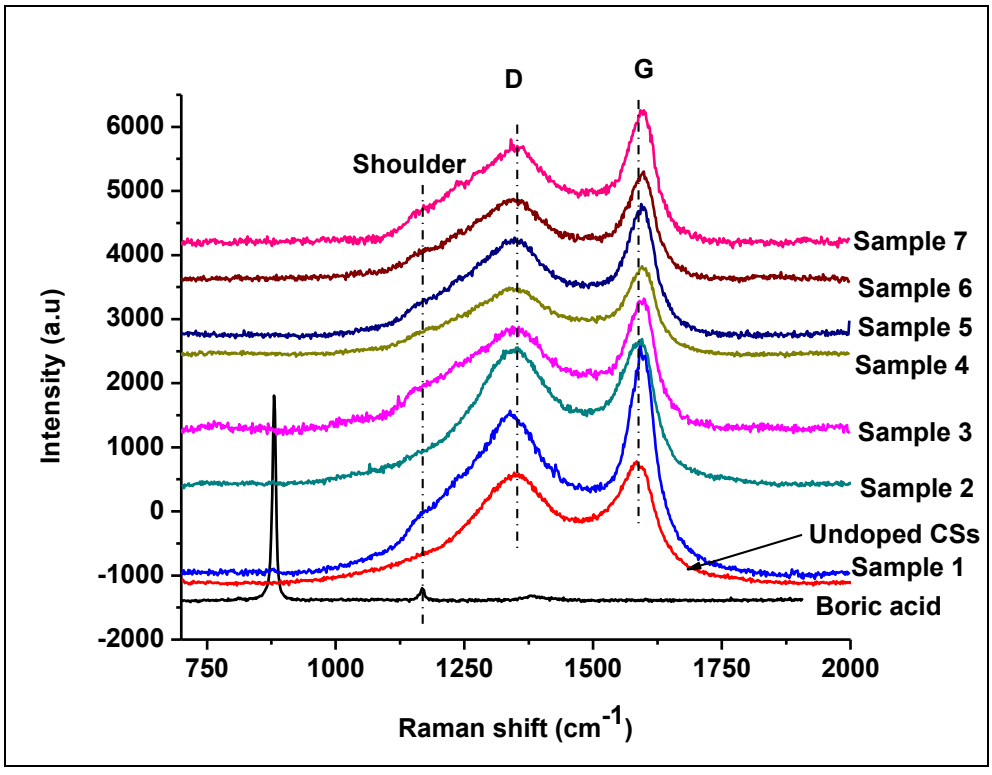


Figure 6.13: Raman spectra for boric acid, undoped and boron-doped CSs with excitation wavelength of 514.5 nm.

The D-band was weaker compared to the G-band for all the B-doped CSs, which indicated a high degree of C-C sp^2 order, corresponding to B-CSs of good crystallinity. This effect was also confirmed by the observed I_D/I_G ratios, which are usually used to measure the quality of the carbon materials. Compared to the undoped CSs, the I_D/I_G ratios for samples 1-7 were lower and increased with an increase in H_2 content during the B-CS synthesis (Table 6.6).

This observation indicated that the crystal qualities of the CSs were improved by the boron doping. The G-band frequency shifted from 1588 cm^{-1} for the undoped CSs to 1593 cm^{-1} for sample 2. The D-band frequency downshifted from 1347 cm^{-1} for the undoped CSs to 1343 cm^{-1} for sample 2. The upshift of the G-band and downshift of the D-band were attributed to boron incorporation into the CSs. An upshift of the G-band position by 6 cm^{-1} and a downshift of the D-band by 3 cm^{-1} has been previously reported when boron content exceeded 2 at.%.[59] Dresselhaus *et al.*[60] and others[61] attributed the upshift of the G-band frequency for the boron concentration exceeding 2 at.% to the transfer of hole carriers from doped boron to MWCNTs.

Table 6.5: D-, G-band and I_D/I_G ratios of undoped and B-doped CSs.

Sample number	Type of furnace	Ar (%)	H_2 (%)	D-band (cm^{-1})	G-band (cm^{-1})	I_D/I_G ratio
Undoped CSs	Vertical	100	0	1347	1588	1.27
Sample 1	Horizontal	100	0	1334	1595	0.43
Sample 2	Vertical	100	0	1343	1593	0.85
Sample 3	Vertical	95	5	1345	1595	0.90
Sample 4	Vertical	90	10	1342	1596	0.95
Sample 5	Vertical	80	20	1342	1595	0.93
Sample 6	Vertical	50	50	1342	1596	0.88
Sample 7	Vertical	0	100	1347	1596	0.97
Washed Sample 2	Vertical	0	100	1345	1592	0.82

Generally, high incorporation of boron into carbon materials leads to more disordered carbon structures, with poorer crystallinity than found at low boron incorporation.[62,63] Mondal *et al.*[62] and Chen *et al.*[63] reported that the I_D/I_G ratio increased with decreasing boron concentration in B-doped multiwalled CNTs. We observed that the I_D/I_G ratio was higher in sample 7 than in sample 2 and this indicated a lower degree of C-C sp^2 order at higher B doping concentration (as estimated by TGA results), in agreement with the literature data.[62,63] This phenomenon was also evidenced by XRD data, in which sample 7 showed a broader (002) carbon peak corresponding to a less crystalline structure than was observed in sample 2.

There is a shoulder peak observed around ~1167 cm^{-1} in the spectra of all the B-CSs (i.e. samples 1-7), which slightly broadened as the H_2 content increased during the synthesis. This

shoulder peak coincides with the peak at 1167 cm^{-1} found in the Raman spectrum of boric acid. It is clear that a shoulder peak at 1167 cm^{-1} in the B-CSs originated from B_2O_3. We attribute the presence of this shoulder peak to the effect of doping B atoms into the carbon sphere structure. The observed higher I_D/I_G ratio and the absence of the shoulder peak (~1167 cm^{-1}) in the undoped CSs may demonstrate the effect of doping in the B-CSs. Figure 6.14 presents the Raman spectra of boric acid, sample 2 and sample 2 washed with boiling water. The I_D/I_G ratio and D- and G-band positions of the washed sample 2 are also presented in Table 6.6. The figure reveals that there is still a shoulder peak at ~1190 cm^{-1} in the washed sample 2 which resembles the peak at 1167 cm^{-1} found in the Raman spectra of the unwashed sample 2 and H_3BO_3. The washed sample 2 indicated the presence of B_2O_3 in the sample, as was also confirmed by XRD and TGA data. Notably, the intensity of the D- and G-bands for the washed sample became stronger and the I_D/I_G ratio was a bit lower as compared to the unwashed sample 2. This indicated that the crystal quality of sample 2 improved after washing.

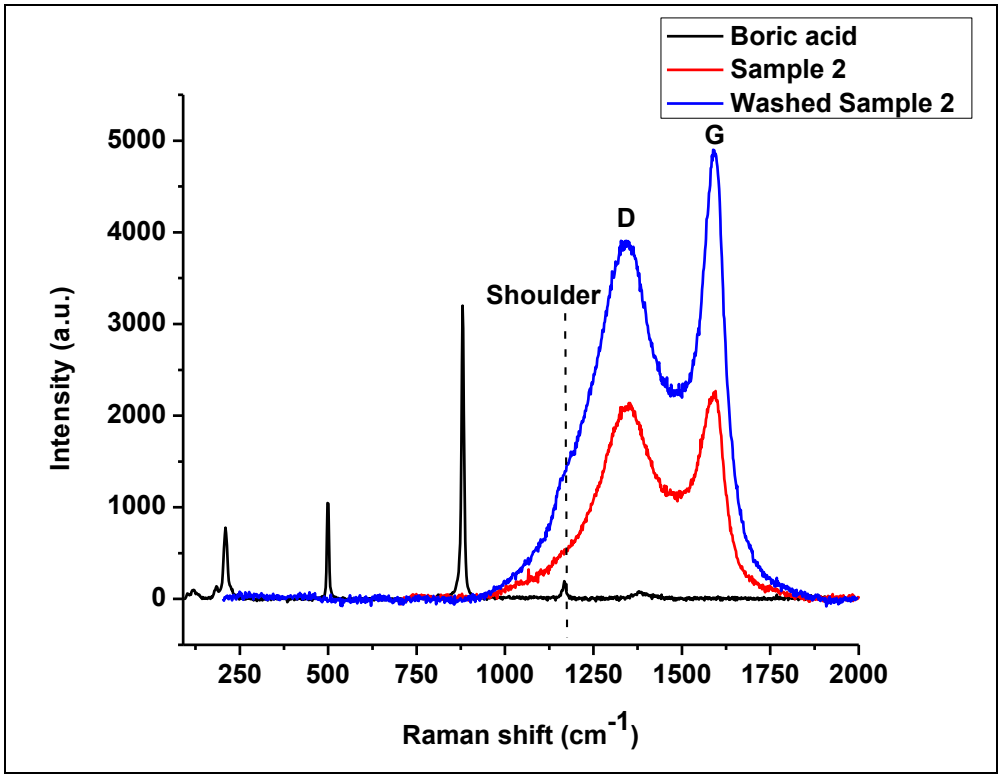


Figure 6.14: Raman spectra for boric acid, unwashed and washed sample 2, with excitation wavelength of 514.5 nm.

6.3.5 FT-IR studies of undoped and B-doped CSs

Figure 6.15 presents the FT-IR spectra of boric acid, undoped and boron-doped CSs. The following bands are present in the spectrum of the H_3BO_3 as shown in Figure 6.15: ~549, 630, 701, 882, 1020, 1055, 1193, 1450, 2255, 2356, 2514 and 3185 cm^{-1}. The observed wavenumbers and the proposed assignments are shown in Table 6.6. These positions coincide with FT-IR bands of boric acid reported by Andrews *et al.*[64] and others.[65(a-d)] According to Sankaran and Viswanathan,[66] bands at 1050-1200 cm^{-1} are characteristics of a C-B bond in boron substituted CNTs. Oki and co-workers[67] observed B_2O_3 FT-IR bands at 1458, 1195 and 795 cm^{-1} in their CNT-B_2O_3 nanocomposites.

The FT-IR spectra of the B-CSs are identical and the FT-IR peaks from boric acid are clearly observed in the boron-containing carbon spheres. The boric acid bands found in B-CSs are attributed to B_2O_3 on the B-CSs surface which reacted with H_2O (moisture). This observation confirmed boron incorporation into the CSs and is in agreement with the results of XPS, XRD, Raman spectroscopy and TGA of the CSs. It can be observed that the FT-IR bands corresponding to B_2O_3 in sample 7 are more intense when compared to those in sample 2. This result further confirmed more B content in sample 7 than in sample 2, in good agreement with the results obtained from the other surface techniques, Raman spectroscopy and XPS. The undoped CSs spectrum did not show any bands corresponding to boric acid. Instead it showed bands at ~2000 cm^{-1} (the highlighted region in Figure 6.15), which can be associated with graphitic carbon. These bands are also found in all B-CS spectra and are absent in the boric acid spectrum.

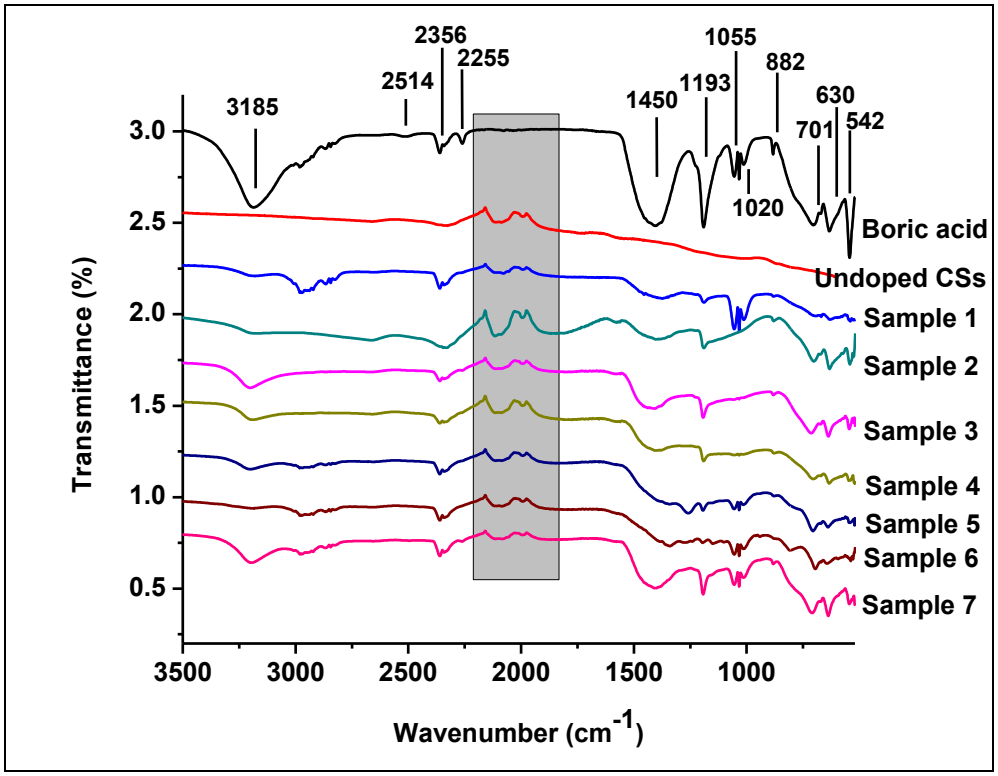


Figure 6.15: FT-IR spectra of boric acid, undoped and boron-doped CSs.

Table 6.6: Wavenumbers and assignment of Infrared Absorption bands for boric acid.

Position (cm^{-1})	**Assignment**	**Reference**
549	O-B-O bending	[65(c)]
630	Symmetric BO_3 deformation	[65 (a-d)]
701	Symmetric BO_3 deformation	[65(c)]
882	Symmetric B-O stretching vibrations	[65 (a-d)]
1055 and 1020	B-O-H bending	[64]
1193	Asymmetric B-O-H bending	[65 (a-d)]
1450	Asymmetric B-O stretching vibration	[65 (a-d)]
2255, 2356, 2514	Overtone bands involving B-O bending and stretching vibrations	[65(c)]
3270 s	Symmetric O-H stretching vibration	[65 (a-d)]

Figure 6.16(a) compares the FT-IR spectra of boric acid, unwashed sample 2 and washed sample 2 with boiling water. The FT-IR spectra revealed that after sample 2 was washed with boiling water, most of the bands seen in unwashed sample 2 due to boron incorporation were removed and some decreased in intensity, as shown in the magnified FT-IR spectrum in the

1200-550 cm^{-1} frequency region (see Figure 6.16(b)). This implies that the B_2O_3 was contained in the carbon spheres. The FT-IR data leads to similar conclusions as found for the XRD, Raman spectroscopy and TGA results for the washed sample 2.

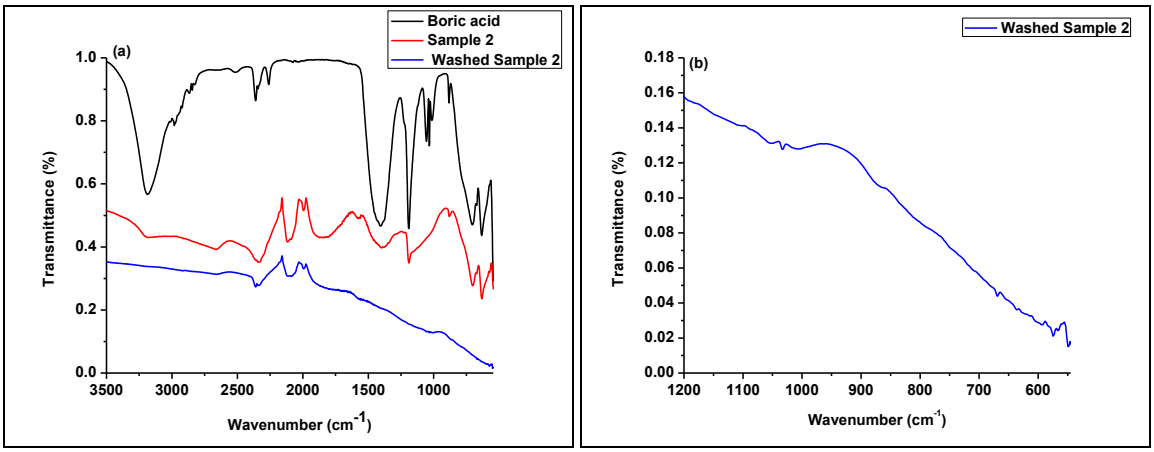


Figure 6.16: FT-IR spectra of (a) boric acid, unwashed and washed sample 2; (b) magnified FT-IR spectrum of washed sample 2.

6.3.6 Mechanism of core-shell structures formation

The mechanism of the formation of the core-single-shelled and core-double-shelled structures is still an open question and needs further study. When similar experiments are carried out in a tube furnace without using trimethylborate,[46] the carbon materials form solid CSs. It is clear that the boron source played a key role in the morphology of the B-CSs, leading to core-shell structures in the presence of both Ar and Ar/H_2 carrier gases. In addition, as mentioned earlier, H_2 gas also had an effect on the formation of core-double-shell B-CSs. Carbon core-shell structures are typically made by depositing a carbon deposit on a spherical template. In their studies in our research group, Ravat *et al.*[42] have made B-doped hollow CSs by passing boron and carbon source over Stöber silica spheres as templates at high temperature. The carbon covered silica spheres were treated with HF to remove the silica and give hollow carbon spheres.

In this study, the $(CH_3O)_3B$ source readily decomposes on both the silica quartz tube walls and on carbon nuclei in the gas phase to give core-shell structures with the B-doped carbon creating the shell and the silica creating the core. The deposition of the $(CH_3O)_3B$ on the

quartz tube also leads to an interaction of the $(CH_3O)_3B$ with the SiO_2 (quartz) resulting in the tube becoming opaque, brittle and weakened.

Reaction of "BOR" species with the carbon generated spherical $C_xB_yO_z$ species and at the high temperature the B and O (and some C) were ejected from the spheres leading to the core-shell or hollow structure. It is believed that the bubble effect on the surface of the core-shell CSs relates to the release of the B, O (and C) species from the spheres. The low B content in not unusual and relates to the stability of the "CBO" spheres formed at high temperature.

6.4 Conclusions

This paper reports a novel method for the synthesis of core-shell carbon spheres by the direct reaction of trimethyl borate as the boron/carbon source and C_2H_2 as the carbon source at 900 °C in a horizontal and a vertical furnace, without using a catalyst. In this study, the effects of boron doping and flow ratios of argon and hydrogen gases on the morphology of the grown boron-doped carbon spheres were studied. When compared to undoped CSs, a significant change in morphology, size, and yield of the CSs on boron doping was observed. The experimental results revealed that the yield and morphological carbon structures were strongly dependent on the flow ratio of Ar and H_2 gases, in which addition of H_2 gas led to the formation of a mixture of single- and double-core shell structured B-CSs.

XPS, TGA, XRD, FT-IR and Raman spectroscopy confirmed the incorporation of boron atoms into the carbon spheres. From the deconvoluted B 1s spectrum, it is clear that the boron atoms in the B-CSs exist in the C-B-O system. Based on the TGA data collected, large quantities of boron were incorporated into the carbon spheres. As this study suggests, when CSs are doped with boron, they decompose more rapidly, as compared to undoped CSs. Overall, the introduction of boron into carbon spheres led to more crystalline structures than found for the undoped CSs as evidenced by XRD and Raman spectroscopy. In addition, it was observed that washing with water reduced the of boron content of the B-CSs. The existence of disorder in the B-CSs indicates that they may be useful as catalyst supports. This synthesis method has the potential for large-scale synthesis of boron-doped carbon spheres.

References

1. (a) N.J. Coville, S.D. Mhlanga, E.N. Nxumalo and A. Shaikjee, *S. Afr. J. Sci.*, 2011, **107**, 1-15; (b) A.A. Deshmukh, S.D. Mhlanga and N.J. Coville, *Mater. Sci. Eng. R*, 2010, **70**, 1-28.
2. L. Li, H. Song and X. Chen, *Carbon*, 2006, **44**, 587-610.
3. F.P. Hu, Z. Wang, Y. Li, C. Li, X. Zhang and P.K. Shen, *J. Power Sources*, 2008, **177**, 61-66.
4. M. Moyo, M.A.M. Motchelaho, H. Xiong, L.L. Jewell and N.J. Coville, *Appl. Catal., A: General*, 2012, **413-414**, 113-119.
5. H. Xiong, M. Moyo, M.A.M. Motchelaho, L.L. Jewell and N.J. Coville, *Appl. Catal., A: General*, 2010, **388**, 168-178.
6. S.D. Mhlanga, K.C. Mondal, N. Naidoo, N. Kunjuzwa, M.J. Witcomb and N.J. Coville, *S. Afr. J. Sci.*, 2009, **105**, 304-308.
7. K.T. Lee, Y.S. Jung and S.M. Oh, *J. Am. Chem. Soc.*, 2003, **125**, 5652-5653.
8. Y. Wang, F.B. Su, J.Y. Lee and X.S. Zhao, *Chem. Mater.*, 2006, **18**, 1347-1353.
9. Z.Y. Zhong, Y.D. Yin, B. Gates and Y.N. Xia, *Adv. Mater.*, 2000, **12**, 206-209.
10. W.H. Shen, Y.F. Zhu, X.P. Dong, and J.L. Shi, *Chem. Lett.*, 2005, **34**, 840-841.
11. Z.H. Wen, Q. Wang, Q. Zhang and J.H. Li, *Electrochem. Commun.*, 2007, **9**, 1867-1872.
12. G. Hu, D. Ma, M. Cheng, L. Liu and X. Bao, *Chem. Commun.*, 2002, 1948-1949.
13. L.Q. Xu, W.G. Zhang, Q. Yang, Y.W. Ding, W.C. Yu and Y.T. Qian, *Carbon*, 2005, **43**, 1090-1092.
14. G.F. Zou, D.B. Yu, J. Lu, D.B. Wang, C.L. Jiang and Y.T. Qian, *Solid State Commun.*, 2004, **131**, 741-752.
15. W. Liu, M.W. Shao, Q. Tang, X.Y. Chen, Z.P. Liu and Y.T. Qian, *Carbon*, 2003, **41**, 1682-1685.
16. X.G. Yang, C. Li, W. Wang, B.J. Yang, S.Y. Zhang and Y.T. Qian, *Chem. Commun.*, 2004, **3**, 342-343.
17. C.Z. Wu, X. Zhu, L.L. Ye, C.Z. Ou Yang, S.Q. Hu, L.Y. Lei and Y. Xie, *Inorg. Chem.*, 2006, **45**, 8543-8550.
18. Z.F. Wang, P.F. Xiao and N.Y. He, *Carbon*, 2006, **44**, 3277-3284.
19. Y.D. Xia and R. Mokaya, *Adv. Mater.*, 2004, **16**, 886-891.

20. J. Etzkorn, H.A. Therese, F. Rocker, N. Zink, U. Kolb and W. Tremel, *Adv. Mater.*, 2005, **17**, 2372-2375.
21. J.W. Jang, C.E. Lee, S.C. Lyu, T.J. Lee and C.J. Lee, *Appl. Phys. Lett.*, 2004, **84**, 2877-2879.
22. A.A. Koós, F. Dillon, E.A. Obraztsova, A. Crossley and N. Grobert, *Carbon*, 2010, **48**, 3033-3041.
23. Z.N. Tetana, S.D. Mhlanga, R.W.M. Krause and N.J. Coville, Synthesis of Boron-doped MWCNTs, *to be published*.
24. B.C. Satishkumar, A. Govindaraj, K.R. Harikumar, J.-P. Zhang, A.K. Cheetham and C.N.R. Rao, *Chem. Phys. Lett.*, 1999, **300**, 473-477.
25. O. Stephan, P.M. Ajayan, C. Colliex, Ph. Redlich, J.M. Lambert, P. Bernier and P. Lefin, *Science*, 1994, **266**, 1683-1685.
26. Ph. Redlich, J. Loeflller, P.M. Ajayan, J. Bill, F. Aldinger and M. Rühle, *Chem. Phys.Lett.*, 1996, **260**, 465-470.
27. D. L. Carroll, Ph. Redlich, X. Blasé, J.-C. Charlier, S. Curran, P.M. Ajayan, S. Roth and M. Rühle, *Phys. Rev. Lett.*, 1998, **81**, 2332-2335.
28. A.A. Deshmukh, R. Ul Islam, M.J. Witcomb, W.A.L. van Otterlo and N.J. Coville, *Chem.Cat.Chem.*, 2010, **2**, 51-54.
29. X. Zhou, Z. Yang, H. Nie, Z. Yao, L. Zhang and S. Huang, *J. Power Sources*, 2011, **196**, 9970- 9974.
30. Y. Liao, L. Gao, X. Zhang and J. Chen, *Mater. Res. Bull.*, 2012, **47**, 1625-1629.
31. Z. Zhang, R. Zhang, C. Li, L. Yuan, P. Li, L. Yao and S. Liu, *Electroanal.*, 2012, **24**, 1424-1430.
32. F. Ma, H. Zhao, L. Sun, Q. Li, L. Huo, T. Xia, S. Gao, G. Pang, Z. Shi and S. Feng, *J. Mater. Chem.*, 2012, **22**, 13464-13468.
33. J.L. Blackburn,Y. Yan, C. Engtrakul, P.A. Parilla, K. Jones, T. Gennett, A.C. Dillon and M.J. Heben *Chem. Mater.*, 2006, **18**, 2558-2566.
34. B. Wang, Y. Ma, Y. Wu, N. Li, Y. Huang and Y. Chen, *Carbon*, 2009, **47**, 2112-2142.
35. R. Moradian and S. Azadi, *Physica E*, 2006, **35**, 157-160.
36. Z. R. Ismagilov, A.E. Shalaginaa, O.Yu. Podyacheva, A.V. Ischenko, L.S. Kibis, A.I. Boronin, Y.A. Chesalov, D. I. Kochubey, A.I. Romanenko, O.B. Anikeeva, T.I. Buryakov and E.N. Tkachev, *Carbon*, 2009, **47**, 1922-1929.
37. T. Morita and N. Takami, *Electrochim. Acta*, 2004, **49**, 2591-2599.

38. L.E. Jones and P.A. Thrower, *Carbon*, 1991, **29**, 251-269.
39. K.C. Mondal, A.M. Strydom, Z. Tetana, S.D. Mhlanga, M.J. Witcomb, J. Havel, R.M. Erasmus and N.J. Coville, *Mater. Chem. Phys.*, 2009, **114**, 973-977.
40. K. Hidetaka, M. Ryoko, K. Hajime, S. Akihiro, H. Hiroki and I. Michio, *Tanso*, 2005, **219**, 221-225.
41. Zhang, G. Wen, X. Huang, B. Zhong and H. Yu, *Cryst. Eng. Comm.*, 2010, **12**, 3506-510.
42. V. Ravat, I. Nongwe and N.J. Coville, *Chem.Cat.Chem.*, 2012, **4**, 1930-1934.
43. A.B. Bose and J. Yang, Microspheres and their methods of preparation, Application number: 12/720, 102, US Patent 2010/0237295 A1, Publication date: 23/09/2010.
44. W. Cermignani, T.E. Paulson, C. Onneby, and C.G. Pantano, *Carbon*, 1995, **33**, 367-374.
45. L. Dong, J. Jiao, S. Foxley, D.W. Tuggle, C.L. Mosher and G.H. Grathoff, *J. Nanosci. Nanotechnol.*, 2002, **2**, 155-160.
46. Z.N. Tetana, S.D. Mhlanga, R.W.M. Krause and N.J. Coville, Large-scale Synthesis of Nitrogen-Doped Carbon Spheres (N-CSs) and undoped Carbon Spheres (CSs) by the vertical CVD reactor, *to be published.*
47. J.-Y. Miao, D.W. Hwang, K.V. Narasimhulu, P.-I. Lin, Y.-T. Chen, S.-H. Lin and L.-P. Hwang, *Carbon*, 2004, **42**, 813-822.
48. Y. Liu, L. Zhang, L. Cheng, W. Yang and Y. Xu, *J. Ceram. Process. Res.*, 2009, **10**, 257-262.
49. D.P. Hashim, N.T. Narayanan, J.M. Romo-Herrera, D.A. Cullen, M.G. Hahm, Peter Lezzi, J.R. Suttle, D. Kelkhoff, E. Muñoz-Sandoval, S. Ganguli, A.K. Roy, D.J. Smith, R. Vajtai, B.G. Sumpter, V. Meunier, H. Terrones, M. Mauricio, Terrones and P.M. Ajayan, *Sci. Rep.*, 2012, **2**, 363/1-363/8.
50. F.H. Monteiro, D.G. Larrude, M.E.H. Maia da Costa, L.A. Terrazos, R.B. Capaz, and F.L. Freire, Jr, *J. Phys. Chem. C*, 2012, **116**, 3281-3285.
51. P. Ayala, M.H. Rümmeli, T. Gemming, E. Kauppinen, H. Kuzmany and T. Pichler, *Phys. Status Solidi B*, 2008, **245**, 1935-1938.
52. P. Ayala, W. Plank, A. Grueneis, E.I. Kauppinen, M.H. Rümmeli, H. Kuzmany and T. Pichler, *J. Mater. Chem.*, 2008, **18**, 5676-5681.
53. P. Ayala, J. Reppert, M. Grobosch, M. Knupfer, T. Pichler, and A.M. Rao, *Appl. Phys. Lett.*, 2010, **96**, 183110-183113.
54. S.C. Lyu, J.H. Han, K.W. Shin and J.H. Sok, *Carbon*, 2011, **49**, 1532-1541.

55. L.S. Panchalkarla, A. Govindaraj and C.N.R. Rao, *ACS Nano*, 2007, **1**, 494-500.
56. T.I.T. Okpalugo, P. Papakonstantinou, H. Murphy, J. McLaughlin and N.M.D. Brown, 2005, *Carbon*, **43**, 153-161.
57. C. Nyambo, E. Kandare and C.A. Wilkie, *Polym. Degrad. Stab.*, 2009, **94**, 513-520.
58. D.P. Singh, P.K. Iyer and P.K. Giri, *J. Appl. Phys.*, 2010, **108**, 084313-0843110.
59. M. Endo, T. Hayashi, S.-H. Hong, T. Enoki and M.S. Dresselhaus. *J. Appl. Phys.*, 2001, **90**, 5670-5674.
60. M.S. Dresselhaus, F. Villalpando-Paez, Ge.G. Samsonidze, S.G. Chou, G. Dresselhaus, J. Jiang, R. Saito, A. G. Souza Filho, A. Jorio, M. Endo and Y.-A. Kim, *Physica E*, 2007, **37**, 81-87.
61. S. Ishii, T. Watanabe, S. Ueda, S. Tsuda, T. Yamaguchi and Y. Takano, *Appl. Phys. Lett.*, 2008, **92**, 202116/1-202116/3.
62. K.C. Mondal, N. J. Coville, M.J. Witcomb, G. Tejral and J. Havel, *Chem. Phys. Lett.*, 2007, **437**, 87-91.
63. C.F. Chen, C.L. Tsai and C.L. Lin, *Diam. Rel. Mater.*, 2003, **12**, 1500-1504.
64. L. Andrews and T.R. Burkholder, *J. Phys. Chem.*, 1992, **97**, 7203-7210.
65. (a) E. F. Medvedev and A. Sh. Komarevskaya, *Glass Ceram.*, 2007, **64**, 42-46; (b) R.E. Zeebe, *Geochim. Cosmochim.Acta*, 2005, **69**, 2753-2766; (c) J.P. Parsons and M.E.Milberg, *J. Am. Ceram. Soc.*, 1960, **43**, 326-330; (d) S. Mondal and A.K. Banthia, *J. Eur. Ceram. Soc.*, 2005, **25**, 287-29.
66. M. Sankaran and B. Viswanathan, *Carbon*, 2007, **45**, 1628-1635.
67. A. Oki, L. Adams and Z. Luo, *Inorg. Chem. Commun.*, 2008, **11**, 275-278.

Appendix D: Supplementary material

Table S1: Surface areas, pore volume and pore diameters of undoped CSs and B-CSs.

Sample ID	Type of furnace	Ar (%)	H_2 (%)	Surface Area (m^2/g)	Pore volume (cm^3/g)	Pore size (nm)
Undoped CSs	Vertical	100	0	11.1	0.023	8.4
Sample 1	Horizontal	100	0	0.96	0.012	51.7
Sample 2	Vertical	100	0	7.51	0.0127	6.8
Sample 3	Vertical	95	5	15.0	0.0444	11.9
Sample 4	Vertical	90	10	11.2	0.0294	10.7
Sample 5	Vertical	80	20	10.4	0.0297	11.7
Sample 6	Vertical	50	50	12.4	0.0325	10.6
Sample 7	Vertical	0	100	14.1	0.0378	10.8

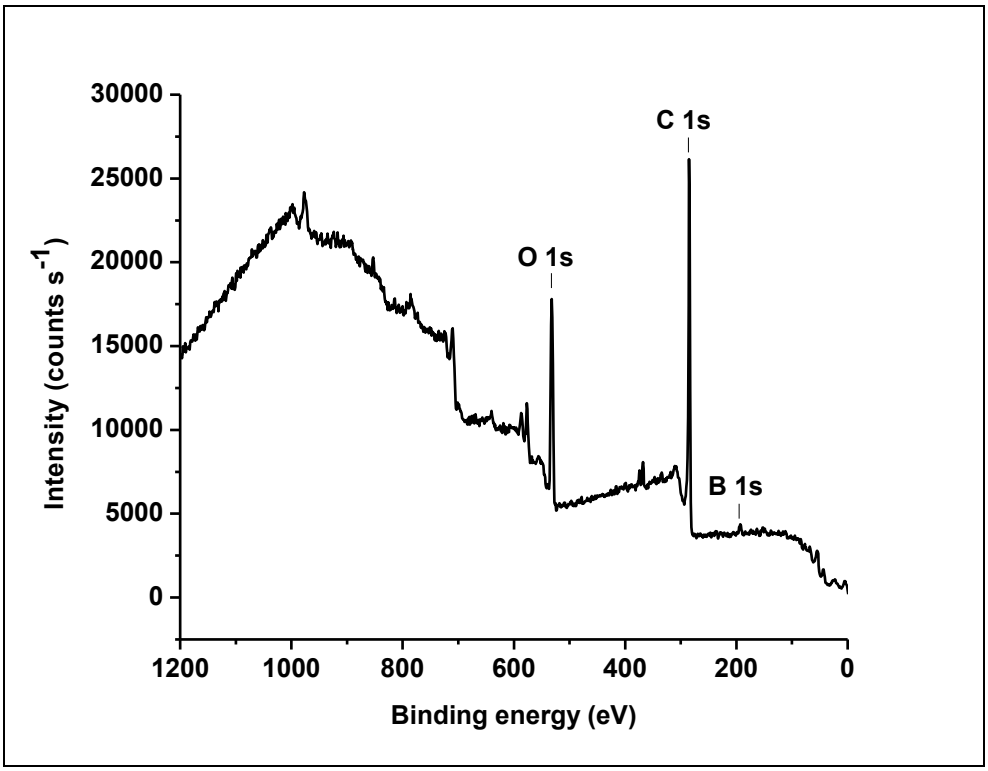


Figure S1: XPS survey spectrum for sample 2.

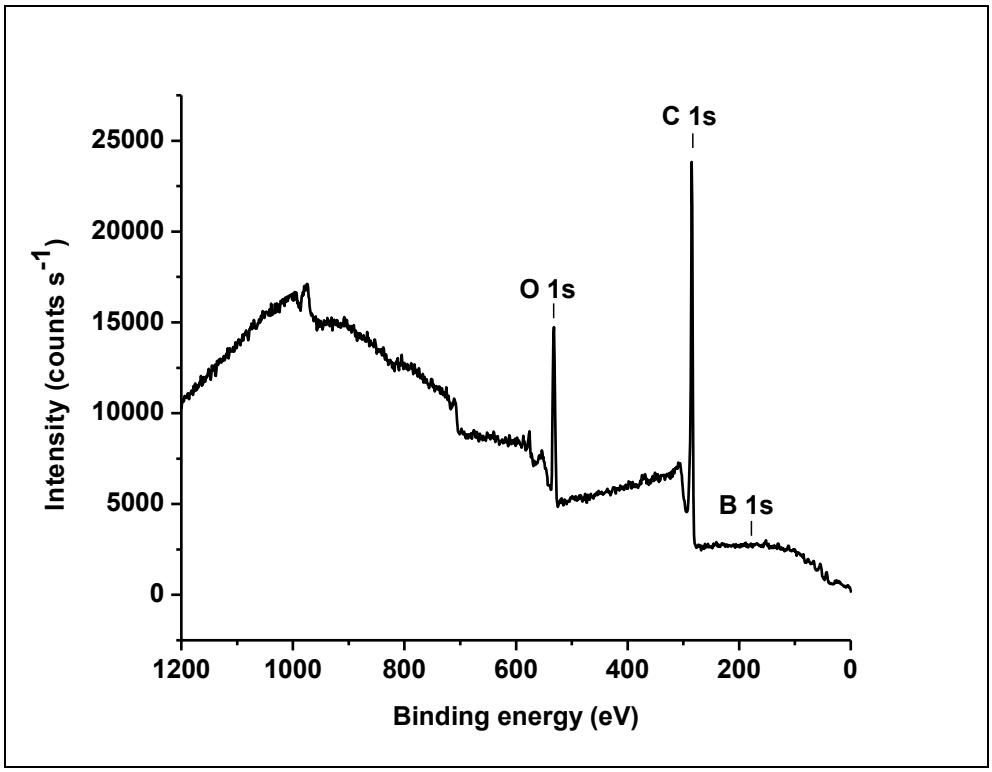


Figure S2: XPS survey spectrum for sample 7.

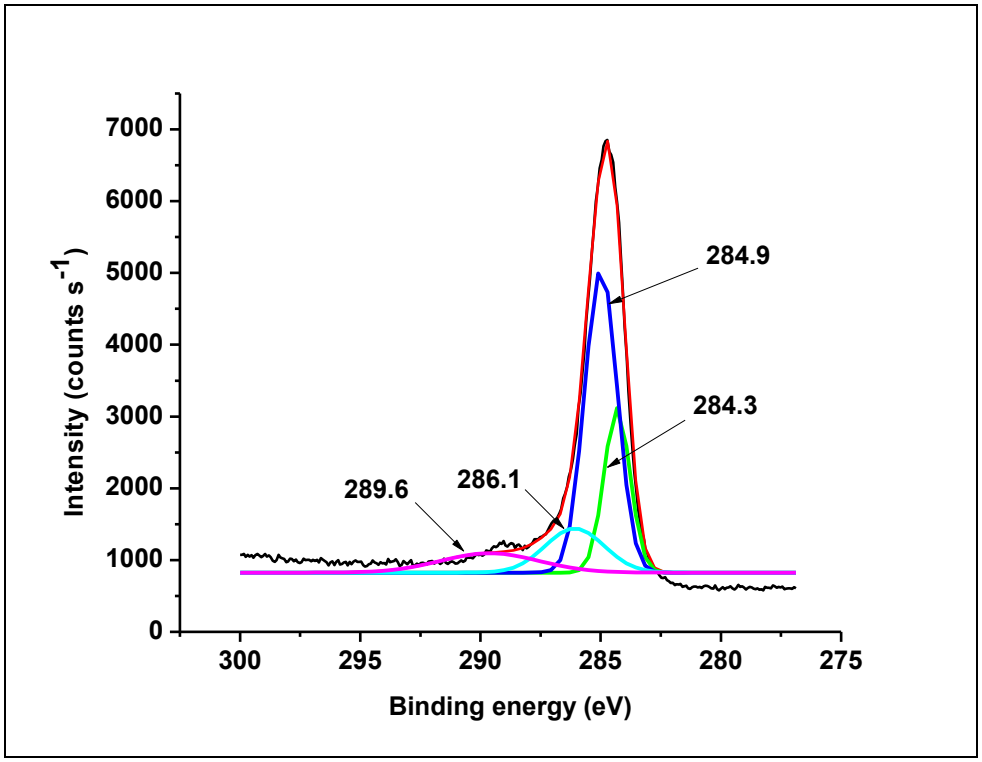


Figure S3: C 1s XPS spectrum for sample 2.

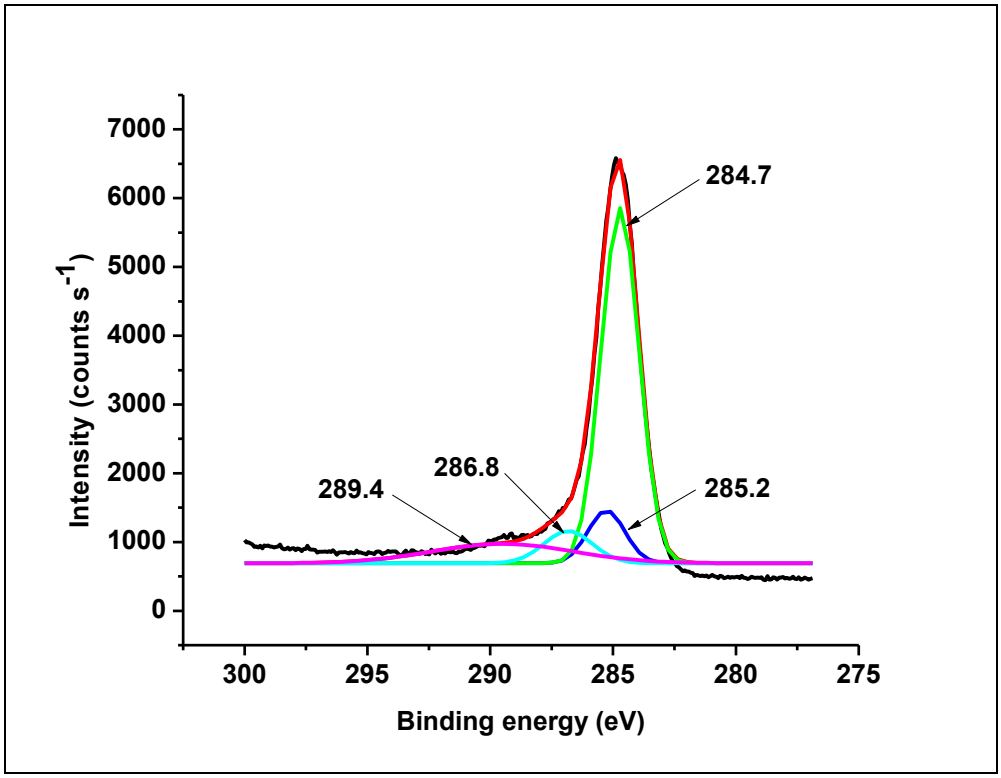


Figure S4: C 1s XPS spectrum for sample 7.

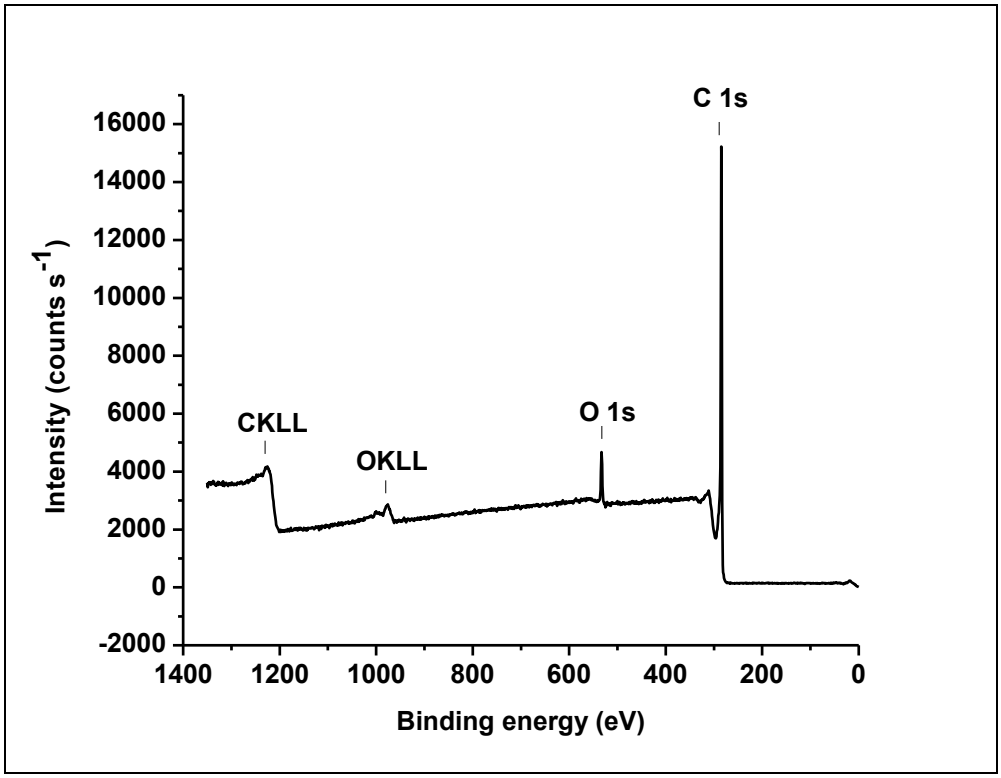


Figure S5: XPS survey spectrum for undoped CSs.

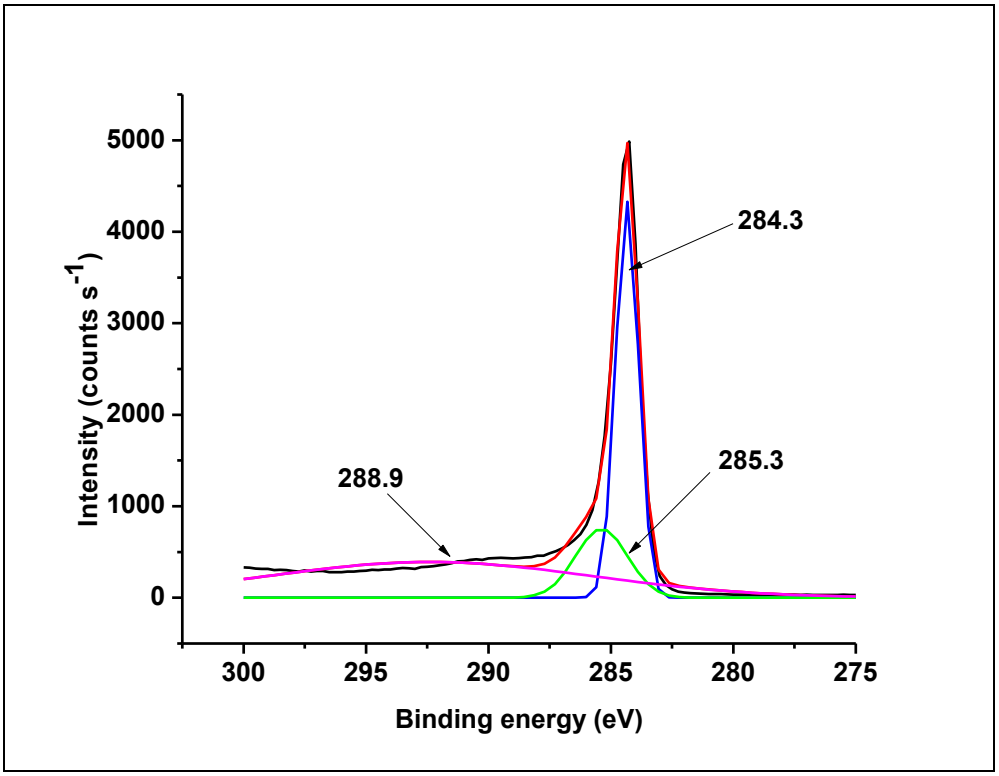


Figure S6: C 1s XPS spectrum for undoped CSs.

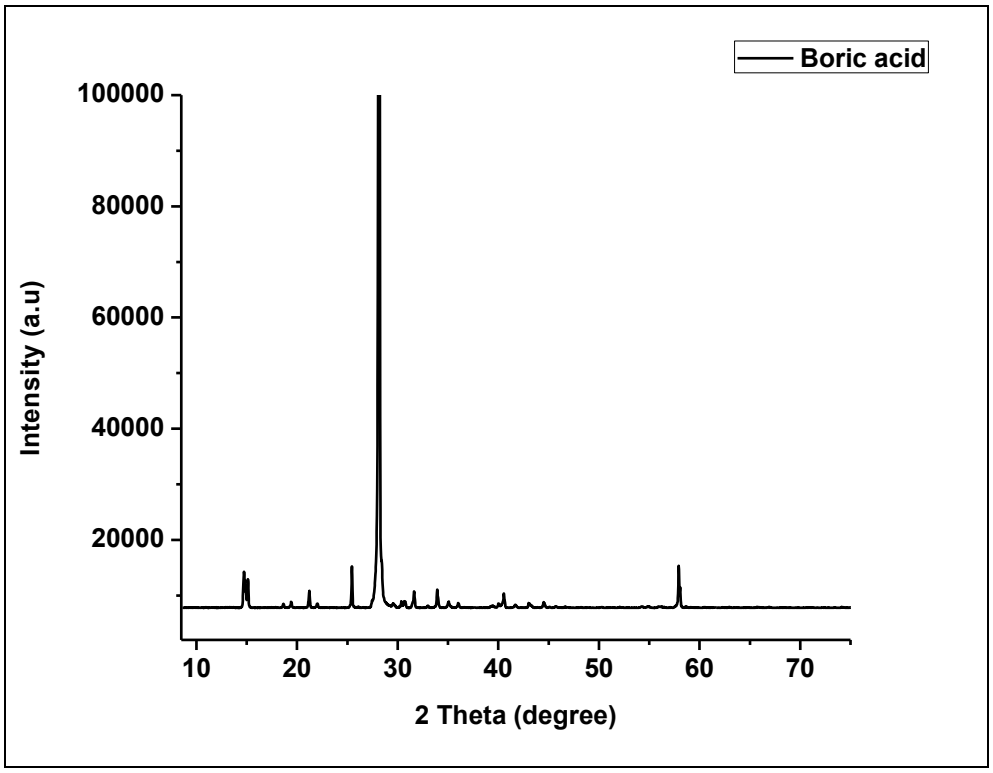


Figure S7: XRD pattern for boric acid.

CHAPTER 7

Photocatalytic Activities of Carbon Nanomaterials Coated with TiO_2 for the degradation of Erythrosine B

7.1 Introduction

In recent years, there has been enormous interest that has been devoted to developing a variety of new and advanced materials to protect the environment, by removing toxic and harmful substances from air, soil and wastewater.[1a,b] In particular, the treatment of dye-containing wastewater generated from the dye manufacturing industries, textile, paint, chemical, printing, food, cosmetic industries, etc., is an environmental problem. Many dyes pose environmental hazards, owing to their toxicity, carcinogenic nature and non-biodegradability. With the mass production of dyes and the continuous increasing demand for clean water, the dye-containing wastewaters need to be treated before being discharged into the drainage system. Thus, advanced and cheap methods are necessary to degrade these organic pollutants or to convert them into non-hazardous end-products. Many attempts have been made to remove these dyes from polluted water, such as flocculation, adsorption, biological methods and chemical processes. However, these conventional techniques are not suitable because they are non-destructive; they only transfer the non-biodegradable substances into sludge, generating another type of pollution, which needs further treatment.[1a,b] Nevertheless, the use of photocatalytic reactions seems to be a promising approach to this problem.

Heterogeneous photocatalysis using semiconductors is one of the effective techniques used to destroy organic dyes leading to inorganic materials such as carbon dioxide, water, nitrates, and chloride ions.[2a,b] Various semiconductor photocatalysts such as Fe_2O_3, ZnO, ZnS, CdS, $SrTiO_3$ and WO_3 have been extensively studied for removing organic pollutants from water, but titanium dioxide (TiO_2) stands in front of others because its low cost, nontoxicity, good chemical inertness and stability, strong oxidizing power and high photocorrossion resistance.[2b,3,4] However, its technological application is limited by its wide band gap energy (3.2 eV for anatase TiO_2), which facilitates a response to ultra-violet (UV) light but a poor response to visible light that accounts for most of solar energy.[5a,b] When the high energy UV light shines on the TiO_2, it generates electron (e^-) and hole (h^+) pairs which are separated

between the conduction and the valence bands of the semiconductor. The positive holes can oxidize H_2O and OH molecules adsorbed on the surface of TiO_2 to form hydroxyl radicals ($OH^{\bullet}$) which are strong oxidants. The adsorbed oxygen (obtained from the atmosphere) can trap electrons, leading to the formation of superoxide radical anions ($O_2^{\bullet-}$). The hydroxyl radicals and superoxides formed can attack the organic pollutants adsorbed on the surface of TiO_2 to form inorganic materials such as H_2O and CO_2. The photo-generated e^- and h^+ can recombine on the surface of the particle and this also limits the efficiency of TiO_2.[6] Many attempts have been made to enhance the photodegradation efficiency of TiO_2 by doping it with transition metals such as Fe[7] and Cu[8] to inhibit the electron-hole recombination during illumination.[9] Doping TiO_2 with non-metal atoms such as N,[10a,b] C,[11a-c] S,[12] B[13a,b] also leads to narrowing of the band gap energy of TiO_2 and greatly improved photocatalytic degradation of dyes in the visible light region. Some studies seem, however, to contradict these findings. Chen and co-workers[14] reported an increase in the band gap of B-TiO_2. Literature data indicated that increased photoactivity in the visible region could be achieved by using a S/N/C-tridoped TiO_2 catalyst, but band gap narrowing was not observed.[15]

It is generally known that photocatalytic activity of TiO_2 also depends on the phase composition (anatase and rutile) and the TiO_2 particle/crystallite size, which determines its surface area.[16a,b] The efficiency of the TiO_2 is also affected by its low surface area and sintering properties. Large surface area and high adsorption capacity are critical to enhance the photoactivity of a TiO_2 photocatalyst. Aiming to improve the catalytic properties of TiO_2, a co-adsorbent with large surface area such as activated carbon has been used as a support for TiO_2 under visible light in the photodegradation of phenol.[17] The authors reported that activated carbon stimulated the formation of a contact interface between both solids and the activated carbon acted as electron carrier and minimized the electron-hole recombination rate, which is favourable for the improvement of photocatalytic activity. The particular properties of nanostructured carbons make them very attractive for their use in a variety of applications, including wastewater treatment. Fullerenes have been reported to be very efficient for the adsorption of organometallic complexes, e.g. organolead,[18] and other complexes such as 1,2-dichlorobenzene[19] and polycyclic aromatic hydrocarbons (PAHs).[20] Due to their large surface area and unique hollow and layered structures, CNTs have been investigated for use as adsorbents to remove toxic and harmful substances from wastewater. It has been reported that CNTs are good adsorbents for the removal of dioxin,[21] 1,2-dichlorobenzene,[22]

trihalomethanes[23] and PAHs.[20] Their high thermal and chemical stabilities suggest that CNTs can be effective as metal supports and as catalyst supports.

Another promising approach is based on TiO_2-CNT nanocomposites to enhance photocatalytic degradation of organic pollutants. The dispersion of TiO_2 on the CNT surface has been reported to create many active sites for the photocatalytic degradation of pollutants.[24] In particular, MWCNTs, due to their electrical conductivity properties, have been shown to exhibit the ability to trap electrons from the conduction band of TiO_2, thereby forming an interface between MWCNTs and TiO_2, leading to the reduction of the electron-hole recombination.[25,26] There have been very few studies focusing on the use of carbon nanospheres in water treatment. Song and co-workers[27] reported the fast adsorption of silver ions from water by carbon spheres. The application of TiO_2 in the presence of CSs has been reported to enhance the adsorption capability for Cr(VI).[28] CdS nanoparticles coated on the surface of colloidal CSs were shown to have high photocatalytic activity in the degradation of rhodamine B.[29] Carbon nanospheres have also been used as template for the synthesis of porous TiO_2 hollow nanospheres, which were very effective in the photocatalytic degradation of methyl orange.[30] In addition, B-doped titania hollow spheres were prepared using hydrothermally preapared CSs as template.[31] The authors found that the B-doped titania hollow spheres were more efficient for the photocatalytic degradation of Reactive Brilliant Red dye X-3B, when compared to commercial P25 TiO_2. Velasco and co-workers[32] synthesized core-shell TiO_2-C (where the TiO_2 shell was surrounded by a carbon core) and TiO_2 hollow spheres using carbon spheres which showed higher photocatalytic activity towards phenol degradation than commercial TiO_2.

The TiO_2-CNT composites have been prepared previously by many methods, including sol-gel synthesis of TiO_2 in the presence of CNTs, mechanical mixing of TiO_2 and CNTs, electrophoretic deposition, CVD and hydrothermal and micro-emulsion.[33a,b] Although it leads to a heterogeneous, non-uniform coating of TiO_2 on CNTs and random clusters of TiO_2 on CNTs, the sol-gel process remains the preferred method since it requires simple equipment as compared to other methods.[33a]

The pristine CNTs and CSs in principle are chemically inert. For any application, their surface has to be functionalized in order to improve and control their properties. The addition of the functional groups to carbonaceous materials through acid treatment is realized as an opportunity to achieve enhanced dispersion in the intended application. The doping of CNTs

with N and B is aimed at altering their electronic properties; this renders them n-type and p-type semiconductors, respectively.[34] Doped TiO_2 (B and N) has also been used to study photocatalytic degradation reactions but these studies could have a relationship to the C doped TiO_2. TiO_2-MWCNT and TiO_2-CS have been investigated for photocatalytic degradation experiments, but no studies are available in the literature to date, which examine the combination of doped MWCNTs or CSs with TiO_2 (e.g. TiO_2-N-doped MWCNTs). In this regard, we chose to coat TiO_2 with some of the N-doped, B-doped and undoped carbonaceous materials reported in Chapters 3-6. Table 7.1 lists the selected materials used in this study. These photocatalysts (Degussa P25 TiO_2, TiO_2-MWCNTs, TiO_2-N-MWCNTs, TiO_2-B-MWCNTs, TiO_2-CSs, TiO_2-N-CSs and TiO_2-B-CSs) were compared for the photocatalytic degradation efficiency of erythrosine B (EB) (Figure 7.1) in aqueous solution as a model organic pollutant. The prepared catalysts were named as TiO_2-C composite materials, where C denotes each type of carbon nanomaterial (undoped MWCNTs, N-MWCNTs, B-MWCNTs, CSs, N-CSs and B-CSs).

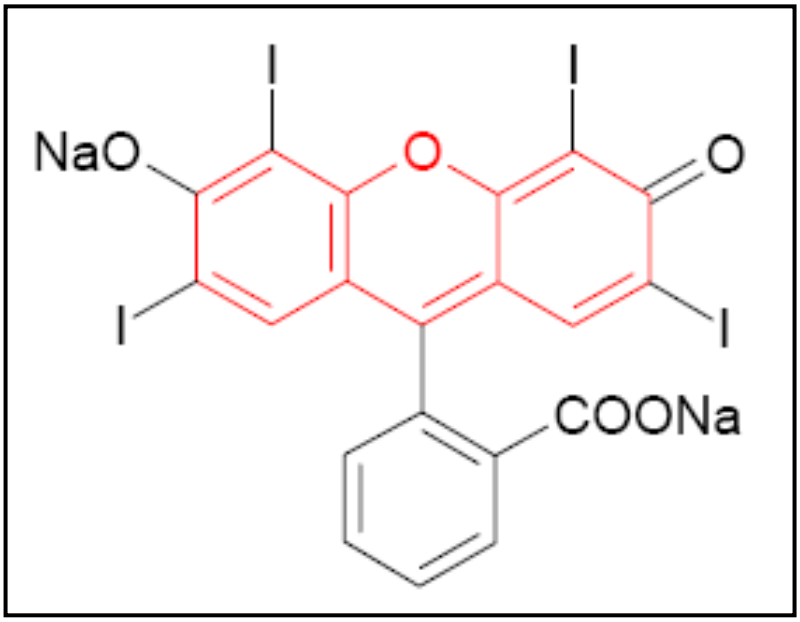


Figure 7.1: Chemical structure of erythrosine B.

7.2 Experimental

Six different types of the synthesized carbon materials, named according to Table 7.1, were used to study the photocatalytic degradation of erythrosine B. Prior to TiO_2 coating, the

carbon materials were treated with HNO_3 to introduce some functional groups on their surfaces. The chosen MWCNTs, N-MWCNTs and B-MWCNTs were functionalized as reported in the previous chapters. The CSs, N-CSs and B-CSs were refluxed in 55% HNO_3 at 100 °C for 17 hours. After cooling to room temperature, the materials were washed with deionized water until a neutral pH of the filtrate was reached. The functionalized carbonaceous materials were then dried in an oven at 120 °C overnight.

Table 7.1: The properties of the carbon materials used in this study.

Sample name	Morphology	Doping level (%) as determined by XPS analysis	Average diameter (nm) as determined by TEM
MWCNTs[a]	Hollow tubes	-	30
N-MWCNTs[b]	Bamboo-like tubes	1.3 at. N	70
B-MWCNTs[c]	Bamboo-like tubes	1.6 at. B	70
CSs[d]	Solid spheres	-	125
N-CSs[e]	Solid spheres	3.1 at. N	125
B-CSs[f]	Core-shell spheres	3.9 at. B	350

a: undoped MWCNTs synthesized at 700 °C (chapter 5); b: nitrogen-doped MWCNTs synthesized at 800 °C and denoted as 800P in chapter 3; c: boron-doped MWCNTs synthesized at 800 °C (chapter 5) ; d: undoped CSs synthesized at 900 °C denoted as CSs-540 in chapter 4; e: N-CSs synthesized at 900 °C denoted as N-CSs-540 in chapter 4; f: B-CSs synthesized at 900 °C denoted as sample 2 in chapter 6.

7.2.1 Synthesis of TiO_2-C composite materials

Reagents: All reagents were used as received. Titanium (IV) butoxide, $Ti[O(CH_2)_3CH_3)_4]$ (≥ 98%, Sigma-Aldrich) was used as a titania precursor. 2-butanol was used as a solvent. Formic acid (~98% purity, Fluka) was purchased from Sigma-Aldrich and used to catalyze the hydrolysis reaction. The commercial TiO_2 (Degussa P25) (~21 nm, ≥ 99.5% purity) used for the comparative studies was purchased from Sigma-Aldrich.

Preparation of TiO_2-0.2%C composite materials: A series of carbon nanostructure supported TiO_2 composite materials (TiO_2-C) were prepared by a modified sol-gel method. The characteristics of the carbon nanostructures used in this study are listed in Table 7.1. For each reaction, the functionalized C materials (0.2% m/m) were sonicated in 2-butanol (10 ml) for 30 min to disperse the C materials. A mixture of titanium (IV) butoxide (10 ml) and 2-

butanol (42 ml) was added drop-wise to the dispersed C materials while stirring vigorously for 30 min, followed by the addition of formic acid (11 ml).[35] After 2 hours of stirring, the precipitate was filtered and washed with 2-butanol followed by washing with deionized water to remove excess butoxide. The wet samples were dried in an oven at 120 °C overnight to remove water. The resulting light-grey samples were ground to fine powders and calcined in air for 4 hours at 400 °C at a heating rate of 5 °C/min in an electric furnace. The resultant materials were characterized by different techniques.

Preparation of TiO_2-10%C composite materials: The preparation of these photocatalysts was done following the same method and weighing the appropriate amounts of C materials to achieve a C:TiO_2 percentage of 10.

7.2.2 Characterization of TiO_2-C composite materials

The structure and morphology of the TiO_2-C composite materials were characterized by transmission electron microscopy (TEM) using a FEI Technai G^2 Spirit electron microscope operated at 120 kV, equipped with X-ray dispersive spectroscopy (EDX) to obtain the bulk chemical information on TiO_2-C composite materials. To prepare the samples for TEM observations, a small amount of each TiO_2-C composite was dispersed in methanol by sonication, and a drop of the suspension was placed on a lacey Cu grid and dried. X-ray diffraction (XRD) patterns were recorded on a Bruker D2 phaser equipped with Cu-Kα radiation (λ = 1.5406 Å), at the operation voltage of 30 kV and current of 10 mA. The average crystallite sizes were estimated by applying the Scherrer equation (Equation 7.1), using the full width at half maximum data of the (101) peak of the TiO_2 anatase phase. The Raman spectra were recorded on a SENTERRA Dispersive Raman Microscope at a laser wavelength of 532 nm, equipped with a cooled charge coupled device detector set at -50 °C. Fourier Transform Infrared (FT-IR) spectroscopy was used to identify functional groups on the materials' surface using a Bruker FT-IR spectrometer (BRUKER TENSOR 27) in the range 4000-500 cm^{-1}. The chemical composition was determined by X-ray photoelectron spectroscopy (XPS) with data obtained on a Kratos Axis Ultra DLD XPS spectrometer equipped with both an Al (monochromatic) and dual Al/Mg anode and a charge neutralizer (Rhodes University, Grahamstown). The operating pressure was kept below $5x10^{-9}$ Torr. The sample was etched with an Ar ion gun (at 4kV) for 5 s to remove residual/adsorbed oxygen

molecules on the surface of the sample. Survey XPS scans were performed with an emission current of 10 mA and the anode (HT) at 15 kV.

$$d = \frac{k\lambda}{\beta \, Cos \, \theta} \quad \text{(Equation 7.1)}$$

where d is the particle size, k is a constant (shape factor, ~0.9), λ is the X-ray wavelength (0.15406 nm), β is the full width at half maximum (FWHM) of the diffraction line and θ is the diffraction angle.

7.2.3 Evaluation of photocatalytic activities of TiO_2-C composite materials

The photocatalytic activity of the TiO_2-C composite materials was measured by the degradation of EB under simulated solar radiation. The commercial TiO_2 was used as a reference material under the same conditions with which the synthesized photocatalysts were compared. For each reaction, 0.1 g of the catalyst was suspended in 100 ml of EB aqueous solution with an initial concentration of 50 ppm under simulated solar radiation. A solar simulator (supplied by Oriel, Newport), equipped with an Oriel 500 W Xe lamp was employed as a source of radiation. The power output was set to 450 W in order to obtain an intensity of 1.000 Wm^{-2} at 25 °C. An Oriel PV reference cell system equipped with a 2x2 cm mono-crystalline Si photovoltaic cell and a Type K thermocouple was used to set the simulator irradiance to 1 sun.[36] Prior to the irradiation, the suspensions were sonicated for 10 min and then magnetically stirred in the dark for 1 hour to allow adsorption/desorption equilibrium to be reached. The first sample (4 ml) was withdrawn at the end of the dark adsorption period. Then, the Xe lamp was switched on to initiate the photocatalytic reaction. Aliquots (4 ml) of the samples were withdrawn at regular intervals (15 min) and immediately filtered through a 0.22 μm PVDF syringe filter for at least 180 min. The degradation of EB was monitored by measuring the absorbance at λ = 525 nm as function of irradiation time with a Shimadzu UV-2450 spectrometer (Japan).

7.3 Results and discussion

7.3.1 Morphology and structure of the TiO_2-C composite materials

The morphology and structure of the TiO_2-C composite materials that were synthesized using the sol-gel method were examined by TEM and compared with TiO_2. Figure 7.2 illustrates the TEM image of commercial TiO_2. It can be seen from the figure that particles are approximately spherically shaped and have a tendency to agglomerate. The average particle size of the TiO_2 ranges from 22-22.5 nm, which agrees with the XRD measurements.

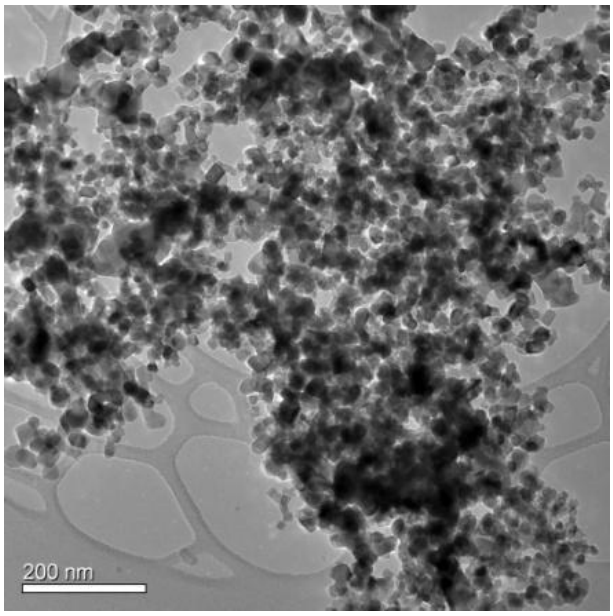


Figure 7.2: TEM image of commercial TiO_2 nanoparticles.

Figures 7.3 and 7.4 display the TEM images of TiO_2-C composite materialscontaining 0.2% m/m and 10% m/m of functionalized carbon nanomaterials, respectively. The TEM images show that TiO_2 nanoparticles were successfully coated on carbon nanomaterials, providing strong evidence of TiO_2 on the well functionalized surface of the original carbon nanomaterials. The TiO_2 nanoparticles showed nearly spherical morphology. Crystallite sizes of the TiO_2 particles in the composites observed from TEM analysis were found to be in the range 10-11 nm, which are in agreement with the values obtained from XRD analysis.

It can be oberved that a loading of 0.2% C in TiO_2-C composites, the carbon nanomaterials were homogeneouly covered by TiO_2 nanoparticles. However, at a loading of 10% C in TiO_2-C composites, the carbon nanomaterials showed poor coverage. This is caused by the

larger amounts of carbon used, which led to poor dispersion of carbon nanomaterials in the solvent (2-butanol) and therefore poor coverage by the TiO_2 nanoparticles. Deposits of TiO_2 nanoparticles on the surface of carbon nanomaterials were also evidenced by EDX analysis. The EDX spectra of the TiO_2-0.2%B-MWCNTs (supplementary Figure S7.1 in Appendix E) and TiO_2-10%B-MWCNTs (supplementary Figure S7.2) composite materials confirmed the presence of carbon, titanium and oxygen.

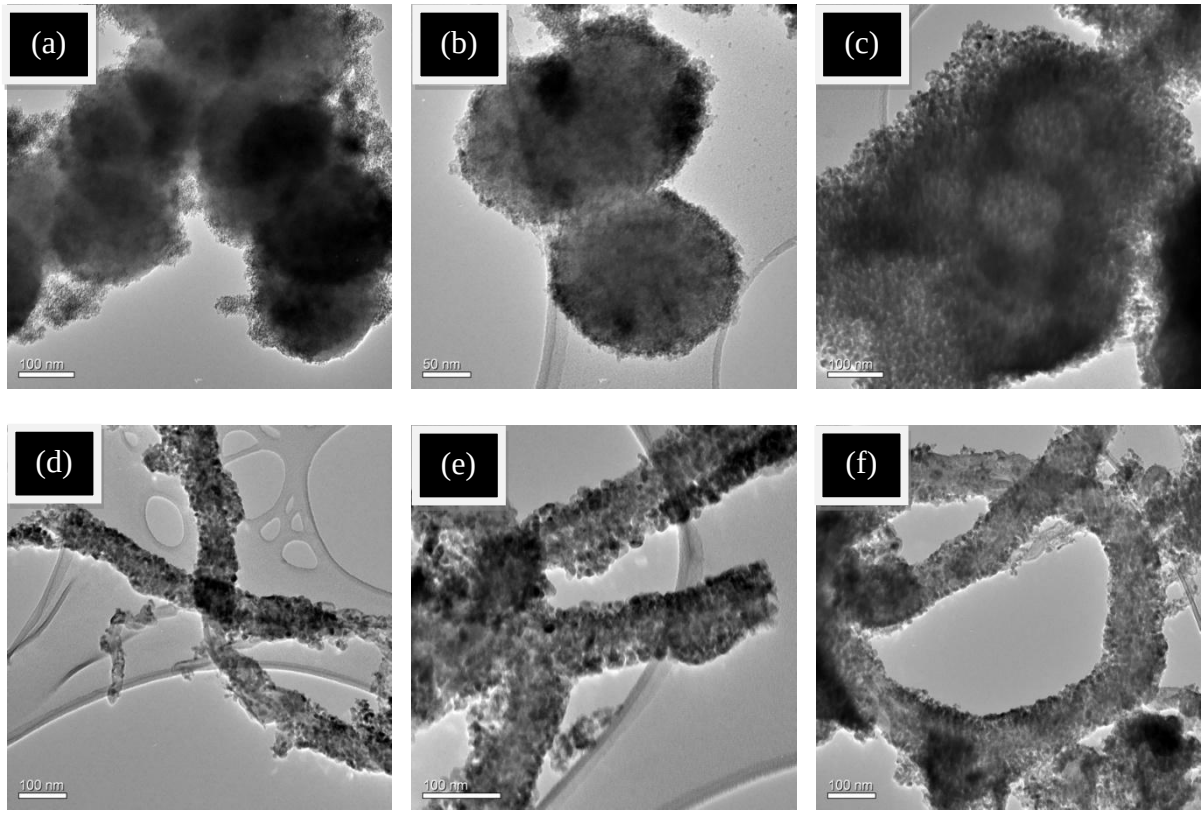


Figure 7.3: TEM images of TiO_2-0.2%C composites: (a) TiO_2-CSs, (b) TiO_2-N-CSs, (c) TiO_2-B-CSs, (d) TiO_2-MWCNTs, (e) TiO_2-N-MWCNTs, and (f) TiO_2-B-MWCNTs.

It was proposed that the defect sites on the surface of the carbon nanomaterials improved the coating by the TiO_2 nanoparticles on the carbon nanomaterials leading to stronger composite formation. TEM observations revealed that the dispersion of the TiO_2 on N-doped and B-doped carbon nanomaterials was better as compared to the undoped ones (Figure 7.3(a,d) and Figure 7.4(a,d)). The better dispersion of TiO_2 on the doped carbon materials could provide the information on the existence of more reactive sites. B-doped and N-doped CNTs by nature have chemically active points which are available for metal or metal oxide nanoparticle anchoring. It has been reported that B-doping into CNTs leads to a uniform

deposition of Pt nanoparticles and also an increase in the electrocatalytic activity for methanol oxidation.[37] SnO_2 coated on N-doped CNTs showed greater photocatalytic activity when compared with SnO_2 coated on undoped CNTs.[38]

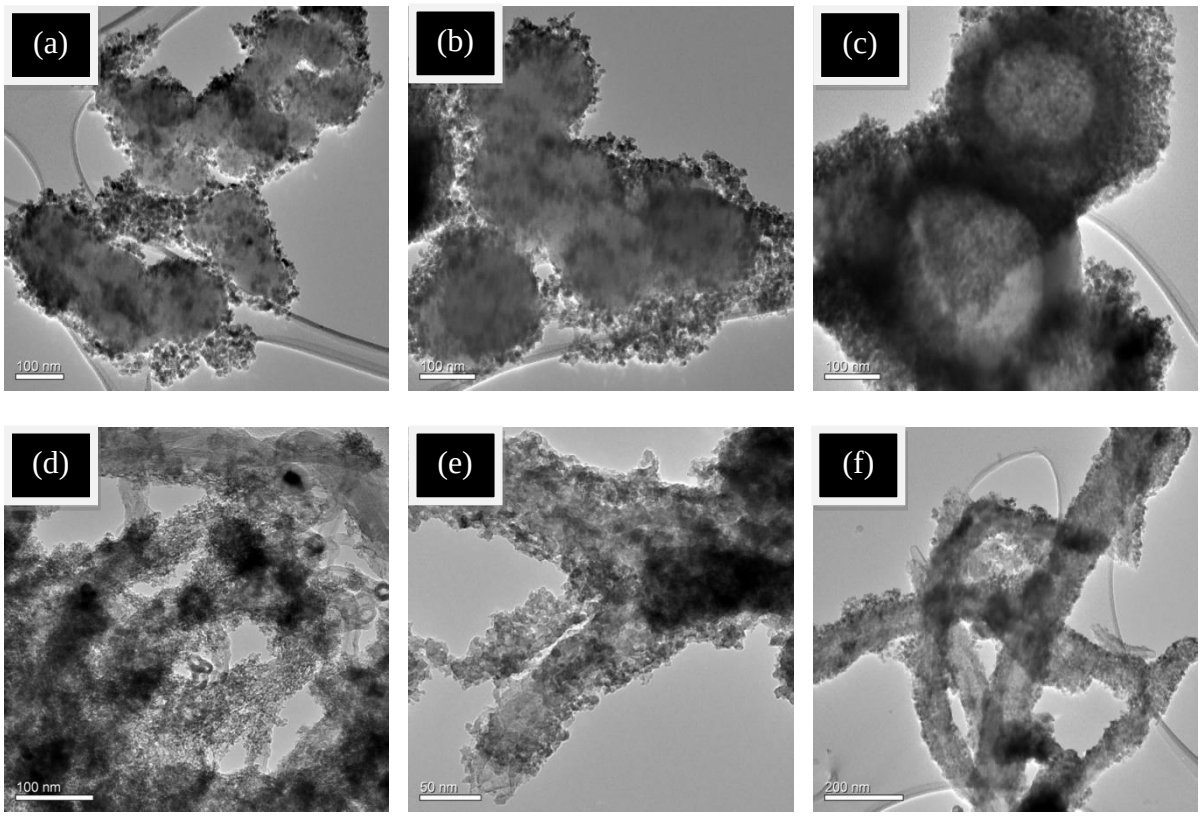


Figure 7.4: TEM images of TiO_2-10%C composites: (a) TiO_2-CSs, (b) TiO_2-N-CSs, (c) TiO_2-B-CSs, (d) TiO_2-MWCNTs, (e) TiO_2-N-MWCNTs, and (f) TiO_2-B-MWCNTs.

7.3.2 XRD analysis of TiO_2-C composite materials

To determine the crystal phase composition of the TiO_2-C composites, XRD measurements were carried out over the diffraction angle range, 10-75°. Figures 7.5 and 7.6 display the XRD patterns of the calcined TiO_2-0.2%C and TiO_2-10%C composite materials, respectively, compared to commercial TiO_2. The diffraction peaks at 25.3, 37.6, 48.1, 53.9, 55.1, 62.7, 69.0, and 70.4° are ascribed to the (101), (004), (200), (105), (211), (204), (116) and (220) planes of TiO_2. This indicates that the particles of TiO_2 in TiO_2-C composites have the anatase phase,[39] which is known to enhance the photocatalytic efficiency of the TiO_2.[40] Thus, carbon nanomaterial inclusion did not cause a change in the crystallite structure of TiO_2. It was noted that the characteristic peaks of the carbon nanostructures such as the (002) reflection could not be seen clearly in all TiO_2-C composites, possibly due to its amorphous

structure and low carbon content in the samples. It can also be considered that the (002) reflection of the C nanomaterials is overlapped by that of anatase TiO_2 (101) reflection, since the crystallinity of TiO_2 is stronger than that of C nanomaterials.[41] As expected, the XRD pattern of the commercial TiO_2 indicated the presence of both anatase and rutile phases of TiO_2. The broader and lower diffraction peaks of TiO_2 in all C-TiO_2 composites suggests a smaller TiO_2 crystallite size[42] and low crystallinity or lattice imperfections[43] as compared to commercial TiO_2. The average particle sizes calculated by the Scherrer equation from the most intense anatase phase (101) in XRD patterns are shown in Table 7.2. The average particle size of commercial TiO_2 was calculated to be 22 nm. The crystallite sizes of the TiO_2-C composites were about half that of the commercial TiO_2. This large decrease in crystallite size indicates that an addition of C material reduced the TiO_2 crystallite size. This outcome may be caused by the strong interaction between the acid pretreated C materials (which possess -COOH and -OH groups) and the -OH groups in the hydrolyzed TiO_2 precursor. In this case, the surface defects of the C nanomaterials may be considered as sites of grain growth for titania crystallites in the TiO_2-C nanocomposites.[44]

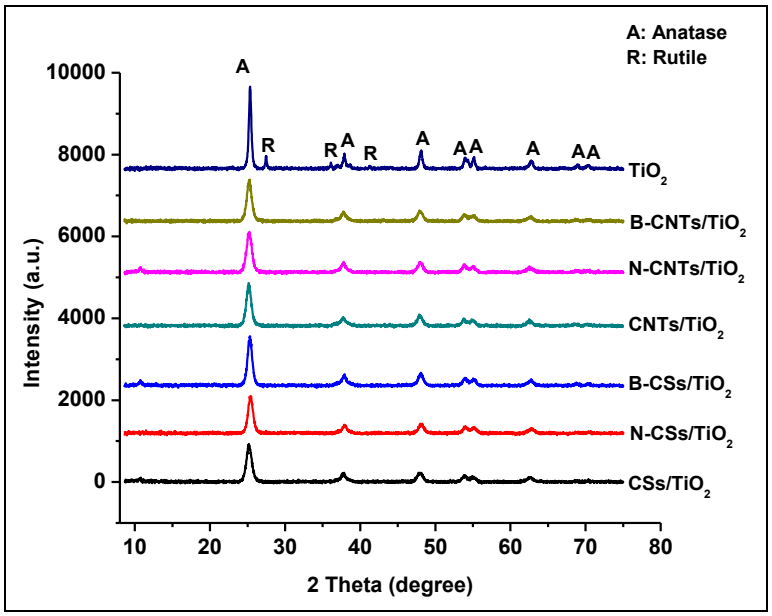


Figure 7.5: XRD patterns of TiO_2-0.2%C composite materials compared with TiO_2.

Interestingly, there was no major difference in the crystallite size of all the TiO_2-C composite materials. This result suggests that the type of C (undoped, nitrogen- or boron-doping) material and the concentration of C (0.2% vs 10%) are not the key factors affecting the size of the TiO_2 particles. However, it has been reported that an increase in MWCNT content can

reduce the crystallite size of TiO_2 in a TiO_2-MWCNT system, and reduced the agglomeration of TiO_2 during the sintering process.[44] Further, Gao *et al.*[33a] reported that the presence of carbon nanotubes (from 0 to 3 wt.%) in the nanocomposites inhibits the TiO_2 growth, resulting in a slight decrease of TiO_2 crystal size, but a further increase of the CNTs (5 to 20 wt.%) showed a moderate increase in the TiO_2 crystal size. It should be added that the different TiO_2-C composites used in this study did not show any significant difference in terms of BET surface areas (not reported). Nevertheless, Wang and co-workers[26] reported that MWCNTs incorporated into TiO_2 nanoparticles can prevent TiO_2 particles from agglomerating and increasing the content of MWCNTs would increase the surface area of the composite materials.

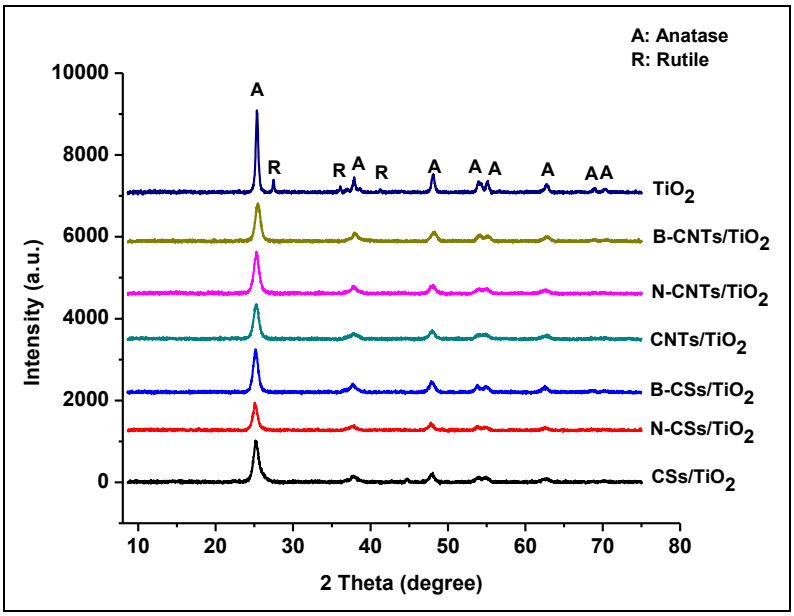


Figure 7.6: XRD patterns of TiO_2-10%C composite materials compared with TiO_2.

Table 7.2: The average particle sizes of TiO_2-C composite materials compared with TiO_2.

Catalyst	TiO_2 crystal size (nm)	Catalyst	TiO_2 crystal size (nm)
Commercial TiO_2	22.3	Commercial TiO_2	22.3
TiO_2-0.2%MWCNTs	11.3	TiO_2-10%MWCNTs	11.4
TiO_2-0.2%N-MWCNTs	10.5	TiO_2-10%N-MWCNTs	11.4
TiO_2-0.2%B-MWCNTs	10	TiO_2-10%B-MWCNTs	10
TiO_2-0.2%CSs	11	TiO_2-10%CSs	10.4
TiO_2-0.2%N-CSs	10.9	TiO_2-10%N-CSs	10.9
TiO_2-0.2%B-CSs	11.4	TiO_2-10%B-CSs	10.1

7.3.3 Raman spectroscopy studies of TiO_2-C composite materials

Raman spectroscopy was also used to confirm the chemical composition of the TiO_2-C composites. Figures 7.7(a,b) and 7.8(a,b) give the Raman spectra of the TiO_2-0.2%C and TiO_2-10%C composites, respectively, in comparison with that of commercial TiO_2. According to literature, the anatase TiO_2 has six Raman active modes ($1A_{1g}$, $2B_{1g}$ and $3E_g$).[45] It has been reported that these six modes appear at 144 cm^{-1} (E_g), 197 cm^{-1} (E_g), 399 cm^{-1} (B_{1g}), 513 cm^{-1} (A_{1g}), 519 cm^{-1} (B1g) and 639 cm^{-1} (E_g).[36,45] Raman spectra bands of rutile TiO_2 have been reported at 143 cm^{-1} (superimposed with the 144 cm^{-1} band due to the anatase phase), 235 cm^{-1}, 447 cm^{-1}, 612 cm^{-1} and 826 cm^{-1} with symmetries of B_{1g}, E_g, E_g, A_{1g} and B_{2g}, respectively.[46] In Figures 7.7a, the Raman peaks of the TiO_2-0.2%C composites are similar to those in the commercial TiO_2 (144, 196, 396, 513 and 636 cm^{-1}), except that the frequency shifted to the right, the line width broadened and their intensities decreased relative to P25 titania. The Raman peaks at 146, 197, 397, 515 and 639 cm^{-1} in the TiO_2-0.2%C composites can be assigned to E_g, E_g, B_{1g}, $A_{1g}+B_{1g}$ and Eg modes of the anatase phase, respectively. It was observed that the E_g mode of the TiO_2-0.2%B-MWCNT dramatically increased to 152 cm^{-1} and the high-frequency Raman lines were broader when compared to other TiO_2-0.2%C composites, which may be a result of the slightly smaller TiO_2 crystallite size. It has been reported that such a shift is due to phonon confinement caused by a decrease in crystal size of anatase.[47] Raman scattering is very sensitive to the crystallinity of the materials. Zhang *et al.*[43] reported that when Raman lines become weak and broad, the samples have local lattice imperfections. Thus, the TiO_2-0.2%C composites to some extent lack good crystallinity. The shifting of the E_g bands of the TiO_2-0.2%C composites towards higher frequency was also associated with some substitution of the Ti^{4+} by carbon forming Ti-O-C bonds in the TiO_2 lattice.[48,49] These observations are consistent with the XRD data, which showed the TiO_2 anatase phase and a lower crystallinity as the particle size decreased with the introduction of C materials. The Raman spectral features of the TiO_2-10%C composite materials (Figure 7.8a) are very similar to those of commercial TiO_2 and their corresponding TiO_2-0.2%C composites. This indicates that the TiO_2 nanoparticles in the TiO_2-10%C composite materials also have anatase structures. However, compared to TiO_2-0.2%C composite materials, the Raman bands of the corresponding TiO_2-10%C composites broadened and shifted to higher wavenumbers, their intensities slightly decreased, suggesting that the addition of more C leads to relatively smaller TiO_2 particles and a decrease in the

crystallinity of anatase, again coinciding with the XRD results. The above further confirm the formation of the chemical bond between carbon nanomaterials and TiO_2.

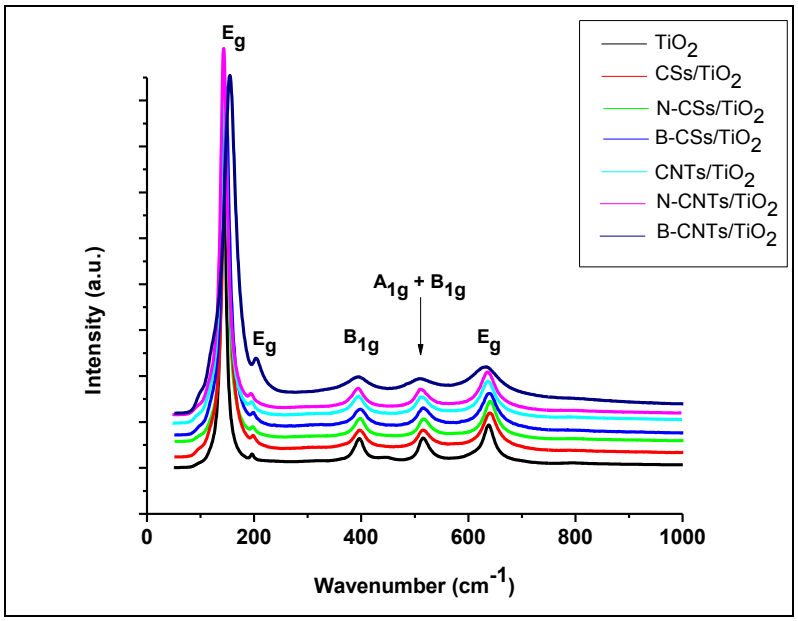


Figure 7.7a: Raman spectra of TiO_2-0.2%C composite materials showing the TiO_2 bands.

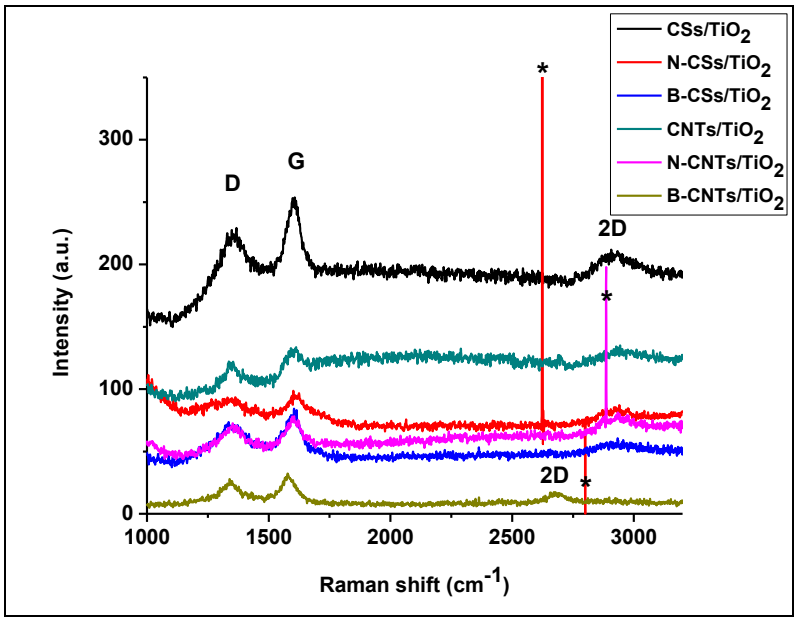


Figure 7.7b: Raman spectra of TiO_2-0.2%C composite materials showing the D, G and 2D-bands. Asterisks in the figure are a result of electric spikes.

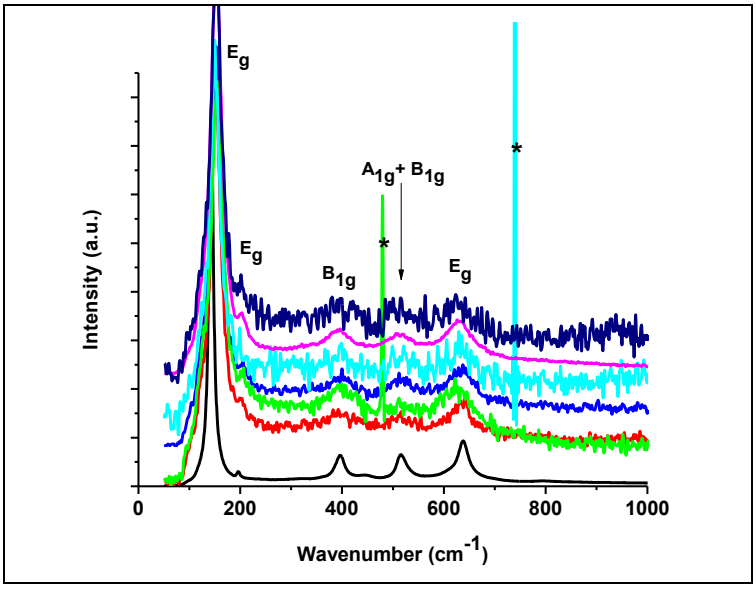


Figure 7.8a: Raman spectra of TiO_2-10%C composite materials showing the TiO_2 bands. Asterisks in the figure are a result of electric spikes.

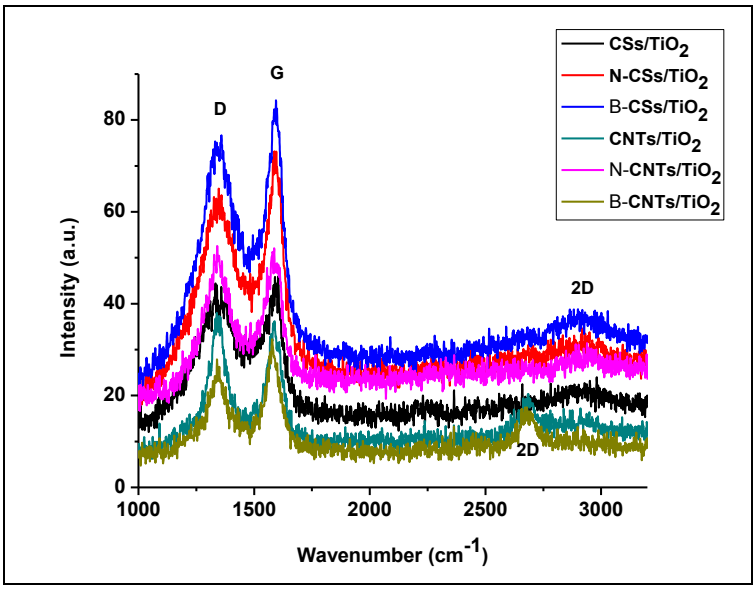


Figure 7.8b: Raman spectra of TiO_2-10%C composite materials showing the D, G and 2D-bands.

Figures 7.7b and 7.8b show the Raman spectra of the TiO_2-0.2%C composites and the corresponding TiO_2-10%C composites in the range 1000-3200 cm^{-1}, respectively. Three Raman bands can be seen near 1354, 1600 and 2670-2900 cm^{-1} in the TiO_2-0.2%C composites and can be ascribed to doped and undoped carbon nanomaterials. The band near 1354 cm^{-1} can be assigned to the disorder-induced sp^2 band (D-band) related to impurities

and amorphous carbon, the peak near 1600 cm^{-1} corresponds to highly oriented E_{2g} mode sp^2 band (G-band), and the peak near 2670-2900 cm^{-1} is the 2D band. Raman spectroscopy data in the respective chapters (3-6) indicated that the carbon nanomaterials (without TiO_2) had many defects on their surfaces. Similar bands, the typical D, G and 2D bands were observed in the corresponding TiO_2-10%C composites. An increase in the D-band intensity and shift of D-band in the Raman spectra of TiO_2-10%C to lower wavenumber ~1347 cm^{-1} can be attributed to the relatively low ordered carbon structure.[50]

It was observed that the TiO_2-0.2%C had a stronger intensity of the TiO_2 bands and relatively weaker D and G bands, but the TiO_2-10%C composites had relatively weaker intensity of TiO_2 bands and stronger D and G bands. It could be considered that the stronger intensity of D and G bands and relatively weaker intensity of TiO_2 bands in TiO_2-10%C composites was a result of higher C loading as compared to the TiO_2-0.2%C materials, although the characteristic peaks of C nanomaterials could hardly been identified from the XRD patterns of all composites. This observation was supported by the presence of uncovered C nanomaterials by TiO_2 as shown in TEM studies in the TiO_2-10%C composites. Higher C content resulted in lower coverage by TiO_2, poor dispersion in the solvent and some bare C nanomaterials, leading to more intense D and G bands. These results are similar to those obtained by Kuvarega *et al.*,[36] which showed that the intensity of the Raman peaks increased with increasing amounts of MWCNTs (from 0.5, 1, 2, 5, to 10%) in the N, Pd TiO_2/MWCNTs composites.

7.3.4 Fourier Transform Infrared (FT-IR) spectroscopy studies of the TiO_2-C composite materials

The nature of surface groups was evaluated by FT-IR spectroscopy. Figures 7.9 and 7.10 display the FR-IR spectra of the TiO_2-0.2%C and TiO_2-10%C composite materials compared with commercial TiO_2, respectively. FT-IR spectra of commercial TiO_2 and TiO_2-C composites show similar shapes. A peak at 3670 cm^{-1} and a weak one ~1645 cm^{-1} in all the samples can be assigned to the stretching vibration and bending vibration of OH on the surface of TiO_2 particles. A highly intense low frequency band at ~525 cm^{-1} appears in the FT-IR spectra of all the materials, which corresponds to the Ti-O stretching vibration. FT-IR spectroscopy was not found to be useful to detect the characteristic carboxylic acid functional groups introduced by acid-treatment of C materials.

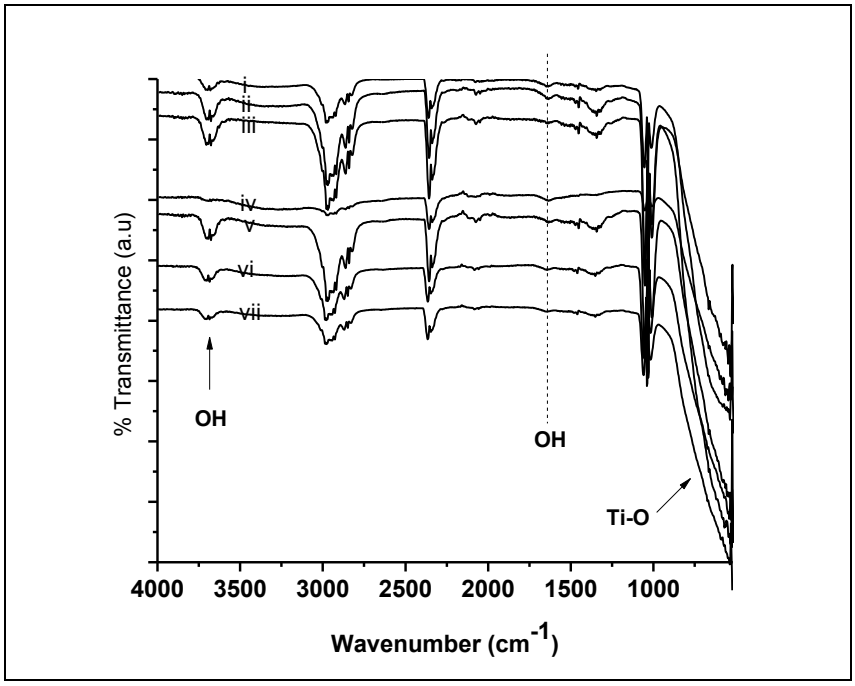


Figure 7.9: FT-IR spectra of TiO_2-0.2%C composite materials: (i) TiO_2, (ii) B-CSs, (iii) N-CSs, (iv) CSs, (v) B-MWCNTs, (vi) N-MWCNTs, (vii) MWCNTs.

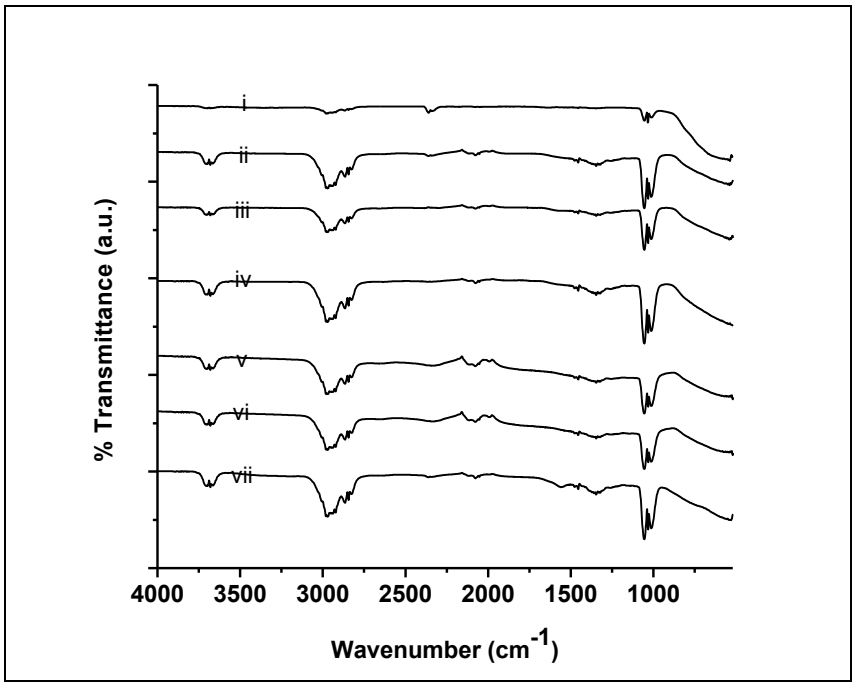


Figure 7.10: FT-IR spectra of TiO_2-10%C composite materials: (i) TiO_2, (ii) B-CSs, (iii) N-CSs, (iv) CSs, (v) B-MWCNTs, (vi) N-MWCNTs, (vii) MWCNTs.

7.3.5 X-ray Photoelectron Spectroscopy (XPS) analysis of the TiO_2-0.2%B-MWCNT composite material

XPS analysis was carried out in order to better understand the composition and chemical bonding of the TiO_2-C composites. The survey XPS spectrum of TiO_2-0.2%B-MWCNT is presented in Figure 7.11. The spectrum indicates that the sample contains C, Ti and O atoms. The binding energies of C 1s, O 1s and Ti 2p are centered at 285 eV, 531 eV and 459 eV with elemental compositions of 11.45%, 61.79%, and 26.76%, respectively. The B signal was too weak to be detected. Figures 7.12, 7.13 and 7.14 show typical C 1s, O 1s and Ti 2p core levels spectra of the TiO_2-0.2%B-MWCNTs, respectively. The C1s spectrum (Figures 7.12) was deconvoluted into three peaks at 284.3 eV, 285.4 eV and 288.5 eV. The peaks at 284.3 eV correspond to sp^2 hybridized C-C, while the one at 285.4 eV can be assigned to C-O[44] and/or defect-containing sp^2 carbon. The peak at 288.5 eV can be assigned to O=C-O and/or Ti-O-C bonds.[48,51a,b] The existence of these functional groups is attributed to the presence of oxidized carbon nanomaterials made during functionalization and could provide increased active sites for direct interaction of C nanomaterials with TiO_2. In this case, the OH groups on TiO_2 surfaces can chemically react with the COOH groups on C nanomaterials to form O=C-O-Ti and/or Ti-O-C bonds.

The oxygen core level spectra of the commercial TiO_2 P25 have been reported to have binding energies at 530.3 eV and 532.4 eV.[52] The high-resolution O 1s XPS spectra presented in Figure 7.13 shows two peaks at 530.7 eV and 531.7 eV, which can be attributed to Ti-O in TiO_2 and the surface –OH groups or chemisorbed water molecules on the TiO_2.[53] These results correlate with the results of FT-IR spectra. It was reported that an enhanced amount of the hydroxyl groups on the surface of the composite can improve the photocatalytic activity.[54] Thus the presence of the OH groups in the composites can have a beneficial effect of increased photocatalytic activity.

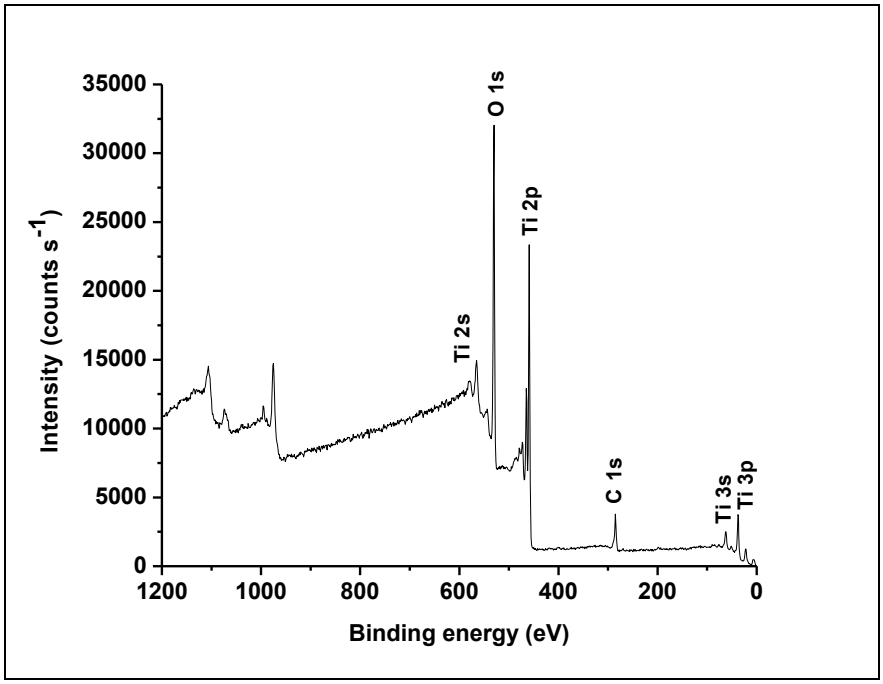


Figure 7.11: XPS survey scan of TiO_2-0.2%B-MWCNT composite.

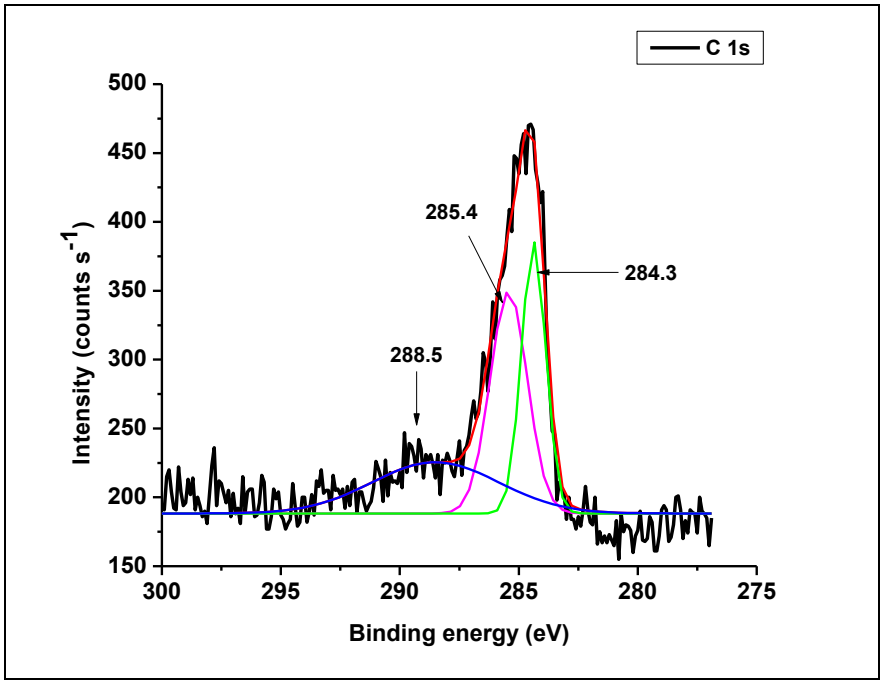


Figure 7.12: Deconvoluted C 1s XPS spectra of the TiO_2-0.2%B-MWCNT composite.

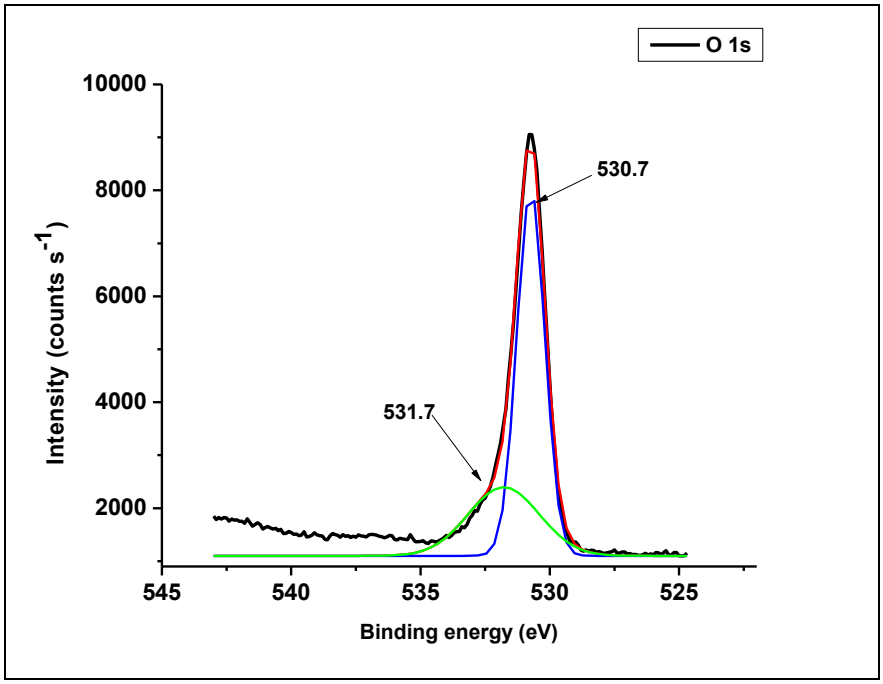


Figure 7.13: Deconvoluted O 1s XPS spectra of the TiO_2-0.2%B-MWCNT composite.

The Ti 2p core level spectra of commercial TiO_2 P25 have been recorded by several researchers. Two peaks observed at 459.0 eV and 464.8 eV were due to Ti^{4+} ($2p_{3/2}$) and Ti^{4+} ($2p_{1/2}$), respectively in TiO_2 P25.[55] XPS characterization of TiO_2 P25 by Alonso-Tellez and co-workers[56] evidenced binding energies of Ti^{4+} ($2p_{3/2}$) and Ti^{4+} ($2p_{1/2}$) at 458.2 eV and 463.9 eV, respectively. The binding energy of Ti ($2p_{3/2}$) in Ti_2O_3, where Ti is in +3 oxidation state, has been reported to be in the range 456.8 to 456.9 eV.[57] In Figure 7.14, three pronounced peaks are observed at binding energies of 458.2 eV, 459.4 eV, and 465.2 eV. The peaks at 458.2 eV and 459.4 eV were both attributed to the Ti ($2p_{3/2}$) state and the peak at 465.2 eV, was attributed to the Ti ($2p_{1/2}$) in Ti^{4+}. The separation between the binding energies of 459.4 and 465.2 eV in the sample was found to be 5.8 eV, consistent with the presence of the normal oxidation state of Ti^{4+} in the TiO_2.[58] In addition, there was no peak observed between 456.8-456.9 eV in the Ti 2p spectrum, indicating the absence of Ti^{3+} in the sample. The observed binding energies (459.4 and 465.2 eV) for the TiO_2-0.2%B-MWCNT are higher than those reported for commercial TiO_2, indicating that the Ti in the composite is in a slightly different chemical environment than that in commercial TiO_2. This suggests substitution of carbon (B-MWCNTs) for oxygen in the TiO_2 lattice. These binding energies values are very close to those reported by Peining *et al.*[59] for TiO_2-MWCNT nanocomposite.

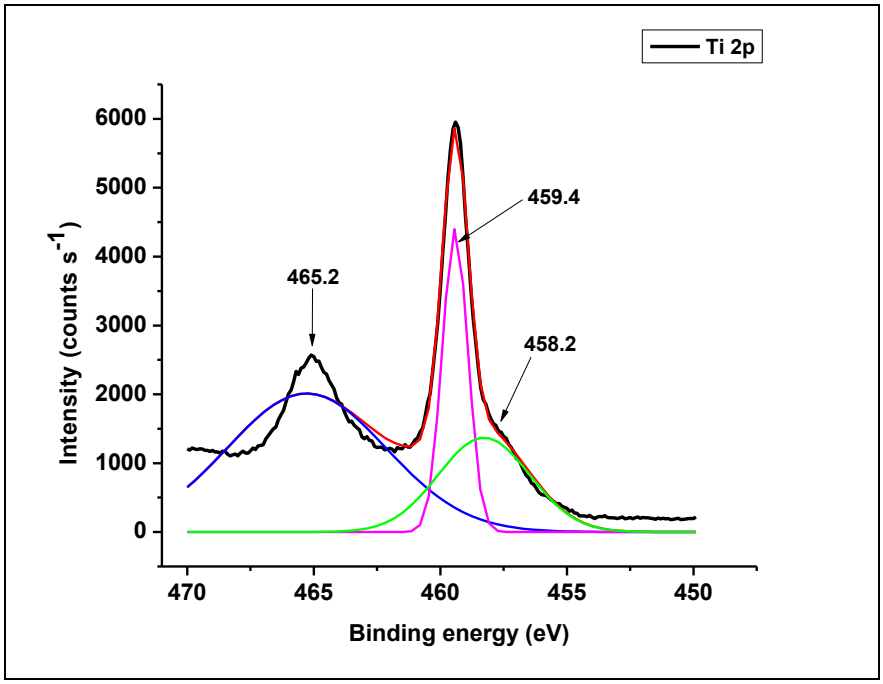


Figure 7.14: Deconvoluted Ti 2p XPS spectra of the TiO_2-0.2%B-MWCNT composite.

7.3.6 Photocatalytic activity of TiO_2-C composite materials

The photocatalytic activities of the TiO_2-0.2%C and TiO_2-10%C composite materials were tested for the degradation of EB under simulated solar light irradiation. Figures 7.15 and 7.16 present the degradation profiles of EB in the presence of TiO_2-0.2%C and TiO_2-10%C composite materials, respectively, with commercial TiO_2 for comparison. As can be seen in Figure 7.16, the photocatalytic degradation rate of various TiO_2-10%C composites decrease in the following order TiO_2>B-MWCNT>N-MWCNT>MWCNT>B-CS>N-CS>CS. The lowest performance of the CSs could be explained in terms of their amorphous nature. The photocatalytic degradation of EB by the TiO_2-10%C composites (Figure 7.16) gave lower degradation performance compared to their corresponding TiO_2-0.2%C composites and commercial TiO_2. The decreased efficiency in the TiO_2-10%C composites could be explained by the non-uniform coating of TiO_2 on the C nanomaterials, showing uncovered C surfaces and random aggregation. These results show that there is an optimum amount of carbon nanomaterial required that can destroy any organic compound. It could be considered that at higher C loadings, the electron-hole pair recombination rate increased[60] or the particles of carbon nanomaterials blocked the light passage and reduced the formation e^--h^+ pairs and active sites. A similar trend was observed for experiments performed under simulated solar light irradiation,[36] in which the lowest loading (N, Pd co-doped TiO_2-0.5%MWCNT) was

found to be the optimum in the degradation of Eosin Yellow compared to N, Pd co-doped TiO_2-(1, 2, 5 and 10%)MWCNT. Table 7.3 displays the dye adsorption and degradation percentages by the TiO_2-0.2%C and TiO_2-10%C composite materials. Table 7.3 shows higher degradation percentages and lower adsorption efficiencies for TiO_2-0.2%C when compared to TiO_2-10%C and neat TiO_2. These results indicate that there was no correlation between photodegradation and dye adsorption, when comparing data for the lower and higher C loadings. For example, the TiO_2-0.2%B-MWCNTs could adsorb 20% of the dye but showed a degradation efficiency of 99% after 3 hours, while TiO_2-10%B-MWCNTs adsorbed 38% of the dye and only 56% degradation on irradiation for 3 hours. However, in other studies, adsorption ability played an important role in the photocatalytic degradation of organic pollutants.[61]

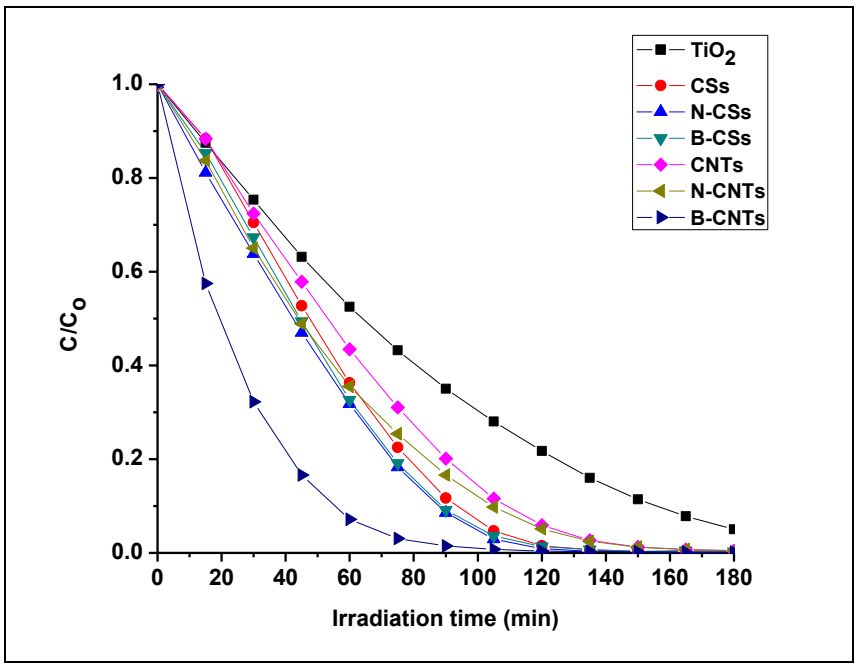


Figure 7.15: Photodegradation of EB by TiO_2-0.2%C composite materials.

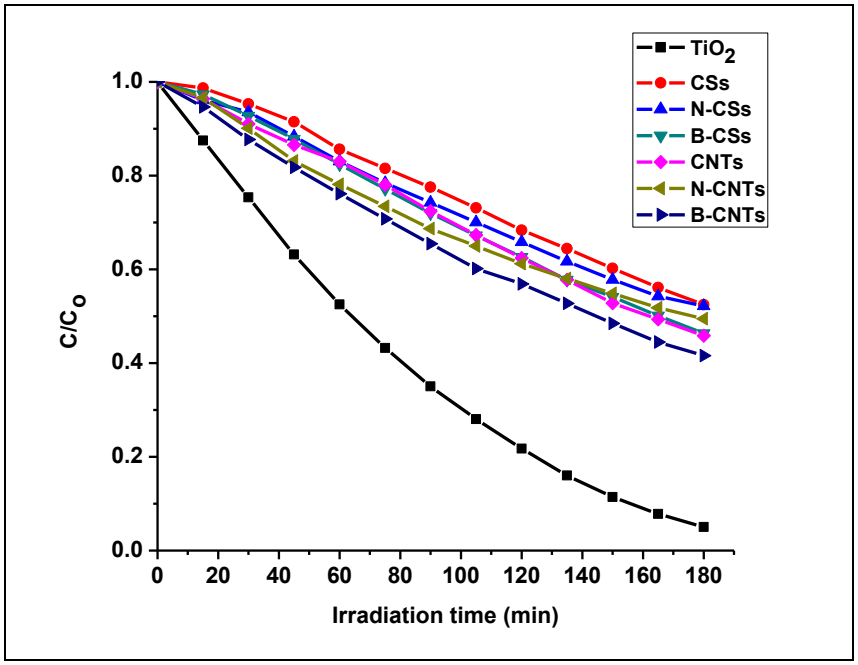


Figure 7.16: Photodegradation of EB by TiO_2-10%C composite materials.

Table 7.3: Dye adsorption and EB photodegradation under simulated solar irradiation.

Catalyst	% Degradation after 180 min (%)	Dye adsorption (%)
TiO_2	94.3	0.10
TiO_2-0.2%CS	99.4	0.31
TiO_2-0.2%N-CS	99.8	0.35
TiO_2-0.2%B-CS	99.7	0.52
TiO_2-0.2%MWCNT	99.5	2.30
TiO_2-0.2%N-MWCNT	99.4	5.5
TiO_2-0.2%B-MWCNT	99.9	20.02
TiO_2-10%CS	45.7	0.66
TiO_2-10%N-CS	46.8	0.76
TiO_2-10%B-CS	52.4	0.85
TiO_2-10%MWCNT	52.4	2.65
TiO_2-10%N-MWCNT	48.8	11.0
TiO_2-10%B-MWCNT	56.0	37.8

It is well known that the combination of MWCNTs with TiO_2 can enhance the photocatalytic degradation of organic pollutants as compared to commercial TiO_2, because MWCNTs can inhibit e^--h^+ recombination by trapping photoexcited electrons generated from the conduction band of TiO_2.[62] In addition, the adsorption ability of the MWCNTs can enhance the catalytic

destruction of organic pollutants. B-MWCNTs have the beneficial effect of increasing the adsorption capacity of O_2 for the Oxygen reduction Reaction (ORR).[63] The boron dopant in the MWCNTs is in the oxidized states (BC_2O or BCO_2) and the positively charged boron atoms are expected to adsorb the O_2 molecule. In nitrogen-doped CNTs, O_2 is adsorbed on the three C atoms adjacent to the N atom, while in pristine CNTs, adsorption of O_2 is not possible since there is no charged site on the tube.[64] In this study, TiO_2-0.2%B-MWCNT showed the highest degradation of EB as compared to other catalysts (Figure 7.15). As mentioned earlier, the TiO_2 anatase phase has better photocatalytic activity than the rutile phase. XRD and Raman results showed that all the composites synthesized here contained only the anatase structure. XRD also showed no significant difference in the TiO_2 crystallite sizes of the TiO_2-C composites. As suggested earlier, there was no direct correlation between the adsorption effect and the degradation efficiency of the EB. In this case, we can consider that the doping effect and the connection between TiO_2 and carbon nanomaterial might play a role in the electron transfer between C and TiO_2. On the basis of literature reports,[62a] mechanism of the photocatalytic activity of TiO_2-C composites can be proposed (Figure 7.17) for theTiO_2-MWCNT composites. Under visible light irradiation, the valence band electrons of TiO_2 can be excited to its conduction band, leaving the positively charged holes behind, and giving rise to the formation e^--h^+ pairs. The holes may react with OH^- or water on the surface of TiO_2 producing hydroxyl radicals ($OH^\bullet$). The $OH^\bullet$ radicals are strong oxidizing agents, which can then destroy the organic dye. On the other hand, the photogenerated electrons can reduce the adsorbed O_2 molecules to create superoxide anion radical ($O_2^{\bullet-}$), which can also degrade the organic dye. At the same time, carbon nanomaterials can adsorb O_2 on its surface, which can react with the promoted electrons in the conduction band to form $O_2^{\bullet-}$ radicals. This leads to an increase in the number of highly reactive species, which can react with the organic dye.

The intrinsic benefit of boron doping is evident. Indeed 97% of EB was degraded by TiO_2-0.2%B-MWCNT within 90 min. This can be attributed to the following reasons (which can lead to the high reduction of e^--h^+ recombination rate): (i) The MWCNTs were doped with boron as BCO_2, which would also adsorb O_2 molecules, that can react with the promoted electrons, thereby increasing the number of $O_2^{\bullet-}$ radicals that can react with the target; (ii) The well-known p-type semiconducting behavior (hole charge carriers) of B-doped CNTs might enhance the photocatalytic activity of TiO_2-B-MWCNT composite. It has been reported that

in B-doped CNTs the holes diffuse away from the Si-nanotube junction, thereby reducing e^--h^+ recombination and hence improving the efficiency of the photovoltaic device.[65]

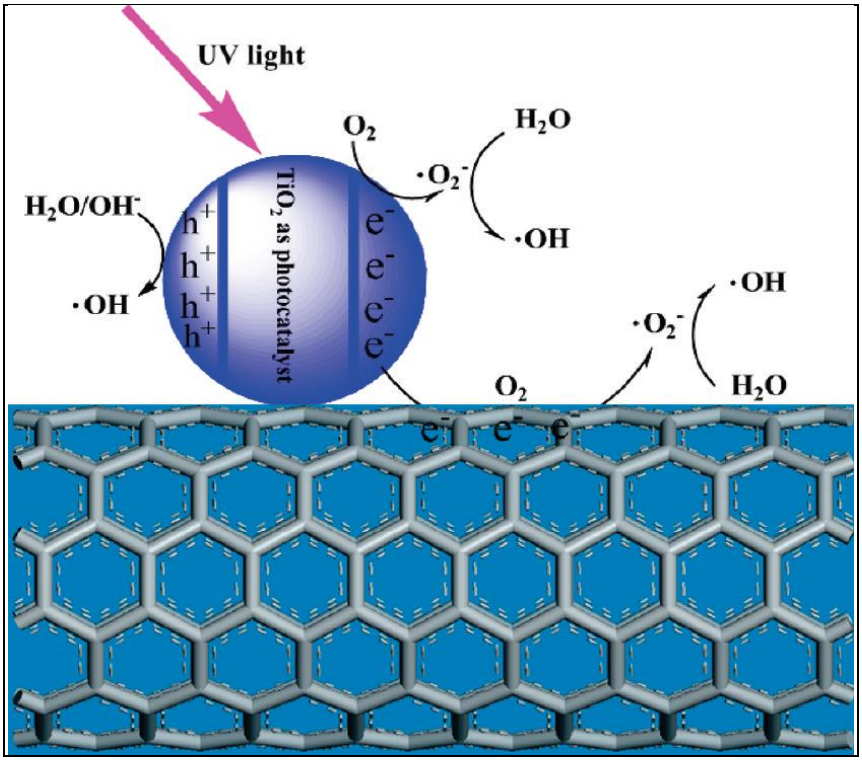


Figure 7.17: A mechanism demonstrating MWCNTs as electron trappers emitted from TiO_2 nanoparticles due to UV irradiation.[62]

The photocatalytic reaction kinetics on the titania surface can be evaluated in terms of rate constants according to a Langmuir-Hinshelwood model:

$$-\frac{dC}{dt} = kC \quad \text{(Equation 7.2)}$$

The integral form of equation 7.2 is: $-\ln\left(\frac{C}{C_0}\right) = kt$ (Equation 7.3), where C_o is the concentration when solar irradiation starts and k represents the photodegradation rate constant. The plots of -ln (C/Co) against irradiation time gives the slope = k. The results are presented in Figures 7.18 and 7.19. The reaction kinetics show that the degradation of EB by TiO_2-C composites followed pseudo-first order kinetics. Table 7.4 shows the rate constants for EB photodegradation by the TiO_2-0.2%C and TiO_2-10%C composite materials. The results show that the rate constants for TiO_2-0.2%C composites were remarkably higher than those for their corresponding TiO_2-10%C composites. Overall, the TiO_2-0.2%B-MWCNT

composite material showed the highest rate constant when compared to all the other composite materials. Thus, boron doping has a strong effect on the degradation efficiency of TiO_2-0.2%B-MWCNT composites. In addition to the electron trapping abilities of CNTs, boron in CNTs can adsorb O_2 molecules which can react with the excited electrons to yield more reactive radicals, thereby delaying the e^--h^+ recombination rate and enhancing the photocatalytic reactivity.

Kuvarega and co-workers[36] reported rate constants similar to ours at lower and higher concentrations of MWCNTs for N, Pd co-doped TiO_2-MWCNTs prepared by the sol-gel method. They reported rate constants of 3.84 x 10^{-2} min^{-1} for N, Pd co-doped TiO_2-0.5%MWCNT and 4.92 x 10^{-3} min^{-1} for N, Pd co-doped TiO_2-10%MWCNT for the photocatalytic degradation of Eosin Yellow under simulated solar irradiation. Wang and co-workers[11a] reported rate constants of 1.55 x 10^{-3} for TiO_2-20%MWCNTs composite material and 0.68 x 10^{-3} min for TiO_2 for the photocatalytic degradation of phenol under visible light. The results indicate increased photoreactive efficiency for lower concentrations of carbonaceous materials in TiO_2-C composites prepared by the sol-gel method.

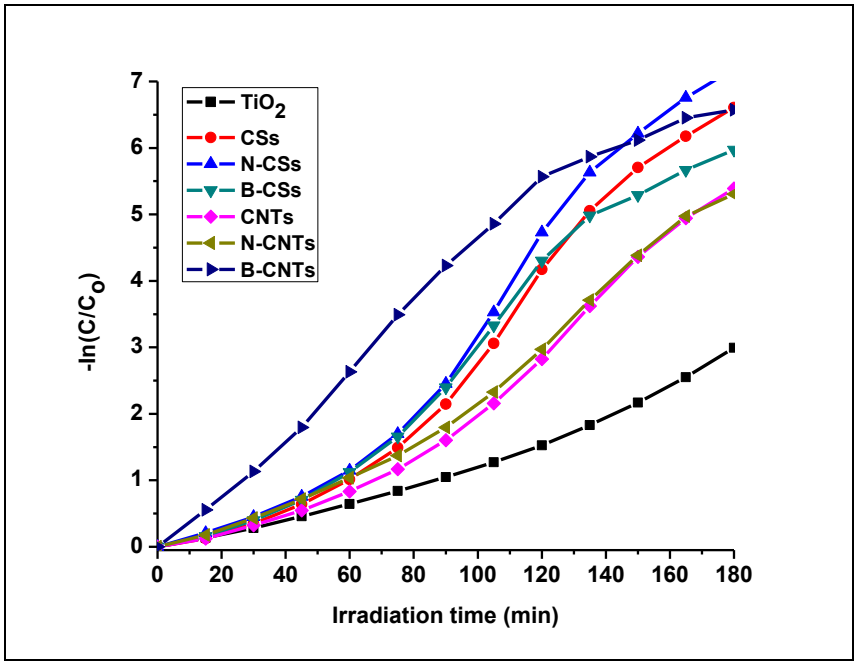


Figure 7.18: Kinetics of EB degradation by TiO_2-0.2%C composite materials.

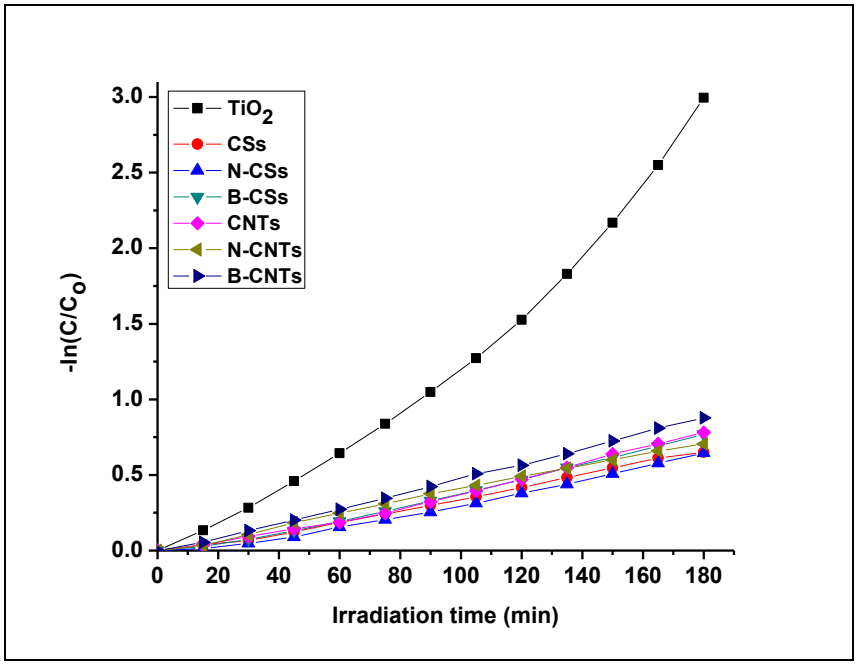


Figure 7.19: Kinetics of EB degradation by TiO_2-10%C composite materials.

Table 7.4: EB photodegradation rate constants under simulated solar irradiation.

Catalyst	Rate constant, k(min^{-1})
TiO_2	1.42 x 10^{-2}
TiO_2-0.2%CS	3.40 x 10^{-2}
TiO_2-0.2%N-CS	3.77 x 10^{-2}
TiO_2-0.2%B-CS	3.28 x 10^{-2}
TiO_2-0.2%MWCNT	2.61 x 10^{-2}
TiO_2-0.2%N-MWCNT	2.67 x 10^{-2}
TiO_2-0.2%B-MWCNT	4.14 x 10^{-2}
TiO_2-10%CS	3.54x 10^{-3}
TiO_2-10%N-CS	3.27 x 10^{-3}
TiO_2-10%B-CS	4.01 x 10^{-3}
TiO_2-10%MWCNT	4.06 x 10^{-3}
TiO_2-10%N-MWCNT	4.01 x 10^{-3}
TiO_2-10%B-MWCNT	4.80 x 10^{-3}

7.4 Conclusion

In summary, we successfully prepared TiO_2-C composite materials from various carbonaceous nanomaterials by a modified sol-gel method. TEM images revealed better homogeneous coverage of TiO_2 nanoparticles on TiO_2-0.2%C that on the TiO_2-10%C composites. XRD patterns of all composites confirmed that anatase was the main crystalline phase in the TiO_2 particles, whereas commercial TiO_2 showed both anatase and rutile crystal structures. In the case of TiO_2-C composites, the broad band between 20 and 25° in the XRD patterns, characteristic of the reflections associated with amorphous carbon was evident. Based on the larger intensity of the diffraction peaks, it might also be considered that the crystallinity is higher in commercial TiO_2 than in TiO_2-C composite materials. The Raman spectroscopy data confirmed the presence of the anatase TiO_2 phase and carbonaceous nanomaterials.

Introduction of carbonaceous nanomaterials into TiO_2 led to smaller TiO_2 particle sizes and doping produced better dispersion, which improved the efficiency of photocatalytic degradation. Moreover, the amount and type of carbon nanomaterial are important parameters in the adsorption and catalytic degradation of the EB. It was found that the addition of carbon at low concentration led to better photoactivity of TiO_2 in the degradation of EB. Boron-doping of MWCNTs gave the best photocatalyst to achieve synergism between B-MWCNTs and TiO_2 nanoparticles. This was associated with a delayed e^--h^+ recombination rate with increasing boron doping. The kinetic studies revealed that the photocatalytic degradation of EB followed pseudo first-order kinetics.

References

1. (a) N. Stock, J. Peller, K. Vinodgopal and P.V. Kamat, *Environ. Sci. Technol.*, 2000, **34**, 1747-1750; (b) S.K. Chaudhuri and B. Sur, *J. Environ. Eng.*, 2000, **126,** 583-594.
2. (a) S. Aryal, C.K. Kim, K.-W. Kim, M.S. Khil and H.Y. Kim, *Mater. Sci. Eng. C*, 2008, **28**, 75-79; (b) M. Stylidi, D.I. Kondarides and X.E. Verykios, *Appl. Catal. B: Environmental*, 2004, **47**, 189-201.
3. A. Fujishima, X. Zhang and D.A. Tryk, *Surf. Sci. Rep.*, 2008, **63**, 515-582.
4. T.K. Tseng, Y.S. Lin, Y.J. Chen and H. Chu, *Int. J. Mol. Sci.*, 2010, **11**, 2336-2361.
5. (a) T. Sugimoto, X. Zhou and A. Muramatsu, *J. Colloid Interface Sci.*, 2003, **259**, 43-52; (b) K. Song, J. Zhou, J. Bao and Y. Feng, *J. Am. Ceram. Soc.*, 2008, **91**, 1369-1371.
6. M. Ni, M.K.H. Leung, D.Y.C. Leung and K. Sumathy, *Renew. Sust. Energy Rev.*, 2007, **11**, 401-425.
7. S.M. Oh, S.S. Kim, J.E. Lee, T. Ishigaki and D.W. Park, *Thin Solid Films*, 2003, **435**, 252-258.
8. B. Xin, P. Wang, D. Ding, J. Liu, Z. Ren and H. Fu, *Appl. Surf. Sci.*, 2008, **254**, 2569-2574.
9. E.C. Buttler and A.P. Davis, *J. Photochem. Photobiol. A*, 1993, **70**, 273-283.
10. (a) R. Asahi, T. Morikawa, T. Ohwaki, K. Aoki and Y. Taga, *Science*, 2001, **293**, 269-271; (b) Y. Nosaka, M. Matsushita, J. Nishino and A.Y. Nosaka, *Sci. Technol. Adv. Mater.*, 2005, **6**, 143-148.
11. (a) W. Wang, P. Serp, P. Kalck and J.L. Faria, *J. Mol. Catal. A: Chemical*, 2005, **235**, 194-199; (b) C. Xu, R. Killmeyer, M.L. Gray and S.U.M. Khan, *Appl. Catal. B: Environmental*, 2006, **64,** 312-317; (c) M. Janus, B. Tryba, M. Inagaki and A.W. Morawski, *Appl. Catal. B: Environmental*, 2004, **52**, 61-67.
12. T. Ohno, *Water Science and Technology*, 2004, **49**, 159-163.
13. (a) W. Zhao, W. Ma, C. Chen, J. Zhao and Z. Shuai, *J. Am. Chem. Soc.*, 2004, **126**, 4782-4783; (b) I.E. Grey, C. Li and C. Macrae, *J. Solid State Chem.*, 1996, **127**, 240-247.
14. D. Chen, D. Yang, Q. Wang and Z. Jiang, *Ind. Eng. Chem. Res.*, 2006, **45**, 4110-4116.
15. A. Zaleska, *Physicochemical Problems of Mineral Processing*, 2008, **42**, 211-222.

16. (a) S.C. Roy, O.K. Varghese, M. Paulose and C.A. Grimes, *ACS Nano Lett.*, 2010, **4**, 1259-1278; (b) Y.H. Tseng, C.S. Kuo, C.H. Huang, Y.Y. Li, P.W. Chou, C.L. Cheng and M.S. Wong, *Nanotechnology*, 2006, **17**, 2490-2497.
17. A. García and J. Matos, *Open Mater. Sci. J.*, 2010, **4**, 2-4.
18. E. Ballesteros, M. Gallego and M. Valcarcel, *J. Chromatogr. A*, 2000, **869**, 101-110.
19. X. Cheng, A.T. Kan and M.B. Tomson, *J. Nanopart. Res.*, 2005, **7**, 555-567.
20. K. Yang, L.Z. Zhu and B.S. Xing, *Environ. Sci. Technol.*, 2006, **40**, 1855-1861.
21. R.Q. Long and R.T. Yang, *J. Am. Chem. Soc.*, 2001, **123**, 2058-2059.
22. X. Peng, Y. Li, Z. Luan, Z. Di, H. Wang, B. Tian, and Z. Jia, *Chem. Phys. Lett.*, 2003, **376**, 154-158.
23. C. Lu, Y.L. Chung and, K.F. Chang, *Water Res.*, 2005, **39**, 1183-1189.
24. M. Zarezade, S. Ghasemi and M.R. Gholami, *Catal. Sci. Technol.*, 2011, **1**, 279-284.
25. B. Gao, C. Peng, G.Z. Chen and G.L. Puma, *Appl. Catal. B*: *Environmental*, 2008, **85**, 17-23.
26. W. Wang, P. Serp, P. Kalck, C.G. Silva and J.L. Faria, *Mater. Res. Bull.*, 2008, **43**, 958-967.
27. X. Song, P. Gunawan, R. Jiang, S.S.J. Leong, K. Wang and R. Xu, *J. Haz. Mater.*, 2011, **194**, 162-168.
28. H. Qian, Y. Hu, Y. Liu, M. Zhou and C. Guo, *Mater. Lett.*, 2012, **68**, 174-177.
29. Y. Hu, Y. Liu, H. Qian, Z. Li and J. Chen, *Langmuir*, 2010, **26**, 18570-18575.
30. H. Zhang, G. Du, W. Lu, L. Cheng, X. Zhu and Z. Jiao, *Cryst. Eng. Comm.*, 2012, **14**, 3793-3801.
31. J. Xu, Y. Ao and M. Chen, *Mater. Lett.*, 2009, **63**, 2442-2444.
32. L.F. Velasco, M. Haro, J. Parmentier, R. Gadiou, C. Vix-Guterl and C.O. Ania, *J. Catalysts*, 2013, 178512/1-178512/9.
33. (a) B. Gao, G.Z. Chen and G.L. Puma, *Appl. Catal. B*: *Environmental*, 2009, **89**, 503-509; (b) D. Eder, *Chem. Rev.*, 2010, **110**, 1348-1385.
34. M. Terrones, A. Jorio, M. Endo, A.M. Rao, Y.A. Kim, T. Hayashi, H. Terrones, J.-C. Charlier, G. Dresselhaus and M.S. Dresselhaus, *Mater. Today*, 2004, **7**, 30-45.
35. J. Zhu, J. Zhang, F. Chen, K. Iino and M. Anpo, *Top. Catal.*, 2005, **35**, 261-268.
36. A.T. Kuvarega, R.W. M. Krause and B.B. Mamba, *J. Nanopart. Res.*, 2012, **14**, 776/1-776/16.
37. S. Wang, T. Cochell and A. Manthiram, *Phys. Chem. Chem. Phys.*, 2012, **14**, 13910-13913.

38. L. Wang, L. Shen, L. Zhu, H. Jin, N. Bimg and L. Wang, *J. Nanomaterials*, 2012, 1-6.
39. Y. Ou, J. Lin, S. Fang and D. Liao, *Chem. Phys. Lett.*, 2006, **429**, 199-203.
40. Y.R. Smith, A. Kar and V.R. Subramanian, *Ind. Eng. Chem. Res.*, 2009, **48**, 10268-10276.
41. Y. Xie, S.H. Heo and S.H. Yoo, *Nanoscale Res.*, 2010, **5**, 603-607.
42. L. Shen, X. Zhang, H. Li, C. Yuan and G. Cao, *J. Phys. Chem. Lett.*, 2011, **2**, 3096-3101.
43. W.F. Zhang, Y.L. He, M.S. Zhang and Q. Chen, *J. Phys. D: Appl. Phys.*, 2000, **33**, 912-916.
44. C.-Y. Yen, Y.-F. Lin, C.-H. Hung, Y.-H. Tseng, C.-C.M. Ma, M.-C. Chang and H. Shao, *Nanotechnology*, 2008, **19**, 045604/1-045604/11.
45. H.C. Choi, Y.M. Jung and S.B. Kim, *Vib. Spectrosc.*, 2005, **37**, 33-38.
46. J.Zhang, M. Li, Z. Feng, J. Chen and C. Li, *J. Phys. Chem. B*, 2006, **110**, 927-935.
47. D. Bersani, P.P. Lottici and X.-Z. Ding, *Appl. Phys. Lett.*, 1998, **72**, 73-75.
48. B. Chai, T. Peng, X. Zhang, J. Mao, K. Li and X. Zhang, *Dalton Trans.*, 2013, **42**, 3402-3409.
49. F. Wang and K. Zhang, *Curr. Appl. Phys.*, 2012, **12**, 346-352.
50. L.-W. Zhang, H.-B. Fu and Y.-F. Zhu, *Adv. Funct. Mater.*, 2008, **18**, 2180-2189.
51. (a) J. Zhong, F. Chen, and J.L. Zhang, *J. Phys. Chem. C*, 2010, **114**, 933-939; (b) B.K. Vijayan, N.M. Dimitrijevic, D.F. Shapiro, J.S. Wu and K.A. Gray, *ACS Catal.*, 2012, **2**, 223-229.
52. S. Hu, F. Li and Z. Fan, *Bull. Korean. Chem. Soc.*, 2012, **33**, 1895-1899.
53. Y. Yu, J.C. Yu, J.-G. Yu, Y.-C. Kwok, Y.-K. Che, J.-C. Zhao, L. Ding, W.-K. Ge and P.-K. Wong, *Appl. Catal. A: General*, 2005, **289**, 186-196.
54. A. Fujishima, T.N. Rao and D.A. Tryk, *J. Photochem. Photobiol. C: Photochem. Rev.*, 2001, **1**, 1-21.
55. K. Nagaveni, M.S. Hegde, N. Ravishankar, G.N. Subbanna and G. Madras, *Langmuir*, 2004, **20**, 2900-2907.
56. A. Alonso-Tellez, R. Masson, D. Robert, N. Keller and V. Keller, *J. Photochem. Photobiol. A: Chemistry*, 2012, **250**, 58-65.
57. C.M. Chan, S. Trigwell and T. Duerig, *Surf. Interface Anal.*, 1990, **15**, 349-354.
58. L. Chen, Y. Ho, W. Guo, C. Huang and T. Pan, *Electrochim. Acta*, 2009, **54**, 3884-3891.

59. Z. Peining, A.S. Nair, Y. Shengyuan, P. Shengjie, N.K. Elumalai and S. Ramakrishna, *J. Photochem. Photobiol. A: Chemistry*, 2012, **231**, 9-18.
60. H. Wang, H.-L. Wang and W.-F. Jiang, *Chemosphere*, 2009, **75**, 1105-1111.
61. D. Robert, S. Parra, C. Pulgarin, A. Krzton and J.V. Weber, *Appl. Surf. Sci.*, 2000, **167**, 51-58.
62. Y.-J. Xu, Y. Zhuang and X. Fu, *J. Phys. Chem. C*, 2010, **114**, 2669-2676.
63. L. Yang, S. Jiang, Y. Zhao, L. Zhu, S. Chen, X. Wang, Q. Wu, J. Ma, Y. Ma and Z. Hu, *Angew. Int. Ed.*, 2011, **50**, 1-6.
64. X. Hu, Y. Wu, H. Li and Z. Zhang, *J. Phys. Chem. C*, 2010, **114**, 9603-9607.
65. V. Saini, Z. Li, S. Bourdo, V.P. Kunets, S. Trigwell, A. Couraud, J. Rioux, C. Boyer, V. Nteziyaremye, E. Dervishi, A.R. Biris, G.J. Salamo, T. Viswanathan and A.S. Biris, *J. Appl. Phys.*, 2011, **109**, 014321/1-014321/6.

Appendix E: Supplementary material

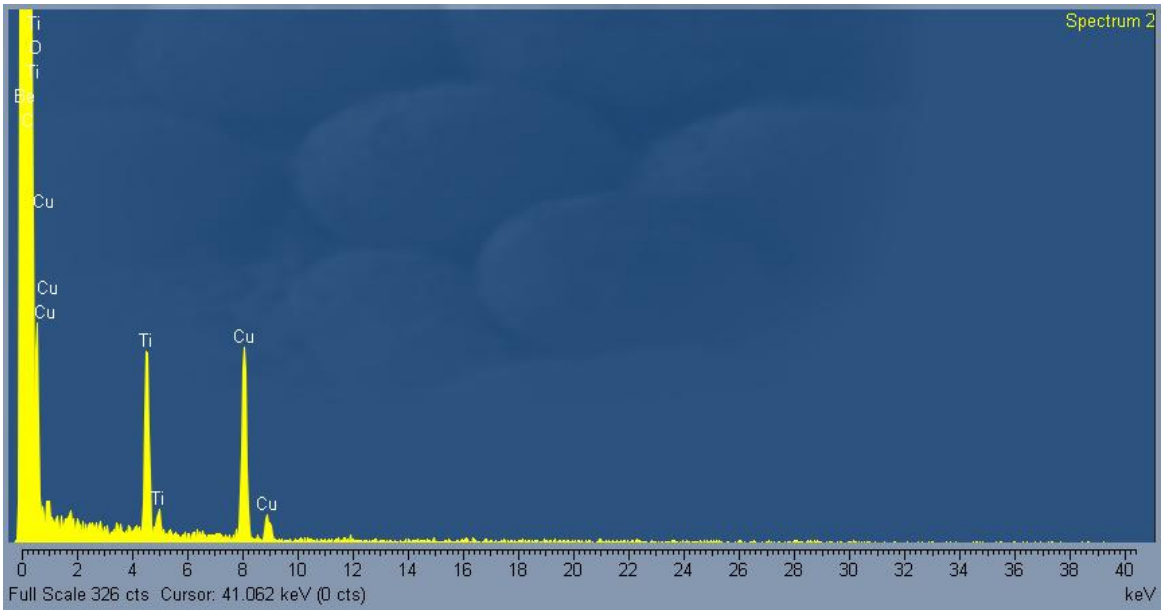


Figure S7.1: EDX spectrum of TiO_2-0.2%B-MWCNTs composite material.

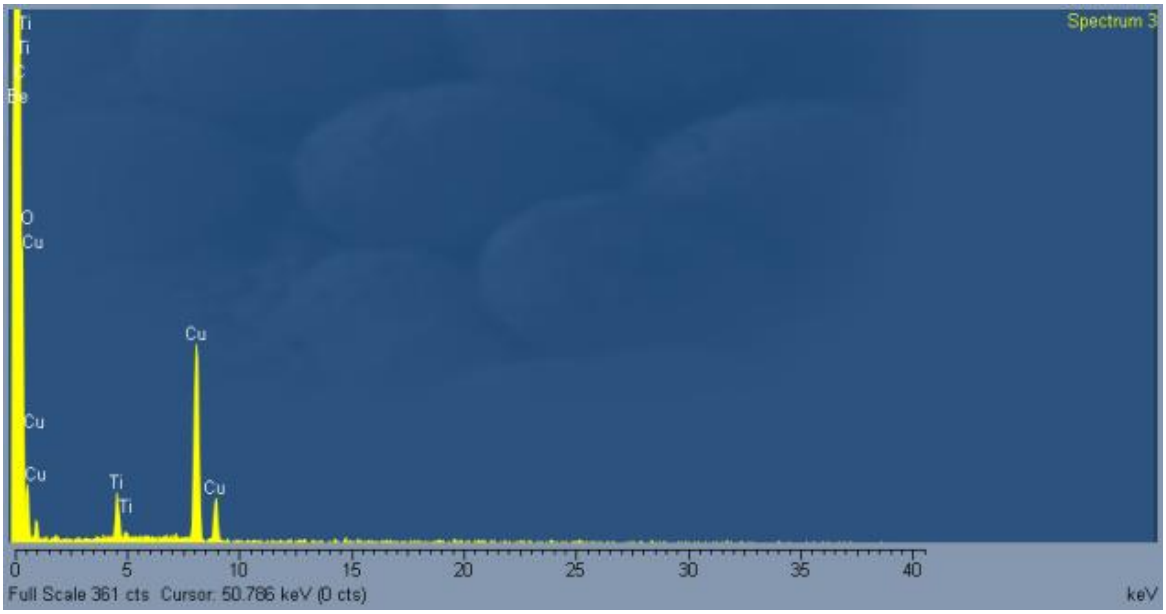


Figure S7.2: EDX spectrum of TiO_2-10%B-MWCNTs composite material.

CHAPTER 8

General Conclusions and Recommendations

The synthesis of N-MWCNTs and B-MWCNTs was achieved by the CVD method in a horizontal reactor over an Fe-Co/$CaCO_3$ catalyst and the morphology of the new materials was confirmed using various characterization techniques. N-CSs and B-CSs have also been grown by the CVD method in a vertical furnace without using a catalyst. The nitrogen and boron sources used for the doping process were acetonitrile and trimethyl borate, respectively. In the chapters 3-6, investigations of the effect of the doping of MWCNTs and CSs with N and B doped were discussed in detail. The doped MWCNTs and CSs were fully studied using a range of techniques such as TEM, SEM, XRD, TGA, BET, XPS, FT-IR, CN elemental analysis and Raman spectroscopy.

A significant influence of the growth temperature and acetonitrile vaporization temperature on the yield, diameter, quality, morphology and thermal stability of the N-MWCNTs was observed. Successful nitrogen doping was evidenced by the presence of the compartmentalized bamboo structures in the MWCNT walls. The bamboo compartment distance decreased with increase in growth temperature and CH_3CN vaporization temperature due to the increased nitrogen content in N-MWCNTs. Higher growth temperatures led to the formation of a mixture of MWCNTs and solid CSs. Raman spectroscopy investigations confirmed that N-MWCNTs have a low degree of graphitization, indicating the presence of defects and disorder in the walls of the N-MWCNTs. The surface defects in the N-MWCNTs were evidenced by the roughness of the N-MWCNT surface.

The study of N-CSs revealed that the incorporated N content, diameter and the yield of N-CSs could be controlled by changing the C_2H_2 and Ar gas flow rates. The TGA data showed that the N-CSs and CSs have high purity (> 99%). N-containing CSs showed a lower degree of disorder when compared to undoped CSs and this closely correlated with the total gas flow rate used. The N-doped CSs showed lower thermal stability and degree of graphitization as compared to the undoped CSs, confirming more defects in the N-CSs.

The effect of using trimethyl borate and various growth temperatures on the production of B-MWCNTs over an Fe-Co/$CaCO_3$catalyst was established. It was found that these two factors led to the formation of rough surfaces and bamboo structured tubes. An increase in reaction temperature during the synthesis of B-MWCNTs resulted in an increase in the average outer diameter of the tubes. At temperatures in the range of 850-900 °C, the formation of other structures such as catalyst filled tubes, solid and core-shell CSs was noted. The study showed that the optimum temperature for producing B-MWCNTs was 800 °C. These core-shell CSs were believed to have formed by a non-catalytic route at high temperature.

Large amounts B-CSs with a core-shell structure were successfully grown at 900 °C from C_2H_2 and trimethyl borate without using any catalyst. The effect of trimethyl borate was clearly significant. This effect was evidenced by TEM studies which showed different morphologies of solid undoped CSs and core-shell BCSs. The morphology, size and yield of the B-CSs was tuned by changing the ratio of the Ar:H_2 and the type of furnace (horizontal vs. vertical furnace).

The purpose of this study was to synthesize boron and nitrogen doped MWCNTs and CSs using the CVD method. These carbon nanomaterials were then used as supports for a TiO_2photocatalystfor the degradation of erythrosine B. Factors such as carbon dopants (B doped, N doped and undoped MWCNTs and CSs), as well as TiO_2:C ratios were explored. The introduction of nitrogen and boron defects in the carbon nanostructures resulted in a strong interaction with the TiO_2 catalysts and this influenced the photocatalytic activity of the TiO_2. TEM studies showed a good coverage of the carbon nanomaterials by anatase TiO_2 at lower C percentages. The lower loading of C materials displayed an improved ability to degrade EB when compared to TiO_2 and higher load C materials.TiO_2-0.2%B-MWCNT showed the highest photoactivity efficiency. From the results, it can be concluded that lower percentages of carbon nanomaterials and doping does improve the photocatalytic properties of TiO_2. In the degradation of erythrosine B, the TiO_2-10%C showed poor performance as compared to commercial TiO_2 and TiO_2-0.2%C composites. These findings confirm the unique properties of the TiO_2-doped carbons nanocomposites as potential functional water-treatment materials.

It can be recalled that during the synthesis of B-CSs, the quartz tube cracked in the middle due to the reaction of boric acid and silica tube. This relates to the decomposition of trimethyl borate which slowly degrades in the presence of moisture or air. It is therefore recommended

that other boron sources which are safe to use and do not decompose as easily be utilized in the production of boron doped carbons.

Determination of the optimum B and N content in the B doped and N doped carbons that can give maximum photoactivity in the degradation of erythrosine B is highly recommended. The remarkable photocatalytic activity of the 0.2%B-MWCNT loading with a boron content of 1.6% towards the degradation of erythrosine B needs to be further investigated.